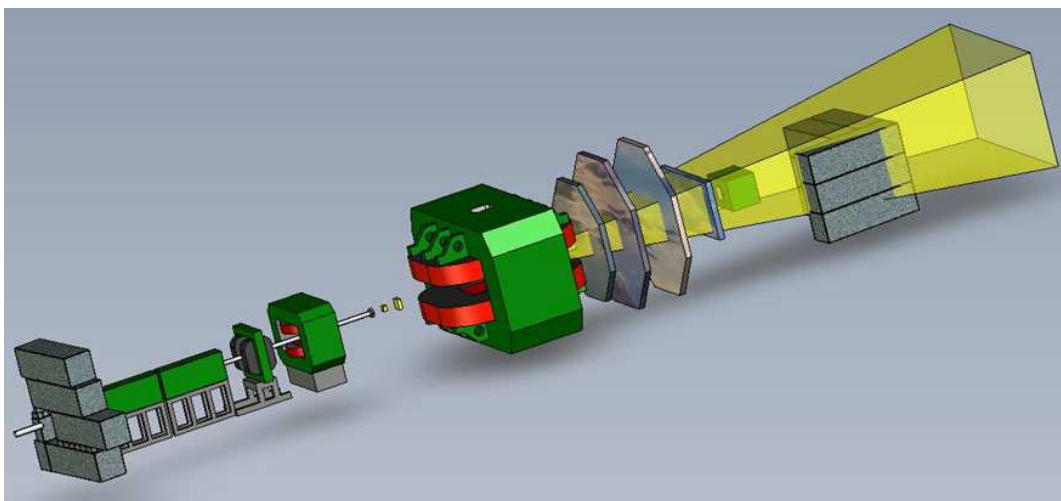# Conceptual Design Report

## BM@N — Baryonic Matter at Nuclotron



## Study of Strange Matter Production in Heavy-Ion Collisions at the Nuclotron

# Abstract

JINR Nuclotron will provide the heavy-ion beams with energies up to 6 A·GeV for isospin symmetric nuclei and 4.65 A·GeV for Au nuclei. In the central heavy-ion collisions at these energies, the nuclear densities of about four times nuclear matter density can be reached. These conditions are well suited to investigate the equation-of-state of dense nuclear matter, which plays a central role for the dynamics of core collapse supernovae and for the stability of neutron stars. At the same time, the heavy-ion collisions are a rich source of strangeness, and the coalescence of kaons with lambdas or lambdas with nucleons will produce a vast variety of multi-strange hyperons or light hypernuclei, respectively. Even the production of light double-hypernuclei or double-strange dibaryons is expected to be measurable in the heavy-ion collisions at Nuclotron energies. The observation of those objects would represent a breakthrough in our understanding of strange matter, and would pave the road for the experimental exploration of the third (strangeness) dimension of the nuclear chart. The extension of the experimental program is related with the study of in-medium effects for vector mesons and strangeness decaying in hadronic modes. The studies of the N+N and N+A reactions for the reference is assumed.

For these purposes, it is proposed to install an experimental setup in the fixed-target hall of Nuclotron with the final goal to perform a research program focused on the production of strange matter in the heavy-ion collisions at beam energies between 2 and 6 A·GeV. The basic setup will comprise a large-acceptance dipole magnet with inner tracking detector modules based on double-sided silicon micro-strip sensors. The outer tracking will be based on the drift chambers and straw tube detector. Particle identification will be based on the time-of-flight measurements.

# Participants

T.O.Ablyazimov[b], P.G.Akishin[b], V.P.Akishina[b], V.D.Aksinenko[a], A.V.Alfeev[a], V.S.Alfeev[a], V.V.Avdejchikov[a], A.V.Averianov[a], S.V.Avramenko[a], V.A.Babkin[a], S.A.Baginyan[b], V.P.Balandin[a], S.N.Basylev[a], D.V.Belyakov[b], I.V.Boguslavsky[a], S.P.Chernenko[a], K.Davkov[a], V.Davkov[a], V.I.Demidova[a], O.Yu.Derenovskaya[b], V.B.Dunin[a], O.V.Fateev[a], Yu.I.Fedorov[a], O.P.Gavrishchuk[a], A.I.Golokhvastov[a], V.M.Golovatyuk[a], N.Grigalashvili[a], Yu.V.Gurchin[a], A.P.Ierusalimov[a], E.-M.Ilgenfritz[a], A.Yu.Isupov[a], V.V.Ivanov[b], Yu.-T.Karachuk[a], G.D.Kekelidze[a], V.D.Kekelidze[a], S.V.Khabarov[a], V.S.Khabarov[a], A.N.Khrenov[a], V.I.Kireev[a], Yu.T.Kiryushin[a], P.I.Kisel[b], E.S.Kokoulina[a], V.I.Kolesnikov[a], A.M.Korotkova[a], N.A.Kuzmin[a], A.V.Kuznezov[a], A.K.Kurilkin[a], P.K.Kurilkin[a], E.A.Ladygin[a], V.P.Ladygin[a], N.B.Ladygina[a], E.I.Litvinenko[c], S.P.Lobastov[a], J.Lukstins[a], D.T.Madigozhin[a], A.I.Malakhov[a], V.V.Mialkovsky[a], Yu.A.Murin[a], S.N.Nagorny[a], V.A.Nikitin[a], P.V.Nomokonov[a], O.V.Okhrimenko[a], A.N.Parfenov[a], V.V.Pavljuchkov[a], V.N.Pechenov[a], O.Yu.Pechenova[a], V.D.Peshekhonov[a], Yu.P.Petukhov[a], S.M.Piyadin[a], A.M.Raportirenko[b], S.G.Reznikov[a], I.A.Rufanov[a], P.A.Rukoyatkin[a], A.V.Shabunov[a], V.Shejnast[b], A.V.Shutov[a], I.V.Slepnev[a], V.M.Slepnev[a], V.I.Suzdalev[a], S.Yu.Sychkov[a], A.A.Terekhin[a], A.V.Terlezky[a], O.V.Teryaev[d], V.V.Tikhomirov[a], V.D.Toneev[d], N.D.Topilin[a], I.A.Tyapkin[a], V.A.Vasendina[a], T.A.Vasiliev[a], A.V.Vishnevsky[a], N.M.Vladimirova[a], S.V.Volgin[a], V.V.Voronyuk[a], A.I.Yukaev[a], Yu.V.Zanevsky[a], A.P.Zinchenko[a], P.V.Zrelov[b], V.N.Zryuev[a]
*Joint Institute for Nuclear Research, Dubna, Russia:*
[a] *Veksler and Baldin Laboratory of High Energy Physics*
[b] *Laboratory of Information Technologies*
[c] *Frank Laboratory of Neutron Physics*
[d] *Bogolyubov Laboratory of Theoretical Physics*

J.Heuser, P.Senger
*GSI Helmholtz-Zentrum für Schwerionenforschung, Darmstadt, Germany*

I.V.Kisel, Yu.Vassiliev
*Goethe University, Frankfurt, Germany*

E.L.Bratkovskaya
*Institute for Theoretical Physics & Frankfurt Institute for Advanced Studies, Goethe University, Frankfurt, Germany*

W.Cassing, V.Konchakovski, O.Linnyk
*Institute for Theoretical Physics, Gissen University, Germany*

V.V.Andreev, N.V.Maksimenko
*Gomel State Technical University, Gomel, Belarus*

S.G.Genchev, I.S.Radkov, S.V.Radnev, G.Rashevski, A.Zenkov
*Laboratory for Technical Developments and Applications, BAS, Sofia, Bulgaria*

B

J.Aichelin, C.Hartnack
*SUBATECH, Nantes University, Ecole des Mines, Nantes, France*

M.I.Barznat, K.K.Gudima
*Institute of Applied Physics, ASM, Kishinev, Moldova*

D.Lipchinski, J.Popovichi
*Advanced Research Institute for Electrical Engineering, Bucharest, Romania*

A.V.Baranova, G.A.Bogdanova, E.E.Boos, A.A.Ershov, D.E.Karmanov, M.G.Korolev, E.O.Kurbatov, V.V.Lenok, I.P.Lokhtin, L.V.Malinina, M.M.Merkin, A.M.Snigirev, V.Yu.Volkov, A.G.Voronin
*Skobeltsyn Institute of Nuclear Physics, Moscow State University, Moscow, Russia*

F.F.Guber, A.P.Ivashkin, A.B.Kurepin, A.S.Sadovsky, V.V.Tiflov, E.A.Usenko
*Institute for Nuclear Research of RAS, Moscow, Russia*

S.V.Donskov, V.A.Gapienko, S.N.Golovnya, A.G.Kholodenko, Yu.V.Mikhaylov, V.A.Polyakov, V.N.Riadovikov, A.A.Semak, Yu.P.Tsupa, M.N.Ukhanov, A.P.Vorobiev
*State Scientific Center of RF — Institute of High Energy Physics, Protvino, Russia*

V.V.Syshchenko, I.E.Vnukov
*Belgorod State University, Belgorod, Russia*

A.Yu.Kutov
*DM of Komi National Center, Ural Branch of RAS, Syktyvkar, Russia*

M.Martinska, J.Urban, S.Vokal
*P.-J.Shafarik University, Koshice, Slovakia*

M.Janek, B.Trpisova
*Physics Department, University of Zilina, Zilina, Slovak Republic*

V.E.Kovtun, A.L.Shkilyov, I.I.Zaljubovsky
*V.N.Karazin Kharkov National University, Kharkov, Ukraine*

V.N.Lyashchenko, S.N.Reva, A.A.Turchin
*National Science Center Kharkov Institute of Physics and Technology, Kharkov, Ukraine*

A.Kugler, V.Kushpil, O.Svoboda, P.Tlusty
*Nuclear Physics Institute, Academy of Sciences of Czech Republic, Rez, Czech Republic*

Z.Deng, X.Huang, Y.Li, J.Wang, Y.Wang, X.Zhu
*Department of Engineering Physics, Tsinghua University, Beijing, China*

I.A.Bolshakova, S.Gumen, V.Hayduchok, V.Ivanets, I.Kogut, B.Kopko, Y.Kost, N.Kovaljova, L.Kozachenko, M.Kravets, A.Levchenko, O.Makido, A.Moroz, Y.Nakalov, I.Palynyak, L.Rakhlin, H.Shapovalov, F.Shurygin, I.Sushko, S.Tymoshyn, H.Voroshylo, V.Yerashok, Y.Zagachevskyi
*Lviv Polytechnic National University, Lviv, Ukraine*

D

# Contents

# Chapter 1

# Introduction

High-energy heavy-ion collisions offer the unique possibility to create and investigate hot and dense matter in the laboratory. In the collision zone, the matter is heated up and compressed for a very short period of time. If the energy density in the formed fireball is sufficiently large the quark-gluon substructure of nucleons becomes visible. At moderate temperatures, nucleons are excited to short-lived states (baryonic resonances) which decay by the emission of (one or several) mesons. At higher temperatures, also baryon-antibaryon pairs are created. This mixture of baryons, antibaryons and mesons, all strongly interacting particles, is denoted as hadronic matter, or baryonic matter if baryons dominate. At even higher temperatures or densities the hadrons melt, and the constituents, the quarks and gluons, form a new phase, the Quark-Gluon Plasma (QGP). Relativistic heavy-ion collision experiments thus provide the opportunity to address fundamental aspects of Quantum Chromodynamics (QCD):

• the equation-of-state (EoS) of strongly interacting matter at high temperatures and high net-baryon densities;

• the microscopic structure of strongly interacting matter as a function of temperature and baryon density;

• the in-medium modifications of hadrons which might provide information on the onset of chiral symmetry restoration.

The nuclear matter EoS plays an important role for the dynamics of core collapse supernova and for the stability of neutron stars. In type II supernova explosions, the symmetric nuclear matter is compressed to 2—3 times saturation density $\rho_0$. These conditions are realized in heavy-ion collisions at BEVALAC/SIS18 beam energies, although the temperatures reached in nuclear collisions are higher than those in the core of a supernova. Heavy-ion experiments at BEVALAC/SIS18 (1—2 A·GeV) have explored the collective flow of nucleons and studied the production of pions and strange particles. In particular the data on $K^+$ production obtained at the SIS18 provided evidence for a soft nuclear matter EoS and for the modification of kaon/antikaon properties in the dense hadronic environment.

The experiments at BNL-AGS (2—11 A·GeV) have measured the yields and momentum spectra of various particle species in heavy-ion collisions and provided information on the collective flow of hadrons. These data have established the scenario of an expanding and approximately thermalized source with a common chemical freeze-out of all particles. A major achievement of the experiments at AGS was the measurement of the excitation function of collective flow of protons $v_2$ which is linked to the EoS of dense nuclear matter.

Furthermore, experiments at CERN-SPS (20—158 A·GeV) extended the list of hadrons observed in heavy-ion collisions up to multi-strange hyperons and confirmed the picture of

an almost chemically equilibrated fireball. The particle yields and event-wise fluctuations measured in Pb+Pb collisions exhibit intriguing features at the low SPS energies, which have been interpreted as signatures for the onset of deconfinement.

Whereas the ratio of produced mesons to baryons in the fireball increases with collision energy, i.e. the baryon chemical potential decreases, the Nuclotron energy range of 2—6 A·GeV produces a baryon dominated fireball contrary to upper SPS or even RHIC energies. The baryon densities expected in such collisions are shown in Fig. 1.1 as a function of time for central Au+Au collisions at different beam energies as calculated with the QGSM transport model [1]. The Fig. 1.1 illustrates that at Nuclotron beam energies the nucleon densities in the collision zone of two gold nuclei exceed the saturation density by a factor of 3—4. At these densities the nucleons start to overlap, and it is expected that under such extreme conditions the onset of chiral symmetry restoration might occur although the quarks are still confined. In this case, the bulk properties (e.g. the energy density) are dominated by quarks which occupy the Fermi sea, whereas baryons represent the excited states. Due to the increase of the degrees of freedom with respect to hadronic matter this particular state can be regarded as a new phase of matter, where quarks and baryons coexist. This so called "quarkyonic" phase [2] is predicted to be located at large baryo-chemical potentials and moderate temperatures, and, therefore, may be produced in heavy-ion collisions at Nuclotron beam energies (see Fig. 1.2).
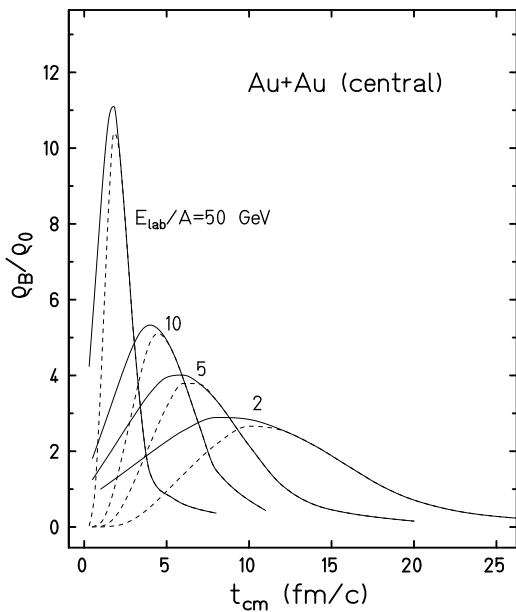


Figure 1.1: Nuclear density reached in the reaction volume of two colliding Au nuclei at various beam energies as a function of time (taken from [1]).
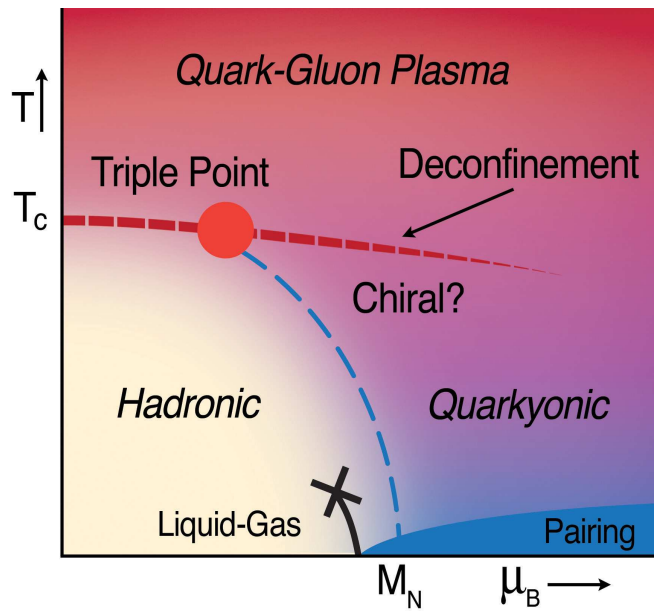
Figure 1.2: Sketch of the QCD Phase diagram (taken from [2]).

The latter expectation is supported by lattice QCD (lQCD) calculations that suggest a phase transition to partonic degrees of freedom to occur at a critical temperature $T_c \approx 160$ MeV, which corresponds to a critical energy density of $\epsilon_c \sim 0.5$ GeV/fm$^3$. These energy densities are expected to be reached at top Nuclotron energies in the center of the fireball since the energy density of normal nuclear matter corresponds to $\sim 0.15$ GeV/fm$^3$. Furthermore, the QCD theory describes hadrons as many-body bound or resonant states

of partonic constituents. While the properties of hadrons are rather well known in free space (embedded in a nonperturbative QCD vacuum), the mass and lifetime of hadrons in a baryonic and/or mesonic environment are a subject of current research with the goal to achieve a better understanding of the strong interaction and the nature of confinement. In this context the modification of hadron properties in nuclear matter is of fundamental interest (cf. [3–14] for the leading concepts) since QCD sum rules [4,7,15] as well as QCD inspired effective Lagrangian models [3,6,8–13] predict significant changes of hadrons and in particular strange ($K$, $\bar{K}$ and $K^*$) as well as vector ($\rho$, $\omega$ and $\phi$) mesons properties with increasing of nuclear density $\rho_N$ and/or temperature $T$.

The relevant degrees of freedom at Nuclotron energies are first of all the nucleons and their excited states followed by light and strange mesons (and their excitations). As mentioned above also the partonic degrees of freedom should show up in small space-time volumes and leave their traces in final hadronic observables. Since charm degrees of freedom are subthreshold at Nuclotron energies, the focus will be on hadrons with strangeness, which are early produced in the collision and not present in the initial state of the two colliding nuclei unlike nucleons made up from light $(u, d)$-quarks.

Furthermore, particle correlations — in particular strange particle correlations — might serve as an indication for a phase coexistence, which is expected to cause clustering or clumping of particles. Non-statistical fluctuations of charges, particle abundances or mean transverse momenta measured event-by-event have been proposed as a signature for critical opalescence, which might occur close to the critical endpoint in the phase diagram of strongly interacting matter.

In order to obtain a consistent picture one has to investigate a large set of observables and to search for a non-monotonous behaviour in the excitation functions. The quest is to identify signatures of the hadron-parton mixed phase at Nuclotron energies and to explore the properties of hadrons (and their excited states) at high baryon density in order to find out the way to chiral symmetry restoration. It is obvious that those observables, which are generated in the early phase of the collision, are the most promising candidates in this respect. One of the observables developed early is the elliptic flow $v_2$ as it is strongly related to the initial anisotropic fireball shape in coordinate space. Higher order harmonics $v_3, v_4$ in the azimuthal angular distribution of hadrons — as observed at RHIC energies — might provide further information on the transport properties of the fireball constituents.

## 1.1 Strange and multi-strange hadrons in a hot and dense nuclear medium

The in-medium properties of kaons have been primarily investigated due to their relevance for the neutron star phenomenology and for kaonic atoms. In the interior of a neutron star a strongly attractive kaon-nucleon interaction may lead to kaon condensation as suggested by Kaplan and Nelson [16]. The theoretical research work on the topic of in-medium properties of hadrons was triggered also in part by the early suggestion of Brown and Rho [17], that the modifications of hadron masses should scale with the scalar quark condensate $\langle q\bar{q}\rangle$ at finite density. The first attempts to extract the antikaon-nucleus potential from the analysis of kaonic-atom data were in favor of very strong attractive potentials of the order of $-150$ to $-200$ MeV close to normal nuclear matter density $\rho_0$ [18,19]. However, in-medium self-consistent calculations based on a chiral Lagrangian [20,21] or coupled-channel G-matrix

theory (within meson-exchange potentials) [22] predicted an only moderate attractive depth of $-50$ to $-80$ MeV at density of $\rho_0$.

The in-medium modification of kaon/antikaon properties can be explored experimentally in relativistic heavy-ion collisions at moderate bombarding energies. Transport models have revealed [23–30] that the collective flow pattern of $K^+$ mesons [23] as well as the abundance and the spectra of antikaons depend on the in-medium modifications of these particles. The comparison of these calculations with experimental results on $K^\pm$ production in nucleus-nucleus collisions at SIS energies of 1—2 A·GeV [31,32] allowed for a quantitative determination of these modifications for kaons, whereas for antikaons having a broad and structured spectral function the theoretical tools have still to be further developed.

The problem with the antikaon potential at finite baryon density is that the antikaon-nucleon amplitude in the $I = 0$ isospin channel is dominated by the $\Lambda(1405)$ resonant structure [33], which in free space is only 27 MeV below the $\bar{K}N$ threshold. It is presently not clear whether this physical resonance is a real excited state of a strange baryon, or it is some short living intermediate state, which can be generated dynamically in a coupled channel unitarized approach using a realistic meson-baryon interaction. The coupling between the $\bar{K}N$ and $\pi Y$ ($Y = \Lambda, \Sigma$) channels is essential in these calculations and therefore the in-medium properties of other particles enter the calculation of the pole position and the width of the $\Lambda(1405)$ in matter.

It has also been shown that a self-consistent treatment of the $\bar{K}$ self energy has a strong impact on the scattering amplitudes [20–22, 28, 34] and thus on the in-medium properties of the antikaon. Due to the complexity of this many-body problem the actual antikaon self energy (or potential) is still a matter of debate. Information on strange vector meson ($K^*$) properties in the medium is not available up to now, these excited states will open up a new window at the Nuclotron.

Present experimental facilities are too limited in energy (1.25 A·GeV is the highest energy presently available for Au+Au collisions at the SIS). One needs excitation functions for different symmetric systems, in which different densities are achieved. The theoretical calculations predict that the onset of kaon condensation should yield a sudden increase of the antikaon yield at a few times the saturation density $\rho_0$. Thus measuring the excitation function of $K^-$ in heavy-ion reactions above $\sim 2$ A·GeV would immediately give a lower limit of the baryon density, at which such a condensate could be obtained.

The detailed comparison of transport simulations involving different in-medium scenarios with experimental data show that we are still far away from a consistent understanding of in-medium strangeness production (see the review [35] for details and references therein). Thus, similar to the light vector meson sector probed predominantly by dilepton measurements, new developments are required from both sides, theory and experiment.

## 1.2   Study of in-medium effects of vector mesons

An experimental evidence for the modification of vector mesons has been obtained from the enhanced production of lepton pairs above known sources in nucleus-nucleus collisions at SPS energies [36, 37]. As proposed by Li, Ko, and Brown [38], the observed enhancement in the invariant mass range of $0.3 \leq M \leq 0.7$ GeV might be due to a shift of the $\rho$ meson mass following Brown-Rho scaling [3] or the Hatsuda and Lee sum rule prediction [4]. The microscopic transport studies of these mesons within the HSD and UrQMD models [26, 39–41] have given support for this interpretation [38]. On the other hand, also more

conventional approaches that describe a melting of the $\rho$ meson in the medium due to the strong hadronic coupling (along the line of Refs. [5, 6, 8, 10, 13]) have also been found to be compatible with the early CERES data [10, 39, 42–44].

This ambiguous situation has been clarified to some extent by the NA60 collaboration because the invariant mass spectra for $\mu^+\mu^-$ pairs from In+In collisions at 158 A·GeV favored clearly the "melting $\rho$" scenario [45]. Also the latest data from the CERES collaboration (with enhanced mass resolution) [46] show a preference for the "melting $\rho$" scenario [47–52]. At large invariant masses above 1 GeV the dilepton yield is dominated by the radiation from the QGP (see the recent PHSD study [52] and references therein).

In 2007 the PHENIX collaboration has presented the first dilepton data from p+p and Au+Au collisions at Relativistic Heavy Ion Collider (RHIC) energies of $\sqrt{s} = 200$ GeV [53], which show an even larger enhancement in Au+Au reactions (relative to p+p ones) of the invariant mass regime from 0.2 to 0.6 GeV/c$^2$ than the data at SPS energies [45, 46]. The question arises if this sizeable enhancement can be attributed to in-medium modifications of the $\rho$ and $\omega$ mesons (as at SPS energies) or the enhancement is in part due to new radiative channels [52] from the strongly-interacting Quark-Gluon Plasma (sQGP). Detailed calculations within the PHSD approach have shown that none of these scenarios is able to reproduce the observed enhancement. This issue is even more exciting because the recent data on dileptons from the STAR collaboration [54] can well be reproduced by the PHSD model [55] including the dominant partonic as well as hadronic production channels. Future experiments at RHIC will have to clarify the situation.

Moreover, already around 1990 the dileptons have been measured in heavy-ion collisions at BEVALAC by the DLS collaboration [56] at incident energies of 1—2 A·GeV. For about a decade these data could not be reproduced by the theoretical models even after including different in-medium scenarios like collisional broadening or the assumption of dropping masses of vector mesons [41, 57, 58]. This fact named "DLS-puzzle" has been clarified in 2008:
i) from the experimental side, where the HADES collaboration has independently confirmed the DLS measurements [59];
ii) from the theoretical side by including in the transport simulations [60] an enhanced bremsstrahlung radiation from elementary p+n and p+p quasi-elastic reactions based on updated one-boson-exchange (OBE) calculations [61].

The experience from the last decades shows that the final shape of the dilepton spectra in the $\rho$ mass region as well as other observables (e.g. $p_T$ spectra, rapidity spectra, elliptic flow) are very sensitive to the details of the in-medium spectral functions and to the in-medium cross sections employed in the microscopic transport calculations. Despite of the obvious progress made the many questions have not found an answer yet and require new high precision experimental data to clarify the situation. Especially nucleus-nucleus collisions from 2 to 6 A·GeV are promising in this respect since the vector mesons are more abundantly produced than at SIS energies and the baryon densities are higher.

One of the new experimental probes is the anisotropy in the dilepton angular distribution. Since dileptons from different channels are emitted under different angles, there is an anisotropy in the dilepton angular spectra, which is also modified by the medium effects [62–64]. The anisotropy coefficients in the angular distributions should be measured for varying invariant masses. Moreover, the same coefficients can be measured for hadronic observables ($\pi^+\pi^-$ and $K^+K^-$ pairs) to be compared.

## 1.3   Strangeness in elementary p+p reactions and proton-induced reactions p+A

In order to obtain robust conclusions on in-medium effects on strange hadrons in heavy-ion collisions it is very important to know the particle production in elementary reactions, i.e. in baryon+baryon as well as meson+baryon channels, in a differential way. In low energy p+p reactions the particles are produced dominantly in binary $2 \to 2$ or ternary $2 \to 3$ reactions according to the available phase space, which can be described by resonance or OBE models. The reaction with the highest energy, where such a behaviour has been measured, is the $K^+$ production at 2.5 GeV. With increasing incident energy the multi-particle production starts to dominate. For even higher energies the string models describe the data obtained in p+p reactions very well. It is presently unknown when and how the transition between many-body phase space and string models takes place. It is also very important for all theoretical models to learn about this transition because the dynamics of the heavy-ion reaction depends strongly on the underlying reaction mechanism. The lack of this knowledge for the hadronic many-body problem limits presently the predictive power of the simulation models, which have to be improved in order to describe quantitatively the particle spectra at RHIC and LHC. Therefore it is mandatory to measure systematically the transverse and longitudinal spectra as well as the multiplicity of selected hadrons as a function of the beam energy in elementary reactions.

For many particles the reaction mechanism in elementary reactions is not precisely known or theoretical approaches give quite different results. One may take as an example the $K^+$ production: a $K^+$ meson can be produced either by the exchange of a kaon between the colliding nucleons, or by the exchange of a pion. The effective coupling constants are not known also. The theory is able to fix them for p+p collisions from the experimental data and to achieve a good description of the cross section. However, the extrapolation to kaon production in p+n collisions already depends crucially on the exchanged particle. This is true also for reaction channels involving short-lived resonances. Kaon production in p+n collision is only measured close to the threshold, where the final state interactions are still to play an important role. To understand the strangeness production in the several GeV region as well as to identify the reaction mechanism the measurements of the p+n channels are mandatory also.

Similar arguments hold for the vector-meson production in elementary reactions. Their cross sections are unknown from the experimental side and not well understood also from the theoretical side. On the other hand, the elementary reactions near thresholds are very important for the nuclear dynamics at high relativistic energies, i.e. much above the Nuclotron energy ($< 5$ A·GeV), where they occur in terms of secondary collisions.

Another issue, where the Nuclotron can provide a novel answer, relates to the study of polarization phenomena of (strange) hadrons. In particular, transversely (to the scattering plane) polarized hyperons can be formed in collisions of unpolarized hadrons; their polarization might be reconstructed in elementary p+p reactions and even seen in p+A collisions.

## 1.4   Multi-strange nuclei, strange dibaryons, and strangelets

Central heavy-ion reactions of Au+Au (or Pb+Pb) provide an abundant source of strangeness. This opens the exciting perspective to explore the formation of composite objects with

multiple units of strangeness. Exotic forms of deeply bound objects with strangeness have been proposed long ago [65] as condensed states of matter, either consisting of baryons or quarks. For example, the $H$ dibaryon (a 6-quark state) was predicted first by Jaffe [66]; later a multitude of bound dibaryon states with strangeness were proposed using quark potentials [67, 68] or the Skyrme model [69]. However, the non-observation of multi-quark bags, e.g. strangelets and (strange) dibaryons is still one of the open problems of intermediate and high energy physics. The early theoretical models based on SU(3) and SU(6) symmetries [70, 71] and on Regge theory [72] suggest that dibaryons should exist. More recently, even QCD-inspired models predict dibaryons with strangeness S = 0, −1, and −2 in the invariant mass range between 2 and 3 GeV [66,73,74]. Unfortunately, masses and widths of the expected 6-quark states are differ considerably for these models, so the guidance from theory is very limited.

On the conventional hadronic side, however, hypernuclei are known to exist already for a long time [75, 76]. The double $\Lambda$ hypernuclear events reported so far are closely related to the $H$ dibaryon [77]. Metastable exotic multi-hypernuclear objects (MEMOs) as well as purely hyperonic systems of $\Lambda$ and $\Xi$ particles were introduced in [78, 79] as the hadronic counterparts to multi-strange quark bags (strangelets) [80,81]. In addition it has been shown that the hyperon+hyperon binding energy in bulk matter is considerably enhanced [82].

There are several searches in heavy-ion collisions for the $H$ dibaryon [83, 84] and for long-lived strangelets [85, 86] with high sensitivities. The hypernuclei $^{3}_{\Lambda}$H and $^{4}_{\Lambda}$H have been detected in heavy-ion reactions at AGS by the E864 collaboration [87, 88]. A major uncertainty for the detection of such speculative states is their (meta)stability. The MEMOs, for example, consist of nucleons, $\Lambda$, and $\Xi$ particles and are stabilized due to the Pauli principle. The presented MEMO candidates are expected to possess binding energies up to $E_B/A_B \sim -22$ MeV [81] due to attractive hyperon+hyperon interactions. Only few investigations about the weak decay of dibaryons exist so far, so the future studies at Nuclotron will provide promising perspectives to possibly find new states of (short lived) strange objects.

# Chapter 2

# Achievements at SIS and AGS

## 2.1 SIS energies

### 2.1.1 Equation of State

The understanding of the global properties of infinite nuclear matter, described by the nuclear EoS, is certainly one of the most challenging questions in nuclear physics. Especially the change in the behavior of matter with density is a key property, which is relevant also outside of the nuclear physics domain. It plays a major role in the understanding of astrophysical phenomena, e.g. the structure of neutron stars. Indeed, these are expected to have densities around $2\rho_0$ to $5\rho_0$ just those reached in relativistic heavy-ion collisions at Nuclotron [89].

Since the nuclear EoS describes the properties of infinite nuclear matter without Coulomb interactions, it is therefore given by the volume energy only. The EoS describes the variation of the energy $E(T = 0, \rho/\rho_0)$ when the nuclear density is changed to values different from the saturation density $\rho_0$ at zero temperature. Often nuclear matter is assumed to be isospin saturated, but one can also consider asymmetric nuclear matter, where the symmetry energy term is present. In fact, the density dependence of the symmetry energy has recently been of great interest [90].

The compression modulus $K$ ("compressibility") of the nucleus corresponds to the curvature of the volume energy at $\rho = \rho_0$ (for $T = 0$) and defined as

$$K = -V\frac{\mathrm{d}p}{\mathrm{d}V} = 9\rho^2\frac{\mathrm{d}^2 E/A(\rho)}{(\mathrm{d}\rho)^2}|_{\rho=\rho_0} \; . \tag{2.1}$$

An equation of state with a rather low value of the compression modulus $K$ yields a weak repulsion of compressed nuclear matter and thus describes "soft" matter. A high value of $K$ causes a strong repulsion of nuclear matter under compression (called a "stiff" EoS).

Theoretical approaches like the Brückner-Hartree-Fock approach [91] are valid for densities moderately above and below the normal nuclear matter density and therefore at higher densities reached in heavy-ion collisions this approach comes to the limit of its validity, as discussed here.

Many attempts have been made to determine the EoS from experiments using heavy nuclei. Three experimental observables have been studied to extract information on the nuclear EoS:

i) the strength distribution of giant isoscalar monopole resonances [92],

ii) the in-plane sideward flow of nucleons in semi-central heavy-ion reactions at energies of

100—400 A·MeV [93], and

iii) the production of $K^+$ mesons in heavy-ion reactions at energies around 1 A·GeV suggested in [94] and recently studied in [29].

The most promising method for the study of nuclear matter properties at high densities is the kaon production in (mainly central) heavy-ion collisions. Here, the yield of $K^+$ depends sensitively on the density and the energetic condition during the interaction.
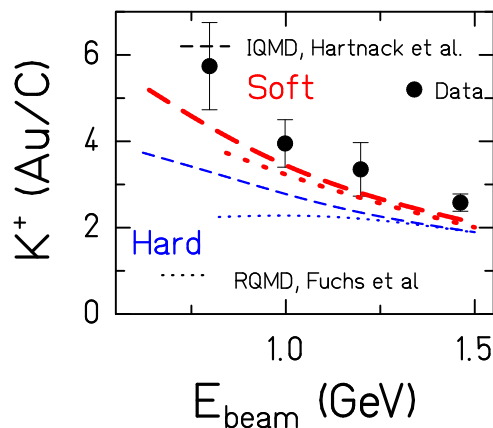


Figure 2.1: *The experimental $K^+$ excitation functions [95] of the double ratio (2.2) (the $K^+$ multiplicities per mass number A obtained from Au+Au divided by the one from C+C) vs beam energy in comparison with RQMD [30] (dotted) and IQMD [29] (dashed) calculations. The results of a "soft" (bold red curve) EoS are compared with a "stiff" (thin blue) EoS (taken from [35]).*

As mentioned above, $K^+$ production under the N+N threshold requires several (inelastic) collisions, because the energy of first-chance collisions is not sufficient. Due to strangeness conservation the $\Lambda$ has to be created together with $K^+$. Hence the threshold is of 671 MeV in the center of mass. The most effective way to accumulate energy is the conversion of nucleon into $\Delta$ and production of $K^+$ in a subsequent collision via $\Delta N \to NK^+\Lambda$. Two effects influence the yield of produced $K^+$ versus the density reached in the collision, so give us access to the "stiffness" of the EoS. For the "soft" EoS a lower energy is needed to compress matter and hence (i) more energy is available for the $K^+$ production and (ii) the density can be reached in these reactions is higher. The latter effect is the most important one, because a higher density leads to a smaller average free path, and therefore the probability for $\Delta$ to collide before decay is higher. Hence, the $K^+$ yield increases. It was found that the most sensitive observable for the "stiffness" of EoS so far is the double ratio of the $K^+$ yields in collision of heavy and light systems [95]:

$$(M_{K^+}/A)_{\text{Au+Au}}/(M_{K^+}/A)_{\text{C+C}} \ . \tag{2.2}$$

This ratio is plotted in Fig. 2.1 as a function of the beam energy for a "soft" (bold red) and a "stiff" (thin blue) EoS IQMD [29] calculations (dashed curves) together with the data from KaoS collaboration [95]. The calculations by Fuchs et al. [30] are also shown as dotted lines. This figure elucidates again that the sensitivity on the EoS is highest at the lowest beam energies and demonstrates that only a "soft" EoS is compatible with the experimental data of the KaoS collaboration [30, 95].
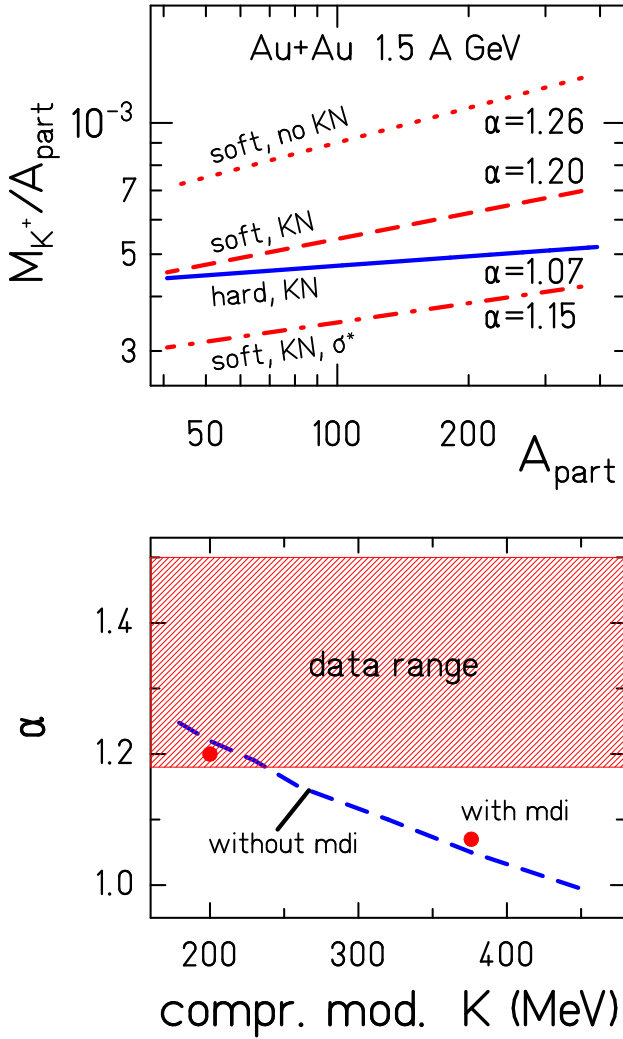
Figure 2.2: Dependence of the $K^+$ scaling on the nuclear EoS. We present this dependence in form of (2.3). On the top it is shown for different options: A "stiff" EoS with $KN$ potential (solid line), the other three lines show a "soft" EoS: without $KN$ potential and $\sigma(N\Delta)$ from Tsushima [97, 98] (dotted line), with $KN$ potential and the same parameterization of the cross section (dashed line) and with $KN$ potential and $\sigma(\mathrm{N}\Delta) = (3/4)\sigma(\mathrm{NN})$ (dash-dotted line). On the bottom the exponent $\alpha$ is shown as a function of the compression modulus $K$ for calculations with momentum-dependent interactions (mdi) and for static interactions (dashed line) (taken from [35]).

On a logarithmic scale $M/A_{\mathrm{part}}$ exhibits an almost linear increase with number of participating nucleons $A_{\mathrm{part}}$. The curves can therefore be characterized by

$$M/A_{\mathrm{part}} \propto A_{\mathrm{part}}^{\alpha} \tag{2.3}$$

with a characteristic slope parameter $\alpha$. The bottom part of Fig. 2.2 shows the slope parameter $\alpha$ as a function of the compression modulus $K$ for the standard $N\Delta \to K^+NN$ cross section and including the $KN$ potential. For this observable also the data of the KaoS collaboration [96] are only compatible with values of $K$ around 200 MeV.

Thus two independent observables point towards a rather low compression modulus.


## 2.1.2   In-medium effects with strangeness at SIS

As it has been observed in the first experiments, the $K^+$ and $K^-$ yields close to threshold behave completely different in comparison with the extrapolation from the elementary production cross sections $NN \to NK^+\Lambda$ and $NN \to NNK^+K^-$. This observation can be seen in Fig. 2.3, which shows the multiplicity of $K^+$ and $K^-$ mesons per participating nucleon $A_{\mathrm{part}}$ in nucleon-nucleon and heavy-ion collisions as a function of the energy above threshold in the NN system, $\sqrt{s} - \sqrt{s_{\mathrm{thres}}}$. Whereas in heavy-ion reactions the $K^-$ and $K^+$ yields are very similar around their respective thresholds, the elementary cross sections show the order
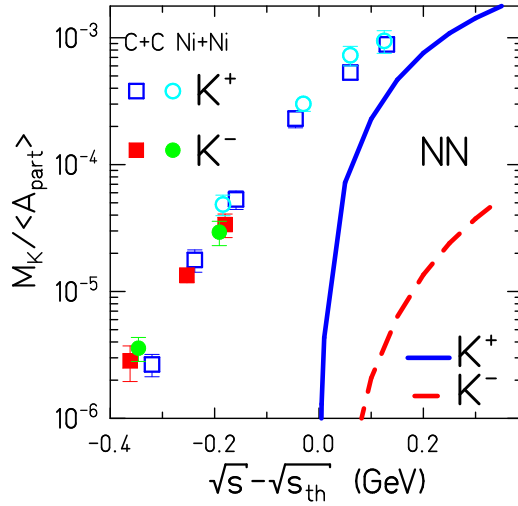
*Figure 2.3: Excitation function of the $K^+$ yield in $NN \to NK^+\Lambda$ reactions and $K^-$ yield in $NN \to NNK^+K^-$ reactions in comparison with the total production of $K^+$ and $K^-$ mesons in the heavy-ion collisions (taken from [35]).*

of magnitude differences. The origin of this observation is a new $K^-$ production mechanism in heavy-ion reactions, which is absent in nucleon-nucleon collisions: the strange baryon can transfer its strange quark to a $K^-$ at threshold energies, thus most of the observed $K^-$ mesons are produced by secondary interactions $BY \to NNK^-$ or $\Lambda(\Sigma)\pi \to K^-N$.

### 2.1.2.1 Yields and ratios
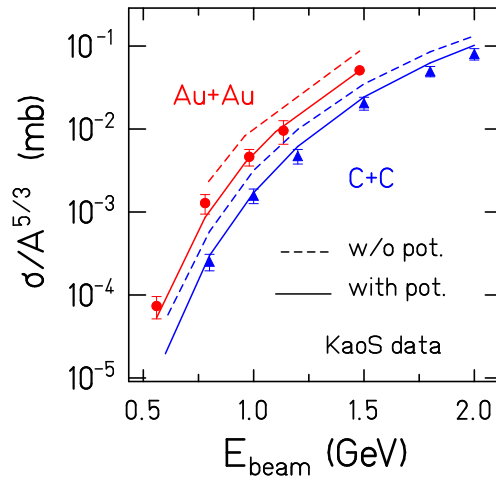


*Figure 2.4: Excitation function of the inclusive $K^+$ cross section in C+C and Au+Au collisions divided by $A^{5/3}$ with and without the $K^+$ nucleus potential. The symbols represent the experimental results of the KaoS collaboration [96] (taken from [35]).*

The excitation function of the $K^+$ yield from the experiment [96] and theoretical calculations for inclusive Au+Au and C+C reactions is shown in Fig. 2.4. The dashed lines present the theoretical results assuming a vanishing $K^+$ nucleus potential, and the solid ones include the $K^+$ nucleus potential. In order to demonstrate the high collectivity of the $K^+$ production, the cross sections in this figure are divided by $A^{5/3}$. If the $K^+$ multiplicities are proportional to the system size (i.e. to the number of participating nucleons), $\sigma/A^{5/3}$
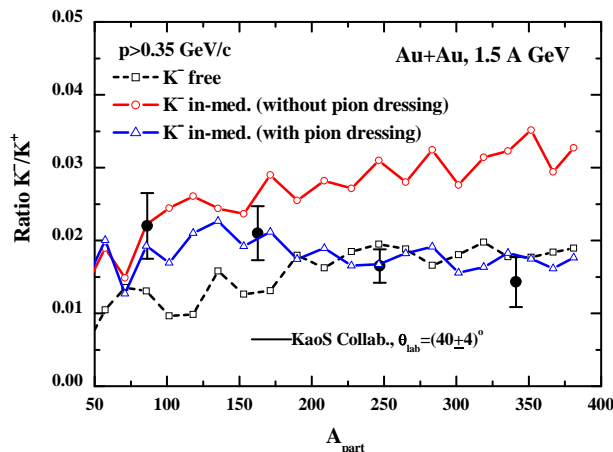
*Figure 2.5: The $K^-/K^+$ ratio as a function of centrality, expressed in terms of the number of participating nucleons $A_{\mathrm{part}}$, for the system Au+Au at 1.5 A·GeV and $\theta_{cm} = (90 \pm 10)°$ including a momentum cut $p_{cm} \geq 0.35$ GeV/c, as well as the experimental data [32]. The dashed line corresponds to the HSD results with "free" spectral function of antikaons, the solid lines — G-matrix calculation with (open triangles) and without (open circles) pion dressing (taken from [27]).*

is constant, and the results for both systems coincide. However, the data show that for the heavier Au+Au system $\sigma/A^{5/3}$ is up to 5 times higher than for the lighter C+C one. The origin of this enhancement is the higher compression, which leads to a smaller average free path and, as a consequence, to more steps of processes. The influence of the $K^+$ nucleus potential depends on the system size and the beam energy. While a considerable change is observed as a function of the beam energy, the influence of the system size is rather small.

The example of the accounting of in-medium effects on observables with $K^-$ is illustrated in Fig. 2.5, which shows the HSD calculations for the $K^-/K^+$ ratio in Au+Au collisions at 1.5 A·GeV as a function of centrality. Also the experimental data from the KaoS collaboration [32] are depicted in Fig. 2.5. The "free" calculations, as well as $G$-matrix ones without pion dressing, are not consistent with the experimental ratio, whereas the full $G$-matrix results with pion dressing (solid line with open triangles) reproduce the slight decreasing with $A_{\mathrm{part}}$ increasing experimentally observed. Thus the $K^-/K^+$ ratio is an informative observable for the in-medium scenarios.

### 2.1.2.2   Rapidity distributions

The experimental $dN/dy$ distribution of $K^0$ is shown in Fig. 2.6 in comparison with IQMD and HSD calculations. This distribution [99] should be (besides the isospin effects) identical to that of the $K^+$. The free $dN/dy$ from IQMD is larger due to different isospin assumptions. The agreement between the experiment and IQMD calculations is reasonable, if the $K^+$ nucleus potential is employed. Without the $K^+$ nucleus potential the IQMD over-predicts the yield by a factor of two. HSD calculations also reproduce the data quite well when employing a $K^+$ nucleus potential for the kaons.

### 2.1.2.3   Slope parameter and $p_T$, $m_T$ spectra

The experimental inverse slope parameter T as a function of the rapidity is displayed in Fig. 2.7 for $K^0$ spectra measured by FOPI in comparison with the two model predictions. The Ni+Ni data at 1.93 A·GeV are well described by both model approaches.
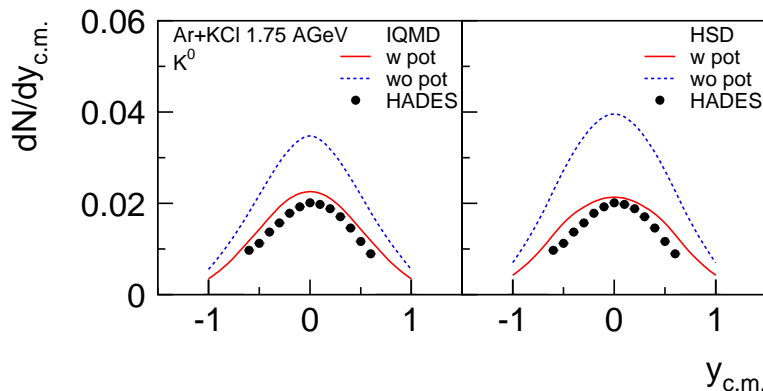
*Figure 2.6: Rapidity distribution $dN/dy$ for $K^0$ from the central Ar+KCl collisions at 1.75 A·GeV as measured [99] by the HADES collaboration (taken from [35]) in comparison with IQMD (left) and HSD (right) calculations.*
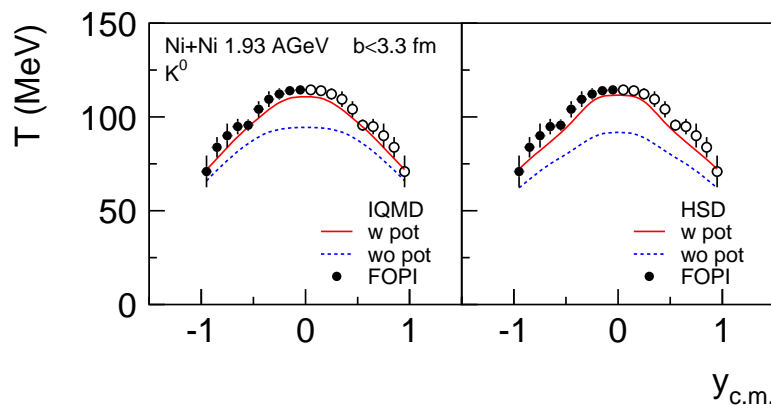


*Figure 2.7: The inverse slope parameter T for the $K^0$ spectra from the central ($b < 3.3$ fm) Ni+Ni collisions at 1.93 A·GeV as measured (and extrapolated to $4\pi$) by the FOPI collaboration in comparison with those obtained in IQMD (left) and HSD (right) calculations (taken from [35]).*

Since $K^-$ mesons are produced dominantly by the strange quark exchange with hyperons $\pi Y \to \bar{K} N$, it is important to have under control the hyperon dynamics. The $\Lambda N$ cross section is larger than the $K^+ N$ one, therefore the $\Lambda$ adopts rapidly the properties of its environment. It is expected that $\Lambda$ final distribution differs substantially from that at production.

The experimental $m_T$ spectra for different rapidity ranges from Ar+KCl at 1.75 A·GeV [100] are shown in Fig. 2.8. These data are compared to IQMD (left) and HSD (right) calculations presented by the histograms. The influence of the $K^+$ nucleus potential is visible. It increases the threshold and therefore reduces the number of $\Lambda$, which are created together with the $K^+/K^0$ in $BB \to YNK^{+/0}$ reactions.

### 2.1.2.4 Azimuthal angular distributions, collective flow

The phenomenon of collective flow can be characterized in terms of anisotropies of the azimuthal emission pattern, expressed in terms of a Fourier series

$$\frac{\mathrm{d}N}{\mathrm{d}\phi}(\phi) \propto 1 + 2v_1 \cos(\phi) + 2v_2 \cos(2\phi) + \dots \, , \qquad (2.4)$$
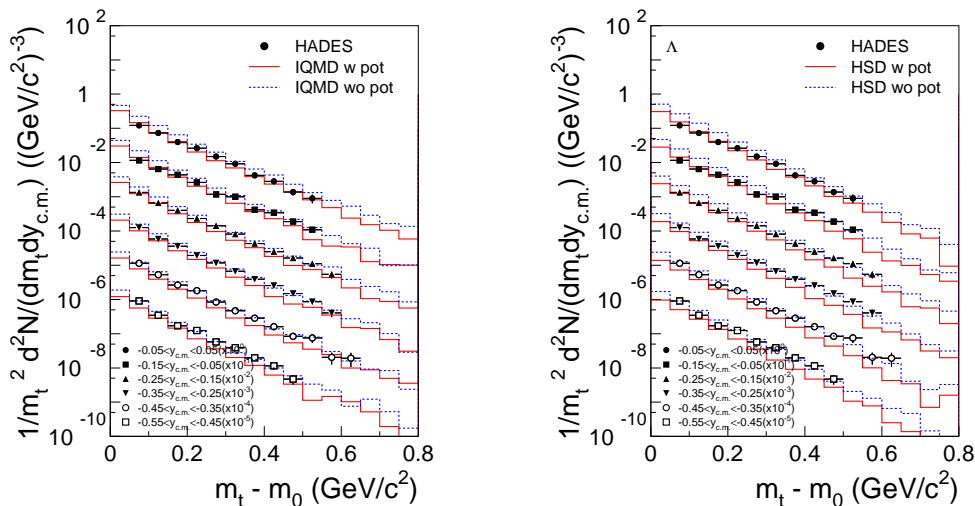
*Figure 2.8: The $m_T$ spectra of $\Lambda$ for different rapidity ranges from the Ar+KCl collisions at 1.75 A·GeV. The experimental results [100] of the HADES collaboration are compared with predictions of IQMD and HSD calculations with (red solid line) and without (blue dashed line) the $K^+$ nucleus potential (taken from [35]).*

which allows one a transparent interpretation of the $v_1$, $v_2$, ... coefficients. The dipole term $v_1$ arises from a collective sideward deflection of the particles in the reaction plane and characterizes the transverse flow in the reaction plane. The second harmonic $v_2$ describes the emission pattern perpendicular to the reaction plane. For negative $v_2$ one has a preferential out-of-plane emission, called squeeze-out. At SIS energies the pions are emitted dominantly out-of-plane [101, 102] due to shadowing by the spectator nucleons. Since the $K^-$ average free path is comparable to that of the pions, one might expect the same phenomenon for $K^-$ while the average free path of $K^+$ mesons is large and no squeeze-out signal should be observed. These arguments hold when the final state interaction is exclusively determined by the scattering and absorption processes.

The first data on $K^+$ azimuthal asymmetries [103] shows a clear squeeze-out signal for mid-rapidity kaons. In corresponding transport calculations [23, 103, 104] the data could only be reproduced by the presence of the repulsive $K^+$ mean field. Elastic rescattering of $K^+$ mesons was found to be too weak to create the observed squeeze-out signal [35]. If the repulsive potential is taken into account, the kaons are driven by potential gradients preferentially out-of-plane. Thus, the repulsive potential leads to an additional dynamical focusing out of the reaction plane.

The azimuthal distributions for semi-central Au+Au reactions at 1 A·GeV and Ni+Ni at 1.93 A·GeV [105] are shown in Fig. 2.9. For the Au+Au case we compare RQMD [106] and GiBUU [107] calculations with the KaoS data [103]. The results confirm the findings that the in-medium potential is needed in order to explain the experimental squeeze-out signal. Another interesting observation is the fact that the Lorentz force, present in covariant dynamics, has only a small influence on the out-of-plane flow, contrary to the in-plane flow discussed above [107]. The right panel in Fig. 2.9 shows also HSD calculation results. There exists a convergence of the various transport models on the conclusion that the azimuthal $K^+$ emission pattern requires a repulsive mean field. This is supported by Fig. 2.10, which shows the in-plane flow of $K^+$ calculated using RQMD [106] in comparison to the FOPI data [108].
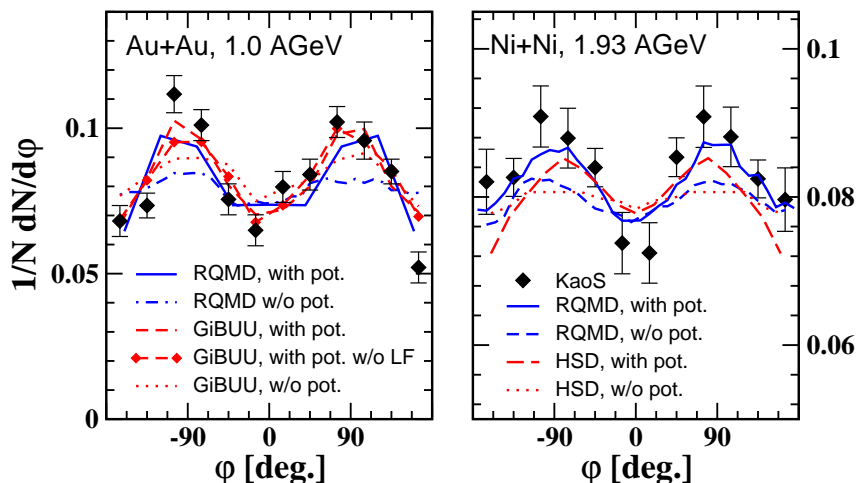
*Figure 2.9: The $K^+$ azimuthal angular distributions from the semi-central Au+Au reactions at 1.0 A·GeV and Ni+Ni reactions at 1.93 A·GeV. The RQMD [106], GiBUU [107], and HSD [25] calculations with and without in-medium potential are compared to data from KaoS [103, 105] (taken from [109]).*
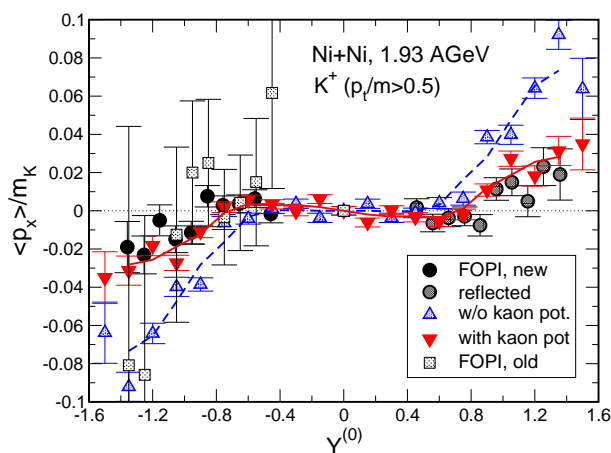


*Figure 2.10: Transverse $K^+$ flow in 1.93 A·GeV $^{58}Ni + ^{58}Ni$ reaction at impact parameter $b \leq 4$ fm. RQMD calculations with and without kaon in-medium potential are compared to FOPI data [110] (old) and [108] (new). The Lorentz force is included (taken from [109]).*

### 2.1.3 Multi-strangeness and hypernuclei at SIS

Due to the limitation in beam energy the study of multi-strange baryons, mesons with hidden strangeness, and hypernuclei is at the border line of the present SIS facility. Nevertheless, two groups, HADES [111, 112] and FOPI [113], have reported results for $\phi$ mesons and $\Xi$ baryons, albeit in a very limited region of the phase space. Theory under-estimates the $\phi$ production by at least a factor of two, assuming an extrapolation of the DISTO data for $\phi$ production up to energies close to threshold, whereas for the $\Xi$ production even the reaction mechanism is unknown. Without a systematic approach to $\Xi$ production understanding in the elementary collisions at threshold energies the predictions for heavy-ion collisions remain speculative.

Recently several groups have started to explore the GSI potential for producing hypernuclei in heavy-ion collisions. Hypernuclei like hyper-triton have been observed close to the target rapidity. A detailed analysis of the data is presently under way.

## 2.2  AGS energies

The Alternating Gradient Synchrotron (AGS) at BNL provided the possibility to study heavy-ion collisions from 2 up to 14.5 A·GeV using the fixed target setups. It allowed to provide comprehensive measurements of identified particle spectra and different observables such as collective flow, HBT, etc.

### 2.2.1  "Bulk" observables with strangeness
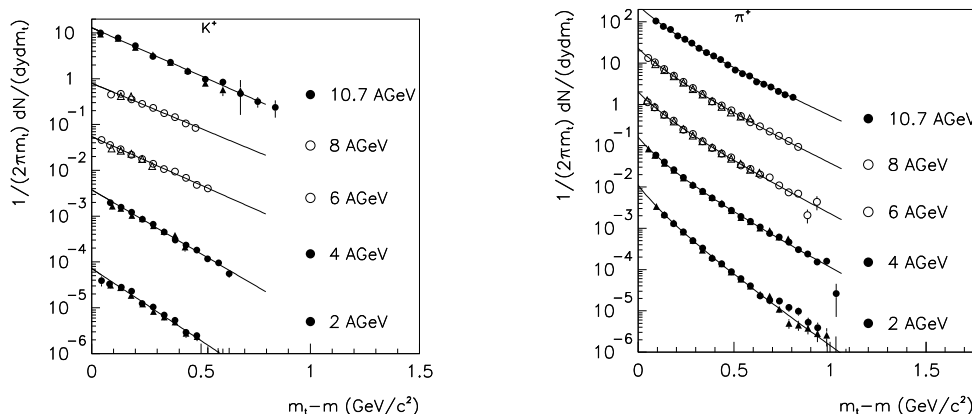


*Figure 2.11: The invariant yields of $K^+$ (left) and $\pi^+$ (right) as a function of $m_T$ at mid-rapidity from the Au+Au collisions at different beam energies. For each energy the spectrum just back/forward of mid-rapidity is shown by circles/triangles. The data from E866 and E917 are displayed by closed and open symbols, respectively. The data at 10.7 A·GeV are shown at the correct scale, other data are divided by successive powers of 10 for clarity. The errors are statistical only (taken from [114]).*

The AGS experiments have provided a variety of data on "general" observables, such as particle multiplicities and their ratios, rapidity distributions, and $p_T$ spectra for protons, pions and strange particles. The $m_T$ spectra for $K^+$ and $\pi^+$ at the energy range from 2 to 10.7 A·GeV for Au+Au collisions are shown in Fig. 2.11. The mean transverse mass $m_T$ as well as the inverse slope parameter (extracted by an exponential fit to the $m_T$ spectra) show a smooth rise with incident energy, because a larger fraction of the extra available energy is converted to particle production rather than into increasing the transverse energy per particle. This leads to the rapid increasing of the particle yields as shown in Fig. 2.12.

A significant importance has the measurements of the $K^+/\pi^+$ (see Fig. 2.13), $K^-/\pi^-$, and $\Lambda/\pi$ yield ratios, which were later complemented by the measurements at SPS, RHIC, and LHC energies. The $K^+/\pi^+$ ratio shows a rapid rise at energy increasing with a maximum ("horn") at incident energy of $\sim 20$ A·GeV and a saturation at SPS energies. The non-monotonic behaviour ("step") has been observed also for the excitation function of the inverse slope parameter for $K^+, K^-$ mesons, which grows up to top AGS energies and then shows a saturation up to RHIC energies. The "horn" and "step" have been interpreted as a possible indication for the observation of deconfinement in the fireball [115] (see, e.g. [109] for a review on this issue). However, at AGS energies the rapid rise of the particle yield ratios essentially relates to a hadronic origin — the opening of new multi-particle production channels and multiple final state rescatterings. This clearly indicated by the fact that the $K^+/\pi^+$ ratio for Au+Au collisions is substantially larger then one for p+p reactions as shown by the hatched region in Fig. 2.13.
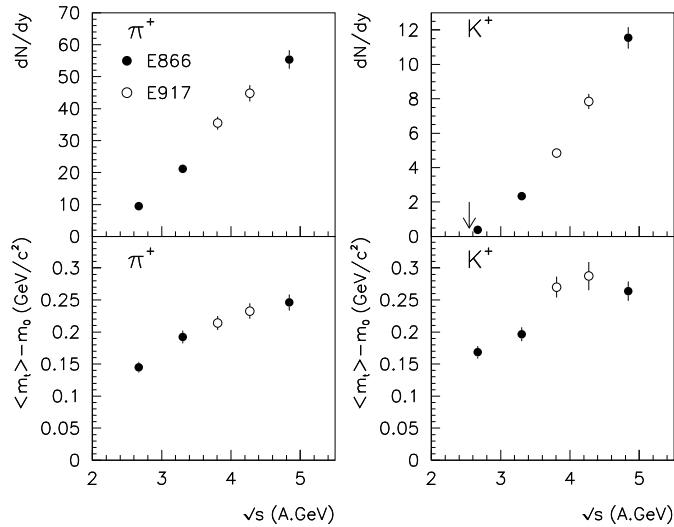
*Figure 2.12: The yields of $\pi^+$ (left) and $K^+$ (right) at the mid-rapidity (top panels) from the central Au+Au reactions as a function of the initial available beam energy. The data from E866 and E917 are shown by closed and open circles, respectively. The average transverse mass $m_T$ minus the rest mass for $\pi^+$ (left) and $K^+$ (right) at the same rapidity (low panels). The arrow indicates the threshold energy for $K^+$ production in the p+p reaction (taken from [114]).*

Also the AGS experiments E895 and E810 have measured multi-strange baryons $(\Lambda, \Sigma, \Xi)$ in the Au+Au collisions at 6 A·GeV and in the Si+Au collisions at 14.5 A·GeV [116]. The centrality dependence for the multiplicities of $\Xi^-$ and $(\Lambda + \Sigma^0)$ as well as their ratio $\Xi^-/(\Lambda+\Sigma^0)$ are shown in Fig. 2.14 in comparison with the RQMD model results [117]. The multiplicity ratio $\Xi^-/(\Lambda + \Sigma^0)$ is compared with the statistical model predictions [118] at higher incident energies in Fig. 2.15. The measurements are rather close to the threshold for $\Xi^-$ production and therefore provide an important test of model predictions. In the central collisions the $\Xi^-$ yield was found to be in a good agreement with statistical and transport model predictions. This fact was interpreted as the suggestion that multi-strange hadron production achieves a chemical equilibrium in the high baryon-density nuclear matter.

Thus a relevant finding at AGS energies has been the success of statistical models [119, 120] in describing the particle abundances and ratios at mid-rapidity, which shows that
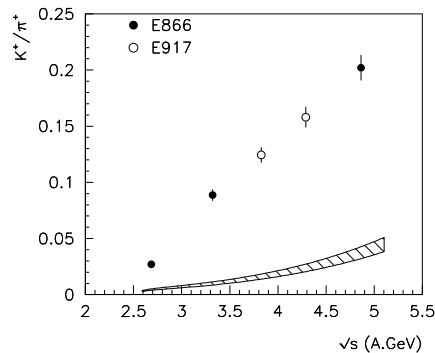


*Figure 2.13: The ratio of $dN/dy$ for $K^+$ and $\pi^+$ at mid-rapidity from the central Au+Au reactions as a function of the initial available energy. The data from E866 and E917 are shown by closed and open circles, respectively. The hatched region covers $\pm 1\sigma$ around the $K^+/\pi^+$ ratio for p+p reactions, see text for details (taken from [114]).*
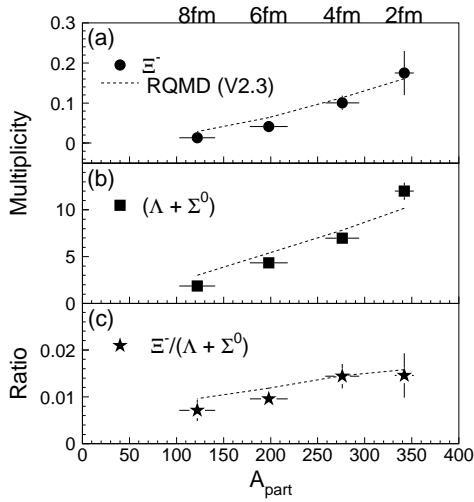
Figure 2.14: Panels (a) and (b) show the $A_{part}$ dependence of the $\Xi^-$ (circles) and $(\Lambda + \Sigma^0)$ (squares) multiplicities from the Au+Au collisions at 6 A·GeV, respectively. Panel (c) shows the corresponding multiplicity ratio $\Xi^-/(\Lambda + \Sigma^0)$ (stars) as a function of $A_{part}$. The RQMD calculation results [117] are indicated by the dotted lines (taken from [116]).
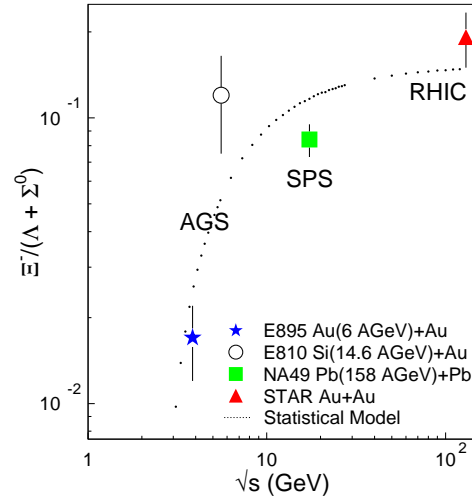
Figure 2.15: The multiplicity ratio of $\Xi^-/(\Lambda + \Sigma^0)$ as a function of $\sqrt{s}$. The closed symbols correspond to central collisions of symmetric systems Au+Au and Pb+Pb, the open circles — the asymmetric system Si+Au. The dotted line shows results of the statistical model [118] for the central Au+Au collisions (taken from [116]).

in the central heavy-ion collisions the fireball-matter achieves a chemical equilibrium and can be approximately described by a grand canonical ensemble with the strangeness saturation factor $\sim 1$. However, the statistical models failed to explain the strong enhancement of the antibaryon $(\bar{\Lambda} + \bar{\Sigma}^0)/\bar{p}$ ratios from the peripheral to central Au+Au collisions measured at 11.6 A·GeV [121]. This ratio is enhanced relative to corresponding ratios in p+p collisions and is large when compared with thermal fits of heavy-ion data. This enhancement might be partially attributed to the weak absorption of $\bar{\Lambda}$ and $\bar{p}$ in the hadronic medium.

## 2.2.2  EoS and in-medium potentials from collective flow

The E895 collaboration has measured the proton elliptic flow for the Au+Au system spanning the beam energy range 2—8 A·GeV [122] (see Fig. 2.16). The excitation function vs beam energy shows a transition from negative to positive elliptic flow at $E_{tr} \sim 4$ A·GeV. A comparison with calculations from the relativistic Boltzmann-equation model [123] suggests a softening of the nuclear EoS from a "stiff" ($K \sim 380$ MeV) at low beam energies ($E_{beam} \leq 2$ A·GeV) to a softer ($K \sim 210$ MeV) at higher energies ($E_{beam} \geq 4$ A·GeV), where the calculated baryon density $\rho \sim 4\rho_0$.

This is also supported by study of the centrality dependence of the protons elliptic flow in 2—6 A·GeV Au+Au collisions [124] as displayed in Fig. 2.17. The elliptic flow shows an essentially linear dependence on impact parameter $b$ in the range $1.5 \lesssim b \lesssim 8$ fm with a negative slope at 2 A·GeV, approximately zero slope at 4 A·GeV, and a positive slope at 6 A·GeV. The approximately linear dependence (exhibited by the data) can be understood in terms of the collision geometry and the development of transverse expansion of the participant matter. At 2 A·GeV the spectator velocities are relatively slow, and the passage time is
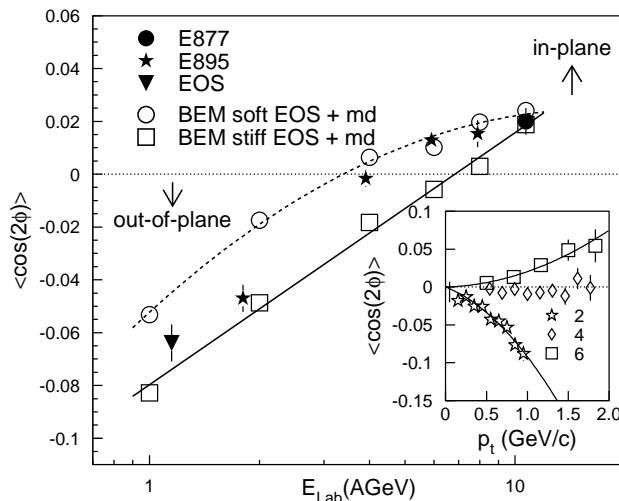
*Figure 2.16: Elliptic flow excitation function for Au+Au in comparison to results of a transport model. The closed symbols are experimental data [122]. The dashed curve (open circles) and the solid curve (open squares) are results of the relativistic Boltzmann-equation model [123] for "soft" and "stiff" EoS (both with momentum dependent potentials), respectively. The inset shows the (dispersion corrected) transverse momentum dependence of the elliptic flow for 2, 4, and 6 A·GeV beams (taken from [122]).*

relatively long. The expansion of the participant matter occurs rapidly, but the spectators shadow the in-plane direction, thus driving the nucleons to squeeze-out, i.e. perpendicular to the reaction plane. At 6 A·GeV the spectator passage time is short in comparison with the expansion time and a preferential in-plane emission is observed. The underlying baryon dynamics can be modeled by a proper choice of the corresponding EoS. The results of the relativistic Boltzmann-equation model [123] with a "stiff" ($K = 380$ MeV), a "soft" ($K = 210$ MeV), and an intermediate ($K = 300$ MeV) momentum-dependent EOS are presented in Fig. 2.17. This comparison clearly demonstrates that elliptic flow measurements provide distinctly more stringent constraints on different forms of the EoS. Such additional discriminating power is critical to the resolution of outstanding issues related to the EoS of the high-density nuclear matter.

The sideward flow has been measured also for strange particles, i.e. $\Lambda$ and kaons. The left panel of Fig. 2.18 shows the sideward flow $\langle p^x \rangle$ versus rapidity for $\Lambda$ (stars) and protons (closed circles and open ones for reflected p) from Au+Au collisions at 2, 4, and 6 A·GeV [125]. The right panel of Fig. 2.18 displays the $K^0$ meson flow from Au+Au collisions at 4 A·GeV (open symbols) and 6 A·GeV (closed symbols). The $\Lambda$ hyperons show a smaller sideward flow than protons since the $\Lambda N$ potential scales approximately as $2/3$ of the p$N$ one. The $K_s^0$ (depicted in Fig. 2.18) exhibit a strong anti-flow signal, which increases strongly with beam energy. The RQMD model, which does not contain any kaon potential, may serve as a baseline for the effects of rescattering. Its failure to reproduce even the sign of the flow is a strong hint for the existence of a strong repulsive kaon potential. Employing a strong density dependence of the kaon potential, a calculation with the transport model ART is able to reproduce the sign and the strength of the $K^0$ flow [126].

Thus, the AGS data have demonstrated a strong sensitivity of flow observables to the EoS and in-medium potentials for the different hadron species, which can be extracted from transport approaches once the latter are able to reproduce all independent observables simultaneously.
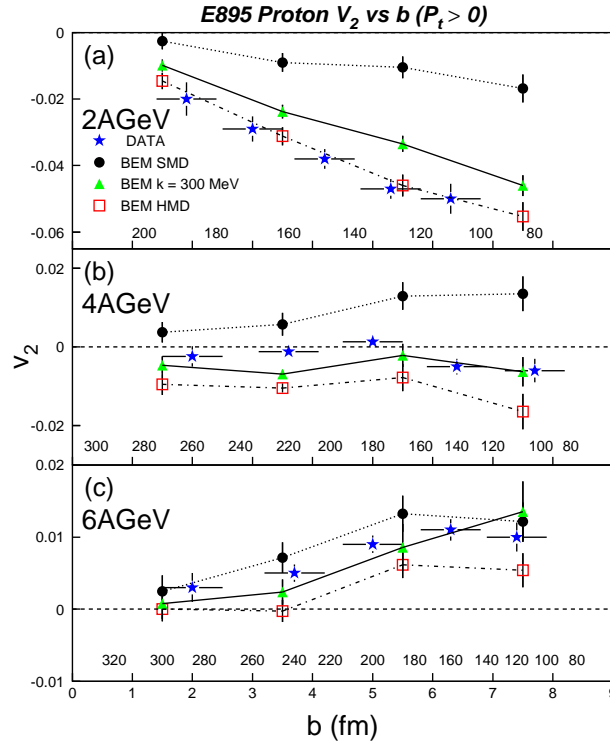
Figure 2.17: The elliptic flow $v_2$ as a function of $b$ ($p_T > 0$) and identified charged particles multiplicity for 2 (a), 4 (b), and 6 A·GeV (c) Au+Au collisions. The E895 data [124] are closed stars. The Boltzmann-equation model calculations with "stiff" $K = 380$ MeV (open squares), "soft" $K = 210$ MeV (closed circles), and intermediate $K = 300$ MeV (closed triangles) momentum-dependent EoS (taken from [124]).
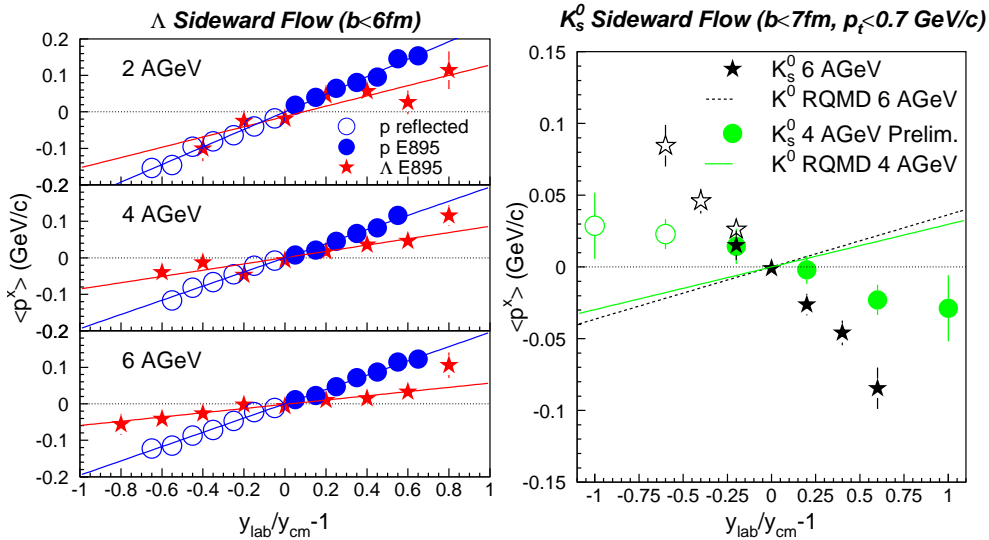


Figure 2.18: Experimental sideward flow $\langle p^x \rangle$ versus rapidity for: (left) $\Lambda$ baryons (stars) and protons (closed circles and open ones for reflected p) from Au+Au collisions at 2, 4 and 6 A·GeV; (right) $K^0$ mesons from Au+Au collisions at 4 A·GeV (closed circles) and 6 A·GeV (closed stars) (taken from [125]).

# Chapter 3

# Physical program: Strangeness at Nuclotron

## 3.1 Elementary p+p, p+n and proton induced p+A reactions

Strangeness production in p+p and p+n collisions above a beam energy of 2.54 GeV is an almost unknown land. Forty years ago Hogan et al. [127] measured that at $E_{\text{beam}} = 2.54$ GeV the $K^+$ momentum distribution is compatible with that expected if the final momenta of the particles produced in pp $\rightarrow$ p$\Lambda(\Sigma)K^+$ are distributed according to phase space. However, at a slightly higher energy $E_{\text{beam}} = 2.88$ GeV, this is no longer the case since the data show a rich structure of the momentum distribution related to the opening of new channels above some certain thresholds. However, it has never been investigated if this is due to the production of nuclear resonances like $N(1710)$ or $N(1720)$, due the production of a $\Delta$, which disintegrates into a proton and a pion, or because the reaction is not phase-space dominated as observed at considerably higher energies.

There are two basic models to interpret the experimental data at this intermediate energy region: creation of heavy baryonic resonances, which later decay to the light hadrons, or the excitation of "strings" driven by the strong color fields and pooled between the valence quarks of interacting hadrons. In the latter case the data can be described assuming that in p+p collisions two strings are formed, which decay according to the longitudinal phase space, whereas in transverse direction the average $p_T$ is constant and about 250 MeV/c. The formation of strings is predicted by the QCD based Lund and Dual Parton models. The energy range of Nuclotron offers therefore not only the possibility to study the final state of the elementary reaction necessary to understand the reaction mechanism; as well it offers the possibility to investigate at which energy the hadron dominated final states (characterized by a 3-dimensional phase-space distribution) go over to the parton dominated final states (characterized by a longitudinal phase-space distribution and an approximately constant $\langle p_T \rangle$).

The FOPI [113] and HADES [111, 112] collaborations have recently reported that in heavy-ion reactions close to or below threshold the multi-strange baryons and mesons with hidden strangeness are produced more abundantly than predicted by the transport theories. The predictions of the transport models are based on the extrapolation of the scarce pp $\rightarrow \Xi X$ and pp $\rightarrow \phi X$ data measured at energies well above threshold. Nuclotron can provide the
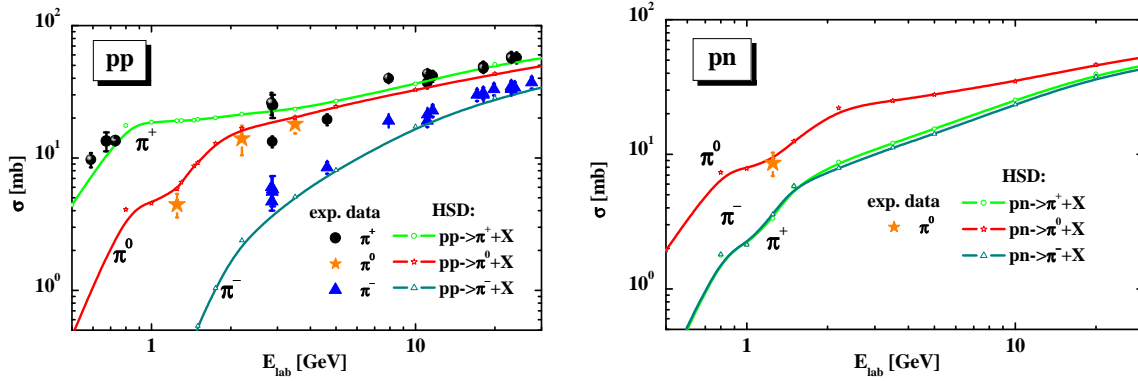
Figure 3.1: *The inclusive pion production cross sections as a function of the proton incident energy $E_{\text{lab}}$ for pp $\rightarrow \pi X$ (left) and pn $\rightarrow \pi X$ (right), where the HADES data (closed stars) are from the extrapolation in [132] (both taken from [133]). The HSD results are shown in terms of lines with open symbols, whereas the experimental data are indicated by the corresponding closed symbols: $\pi^+$ — circles [128, 129], $\pi^0$ — stars [130, 131], $\pi^-$ — triangles [128, 129].*
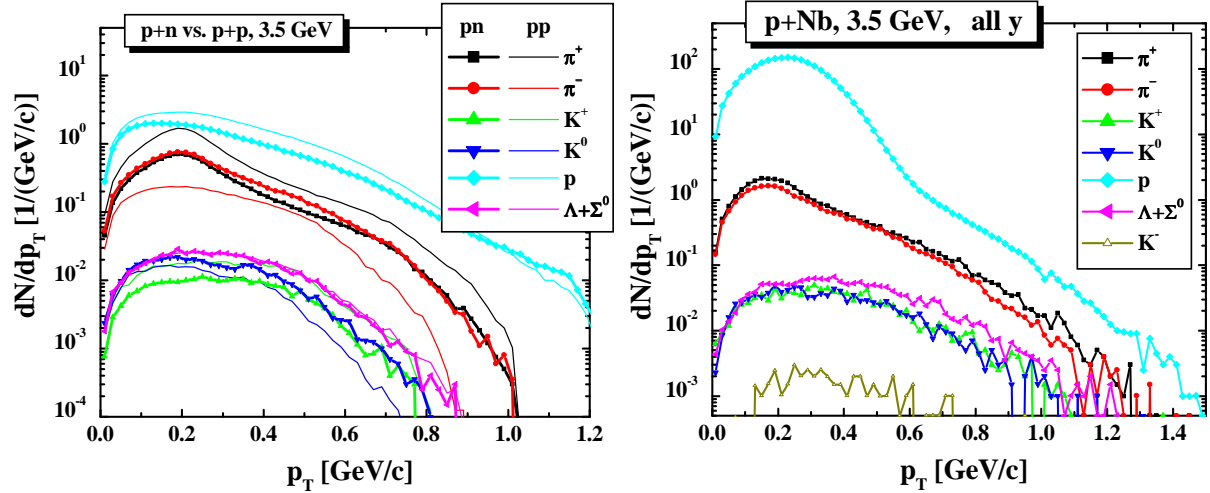


Figure 3.2: *The HSD results for the $p_T$-distribution of $\pi^+$, $\pi^-$, $K^+$, $K^0$, p, and $\Lambda + \Sigma^0$ from p+p collisions (thin lines) and p+n collisions (lines with symbols) at 3.5 GeV into full $4\pi$ acceptance (left) and for the $p_T$-distribution of the same particles and $K^-$ from p+Nb collisions with the same energy and acceptance (right).*

data, which are necessary to clarify this situation by measuring the excitation function of the various production channels close to threshold. Comparing the results for elementary p+p interactions with that for light nuclei the corresponding np $\rightarrow (\Xi)\phi X$ cross section can be inferred. This will allow addressing the question whether in heavy-ion collisions the production of these hadrons is dominated, or at least strongly influenced by channels, which are not possible in elementary reactions like $\Delta(N^*)$p $\rightarrow \Xi X$. The experiments at SIS energies improved our understanding of the complicated reaction mechanism for $K^+$, $K^-$, and $\Lambda$ channels in the heavy-ion collisions [35]. Nuclotron will be able to extend this knowledge to higher energies including the multi-strange baryons and hidden strange mesons production.

Another topic of interest at Nuclotron energies is the nature of 2- and 3-pion production channels in elementary reactions. It is known that at low energies almost all pions are produced via the $\Delta$ resonance. With increasing energy the 2-pion production dominates over the one-pion production, but the error bars for the 2-pion cross section are large — see

Fig. 3.1. Therefore (and since no invariant mass measurements have been performed) the origin of the 2-pion yield is experimentally not studied and theories arrive at quite different conclusions of the role of double $\Delta$ and $N^*$ production channels. The knowledge of the production channel is important also for the study of dilepton yield because $\Delta$ contribute to this yield whereas $N^*$ practically do not. Dileptons, which do not interact strongly after production, are presently the most promising probes to study the high-density phase of the heavy-ion reactions.

Summarizing this section we suggest to perform at Nuclotron:

1) in order to understand the underlying mechanisms of strangeness and light meson production — the measurements of multiplicity, rapidity $y$, $p_T$ spectra and angular distributions in elementary p+p, p+n reactions for (multi)strange mesons ($K$, $\bar{K}$, $K^*$) and baryons ($\Lambda$, $\Sigma$, $\Xi$, $\Omega$) as well as light mesons (pions);

2) in order to identify the production and decay of heavy baryonic and mesonic resonances — the measurements with gate on individual channels with strangeness, e.g. $pp \to N\Lambda(\Sigma)K(+\pi, 2\pi, \dots)$;

3) in order to study the isospin effects and the role of secondary channels, e.g. for strangeness production $\Delta N \to N\Lambda(\Sigma)K$ — the measurements of similar observables in proton-induced reactions on nuclei p+A.

For illustration we present in the left panel of Fig. 3.2 the HSD predictions for the $p_T$-distribution of $\pi^+$, $\pi^-$, $K^+$, $K^0$, p, and $\Lambda + \Sigma^0$ from p+p collisions (thin lines) and from p+n collisions (lines with symbols) at 3.5 GeV into full $4\pi$ acceptance, whereas the right panel of Fig. 3.2 shows the corresponding $p_T$-distributions from p+Nb collisions at the same incident energy. One can clearly see the strong isospin effects — the p+p and p+n $p_T$-spectra differ substantially in magnitude and in shape (cf. thin and thick lines) — related to the opening of different isospin channels. The effect is partly smeared out in p+Nb collisions, where the final spectra achieve an exponential shape due to the isospin combination of p+p, p+n and n+n collisions, final rescatterings, and initial Fermi motion of the target nucleons.

## 3.2 Exploring the properties of dense nuclear matter by heavy-ion reactions

JINR Nuclotron will provide beams of heavy ions with energies up to 6 A·GeV for isospin-symmetric nuclei, and 4.65 A·GeV for Au nuclei. In the central heavy-ion collisions at these energies the nuclear densities about 4—5 times of nuclear matter density can be reached. These conditions are well suited to investigate the EoS of dense nuclear matter, which plays a central role for the dynamics of core collapse supernovae and for the stability of neutron stars. At the same time, the heavy-ion collisions are a rich source of strangeness, and the coalescence of kaons with $\Lambda$ or $\Lambda$ with nucleons will produce a vast variety of multi-strange hyperons or light hypernuclei, respectively. Even the production of light double-hypernuclei or double-strange dibaryons is expected to be measurable in the heavy-ion collisions at Nuclotron energies. The observation of those objects would represent a breakthrough in our understanding of strange matter, and would pave the road for the experimental exploration of the third dimension of the nuclear chart. These studies are complementary to the CBM experimental program at SIS100 [109, 134].

The central question is: which experimental observables are sensitive to the properties
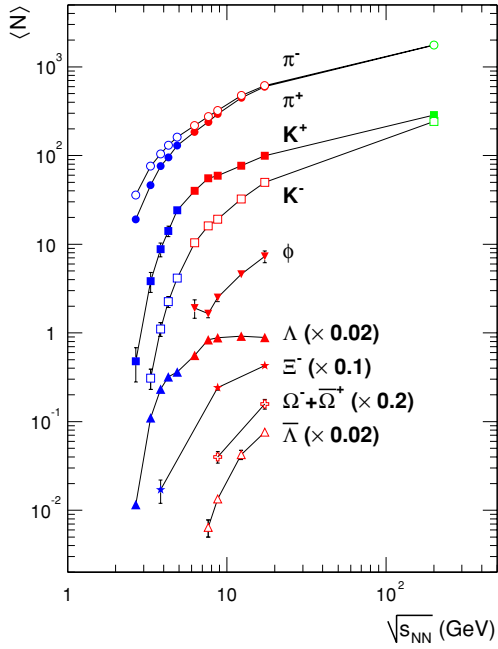
*Figure 3.3: The yield of mesons and (anti)hyperons as a function of beam energy measured in the central collisions of Au+Au (Pb+Pb) (taken from [135]).*
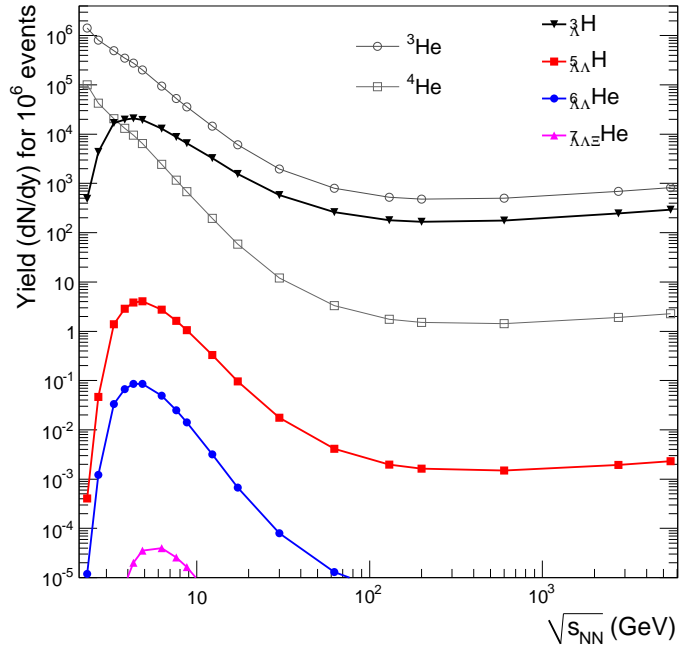
*Figure 3.4: Energy dependence of hypernuclei yields at mid-rapidity for $10^6$ central collisions calculated within a thermal model [136]. The predicted yields of $^3$He and $^4$He nuclei are included for comparison (taken from [136]).*

and the degrees-of-freedom of QCD matter at supra-nuclear densities. We suggest to study the yield and the phase-space distribution of strange ($\Lambda$, $\Sigma$), multi-strange ($\Xi$, $\Omega$) hyperons and strange pseudo-scalar ($K$, $\bar{K}$), strange vector ($K^*$, $\bar{K}^*$) mesons at beam energies close to their production thresholds in the nucleon-nucleon collisions.

The threshold beam energies for reactions pp $\rightarrow \Xi^- K^\pm K^\pm$p and pp $\rightarrow \Omega^- K^\pm K^\pm K^0$p are 3.7 and 7.0 GeV, respectively. However, $\Xi^-$ and $\Omega^-$ hyperons can also be created via strangeness exchange reactions like $\Lambda\Lambda \rightarrow \Xi^-$p and $\Lambda\Xi^- \rightarrow \Omega^-$n as well as $\Lambda K^- \rightarrow \Xi^- \pi^0$ and $\Xi^- K^- \rightarrow \Omega^- \pi^-$. In these cases, the $\Lambda$ and the $K^-$ have been produced in independent reactions such as pp $\rightarrow K^+\Lambda$p and pp $\rightarrow K^+ K^-$pp, which require only 1.6 and 2.5 GeV, respectively. Due to these multiple-step (or three-body) collisions involving $\Lambda$ hyperons and kaons the production of multi-strange hyperons is expected to be enhanced at high densities, and their yield is sensitive to the baryon density reached in the fireball. Therefore, systematic measurements of $\Xi^-$ and $\Omega^-$ hyperon production as a function of beam energy and size of the colliding nuclei offer the possibility to study the nuclear matter EoS, or baryon density fluctuations as they are expected to occur when the system undergoes a first-order phase transition. These fluctuations may also indicate the existence and the location of a QCD critical endpoint as expected by many models. Moreover, the energy distributions of multi-strange hyperons provide information on the fireball temperature and the radial flow at the time of emission.

The proposed experiment would deliver the first data on the production of multi-strange hyperons in the heavy-ion collisions at Nuclotron beam energies. The data situation is illustrated in Fig. 3.3, where the measured excitation function of strange particles is shown for the central collisions of heavy nuclei (Au+Au, Pb+Pb) at beam energies above 2 A·GeV [135]. In conclusion, the systematic measurement of multi-strange hyperons as diagnostic

probes of dense nuclear matter at Nuclotron energies has a substantial discovery potential.

## 3.3  Search for light hypernuclei
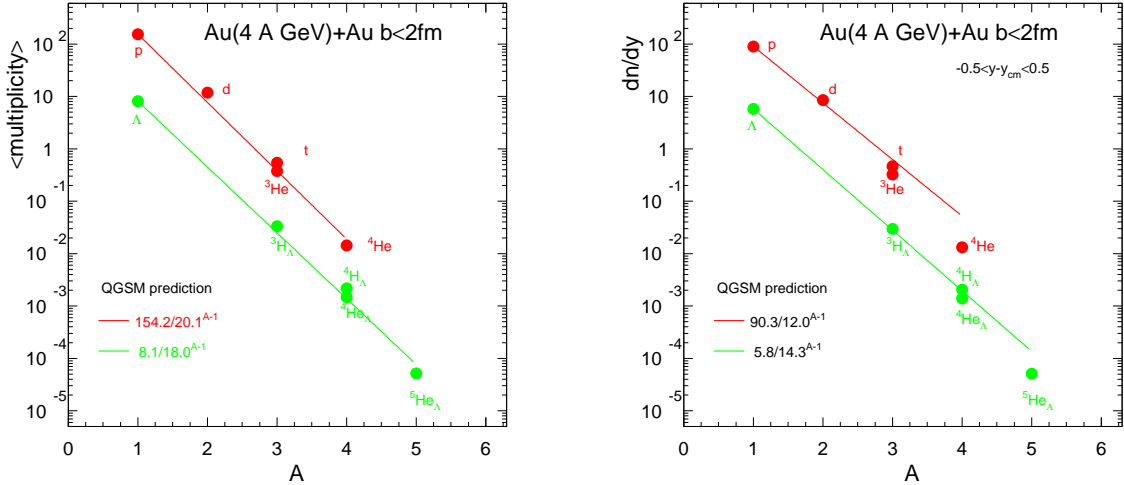


*Figure 3.5: The QGSM model predictions for light clusters and light hypernuclei production from 4 A·GeV Au+Au reactions: multiplicity into $4\pi$ acceptance (left), yield at mid-rapidity (right). See also text for details.*

The search for hypernuclei offers the fascinating perspective to explore the third (i.e. strange) axis of the nuclei chart. Moreover, the investigation of hypernuclei provides information on the hyperon-nucleon and even the hyperon-hyperon interactions, which plays an important role in neutron star models. Most of the known hypernuclei have been produced in experiments with $K^-$ beams on light nuclei. In a strangeness exchange reaction the $s$-quark is transferred from the $K^-$ meson to a nucleon forming a $\Lambda$ hyperon, which was trapped in the nucleus. In violent collisions between the $K^-$ meson and the nucleon a double-strange $\Xi^-$ hyperon may be produced (together with a $K^+$). If the $\Xi^-$ hyperon is trapped in another nucleus, the two strange quarks may be transferred to two nucleons forming two $\Lambda$ hyperons, and eventually a double-$\Lambda$ nucleus is created if the kinematics favor binding. In most of the experiments up to date the decay of the double-$\Lambda$ hypernucleus has been observed in emulsions. Only very few double-$\Lambda$ hypernuclei have been found so far. Heavy-ion collisions, in contrast with $(K^-, K^+)$ charge exchange experiments, can allow one to study such exotic objects as $\Omega^-$ hypernuclei like $^6_\Omega$H.

Recently, the FOPI collaboration at GSI has shown that hypernuclei can also be produced in the heavy-ion collisions. They found quite a number of hyper-triton nuclei close to target rapidity. Presumably they are formed by either coalescence or deuterons, which pick up a $\Lambda$ in this dense environment. These first experimental results have triggered theoretical activities to study the hyper-nucleus production with the same approach, which allowed one to predict the non-strange fragment production very successfully. First results using the Isospin Quantum Molecular Dynamics (IQMD) approach as the underlying transport theory show that hypernucleus production is very sensitive to the phase-space distribution of the nucleons and the $\Lambda$ hyperons, similar to the Hanbury-Brown-Twiss (HBT) effect. The inelasticity of the $\Lambda$ production places the $\Lambda$ hyperons at a different rapidity than the
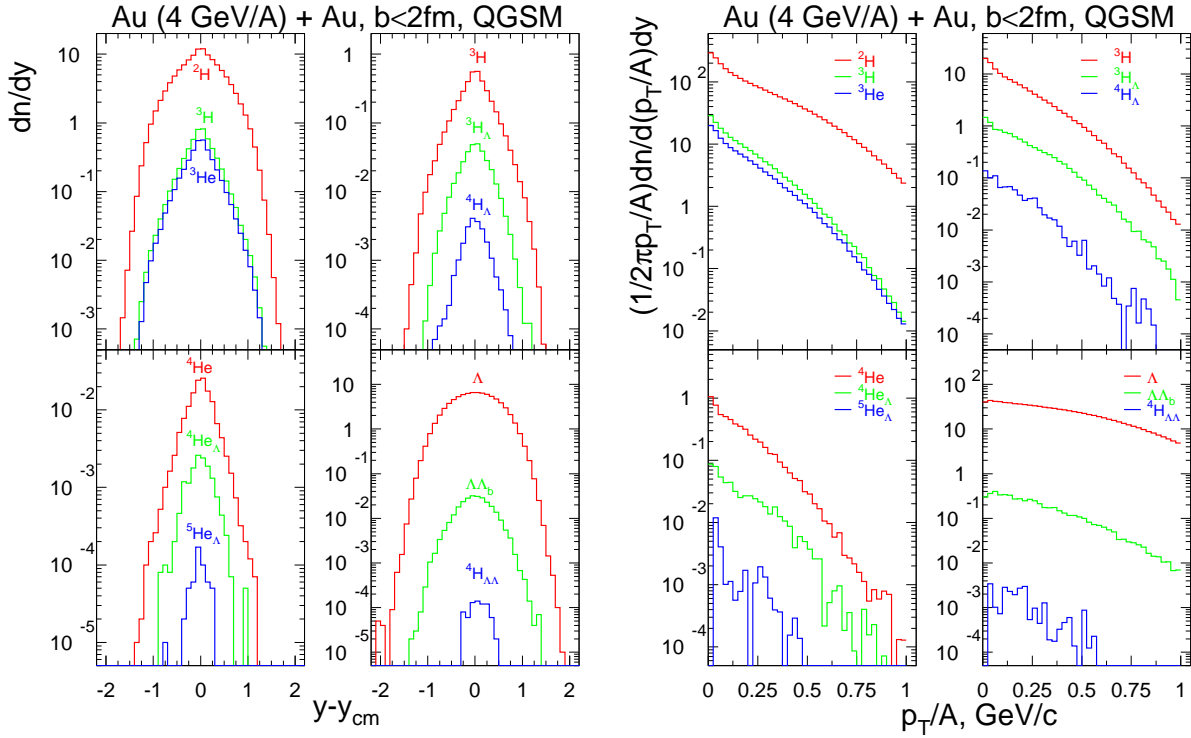
*Figure 3.6: The QGSM model predictions for rapidity (two left columns) and transverse momentum (two right columns) distributions of light clusters and light hypernuclei from 4 A·GeV Au+Au reactions. See text for details.*

spectator nuclei. Therefore a probability to find a coalescence partner depends on the spatial distribution of the nucleons with a momentum similar to that of the $\Lambda$.

The Quark-Gluon String Model (QGSM) [137–139] predicts that at Nuclotron energies the nuclear clusters will also be produced in the heavy-ion reactions around mid-rapidity due to the high baryons density. The QGSM considers the two lowest SU(3) multiplets in mesonic, baryonic and antibaryonic sectors, so the interactions between almost seventy hadron species are treated on the same footing. The high (quark and gluon degrees of freedom) and low (hadronic degrees of freedom) energy end of this model were bridged by the QGSM extension downward on the beam energy using the "mix-and-match" method. Here one assumes that the coalescence criterion used to form the composite particles includes the proximity of nucleons both in momentum and coordinate space. The coordinate coalescence parameters are determined by the relation $r_C = h/p_C$, where $p_C(\mathrm{d}) = 90$, $p_C(\mathrm{t}) = 108$, $p_C(^3\mathrm{He}) = 108$, and $p_C(\alpha) = 115$ MeV/c are adopted from [137]. As a first approximation the same coalescence parameters are used for both conventional fragments and hyper-fragments. The result of such calculations is shown in the left panel of Fig. 3.5, where the multiplicity of different clusters as a function of the cluster mass is displayed for 4 A·GeV Au+Au collisions. In the right panel of Fig. 3.5 the yield of hypernuclei and double-$\Lambda$ hyperons is displayed. It follows the same exponential decrease as a function of the mass, however it always lower than yield of the corresponding non-strange clusters because the number of $\Lambda$ hyperons is much lower than that of neutrons.

The rapidity distribution (left panel) and transverse momentum distribution (right panel) of light clusters and hypernuclei are shown in Fig. 3.6. One can see that they are experimentally accessible by the BM@N setup, which opens the opportunity to study hypernuclei production extensively.

Due to the decrease of the baryon-chemical potential $\mu_B$ with increasing of the beam energy, the maximum $\Lambda$ yield is observed at beam energies between 30 and 40 A·GeV. In the central Pb+Pb collisions at these energies about 50 $\Lambda$ hyperons are produced (see Fig. 3.3). In the central Au+Au collisions at 4 A·GeV still 4 $\Lambda$ hyperons are expected. However, the probability for their coalescence with protons or light nuclei like He increases with decreasing of the beam energy, i.e. decreasing of the fireball temperature and, hence, increasing of He yield. This is illustrated in Fig. 3.4, where the yield of (multi-strange) hypernuclei (as calculated within a thermal model) is plotted as function of the beam energy [136].

The yield of $^3$He and $^4$He strongly increases with decreasing of the beam energy, and the maximum yield of $_{\Lambda\Lambda}^5$H and $_{\Lambda\Lambda}^6$He is predicted for collision energies of $\sqrt{s_{NN}} = 4$—5 GeV ($\approx$ 8—10 A·GeV beam energy for the fixed target experiments). According to this calculation, we expect at Nuclotron energies a yield of $3 \cdot 10^{-8}$ $_{\Lambda\Lambda}^6$He, $10^{-6}$ $_{\Lambda\Lambda}^5$H, and $2 \cdot 10^{-2}$ $_{\Lambda}^3$H per central collision. Experimentally one has to reconstruct the decay chain of the $_{\Lambda\Lambda}^5$H hypernuclei (if it exists), for example: $_{\Lambda\Lambda}^5$H $\rightarrow$ $_{\Lambda}^5$He + $\pi^-$, $_{\Lambda}^5$He $\rightarrow$ $^4$He + p + $\pi^-$. The $_{\Omega}^6$H (if it exists) can be detected using the following chain: $_{\Omega}^6$H $\rightarrow$ $_{\Xi}^6$He + $\pi^-$, $_{\Xi}^6$He $\rightarrow$ $_{\Lambda\Lambda}^6$He $\rightarrow$ $_{\Lambda}^5$He + p + $\pi^-$, $_{\Lambda}^5$He $\rightarrow$ $^4$He + p + $\pi^-$.

The systematic studies of neutron-rich and halo (loosely bound) hypernuclei ($_{\Lambda}^3$H, $_{\Lambda}^4$H, $_{\Lambda}^6$He, etc.) [140] can be performed simultaneously. Part of these measurements requires the detection of light nuclear fragments (e.g. $^4$He) what can be performed using the amplitude information from Silicon Tracker System (or from the scintillation detectors placed in front of STS). The feasibility study will be performed for the beams of $^4$He and $^6$Li [140].

## 3.4 Search for multi-strange meta-stable objects

The forms of meta-stable or even stable objects with strangeness have been proposed long ago as a collapsed states of matter, either consisting of baryons or quarks. Up to date, none of these objects, e.g. strangelets and (strange) di-baryons, have been observed. Moreover, no reliable predictions for the multiplicities of these objects in the heavy-ion collisions at Nuclotron energies are available. At higher energies, calculations with a hybrid model have been performed [141]. With a detector system, which is able to identify hyperons, it is definitely worthwhile to search for a strange di-baryon like a $(\Xi\Lambda)_b$, which decays into two $\Lambda$ hyperons.

## 3.5 Study of the production mechanisms and in-medium properties of strangeness in hot and dense nuclear matter

As discussed in the section 1, the properties of hadrons are modified in hot and dense nuclear matter as produced in the heavy-ion collisions. This affects also the production mechanisms of strange mesons and baryons. There are two basic ways to describe the in-medium effects (see [35] and references therein):

1) "dropping"/"enhancement" mass scenarios [16, 17] or attractive/repulsive mean-field potentials;

2) collisional broadening of the spectral functions of strange particles — kaons and hyperons [20–22].

The in-medium properties of hadrons can be studied experimentally by a measurement of the "bulk" observables since the modification of the excitation functions of "general" observables

— such as yields, collective flow, high order harmonics ($v_3$, $v_4$) and their ratios (e.g. $v_2^2/v_4$), fluctuations and correlations — signals the effects as learned from the AGS experiments.

The following "bulk" observables are necessary to measure:
• yields (i.e. multiplicity, rapidity $dN/dy$, invariant spectra $Ed^3N/d^3p$):
† enhancement of $K^-$, $\bar{K}^0$ yields due to a lowering of the production threshold $s_{\text{th}}$ in the elementary primary baryon-baryon ($BB$) and secondary meson-baryon ($mB$) collisions;
† reduction of $K^+$, $K^0$ yields due to increasing of the production thresholds in elementary reactions.
It should be noted the effect is more pronounced closer to the physical thresholds.
• transverse $p_T$, $m_T$ spectra (i.e. $dN/(m_T \cdot dm_T)$, $dN/(p_T \cdot dp_T)$ spectra).
The in-medium effects lead to a change of the slope of transverse mass spectra, which results in a violation of the general $m_T$ scaling (see [142]). The repulsive potential leads to a hardening of $m_T$ spectra, while an attractive potential leads to a softening of $m_T$ spectra. Thus, by measuring the spectra of kaons/antikaons and pions (as a baseline) one can extract the value of the averaged in-medium meson-nucleus potential.
• The azimuthal anisotropies of the collective transverse flow — directed $v_1$, elliptic $v_2$, and higher harmonics $v_3$, $v_4$, …
The collective flows — "barometers" of the reaction — are very sensitive to the different in-medium scenarios. It is useful to measure dependences on the transverse momentum $p_T$, rapidity $y$, centrality $N_{\text{part}}$ for the flow coefficients $v_2$ and $v_1$, and possibly $v_3$ and $v_4$.

# 3.6   Study of the in-medium properties of vector mesons — perspectives for BM@N

The in-medium modifications or the properties of light vector mesons $\rho, \omega$ (i.e. containing only the light quarks/antiquarks $u$, $d$) and the vector meson with hidden strangeness $\phi$ (made from $\bar{s}$ and $s$ quarks) are under continued investigation from both the theoretical and experimental sides (see section 1.2 and references therein). The heavy-ion collisions at Nuclotron provide a good conditions to study the in-medium effects of vector mesons since the baryon densities are high in this energy region and the reaction times are still quite long compared to the ultra-relativistic energies at SPS and RHIC.

There are two possible ways to study in-medium effects of vector mesons: i) by the dilepton decay mode, i.e. by looking for the di-electron or di-muon emission from the vector mesons decay, and ii) by the hadronic modes, i.e. by reconstruction of the invariant mass of hadronic decay products of vector mesons, e.g. $\rho \to \pi^+\pi^-$, $\omega \to 3\pi$, or $\phi \to K^+K^-$. The hadronic decay channels observation is a quite difficult experimental task due to the strong final-state interactions (re-scattering and absorption) of the hadronic decay products. In this respect dileptons provide a "clean" signal undistorted by the strong interaction with the hadronic medium.

The dilepton mode is a promising future perspective for the BM@N experiment and requires a corresponding upgrade of the setup technical design to allow the dilepton measurements. Nevertheless, the in-medium study of vector mesons can be explored also by the hadronic modes, too. This program will be a natural continuation of the present studies at SIS energies of the FOPI and HADES collaborations [111, 112] to the higher energies and baryon densities.

# 3.7 Study of the EoS with strangeness

As pointed out above the EoS changes the collisional dynamics and correspondingly the particle abundances and spectra as well as the maximal baryon densities and hadronic interaction rates. Accordingly, there is no single observable that may be viewed as a "shooting gun" for the EoS. The experience from studies at SIS and AGS energies shows that only a systematic study of differential particle yields, collective flow harmonics ($v_1$, ..., $v_4$) for all the hadrons and their ratios measured as a function of incident energy, system size and centrality will allow for the robust conclusions. In part the physics program at Nuclotron will be an extension of the studies at AGS, however, including the single- and multi-strange sector, will also allow one to shed novel light on the "strange axis" of the EoS of strongly interacting matter.

## 3.7.1 Study of polarization effects on hyperon production

The local violation of discrete ($C$, $P$, $T$) symmetries in the heavy-ion collisions is currently widely discussed from both the experimental and theoretical points of view. A special attention is paid to the Chiral Magnetic Effect (CME) whose manifestations have been searched experimentally at RHIC and LHC energies during last few years. However, the recent observations in the course of RHIC beam-energy-scan resulted in the picture, which is more likely explained by other mechanisms.

At the same time, there is an analogue of the CME, i.e. the Chiral Vortical Effect [143], with the medium vorticity playing the role of the magnetic field, which may lead to separation of electric and other conserved charges [144]. Moreover, vorticity effects [145] in the appearance of induced axial currents, in the case of strange quarks can manifest [144] themselves in the polarization of Λ hyperons. This polarization is in turn the traditional object of investigations in hadronic physics [146], as it is a clean observable due to the "self-analyzing" weak decays. On the other side, the Λ spin in the non-relativistic quark model is entirely carried by the strange quark and thus its polarization is naturally related to the strange axial current.

The scattering of unpolarized hadrons may lead to the production of transversely (to the scattering plane) polarized hyperons. The situation is changed in the heavy-ion collisions, where the random motion of produced particles leads to a smearing of information on the scattering plane and the disappearance of transverse polarization [147] in favor of a longitudinal one due to indirect Λ hyperons from the weak decays.

It was suggested in [148] to search for a polarization transverse to the reaction plane, however no sign of that was found during the experimental studies at RHIC. It might be that at RHIC energies the chemical potential is too small since a sizeable value is required for a sufficient coupling to vorticity. Accordingly, the mechanism suggested in [144] might be observable at lower energies. Thus one may look for [149] the polarization of Λ hyperons in both elementary p+p and p+A reactions and in the A+A collisions. The comparative analysis of polarization data may provide a signal on the appearance of a new collective behaviour.

Another rotation and vorticity related signal may be provided by various types of so-called handedness originally suggested in [150] for jets, however such signals might be also useful [144] in the heavy-ion collisions. The expected rates (see section 4.4) should allow one to measure the polarization on the several percent level.

## 3.8   The influence of the BM@N setup acceptance on physical observables
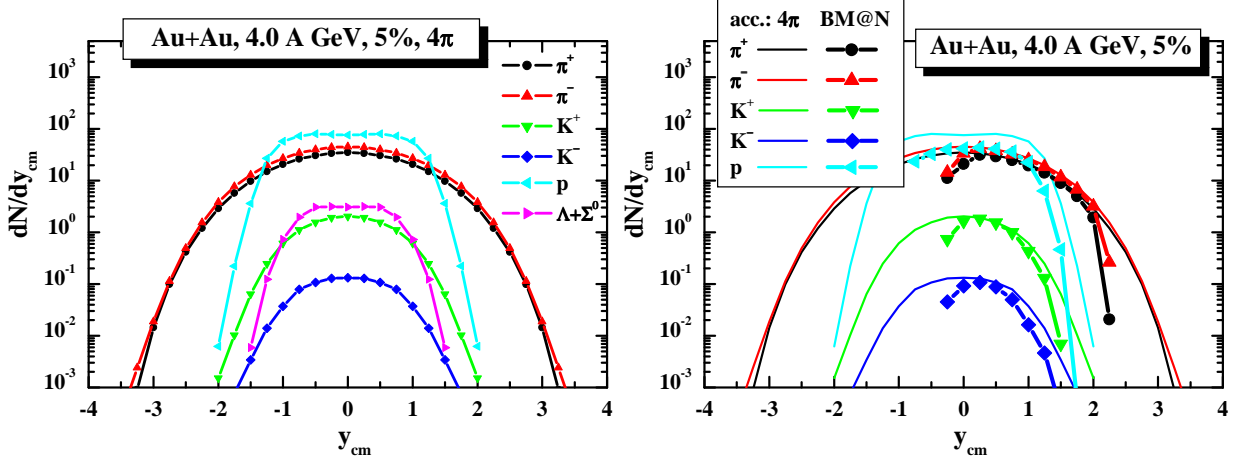


*Figure 3.7: The HSD model simulated rapidity $y_{cm}$ distributions for $\pi^+$, $\pi^-$, $K^+$, $K^-$, p, and $\Lambda + \Sigma^0$ from the central (5 %) Au+Au collisions at 4.0 A·GeV into full $4\pi$ acceptance (left) and BM@N acceptance (right). The $4\pi$ results are also shown for comparison in the right panel as thin lines.*
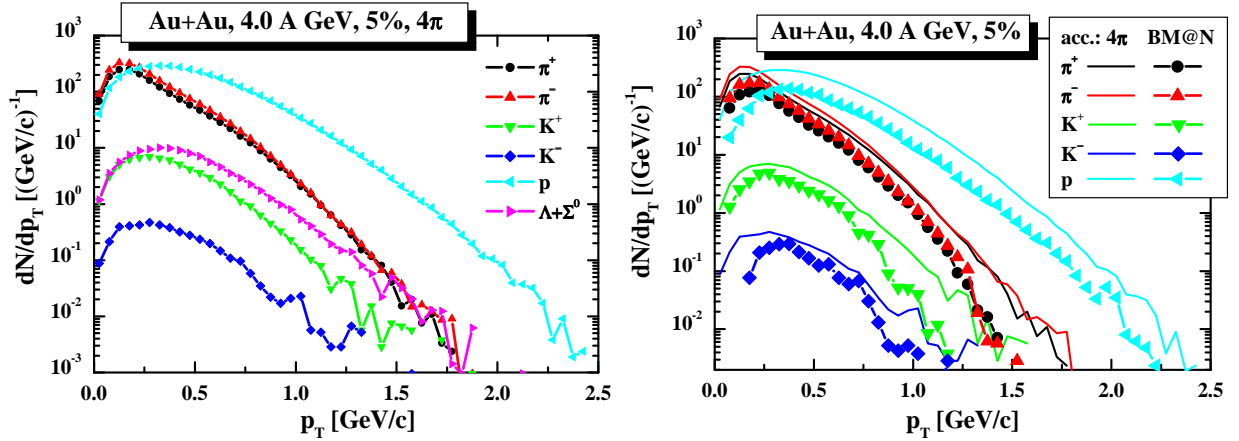


*Figure 3.8: The HSD model simulated transverse momentum $p_T$ distributions for $\pi^+$, $\pi^-$, $K^+$, $K^-$, p, and $\Lambda + \Sigma^0$ from the central (5 %) Au+Au collisions at 4.0 A·GeV into full $4\pi$ acceptance (left) and BM@N acceptance (right). The $4\pi$ results are also shown for comparison in the right panel as thin lines.*

In this section we demonstrate the influence of the BM@N setup acceptance on the "bulk" observables. We use the HSD transport approach [26] for the simulations, which is expected to provide rather reliable results for the global observables also in Nuclotron energy range. The BM@N acceptance will be discussed in detail in section 4. Here we apply the BM@N acceptance matrix in $y$—$p_T$ (see section 4.3) to the HSD full $4\pi$ acceptance results in order to explore the BM@N setup potential for the reconstruction of physical phenomena from the measured observables.

As an example, the HSD model simulations of the rapidity (in the center-of-mass frame) $y_{cm}$ and transverse momentum $p_T$ distributions are shown in Figs. 3.7 and 3.8, respectively, for $\pi^+$, $\pi^-$, $K^+$, $K^-$, p, and $\Lambda + \Sigma^0$ into $4\pi$ acceptance (left panels) and for $\pi^+$, $\pi^-$, $K^+$, $K^-$, p with application of the BM@N acceptance (right panels) from the central (5 %)
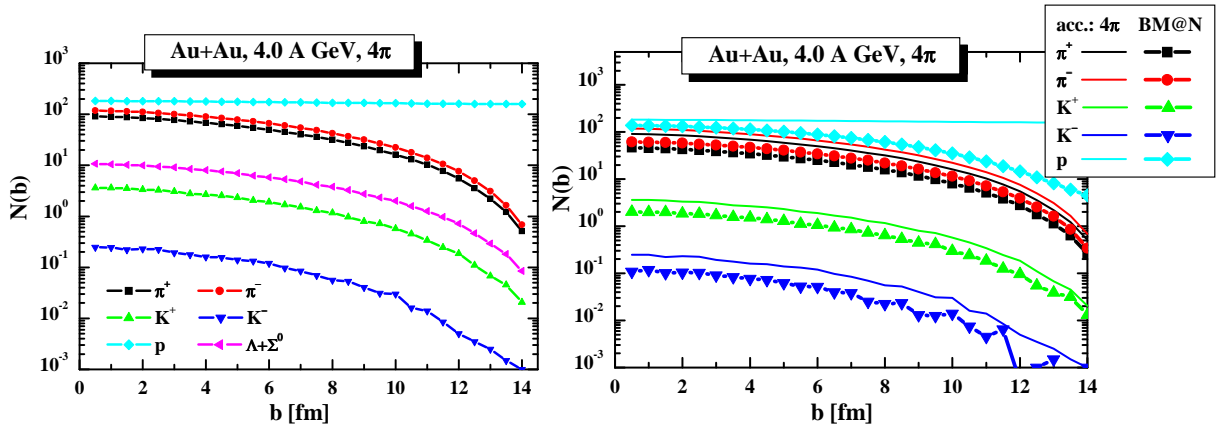
*Figure 3.9: The HSD model calculated multiplicities of $\pi^+$, $\pi^-$, $K^+$, $K^-$, p, and $\Lambda + \Sigma^0$ versus centrality from Au+Au collisions at 4.0 A·GeV into full $4\pi$ acceptance (left panel) and BM@N acceptance (right panel). The $4\pi$ results are also shown for comparison in the right panel as thin lines.*

Au+Au collisions at 4.0 A·GeV. As seen from Fig. 3.7, the BM@N acceptance covers basically the forward rapidity region (as for a fixed target experiment). Since the rapidity window is relatively large, one can expect to reconstruct the major longitudinal expansion of the system by adding the reflection of the measured spectra w.r.t. the center-of-mass mid-rapidity. Similar arguments hold for the transverse momentum direction: Fig. 3.8 demonstrates that the "distortion" of the $p_T$ spectra shape by the BM@N acceptance is not drastic and dominantly results in a "loss" of the absolute yield.

Additionally, the HSD model calculated multiplicities of $\pi^+$, $\pi^-$, $K^+$, $K^-$, p, and $\Lambda + \Sigma^0$ are presented in Fig. 3.9 versus centrality from Au+Au collisions at 4.0 A·GeV into full $4\pi$ acceptance (left panel) and BM@N acceptance (right panel). By comparing the $4\pi$ and BM@N acceptance results one can see that the BM@N acceptance will cover about half of the total multiplicity of hadrons for all centralities. An exception is the total proton yield, which is reduced strongly for peripheral collisions since the BM@N acceptance covers only a small fraction of target rapidity. Consequently, the spectator protons are not seen by the BM@N setup.

# Chapter 4

# Simulation studies

## 4.1 UrQMD input

The main goal of the experiment is to obtain high statistics data for Au+Au collisions at 3.5, 4.0, and 4.65 A·GeV. The simulation of the setup performance has been obtained using UrQMD generator.
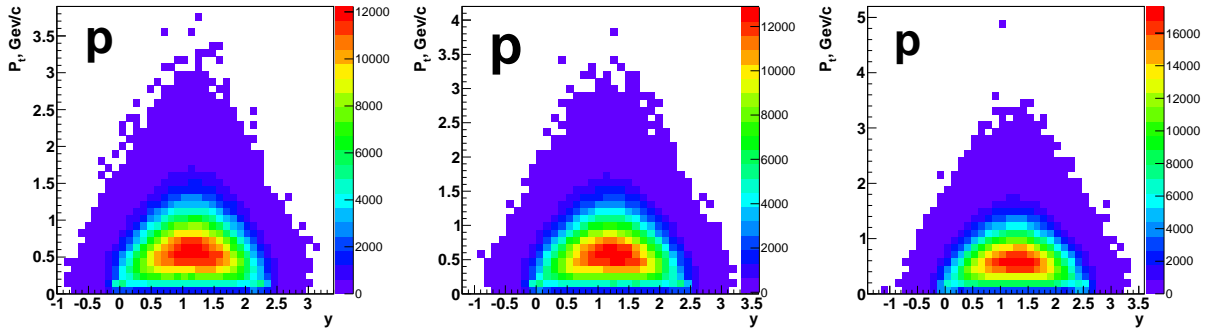


Figure 4.1: From left to right: the $y$—$p_T$ acceptances for protons from the central Au+Au collisions at 3.5, 4.0, and 4.65 A·GeV.
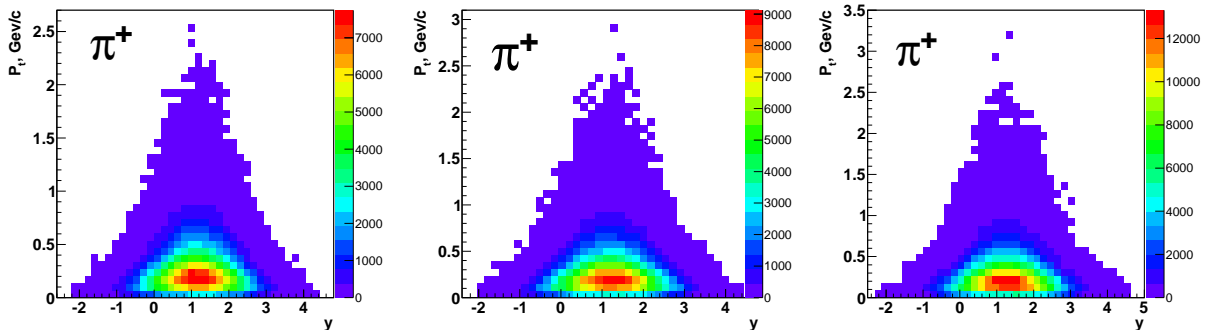


Figure 4.2: From left to right: the $y$—$p_T$ acceptances for $\pi^+$ from the central Au+Au collisions at 3.5, 4.0, and 4.65 A·GeV.

The $y$—$p_T$ acceptances for protons from the central Au+Au collisions at 3.5, 4.0, and 4.65 A·GeV are presented in the left, middle, and right panels in Fig. 4.1, respectively. The $y$—$p_T$ acceptances for positively and negatively charged pions from the central Au+Au
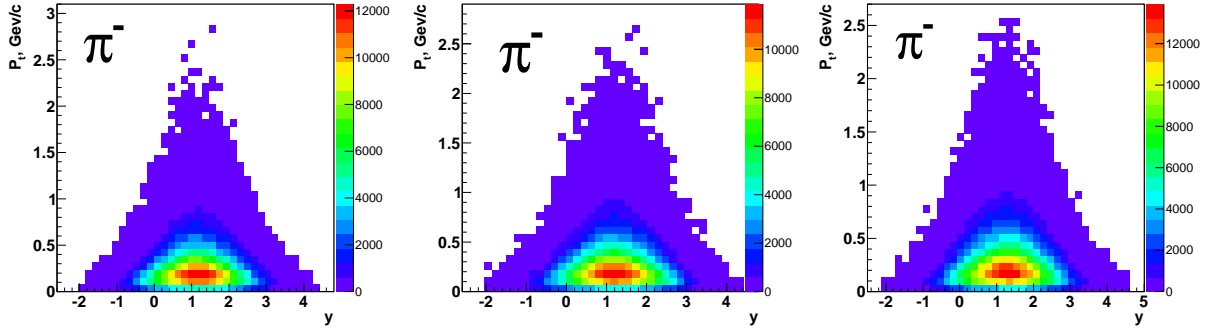
*Figure 4.3: From left to right: the $y$—$p_T$ acceptances for $\pi^-$ from the central Au+Au collisions at 3.5, 4.0, and 4.65 A·GeV.*
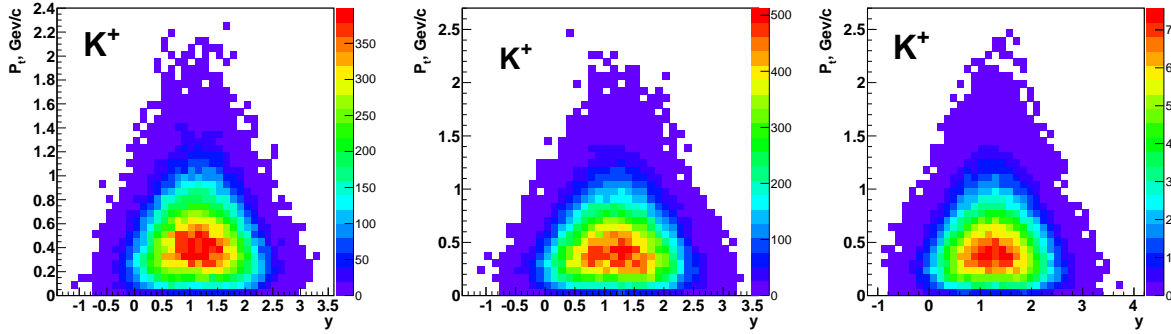


*Figure 4.4: From left to right: the $y$—$p_T$ acceptances for $K^+$ from the central Au+Au collisions at 3.5, 4.0, and 4.65 A·GeV.*

collisions at 3.5, 4.0, and 4.65 A·GeV are presented in the left, middle, and right panels in Fig. 4.2 and Fig. 4.3, respectively. One can see that the $y$—$p_T$ distributions for $\pi^+$ and $\pi^-$ are almost the same, but the yield of $\pi^-$ is approximately 20% larger than for $\pi^+$. The $y$—$p_T$ acceptances for positively and negatively charged kaons from the central Au+Au collisions at 3.5, 4.0, and 4.65 A·GeV are presented in the left, middle, and right panels in Fig. 4.4 and Fig. 4.5, respectively. One can see that the $y$—$p_T$ distributions for $K^+$ and $K^-$ are the same, but the yield of $K^-$ is less for more than one order of magnitude. The multiplicities of charged pions and kaons from the central Au+Au collisions are presented in Table 4.1.

The $y$—$p_T$ acceptances for weakly decaying particles ($K^0$, $\Lambda$ and $\Xi^-$) obtained from $10^4$ central Au+Au collisions at 4.0 A·GeV are presented in the left, middle, and right panels
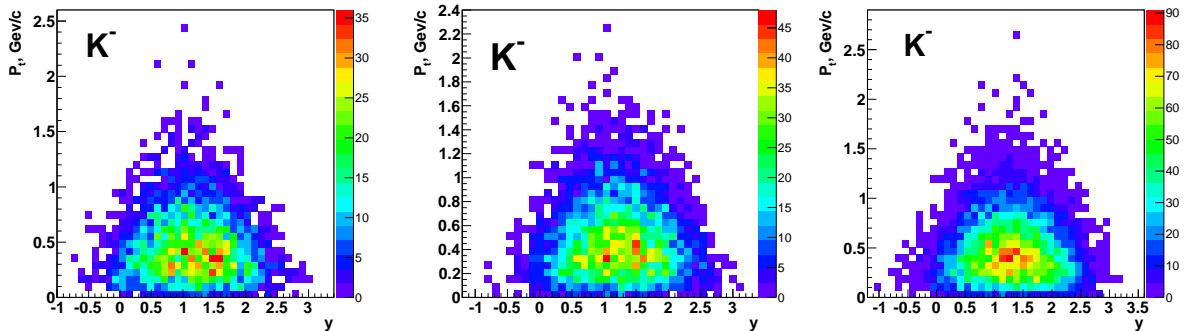


*Figure 4.5: From left to right: the $y$—$p_T$ acceptances for $K^-$ from the central Au+Au collisions at 3.5, 4.0, and 4.65 A·GeV.*
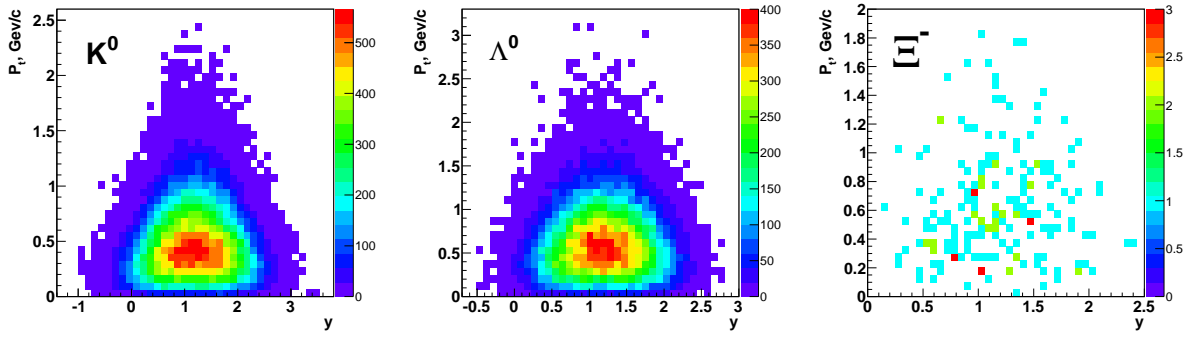
*Figure 4.6: From left to right: the $y$—$p_T$ acceptances for $K^0$, $\Lambda^0$, and $\Xi^-$ particles from the central Au+Au collisions at 4.0 A·GeV.*

*Table 4.1: The multiplicities of charged particles from the central Au+Au collisions at 3.5, 4.0, and 4.65 A·GeV in $4\pi$ acceptance.*

|         | 3.5 A·GeV | 4.0 A·GeV | 4.65 A·GeV |
|---------|-----------|-----------|------------|
| $\pi^-$ | 68.4      | 73.0      | 94.7       |
| $\pi^+$ | 51.0      | 55.9      | 74.4       |
| $K^+$   | 6.1       | 7.2       | 10.1       |
| $K^-$   | 0.4       | 0.6       | 1.0        |

in Fig. 4.6, respectively. The multiplicities of these particles for three different energies are presented in Table 4.2.

## 4.2   Different configurations of the STS

The simulation have been performed using the UrQMD event generator, the BM@N detector model in the GEANT transport code, and the event reconstruction algorithms in the CBMRoot software package. The heart of the BM@N setup is the Silicon Tracker System (STS). The STS detector comprises from four up to eight stations of double-sided silicon micro-strip detectors (pitch 60 $\mu$m, stereo angle 7.5°) located in the field of a large aperture dipole magnet SP41. The time-of-flight system based on the large aperture mRPCs wall is used for the hadrons identification.

For the simulation we use several layouts of the STS. One of them is CBM-like design, namely, eight stations placed on the distances of 30, 40, 50, 60, 70, 80, 90, and 100 cm from the target. Last five stations are suited for the SP41 magnet gap and have the same size. The positions and sizes of the stations are given in Table 4.3.

Second design of the STS consists of four stations only placed on the distances of 30,

*Table 4.2: The multiplicities of weakly decaying particles from the central Au+Au collisions at 3.5, 4.0, and 4.65 A·GeV in $4\pi$ acceptance.*

|            | 3.5 A·GeV | 4.0 A·GeV | 4.65 A·GeV |
|------------|-----------|-----------|------------|
| $K^0$      | 6.9       | 8.0       | 11.2       |
| $\Lambda^0$| 5.1       | 5.9       | 8.2        |
| $\Xi^-$    | 0.015     | 0.020     | 0.040      |

Table 4.3: *V*1 *layout of the BM@N STS used for the simulation.*

| Station | 1 | 2 | 3 | 4 | 5 | 6 | 7 | 8 |
|---|---|---|---|---|---|---|---|---|
| $z$ position, cm | 30 | 40 | 50 | 60 | 70 | 80 | 90 | 100 |
| vertical $r_{\text{out}}$, cm | 13.99 | 18.65 | 23.32 | 27.98 | 27.98 | 27.98 | 27.98 | 27.98 |
| horizontal $r_{\text{out}}$, cm | 23.08 | 30.77 | 34.98 | 39.17 | 39.17 | 39.17 | 39.17 | 39.17 |

Table 4.4: *V*2 *layout of the BM@N STS used for the simulation (4 first stations only).*

| Station | 1 | 2 | 3 | 4 | 5 | 6 | 7 | 8 |
|---|---|---|---|---|---|---|---|---|
| $z$ position, cm | 30 | 40 | 50 | 60 | | | | |
| vertical $r_{\text{out}}$, cm | 13.99 | 18.65 | 23.32 | 27.98 | | | | |
| horizontal $r_{\text{out}}$, cm | 23.08 | 30.77 | 34.98 | 39.17 | | | | |

40, 50, and 60 cm from the target (*V*2 configuration). The positions and sizes of the stations are given in Table 4.4.

Third design of the STS consists of six stations placed on the distances of 30, 40, 50, 60, 100, and 200 cm from the target (*V*3 configuration). Last three stations have the same size. The positions and sizes of the stations are given in Table 4.5. The *V*3 configuration can be used at some stage of the experiment, when the gaseous detectors with good position resolution could be used as two last stations.

## 4.3   Global tracking performance simulations

The simulation of the global tracking performance (using STS subdetector and TOF system — T0 and RPC subdetectors) has been done for three different STS configurations (see Tables 4.3, 4.4, and 4.5).

The RMS of the charged particles momentum reconstruction as a function of the particle momentum for *V*1, *V*2, and *V*3 STS configurations are presented in the left, middle, and right panels in Fig. 4.7, respectively. The momentum resolution as a function of the momentum is approximately the same for all three STS configurations. The charged particles momentum reconstruction for all particles for *V*1, *V*2, and *V*3 STS configurations are shown in the left, middle, and right panels in Fig. 4.8, respectively. The momentum resolution for *V*1 configuration is a bit better than for *V*2 and *V*3 configurations.

The efficiency of the charged particles momentum reconstruction by STS as a function of the particle momentum for *V*1, *V*2, and *V*3 STS configurations are shown in the left, middle, and right panels in Fig. 4.9, respectively. The largest efficiency of the reconstruction is observed for *V*1 configuration, while *V*3 configuration demonstrates decreasing of the efficiency reconstruction at large momenta.

Table 4.5: *V*3 *layout of the BM@N STS used for the simulation.*

| Station | 1 | 2 | 3 | 4 | 5 | 6 | 7 | 8 |
|---|---|---|---|---|---|---|---|---|
| $z$ position, cm | 30 | 40 | 50 | 60 | 100 | 200 | | |
| vertical $r_{\text{out}}$, cm | 13.99 | 18.65 | 23.32 | 27.98 | 27.98 | 27.98 | | |
| horizontal $r_{\text{out}}$, cm | 23.08 | 30.77 | 34.98 | 39.17 | 39.17 | 39.17 | | |
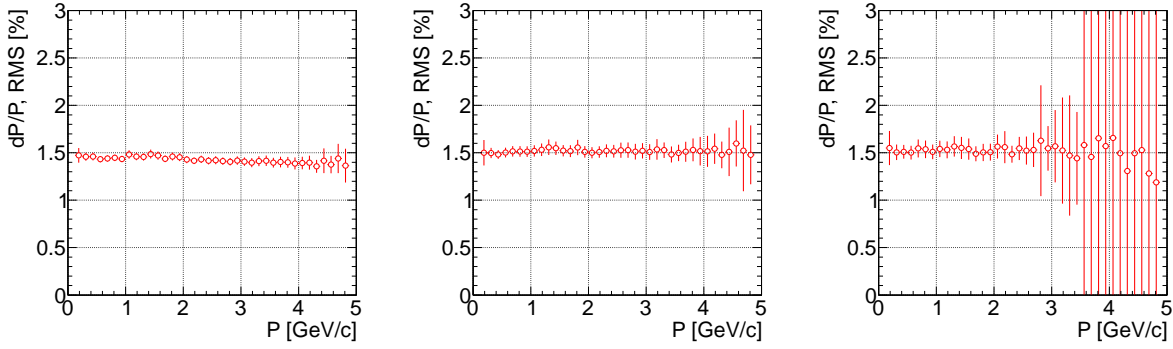
Figure 4.7: From left to right: the RMS of the charged particles momentum reconstruction as a function of the particle momentum for $V1$, $V2$, and $V3$ STS configurations.
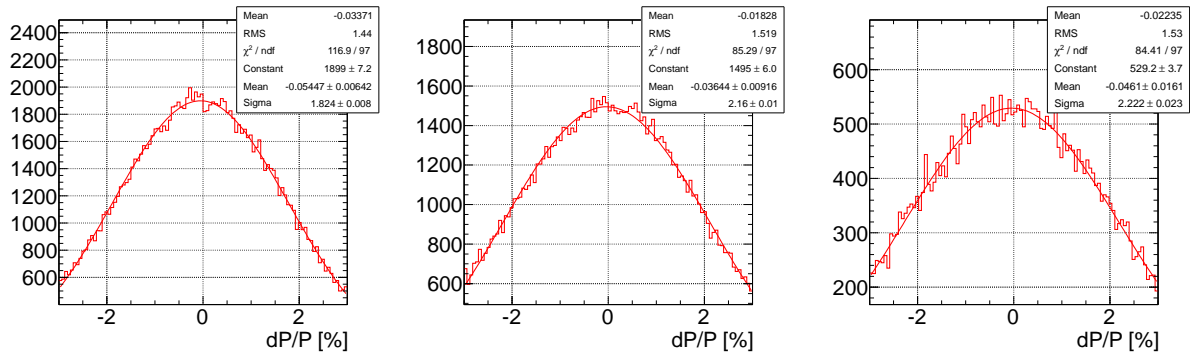


Figure 4.8: From left to right: the charged particles momentum reconstruction for all particles for $V1$, $V2$, and $V3$ STS configurations.

The efficiency of the charged particles momentum reconstruction by STS—TOF as a function of the particle momentum for $V1$, $V2$, and $V3$ STS configurations are shown in the left, middle, and right panels in Fig. 4.10, respectively. Red circles and blue squares represent the results for the reconstruction using STS only and both STS and TOF, respectively. The best reconstruction efficiency almost independent on the particle momentum at $P \geq 1$ GeV/c is provided by the $V1$ configuration.

## 4.4 Acceptances for the charged particles

The $y$—$p_T$ distributions for all charged particles: protons, $\pi^{\pm}$, and $K^{\pm}$ mesons from the UrQMD generated central Au+Au collisions at 4 A·GeV within BM@N setup acceptance,
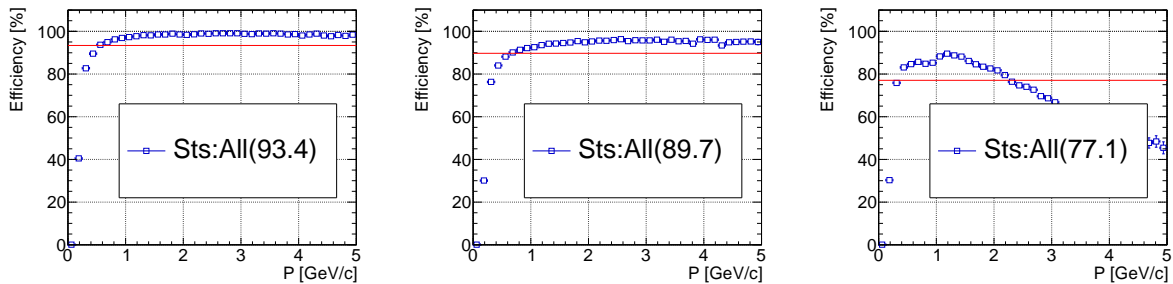


Figure 4.9: From left to right: the efficiency of the charged particles momentum reconstruction by STS as a function of the particle momentum for $V1$, $V2$, and $V3$ STS configurations.
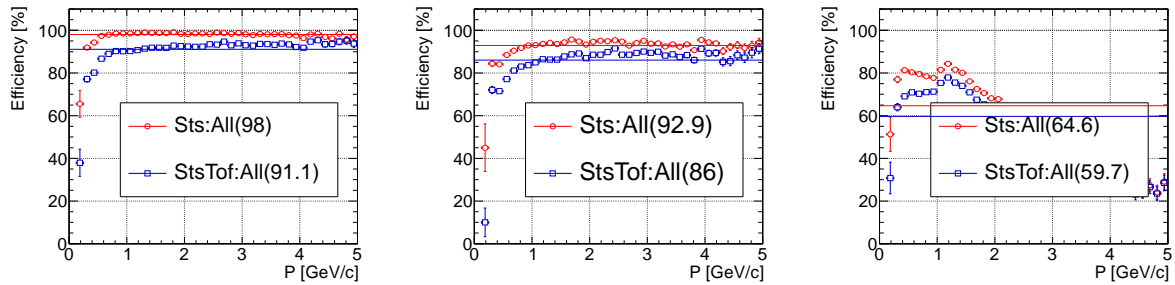
*Figure 4.10: From left to right: the efficiency of the charged particles momentum reconstruction by STS—TOF as a function of the particle momentum for $V1$, $V2$, and $V3$ STS configurations. Red circles and blue squares are the reconstruction using STS and STS—TOF, respectively.*



*Figure 4.11: The $y$—$p_T$ distributions for all charged particles from the central Au+Au collisions at 4 A·GeV from left to right: UrQMD events within BM@N setup acceptance, reconstructed events using STS and TOF, and the reconstruction efficiency.*

the reconstructed events using STS and TOF, and the reconstruction efficiency are shown in Figs. 4.11, 4.12, 4.13, 4.14, 4.15, and 4.16 in the left, central, and right panels, respectively. The simulation has been performed for the $V1$ configuration of the STS (see Table 4.3). One can see that the acceptances are quite large and the reconstruction efficiencies at low $p_T$ are large enough.

The simulation framework is still under development. The optimizations of the BM@N setup are continued.

## 4.5 Weakly decaying particles

Experimentally the $\Lambda$, $\Xi$, and $\Omega$ hyperons can be identified via the topology of their weak decays ($\Lambda \to p\pi^-$, $\Xi \to \Lambda\pi$, $\Omega \to \Lambda K$) (see Fig. 4.17).

The results of the simulations for the $V1$ configuration of the STS are shown in Fig. 4.18, which depicts the invariant mass spectra for $K_s^0$ mesons and $\Lambda$ hyperons for $5 \cdot 10^5$ central Au+Au collisions at 4 A·GeV. The analysis is based on topological cuts only, without particle identification via the time-of-flight determination. The combinatorial background can be further reduced by identifying the decay protons by the time-of-flight measurement. One can see the high reconstruction efficiencies and good signal/background ratios.

The $y$—$p_T$ acceptances for $K_s^0$ mesons (left) and $\Lambda$ hyperons (right) from the central Au+Au collisions at 4 A·GeV are shown in Fig. 4.19. One can see that acceptances are large enough.
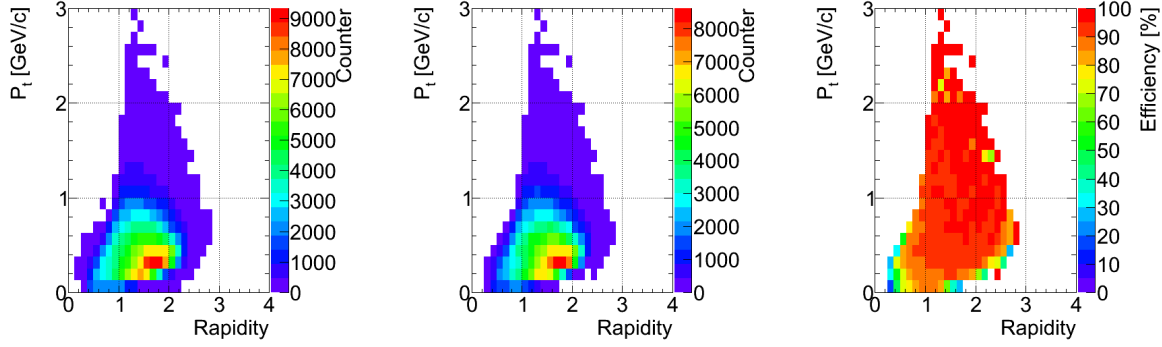
*Figure 4.12: The $y$—$p_T$ distributions for protons from the central Au+Au collisions at 4 A·GeV from left to right: UrQMD events within BM@N setup acceptance, reconstructed events using STS and TOF, and the reconstruction efficiency.*
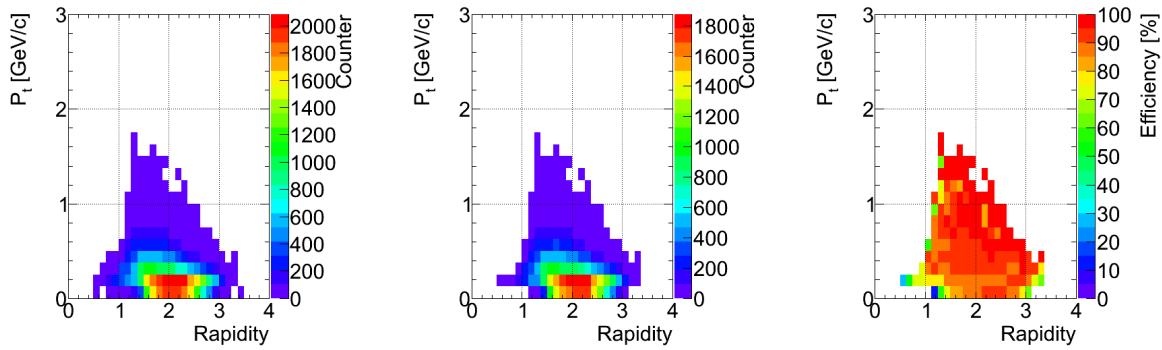


*Figure 4.13: The $y$—$p_T$ distributions for $\pi^+$ mesons from the central Au+Au collisions at 4 A·GeV from left to right: UrQMD events within BM@N setup acceptance, reconstructed events using STS and TOF, and the reconstruction efficiency.*

The simulation results for $V2$ configuration of the STS are shown in Figs. 4.20 and 4.21, which depict the invariant mass spectra for $K_s^0$ mesons and $\Lambda$ hyperons and their $y$—$p_T$ acceptances for the central Au+Au collisions at 4 A·GeV, respectively. The reconstruction efficiencies and signal/background ratios are much worse than for the $V1$ configuration, especially for $K_s^0$ mesons. The acceptances are approximately the same as for the $V1$ configuration.

The simulation results for $V3$ configuration of the STS are shown in Figs. 4.22 and 4.23, which depict the invariant mass spectra for $K_s^0$ mesons and $\Lambda$ hyperons and their $y$—$p_T$ acceptances for the central Au+Au collisions at 4 A·GeV, respectively. The reconstruction efficiencies are approximately two times less than for $V1$ STS configuration with the same signal/background ratios. The acceptances are approximately the same as for the $V1$ configuration.

## 4.6   Cascade hyperon $\Xi^-$ reconstruction

The simulation for the cascade hyperon $\Xi^-$ has been performed for $5 \cdot 10^5$ UrQMD central Au+Au collisions at 4 A·GeV for three different STS configurations. The selection of $\Xi^-$ requires the effective reconstruction of $\Lambda$ decay in the p$\pi^-$ mode and the secondary vertex reconstruction for $\Lambda\pi^-$ (see Fig. 4.17).

The selection efficiencies and $y$—$p_T$ acceptances for $\Xi^-$ hyperons from the central
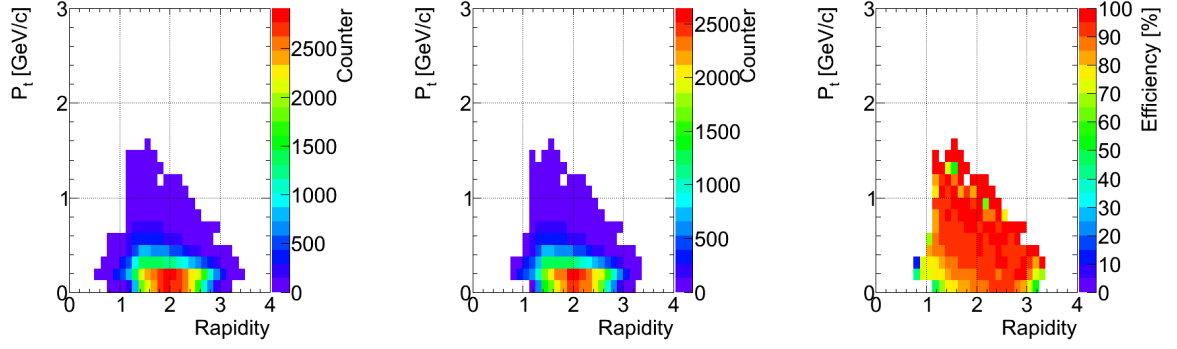
Figure 4.14: The $y$—$p_T$ distributions for $\pi^-$ mesons from the central Au+Au collisions at 4 A·GeV from left to right: UrQMD events within BM@N setup acceptance, reconstructed events using STS and TOF, and the reconstruction efficiency.
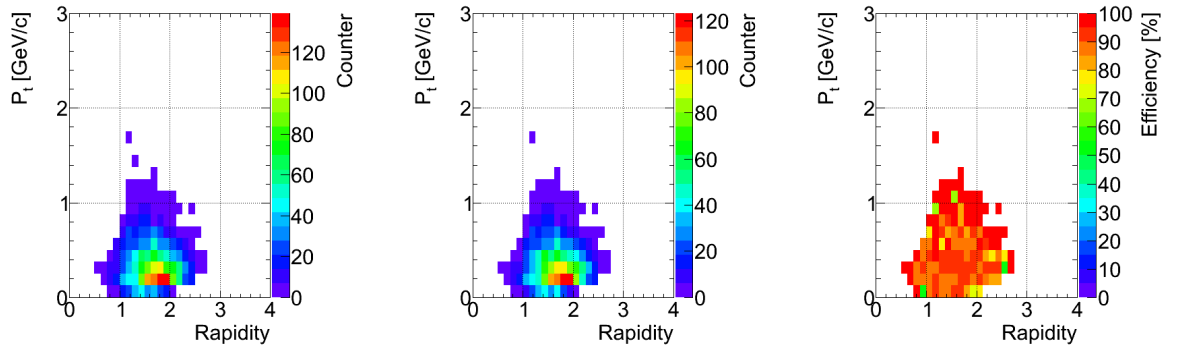


Figure 4.15: The $y$—$p_T$ distributions for $K^+$ mesons from the central Au+Au collisions at 4 A·GeV from left to right: UrQMD events within BM@N setup acceptance, reconstructed events using STS and TOF, and the reconstruction efficiency.

Au+Au collisions at 4.0 A·GeV for three different STS configurations (see Tables 4.3, 4.4, and 4.5) are presented in Figs. 4.24 and 4.25, respectively. The maximal value of the selection efficiency is observed for the $V1$ STS configuration with 8 stations. The $V3$ configuration provides approximately order of magnitude less efficiency. The $V2$ configuration (4 stations only) does not allow us to detect $\Xi^-$ hyperons. One can conclude, that while $K_s^0$ and $\Lambda$ can be detected by any considered STS configuration, the detection of the cascade particles like $\Xi^-$ hyperons certainly requires the full configuration of the STS.
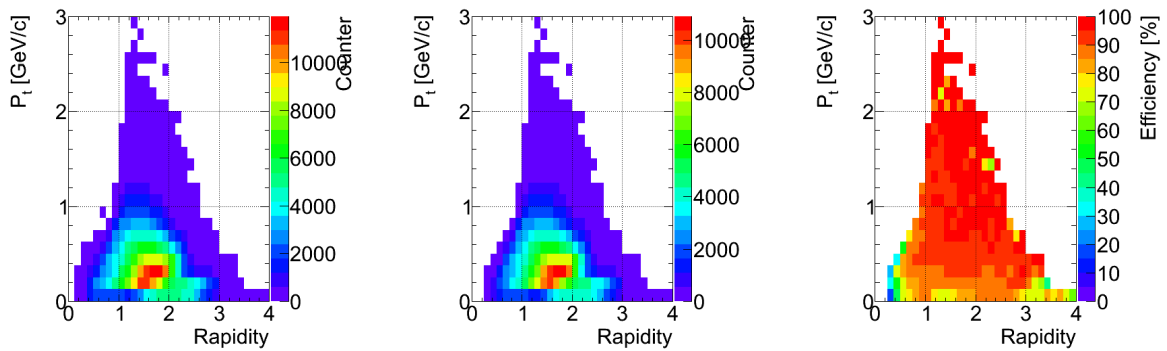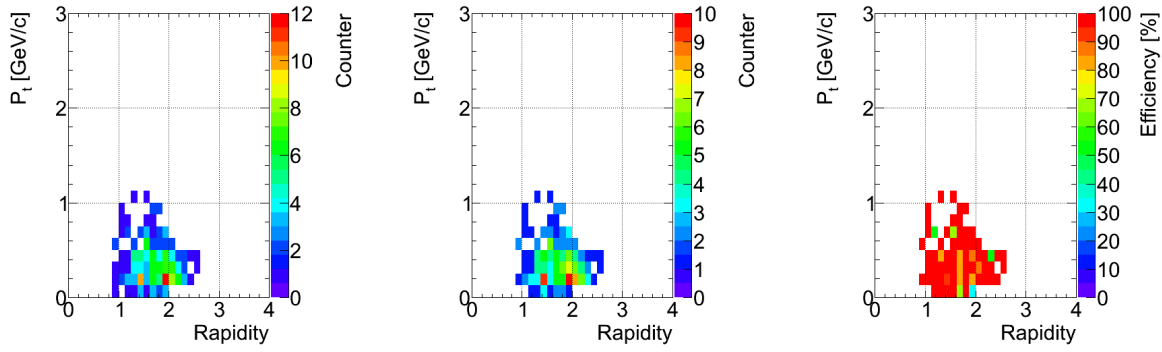
Figure 4.16: The $y$—$p_T$ distributions for $K^-$ mesons from the central Au+Au collisions at 4 A·GeV from left to right: UrQMD events within BM@N setup acceptance, reconstructed events using STS and TOF, and the reconstruction efficiency.
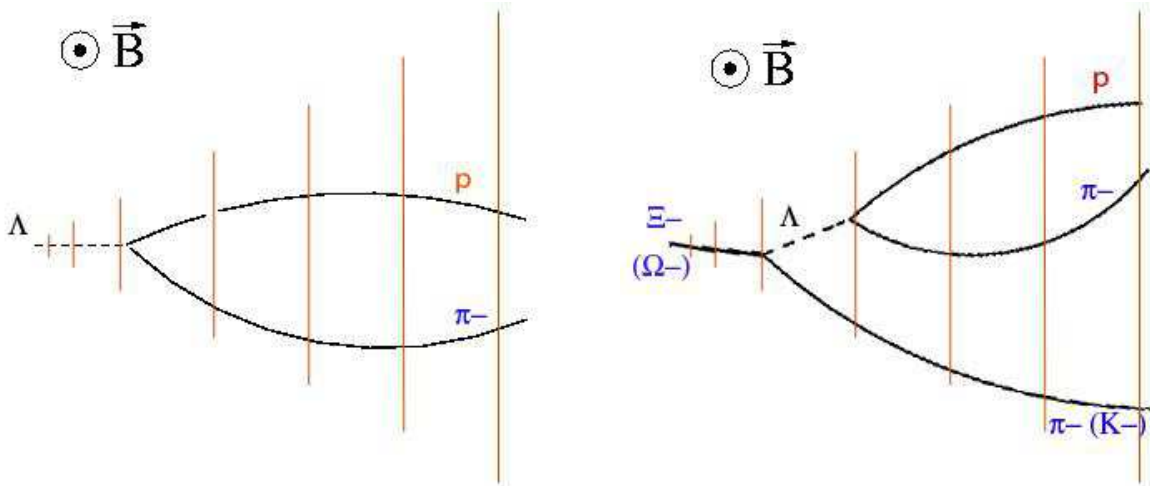


Figure 4.17: Decay topologies for lambda hyperons (left) and for $\Xi^-$ and $\Omega^-$ hyperons (right). Detector planes are indicated as lines, the magnetic field is perpendicular to the figure plane.
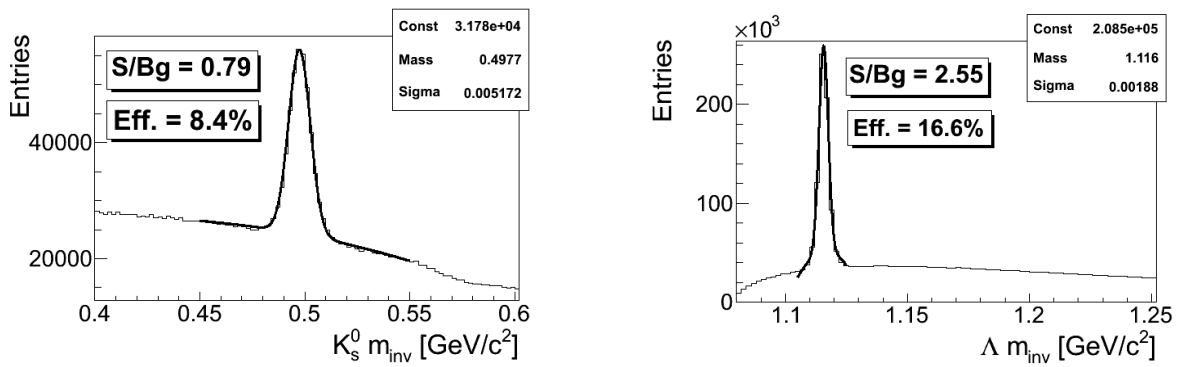


Figure 4.18: Reconstructed $K_s^0$ mesons (left) and $\Lambda$ hyperons (right) from the UrQMD central Au+Au collisions at 4 A·GeV for the V1 STS configuration.
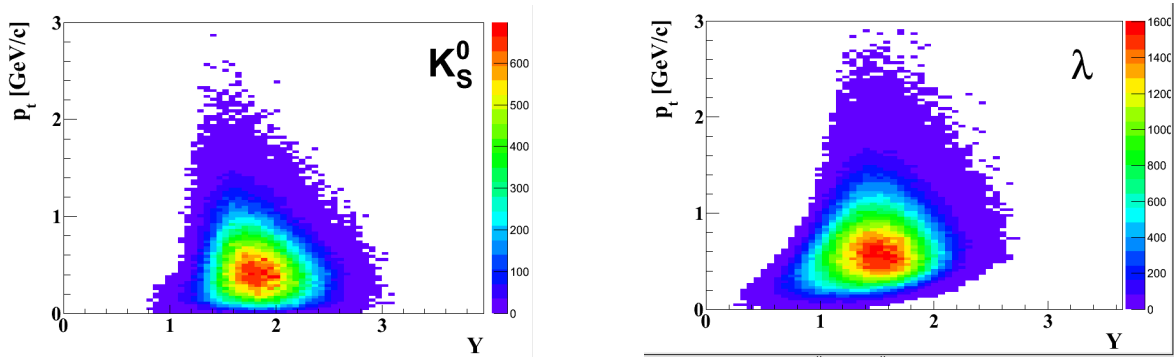
Figure 4.19: The $y$—$p_T$ acceptances for $K_s^0$ mesons (left) and $\Lambda$ hyperons (right) from the central Au+Au collisions at 4 A·GeV for the V1 STS configuration.
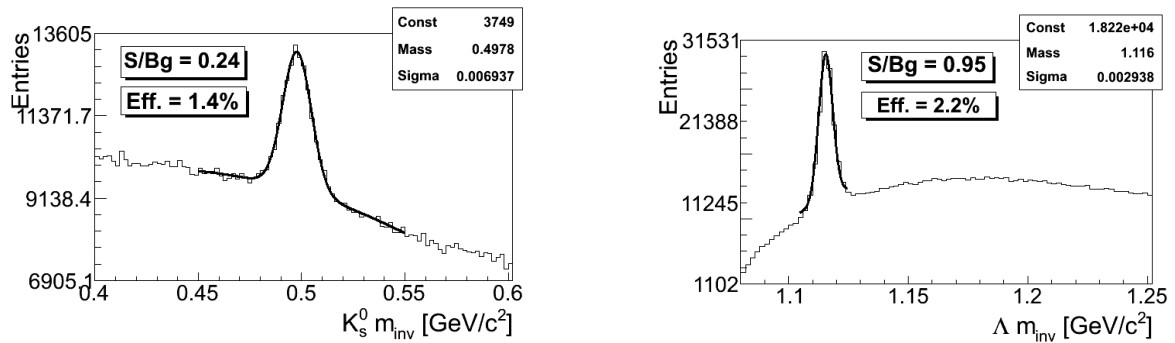


Figure 4.20: Reconstructed $K_s^0$ mesons (left) and $\Lambda$ hyperons (right) from the UrQMD central Au+Au collisions at 4 A·GeV for the V2 STS configuration (first 4 stations).
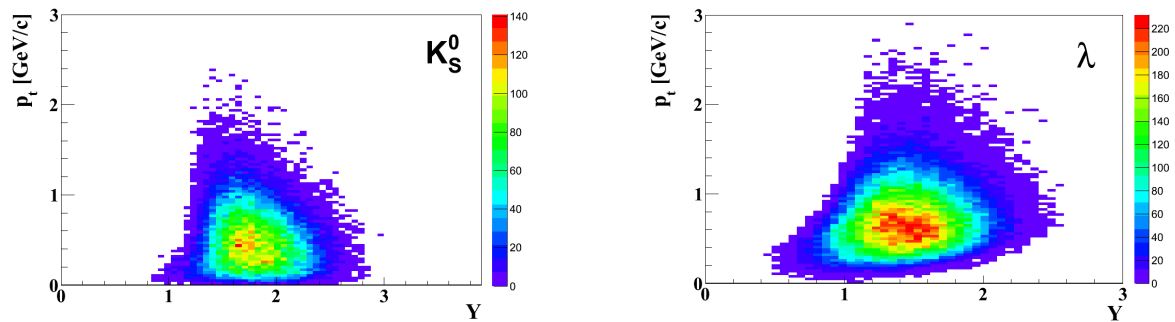


Figure 4.21: The $y$—$p_T$ acceptances for $K_s^0$ mesons (left) and $\Lambda$ hyperons (right) from the central Au+Au collisions at 4 A·GeV for the V2 STS configuration (first 4 stations).
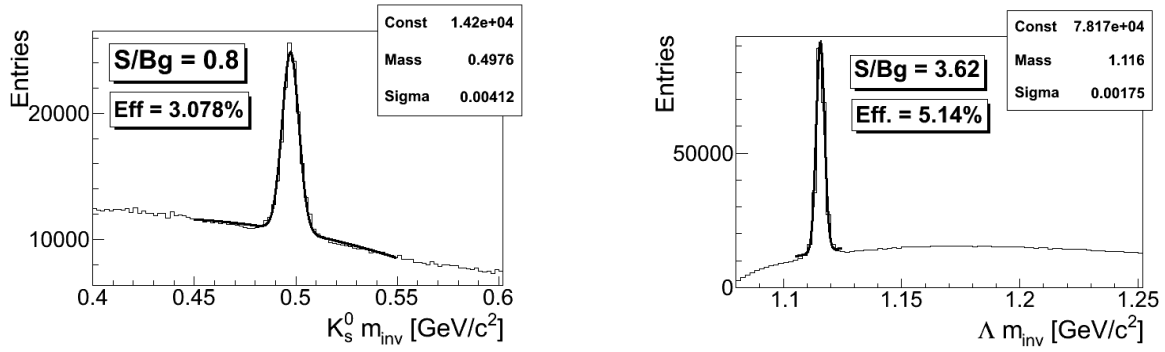
Figure 4.22: *Reconstructed $K_s^0$ mesons (left) and $\Lambda$ hyperons (right) from the UrQMD central Au+Au collisions at 4 A·GeV for the V3 STS configuration (6 stations).*
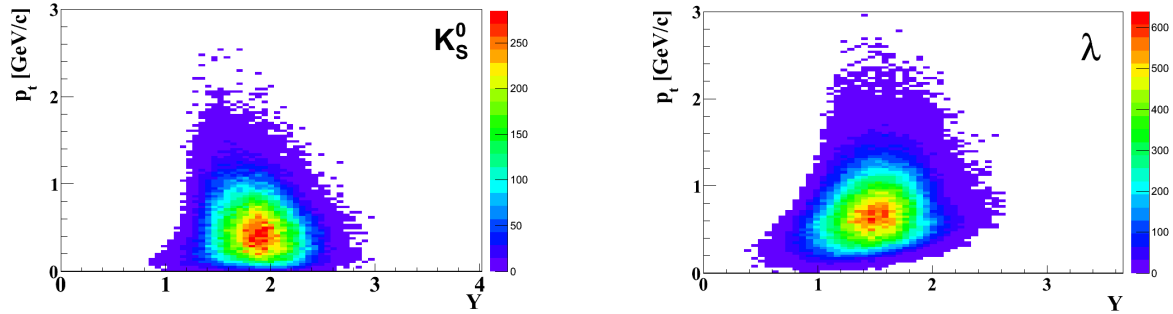


Figure 4.23: *The $y-p_T$ acceptances for $K_s^0$ mesons (left) and $\Lambda$ hyperons (right) from the central Au+Au collisions at 4 A·GeV for the V3 STS configuration (6 stations).*
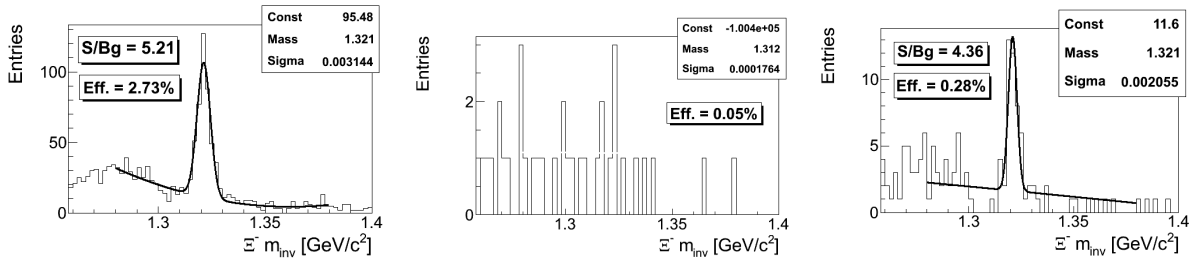


Figure 4.24: *From left to right: the selection efficiency of $\Xi^-$ hyperons from the central Au+Au collisions at 4.0 A·GeV for V1, V2, and V3 STS configurations.*
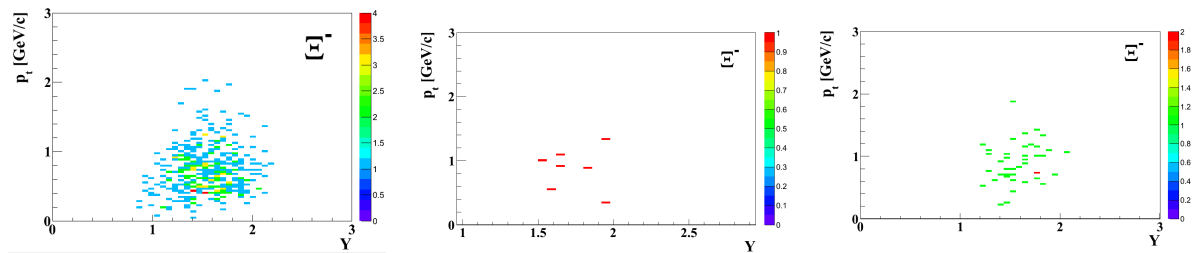


Figure 4.25: *From left to right: the $y-p_T$ acceptances for $\Xi^-$ hyperons from the central Au+Au collisions at 4.0 A·GeV for V1, V2, and V3 STS configurations.*

## 4.7   $^3_\Lambda$H reconstruction
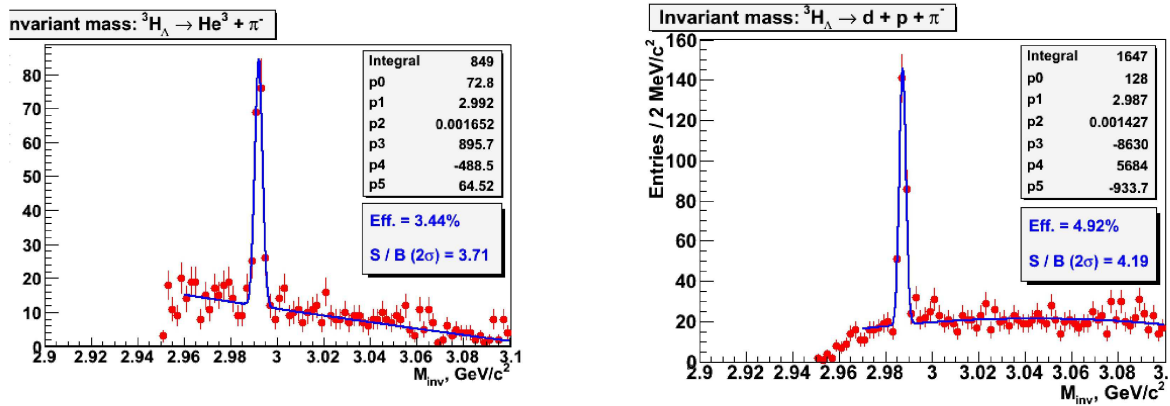


Figure 4.26: *Reconstruction of the hyper-tritons $\left(^3_\Lambda H\right)$ from the DCM [137–139] generated central Au+Au collisions at 4 A·GeV for 2- (left) and 3-body (right) decay channels.*

The simulation results for selection of $^3_\Lambda$H produced in the central Au+Au collisions at 4 A·GeV from the DCM event generator [137–139] are shown in Fig. 4.26. One can see good identification for two- and three-body decay channels depicted in the left and right panels, respectively.

## 4.8   Many-core platform for simulation
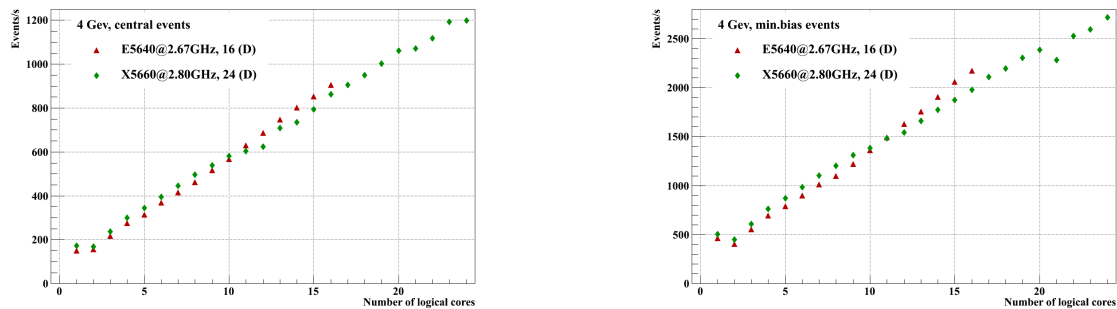


Figure 4.27: *The number of central (left) and minimum bias (right) Au+Au events at 4 A·GeV reconstructed in STS per second versus the number of logical cores for two different configurations of many-core processors.*

Currently the average reconstruction time for the central Au+Au collisions on a single core CPU is quite large. Event level parallelization and computing on many-core platforms yield much higher throughput. The dependence of the central and minimum bias Au+Au events at 4 A·GeV reconstructed in STS per second versus the number of logical cores for two different configurations of many-core processors is demonstrated in Fig. 4.27. The maximal speed is provided by the Intel X5660 at 2.80 GHz with 24 logical cores, e.g. about 2700 minimum bias or 1200 central events per second.

The simulation has been performed using the LIT JINR computing servers.

## 4.9   Counting rate

The expected hyperon yields from the central and minimum bias Au+Au collisions at 4 A·GeV are listed in Table 4.6 . The multiplicities for the central collisions are calculated with the statistical model [136], and were divided by a factor of 4 for the minimum bias collisions. The yields are calculated assuming a typical reaction rate of $10^5$ Hz corresponding to the beam intensity of $10^7$ Hz and the target of 1 % interaction length. This would require a trigger on $\Lambda$ from the secondary vertex. For primary $\Lambda$ a reaction rate of $10^4$ Hz was assumed. The yields of hypernuclei from $10^5$ Hz central Au+Au collisions at 4 A·GeV as calculated with the statistical model [136] are given in Table 4.7. According to the calculations the measurement of $_{\Lambda\Lambda}^5$H seems promising.

Table 4.6: *Expected hyperon yields from the central and minimum bias Au+Au collisions at 4 A·GeV for the reaction rate of 0.1 MHz.*

| Particle | $E_{\mathrm{thr}NN}$, GeV | Multiplicity central | Multiplicity min.bias | $\epsilon$, % | Yield/s min.bias | Yield/week min.bias |
|---|---|---|---|---|---|---|
| $\Xi^-$ | 3.7 | $1\cdot10^{-1}$ | $2.5\cdot10^{-2}$ | 3 | 75 | $4.5\cdot10^7$ |
| $\Omega^-$ | 6.9 | $2\cdot10^{-3}$ | $5.0\cdot10^{-4}$ | 3 | 1.5 | $9.0\cdot10^5$ |
| $\bar{\Lambda}$ | 7.1 | $2\cdot10^{-4}$ | $5.0\cdot10^{-5}$ | 15 | 0.75 | $4.5\cdot10^5$ |
| $\Xi^+$ | 9.0 | $6\cdot10^{-5}$ | $1.5\cdot10^{-5}$ | 3 | $4.5\cdot10^{-2}$ | $2.7\cdot10^4$ |
| $\Omega^+$ | 12.7 | $1\cdot10^{-5}$ | $2.5\cdot10^{-6}$ | 3 | $7.5\cdot10^{-3}$ | $4.5\cdot10^3$ |

Table 4.7: *Expected yields of hypernuclei from the central Au+Au collisions at 4 A·GeV for the reaction rate of 0.1 MHz.*

| Hyper-nuclei | Multiplicity central | $\epsilon$, % | Yield/s central | Yield/week central |
|---|---|---|---|---|
| $_{\Lambda}^3$H | $2\cdot10^{-2}$ | 8 | 160 | $1.0\cdot10^8$ |
| $_{\Lambda\Lambda}^5$H | $1\cdot10^{-6}$ | 1 | $1\cdot10^{-3}$ | $6\cdot10^2$ |
| $_{\Lambda\Lambda}^6$He | $3\cdot10^{-8}$ | 1 | $3\cdot10^{-5}$ | 18 |

The estimations are made for $V1$ configuration of STS (see Table 4.3) and permanent beam as at FAIR. Taking into account the beam duty factor of 0.5 one can expect two times less statistics as indicated in Tables 4.6 and 4.7.

The Nuclotron (JINR, Dubna) will provide the proton beams with energies up to 12 GeV and heavy-ion beams up to 4.65 A·GeV for gold nuclei and 6 A·GeV for isospin-symmetric nuclei. For the commissioning phase of experiment we need the beams of protons, deuterons, carbon, and gold. The proposed experiment can be started using extracted Au beam with intensity of $10^7$ ions per second.

# Chapter 5

# BM@N setup
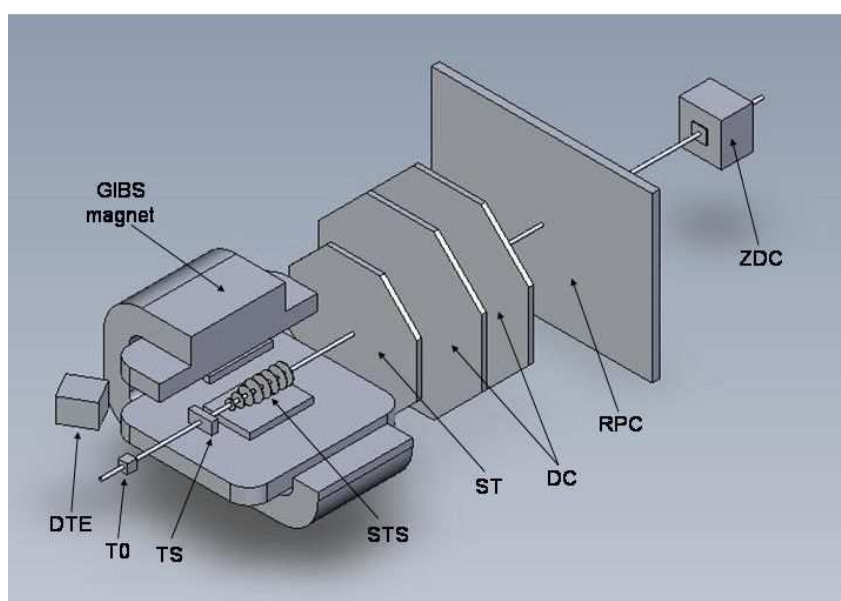


Figure 5.1: Schematic view of the setup with SP41 dipole magnet. TS — target station, T0 — start diamond detector (see section 5.4), STS — silicon tracker (5.2), ST — straw tracker (5.6), DC — drift chambers (5.5), RPC — resistive plate chambers (5.3), ZDC — zero degree calorimeter (5.8), DTE — detector of transverse energy (5.10).

Table 5.1: The BM@N setup configurations for the start version (2014), stage 1 (2015), and stage 2 (2017).

|  | Magnet | Target station | RPC & T0 | ZDC | DC | ST | SciFH | FW | SA STS | WA STS |
|---|---|---|---|---|---|---|---|---|---|---|
| Start version (2014) | + | + | + | + | + | − | + | − | − | − |
| Stage 1 (2015) | + | + | + | + | + | + | + | + | + | − |
| Stage 2 (2017) | + | + | + | + | − | + | − | + | + | + |

The heart of the setup is Silicon Tracker System (STS) [151] placed in the gap of large dipole magnet SP41. The experimental setup will be complemented by a TOF system for
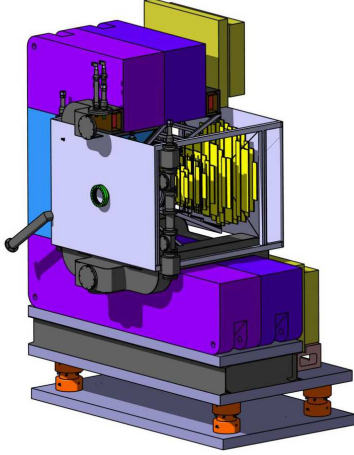
Figure 5.2: Silicon Tracking System comprising eight stations in its thermal enclosure.
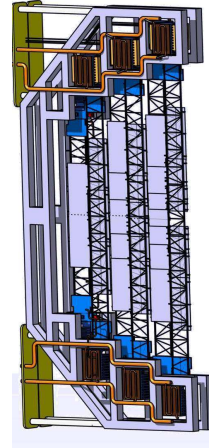


Figure 5.3: Half of a station consisting of light-weight carbon-fibre ladders carrying the sensors, the micro-cables, and the front-end electronics with its cooling.
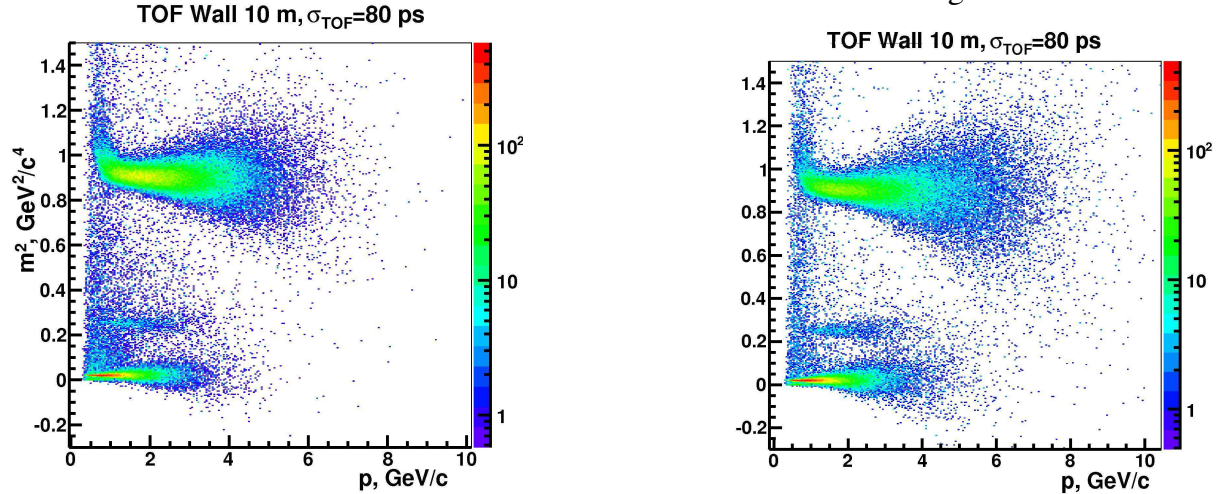


Figure 5.4: The PID $m^2$—$p$ plots using momentum and TOF measurements for the central collisions of Au+Au at 3.5 A·GeV (left) and Cu+Cu at 5.0 A·GeV (right).

particle identification based on Multigap Resistive Plate Chambers (RPC) wall [152, 153] and T0 start detector [154, 155]. Straw tubes (ST) and drift chambers (DC) [185] will be used for intermediate tracking. Centrality measurements will be performed using ZDC (Zero Degree Calorimeter) and DTE (Detector for Transverse Energy). As one of possible ZDC options the PSD (Projectile Spectator Detector) [156] can be used. Electromagnetic calorimeters can be added optionally to measure photons. The schematic layout of the setup is shown in Fig. 5.1.

The simulation presented in the chapter 4 demonstrates that the STS for BM@N detector should comprise eight stations similar to the STS of CBM [151]. The first four stations will be similar to the four stations of CBM, while the last four stations will have the same size as the station 4 to fit into gap of the dipole magnet. Since STS must be operated at −10°C, it sits in a thermal enclosure, which fits into the SP41 magnet gap as illustrated in Fig. 5.2. The double-sided silicon micro-strip sensors will be read out via ultra-thin micro-cables by a free-streaming (i.e. selt-triggered) front-end electronics. The sensors, the cables, and the electronics are mounted on light-weight carbon ladders, which form the stations. Half of
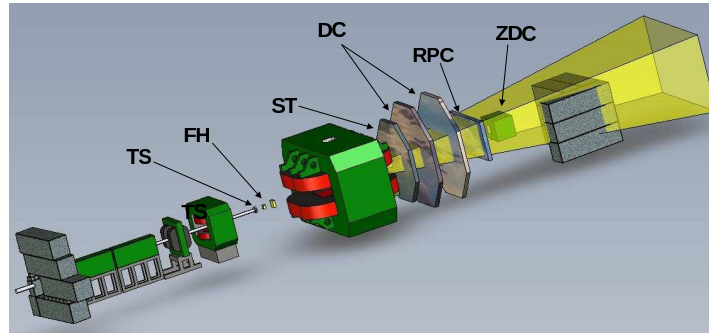
*Figure 5.5: The stage 1 of the BM@N setup: TS — target station, FH — forward tracking hodoscopes (see section 5.7), ST — straw tube tracker, DC — drift chambers, RPC — resistive plate chambers, ZDC — zero degree calorimeter.*
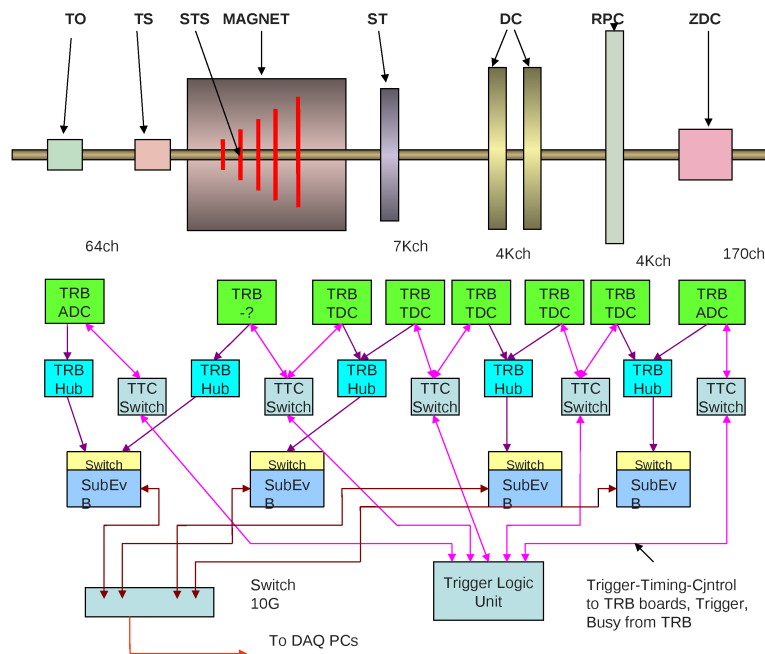


*Figure 5.6: Schematic view of the setup with the possible DAQ layout.*

such a station is depicted in Fig. 5.3.

The particle identification (PID) will be performed using time-of-flight (TOF) measurements. The PID $m^2$—$p$ plots using momentum reconstructed by STS and TOF measurements for the central collisions of Au+Au at 3.5 A·GeV and Cu+Cu at 5.0 A·GeV are presented in the left and right panels in Fig. 5.4. One can see the good PID for the registered hadrons.

The first stage of the experiment (starting from 2015) will be based on the forward and outer trackers only. Straw tubes (ST) and drift chambers (DC) will be used for the tracking after the analyzing magnet SP41. The scintillation fiber hodoscopes (SciFH, see section 5.7) and/or Small Aperture (SA, 5.11) STS will be used for the tracking before the magnet. Particle identification will be based on the RPC wall. This configuration is shown schematically in Fig. 5.5. The possible scheme of the DAQ system is presented in Fig. 5.6.

The BM@N setup configurations for the start version (2014), stage 1 (2015), and stage 2 (2017) are presented in Table 5.1. The start version of the setup will include the modified magnet SP41, target station (TS), part of RPC wall for particle identification using TOF, scintillation fiber hodoscopes (SciFH) and drift chambers (DC) for the tracking before and after magnet, and zero degree calorimeter (ZDC) for the centrality determination. In 2015

the SA STS and Forward Wall (FW, see section 5.9) will be put into operation to improve the reaction plane determination as well as the straw tracker (ST). The stage 2 requires the wide aperture (WA) STS (5.2). Optionally the electromagnetic calorimeters (BGO, lead glass, "shashlyk", 5.10) can be used on the different stages of the BM@N setup.

## 5.1   Analyzing dipole magnet SP41
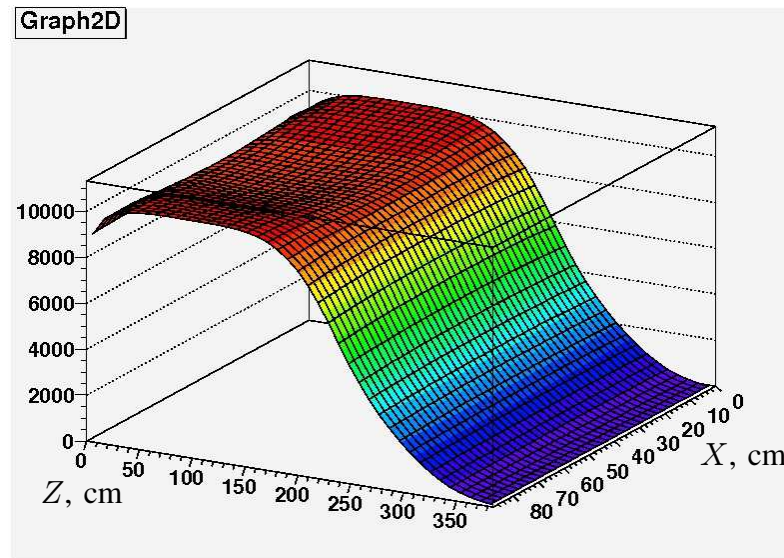


Figure 5.7: *The vertical component $B_y$ (Gs) of the magnetic field in the center of the existing magnet SP41.*
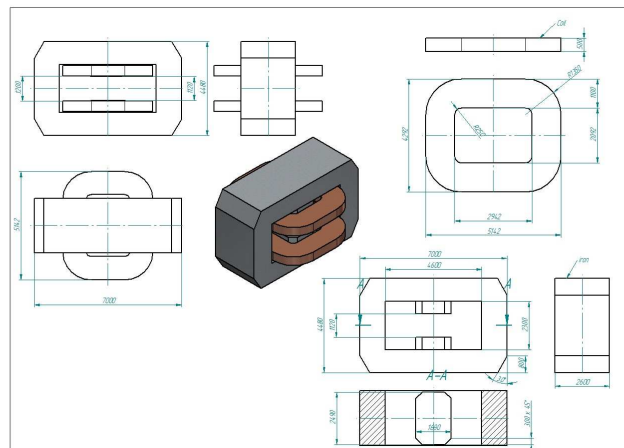


Figure 5.8: *The drawing of the modified dipole magnet SP41.*

The existing SP41 dipole magnet will be used as an analyzing magnet. The length of the pole along the beam is 2.2 m, width in the horizontal direction is 1.2 m, and the height is about 0.75 m. The $2D$ dependence of the magnetic field vertical component $B_y$ of the existing magnet SP41 in $XZ$ plane is shown in Fig.5.7. This magnet has a hole for the photo camera in the upper pole since it was used for the experiments with streamer chamber. As the result the magnetic fields components demonstrate the non-uniform behaviour. SP41 magnet will be modified for the real experiment, namely, the distance between the poles
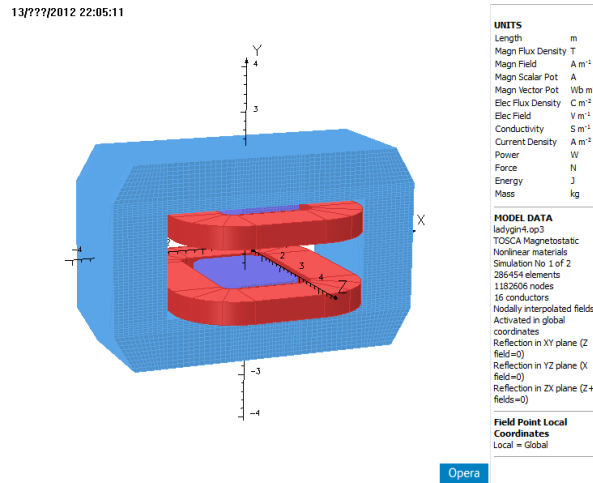
Figure 5.9: SP41 model for the magnetic field TOSCA calculations.
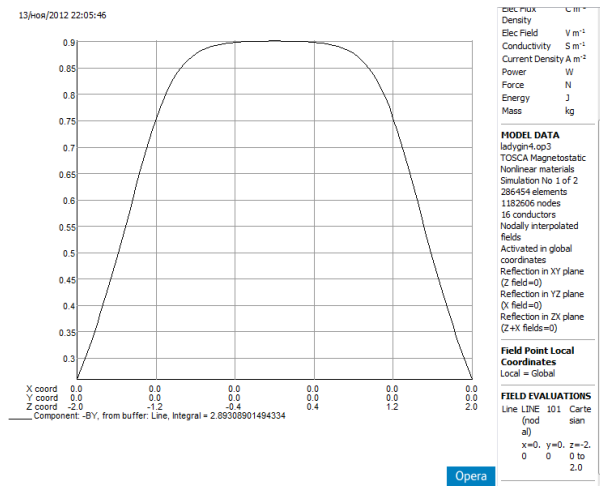


Figure 5.10: The TOSCA calculation results for the magnetic field vertical component $B_y$ in the center of the modified magnet SP41 along the beam direction.

will be enlarged up to 1.05 m and the hole in the upper pole will be filled by the steel-15. The drawing of the modified dipole magnet SP41 and its model for magnetic field TOSCA calculations are presented in Figs. 5.8 and 5.9, respectively.

The TOSCA calculation results for the magnetic field vertical component $B_y$ in the center of the modified magnet SP41 along the beam direction are demonstrated in Fig. 5.10. The field integral is approximately 30 % less than for the existing SP41 magnet.

The $2D$ distributions in $XZ$ plane of the magnetic field vertical component $B_y$ of modified SP41 magnet at $Y = 0$ cm (center of the magnet), $Y = 30$ cm, and $Y = 50$ cm are presented in the left, middle, and right panels in Fig. 5.11. The field demonstrates very smooth behaviour except the region around pole of the magnet ($Y = 50$ cm). The $3D$ results for $B_y$, $B_x$, and $B_z$ components of the magnetic field will be incorporated into the next version of the BM@N setup description for the simulation software.

The works on the modification of the SP41 dipole magnet are started in October 2012. The pictures of the steel plates cutting (October) and dismounting of the SP41 in the 205 experimental hall (December) are presented in Figs. 5.12 and 5.13, respectively.

The measurements of the magnetic field components will be performed using $3D$ Hall probes with the accuracy not worse than 0.05 %. The sketch of the $3D$ Hall probe is
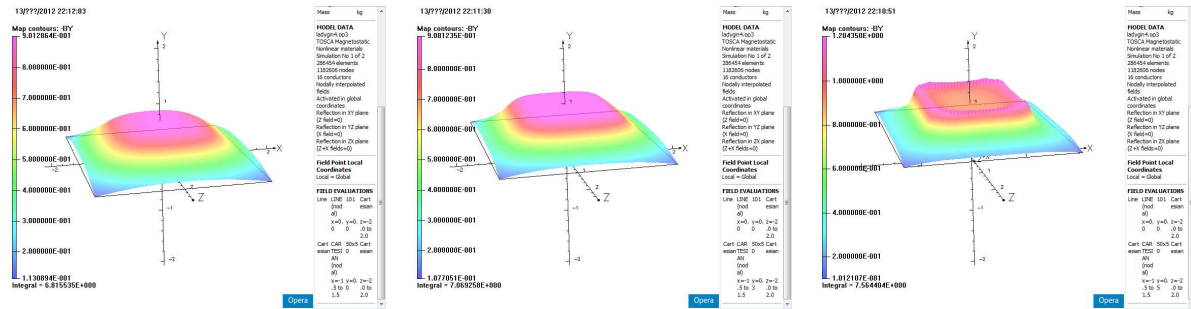
*Figure 5.11: From left to right: $2D$ distributions in $XZ$ plane of the magnetic field vertical component $B_y$ of modified SP41 magnet at $Y = 0$ cm (center of the magnet), $Y = 30$ cm, and $Y = 50$ cm.*



*Figure 5.12: The pictures of the steel plates cutting of the SP41 magnet.*

presented in the left panel in Fig. 5.14. The $3D$ Hall probe includes three orthogonally aligned square-shaped Hall sensors with overall dimensions of $1.1 \times 1.1 \times 0.52$ mm$^3$ and the sensitive element dimensions of $0.2 \times 0.2 \times 0.002$ mm$^3$. Cube made of K8 glass is used as basis for mounting the sensors along the three orthogonal axes $X$, $Y$, $Z$. Cube's dimensions are $(4.0 \pm 0.2) \times (4.0 \pm 0.2) \times (4.0 \pm 0.2)$ mm$^3$. Cube's facets are oriented strictly at $90°$ with the accuracy of $\pm 10'$. Orthogonally aligned sensors comprise the cube's active area with dimensions of $(1.8 \pm 0.2) \times (1.8 \pm 0.2) \times (1.8 \pm 0.2)$ mm$^3$. The base for placing the cube is made of D16T alloy and is shaped as a box with dimensions of $(19.6 \pm 0.2) \times (19.6 \pm 0.2) \times (2.8 \pm 0.1)$ mm$^3$, the tolerance for angles and flatness in the course of production does not exceed $10'$. Probe's master slice with dimensions of $(40.0 \pm 0.1) \times (19.7 \pm 0.1) \times (2.8 \pm 0.1)$ mm$^3$ is made of D16T alloy with the same tolerance of production. Circuit board made of fiber-glass laminate with the copper tracks applied on it for welding the leads. The general view of the probe assembly, namely, the cube with



*Figure 5.13: The picture of the SP41 magnet dismounting in the 205 experimental hall.*
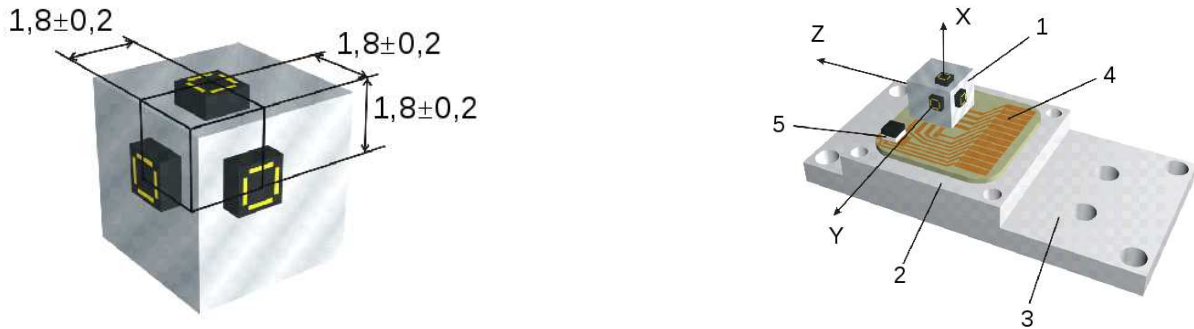
Figure 5.14: 3D Hall probe with the active area $(1.8 \pm 0.2) \times (1.8 \pm 0.2) \times (1.8 \pm 0.2)$ mm$^3$ (left). General view of the assembly (right), where: 1 — cube with sensors; 2 — cube's base; 3 — master slice; 4 — circuit board; 5 — temperature sensor.
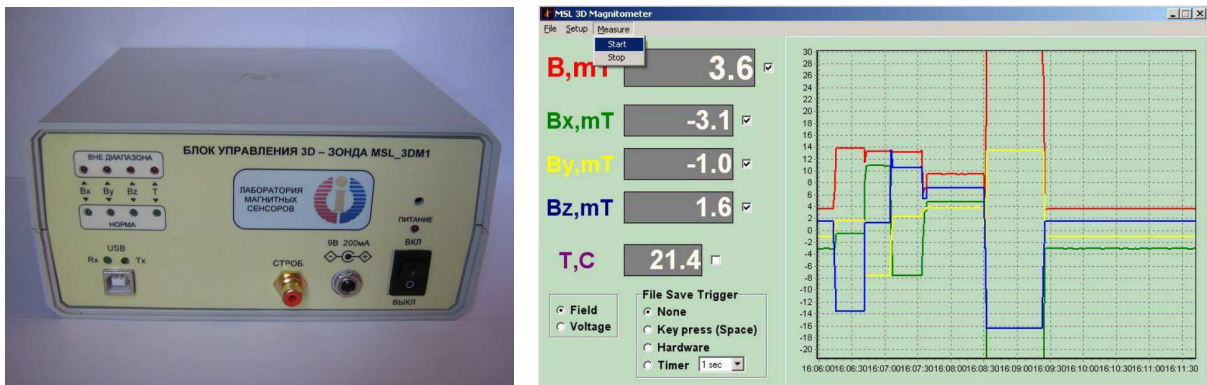


Figure 5.15: Control unit for 3D Hall probe (left) and the software screenshot (right).

sensors, cube's base, master slice, circuit board, and temperature sensor, is presented in the right panel in Fig. 5.14.

The picture of the control unit for 3D Hall probe is shown in the left panel in Fig. 5.15. Main functions of the control unit are to provide:
† the accuracy of the electronic unit's measuring channels of $\sim 0.05$ %;
† the stable current to sensors and thermo-resistor;
† the commutation and amplification of the incoming signals;
† the noise-immune measurements of the weak signals;
† the temperature measurement and the temperature drift compensation;
† the multichannel analog-to-digital conversion of sensors' signals;
† the sensor signal conversion functions;
† the magnetometer — PC connection.

The 3D Magnetometer Software, whose screenshot we can see in the right panel in Fig. 5.15, allows one:
† to set parameters of the data exchange protocol;
† to launch and stop the measurement process;
† to save the data measured.
It also provides the possibility for recording the current value of the magnetic induction with the possibility of program changes. The picture in the right panel in Fig. 5.15 demonstrates the time dependence of the three magnetic field components measured using the 3D Hall probe and represented by the software current version.

## 5.2   STS inner tracking detector

### 5.2.1   The Silicon Tracking System

As the core detector of the BM@N experiment, the Wide Aperture Silicon Tracking System (WA STS) located in the dipole magnet SP41 provides track reconstruction and momentum determination of charged particles from beam-target interactions. The detector system shall work with ion beam energies up to 4.65 A·GeV and 6.0 A·GeV for Au and charge-symmetric nuclei, respectively. The detection of rare probes requires the STS to be capable of interaction rates of up to 0.1 MHz for Au+Au collisions (two orders of magnitude less than for CBM [151]). The typical track multiplicity reaches up to 300 per central Au+Au collision in the aperture of $2.5° < \Theta < 20°$.

The simulations presented in sections 4.2 and 4.3 show that the optimal WA STS has eight stations (similar to STS CBM [151]) extended about 1 m along the beam. WA STS will be built in a thermal enclosure for cooling the silicon sensors in the radiation field. Similar silicon trackers were built for LHC experiments, with the TT tracker of the LHCb experiment being particularly related to the planned CBM and BM@N silicon tracking system due to its forward spectrometer geometry [157].

### 5.2.2   Design constraints

The design of the WA STS for BM@N experiment is based on the concept of the CBM STS [151] due to similarity of the CBM and BM@N experiments. In spite we expect significantly lower counting rate for stage 2 of the BM@N experiment due to lower intensity of the Au beam at Nuclotron than at FAIR, we follow to the design of CBM STS. However, the use of the maximal intensity of the LINAC-booster-Nuclotron chain will provide the interaction rate in the Au+Au collisions up to 10 MHz (with 1 % target) similar to CBM working conditions.

The design of the Silicon Tracking System is based on the following constraints:

**Aperture**
The polar aperture 2.5°—20° defined by the aperture of the modified SP41 magnet is a bit less than polar angle aperture of CBM STS (2.5°—25°), but it allows one to cover the hemisphere in the laboratory frame, i.e. from center-of-mass rapidity close to beam rapidity.

**Spatial resolution**
Simulation studies for CBM [151] have demonstrated that a single-hit resolution of about 25 $\mu$m provides the required momentum resolution mainly determined by multiple scattering. A read-out strip pitch of 58 $\mu$m was chosen matching this requirement.

**Hit rates**
Charged particle rates of about 10 MHz/cm$^2$ are expected in the innermost regions of the STS in CBM experiment. They fall off by two orders of magnitude in the outer regions of the STS. Different read-out strip lengths were chosen for different regions of the STS to keep maximum strip occupancies at the level of a few percent. In the BM@N experiment (stage 2) we expect two orders of magnitude less counting rate.

**Signal shaping time**
In order to avoid pile-up of events, fast self-triggering front-end electronics with a shaping time of the order of 20 ns as in the case of CBM STS [151] will be used. At the stage 2 of the BM@N experiment (0.1 MHz interaction rate) a usual triggered front-end electronics

can be used.

**Single-hit efficiency, track reconstruction efficiency**

A detection layer should provide close to 100 % single-hit efficiency still keeping a low noise hit rate. Earlier studies have shown [157] that a signal-to-noise ratio (the most probable amplitude for a MIP divided by the RMS of the single strip noise distribution) has to be kept exceeding 10 even after signal deterioration due to the radiation damage. The track reconstruction algorithms utilizing the hits shall enable the trajectory finding with an efficiency exceeding 95 % for particle momenta larger than 1 GeV/c.

**Material budget, momentum resolution**

As by design the momentum resolution is dominated by multiple scattering, the material budget of the STS has to be kept as small as possible. The STS is designed such that front-end read-out electronics, cooling and mechanical infrastructure are located outside of the detector acceptance. The momentum resolution required for physics observables is $\Delta p/p \approx 1$ % for eight-station WA STS option.

**Number of read-out channels**

The largest read-out pitch compatible with the required spatial resolution and the longest read-out strips compatible with requirements on occupancy and signal-to-noise performance were chosen in order to minimize the number of read-out channels. Both the number of read-out channels and the material budget in the aperture can be decreased by deployment of double-sided silicon microstrip sensors of appropriate strip length.

**Radiation damage**

The investigations performed for the CBM running scenario of the experiment results in a 1 MeV neutron equivalent fluence in the innermost regions of the STS reaching less than $10^{13}$ per cm$^2$ at SIS100 and $10^{14}$ per cm$^2$ at SIS300. Their replacement is foreseen in case the integrated fluence exceeds those values. Thus standard silicon sensors can be used. The sensors need to be operated at bias voltages of up to 500 V, at a temperature of around $-5°$C to limit radiation damage induced by leakage currents. In the case of BM@N STS the value of $10^{13}$ per cm$^2$ of 1 MeV neutron equivalent fluence will not exceed.

## 5.2.3   Detector concept

The STS will consist of eight planar tracking stations covering the aperture between the polar angles $2.5° < \Theta \lesssim 20°$. Installed in the gap of the dipole magnet, they extend from 30 cm to 1 m downstream of the target.

The hit densities of charged particles at the first and last tracking stations are shown in the profile plots of Fig. 5.16 for minimum bias Au+Au collisions at 25 A·GeV. At a 30 cm distance from the target, the maximum does not exceed 2 hits per cm$^2$, at a 1 m distance — not more than 0.3 hits per cm$^2$. These values can be used as an upper limit for the BM@N experiment.

The material budget in the detector aperture can be minimized by the separation of the the sensing and read-out parts. With a suitable segmentation of the STS detector, the single-strip occupancies with multiple particle hits are small enough even in central Au+Au collisions [151]. This is further detailed in section 5.2.4.5. The combinatorial points arising from the projective topology of the strip detector are resolved by the track reconstruction algorithms as it is described in section 5.2.6.

The building blocks of the STS are illustrated in Fig. 5.17. Three different sizes of microstrip **sensors** are deployed. The basic functional unit is a **module** comprising either an
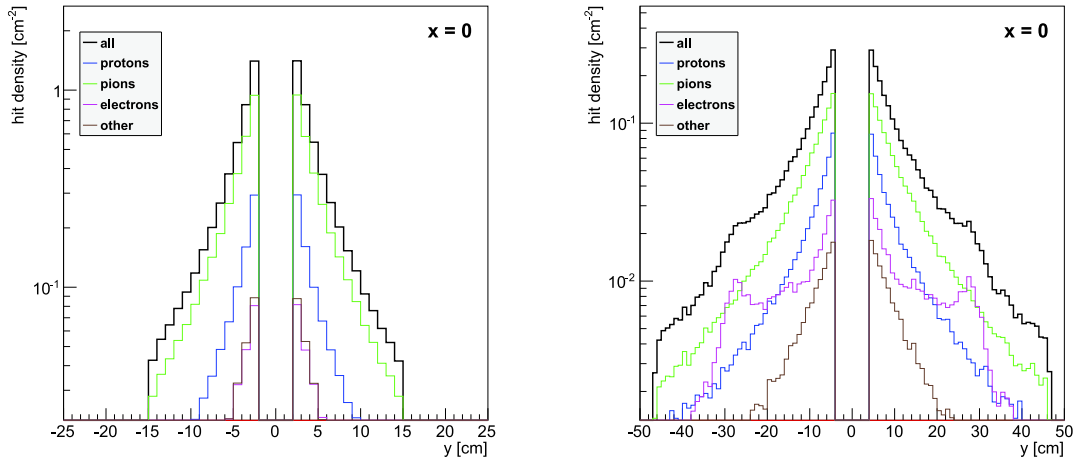
Figure 5.16: *Hit densities of charged particles from minimum-bias 25 A·GeV Au+Au collisions. The profiles along the Y axis (X = 0) in station 1 (left) and 8 (right) are shown.*
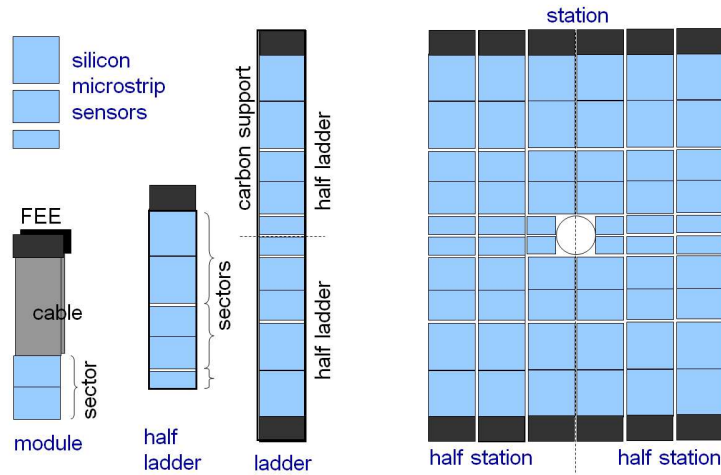


Figure 5.17: *Conceptional layout of the tracking stations and their building blocks.*

individual double-sided silicon microstrip sensor or a daisy-chained set of sensors, multi-line flat read-out cables attached to one edge of either side of the sensors, and two front-end electronics boards, thus forming a **sector** in terms of the read-out. The vertical extent of a sector equals the effective strip length. Modules of different type will be built, differing in their sensor size, number of sensors used, and lengths of the read-out cables. The front-end electronics is the same for all modules. The modules will be arranged on carbon fiber support structures, forming **ladders**, allowing them to be mechanically and electrically integrated into tracking **stations**. A ladder will be populated to form two half-ladders, with the read-out directions oriented towards the top and bottom part of the STS. The ladders will be mounted onto a frame to form a half tracking station, realized from a staggered downstream and upstream part. A station will be built from two half-stations. A small number of different ladder types are considered to be sufficient to build up the STS. Some ladders will require a layout adapted to the hole around the beam pipe.

## 5.2.4 Detector layout

The layout of the CBM STS (which is the base for BM@N WA STS) has been subject of extensive simulation studies during the last years, utilizing the FairRoot [158] framework,

Table 5.2: *Material budget in different positions (read-out sectors) along a STS ladder.*

| sector | 1 | 2 | 3 | 4 | 5 |
|---|---|---|---|---|---|
| per sector, % $X_0$ | 0.3 | 0.3 | 0.3 | 0.3 | 0.3 |
| per cable pair, % $X_0$ | 0 | $2\times0.11$ | $4\times0.11$ | $6\times0.11$ | $8\times0.11$ |
| sector+cables, % $X_0$ | 0.3 | 0.52 | 0.74 | 0.96 | 1.18 |
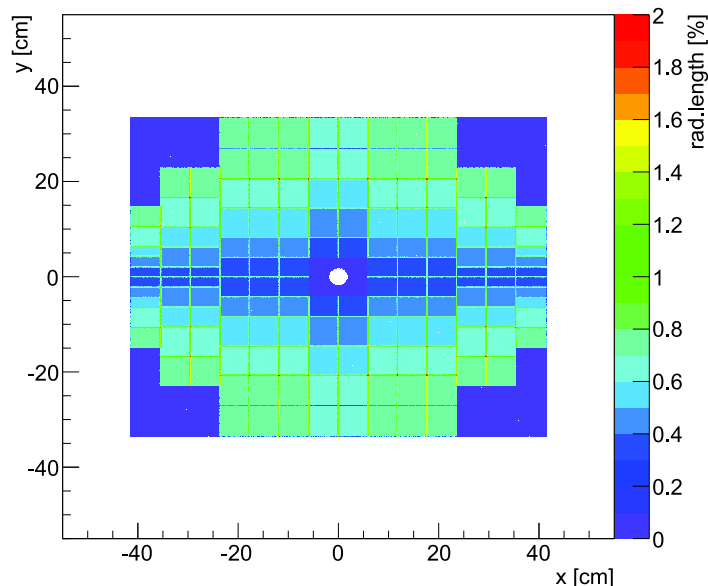


Figure 5.18: *Distribution of material budget in tracking station 4.*

based on ROOT package and the Virtual Monte-Carlo (VMC) interface. For the purposes of the presented studies the Au+Au collisions at 25 A·GeV energy were generated using the UrQMD event generator. The generated final-state particles are followed through the STS detector by the software based on GEANT3 [159]. Particle interaction and energy loss in the material of the detector are simulated and hit positions in the sensitive elements are recorded. A detailed simulation of the detector response (digitizer) and a hit clustering algorithm are implemented in the STS software. The optimization of the STS performance has motivated several choices concerning the detector geometry, such as sensor pitch, number of tracking stations, and their placement within the magnet volume. Conversely, the increasing knowledge of the hardware involved in the detector has been included into the simulations and relevant parameters such as the hit and track reconstruction efficiencies and track parameters are monitored.

The detector system consists of eight tracking stations located at 30, 40, 50, 60, 70, 80, 90, and 100 cm downstream of the target. The stations have a modular structure and are constructed from 300 $\mu$m thick double-sided microstrip sensors. The numbers, positions, and the segmentation of the layers are optimized for efficient track reconstruction and high momentum resolution. For mass production, the number of different sensors and ladder types is minimized.

### 5.2.4.1 Material budget

The geometry description of the STS includes a detailed description of the sensors and the passive materials. The silicon detector is designed minimizing the total amount of material. Silicon sensors 300 $\mu$m in thickness were chosen to give an acceptable balance of signal-to-
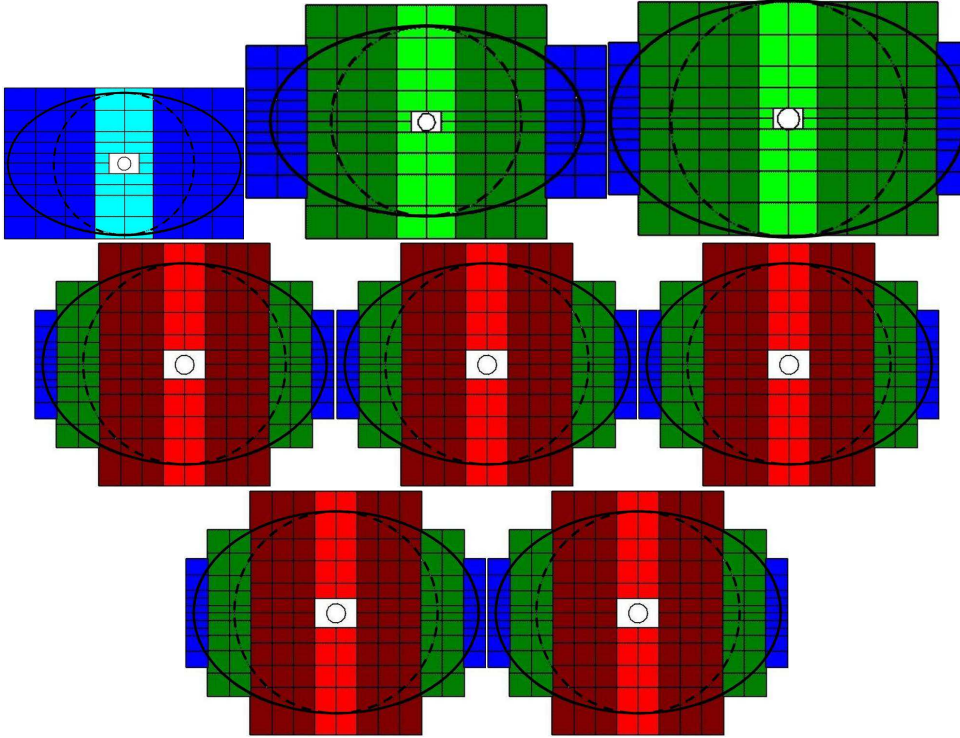
*Figure 5.19: Layout of the STS stations for $V1$ configuration for the BM@N. The most upstream station is shown in the upper left corner, the most downstream station — in the bottom right one. The same color codes denote the same ladder types.*

noise ratio and material budget.

The simulated amount of material for the STS corresponds to 0.3 % of $X_0$ for silicon sensors; an effective thickness is added by the cables where the simulated amount of material equals 120 $\mu$m silicon equivalent giving 0.11 % of $X_0$ per cable layer. A maximum value of approximately 1 %$X_0$ is reached in the outer parts of every station where eight layers of cables overlap. The values of material thickness in one STS ladder are summarized in Table 5.2. The distribution of radiation lengths is exemplarily shown for station 4 in Fig. 5.18.

### 5.2.4.2 Aperture

The STS stations are built from vertically mounted ladders with a fixed horizontal width. The vertical size of the sensors varies to minimize sensor occupancy as well as to reduce

*Table 5.3: Dimensions and acceptance radii of the tracking stations of $V1$ configuration of BM@N WA STS. Several stations are horizontally enlarged. See also Fig. 5.19.*

| station | 1 | 2 | 3 | 4 | 5 | 6 | 7 | 8 |
|---|---|---|---|---|---|---|---|---|
| $Z$ position, cm | 30 | 40 | 50 | 60 | 70 | 80 | 90 | 100 |
| $r_{\text{inn}}$, cm | 1.31 | 1.75 | 2.18 | 2.62 | 3.06 | 3.49 | 3.93 | 4.34 |
| acceptance $\Theta_{\text{inn}}^{\text{hor.,vert.}}$ | 2.5° | 2.5° | 2.5° | 2.5° | 2.5° | 2.5° | 2.5° | 2.5° |
| vertical $r_{\text{out}}$, cm | 13.99 | 18.65 | 23.32 | 27.98 | 27.98 | 27.98 | 27.98 | 27.98 |
| acceptance $\Theta_{\text{out}}^{\text{vert.}}$ | 25° | 25° | 24° | 21° | 18° | 16° | 25° | 25° |
| horizontal increase | 65% | 65% | 50% | 40% | 0% | 0% | 0% | 0% |
| horizontal $r_{\text{out}}$, cm | 23.08 | 30.77 | 34.98 | 39.17 | 39.17 | 39.17 | 39.17 | 39.17 |
| acceptance $\Theta_{\text{out}}^{\text{hor.}}$ | 38° | 37° | 35° | 33° | 29° | 26° | 24° | 22° |

Table 5.4: Sensor and sector geometries in the STS stations.

| sector type | $S1$ | $S1_S$ | $S2$ | $S3$ | $S3_{C2}$ | $S3_{C3}$ |
|---|---|---|---|---|---|---|
| number of daisy-chained sensors | 1 | 1 | 1 | 1 | 2 | 3 |
| width, cm | 6.2 | 3.1 | 6.2 | 6.2 | 6.2 | 6.2 |
| height, cm | 2.2 | 2.2 | 4.2 | 6.2 | 12.4 | 18.6 |
| strip length, cm | 2 | 2 | 4 | 6 | 12 | 18 |
| number of strips | 1024 | 512 | 1024 | 1024 | 1024 | 1024 |
| strip pitch, $\mu$m | 58 | 58 | 58 | 58 | 58 | 58 |

Table 5.5: Breakdown of the ladder types comprising sensors as defined in Table 5.4.

| ladder type | sectors per ladder | sensors per ladder | sensor types in the ladder | number of ladders | length of ladder, cm |
|---|---|---|---|---|---|
| L1 | 10 | 10 | 2x $S1$ $S1$ $S1$ $S2$ $S2$ | 16 | 14 |
| L2 | 10 | 10 | 2x $S1_S$ $S1$ $S1$ $S2$ $S2$ | 2 | 14 |
| L3 | 10 | 10 | 2x $S1$ $S2$ $S2$ $S3$ $S3$ | 28 | 22 |
| L4 | 10 | 10 | 2x $S1_S$ $S2$ $S2$ $S3$ $S3$ | 4 | 22 |
| L5 | 10 | 12 | 2x $S2$ $S2$ $S3$ $S3$ $S3_{C2}$ | 22 | 32 |
| L6 | 8 | 10 | 2x $S2$ $S3$ $S3$ $S3_{C2}$ | 4 | 32 |
| L7 | 10 | 16 | 2x $S2$ $S2$ $S2$ $S3_{C2}$ $S3_{C3}$ | 24 | 44 |
| L8 | 8 | 14 | 2x $S2$ $S3$ $S3_{C2}$ $S3_{C3}$ | 6 | 44 |

the number of cable layers. Vertical ladders consisting of several overlapping sensors are employed in order to cover the full height of the STS sensitive area. Several ladders are arranged side-by-side in order to cover the full acceptance of the STS.

The dimensions of the central hole are determined by the size of the beam pipe that passes through the detector. The beam pipe follows a conical shape, opening up along the beam axis. To approach the beam pipe as close as possible, a different size of the beam pipe hole for every station has been implemented. The dimensions of the central hole quoted in Table 5.3 were calculated with a 2.5° beam pipe opening angle.

The outer dimensions of the STS are determined by the requirement of 25° polar acceptance. Stations 1 to 5 cover a more extended area range in horizontal direction in order to provide efficient reconstruction of low-momentum electrons. The dimensions in Table 5.3 define the nominal size of the STS aperture. Since the detector will be assembled from standard sensors of fixed sizes, the actually covered sensitive area will deviate from these nominal values.
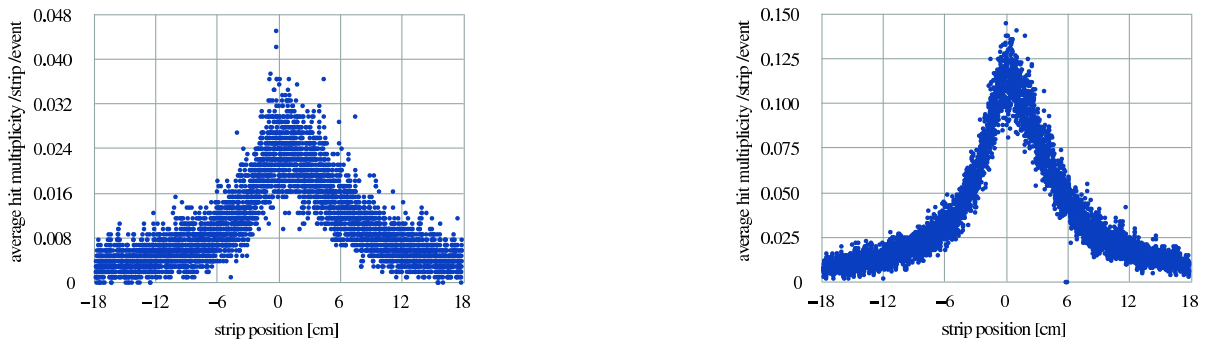


Figure 5.20: Strip occupancies, i.e. average number of particle hits per strip and event, as a function of the horizontal strip position for the sensors closest to the beam line in tracking station 1 for the central Au+Au collisions at 10 A·GeV (left) and 25 A·GeV (right).
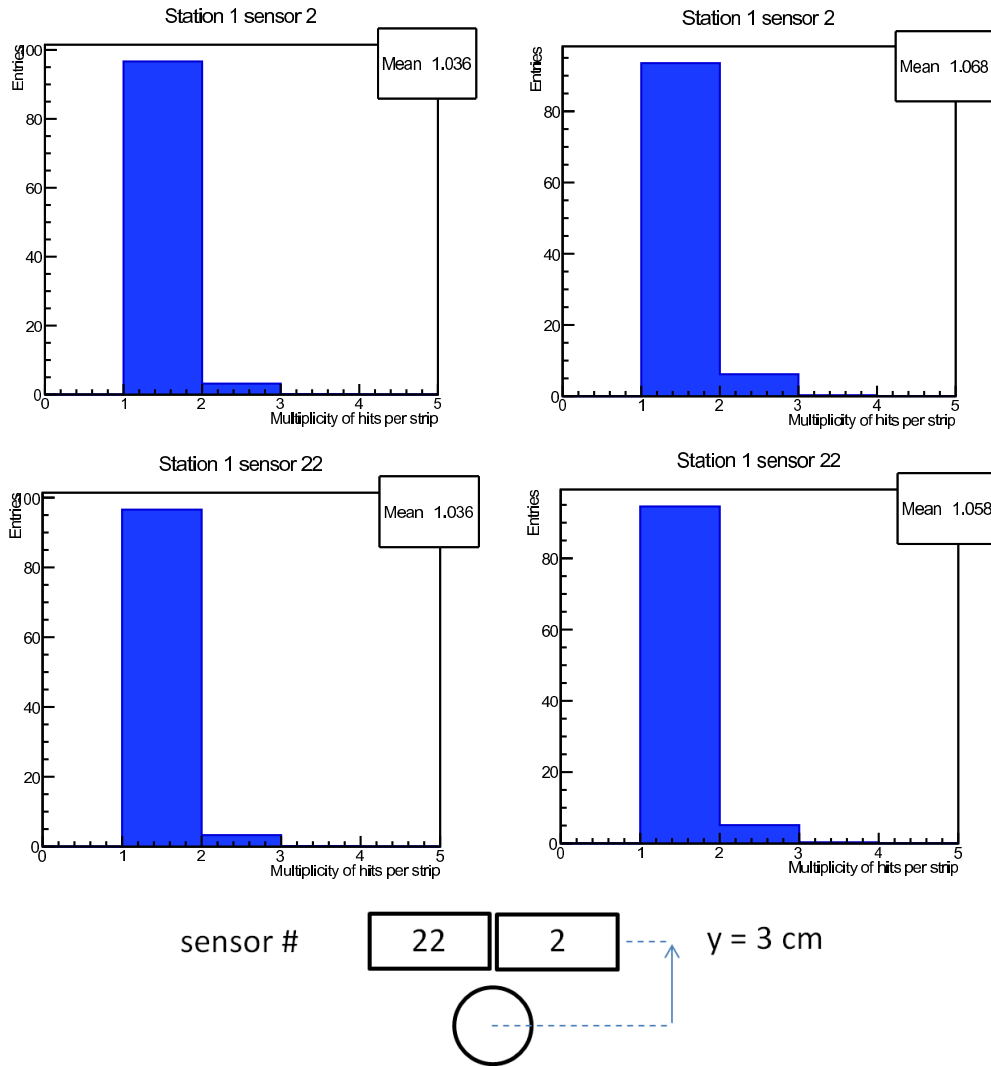
*Figure 5.21: Distribution of incident particle multiplicities per strip in the central Au+Au collisions at 10 A·GeV (left column) and 25 A·GeV (right column) for the two sensors of STS station 1 closest to the beam line. The sketch indicates the position of those sensors with respect to the beam line.*

### 5.2.4.3   Sectorization of ladders

The full STS will use three types of silicon sensors. In the innermost parts of the first two stations, where particle occupancy is expected to reach 5 %, 2 cm high sensors have been chosen: such granularity allows minimizing the number of ghost hits. However, to reduce material budget and to minimize the number of read-out chips, it is possible to use at the outer parts of the stations, where occupancies are lower than 5 %, up to three 6 cm sensors daisy chained together, creating effective strip length up to about 18 cm. Every sensor has a fixed horizontal size of 6 cm. Guard ring structures cause an approximately 1 mm wide non-sensitive band around the edge of the sensor, so that the overall width of the sensor is 6.2 cm. The chosen sensor and sector geometries are summarized in Table 5.4.

The strip occupancies and the required spatial resolution are matched with a strip pitch of 60 $\mu$m. The precise value of 58 $\mu$m was chosen because it allows distributing the sensitive width of the sensor over 1024 strips, corresponding to eight read-out chips of 128 input channels each. With this choice the precise width of the sensitive area is 5.9 cm of the

*Table 5.6: Breakdown of the BM@N STS components (V1 configuration).*

| station | ladders | sectors | sensors | read-out chips | channels |
|---------|---------|---------|---------|----------------|----------|
| 1 | 8 | 80 | 80 | 1280 | 164k |
| 2 | 12 | 120 | 120 | 1920 | 247k |
| 3 | 12 | 120 | 120 | 1920 | 247k |
| 4 | 14 | 136 | 172 | 2176 | 279k |
| 5 | 14 | 136 | 172 | 2176 | 279k |
| 6 | 14 | 136 | 172 | 2176 | 279k |
| 7 | 14 | 136 | 172 | 2176 | 279k |
| 8 | 14 | 136 | 172 | 2176 | 279k |
| Total | 102 | 1000 | 1292 | 16000 | 2053k |
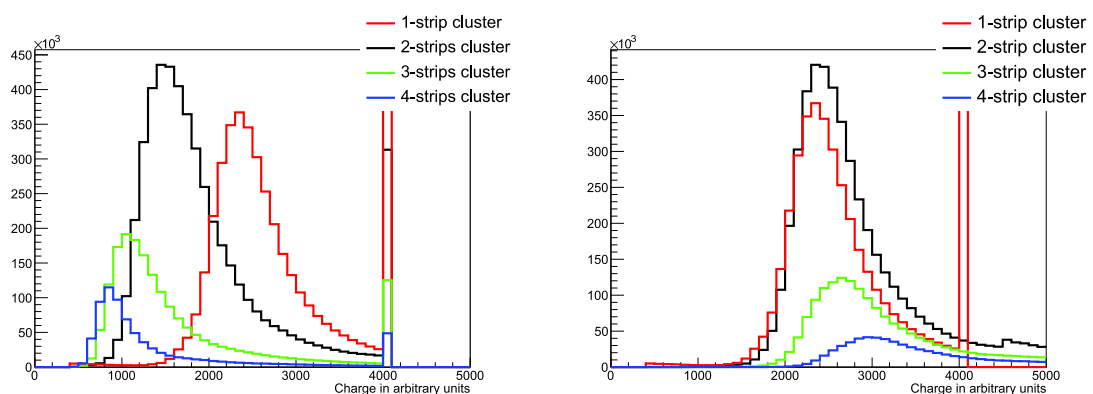


*Figure 5.22: Distribution of the signal: on the most significant strip in a cluster (left); from all strips in a cluster (right). At the upper end of the charge digitization range the overflow bin is filled.*

total 6.2 cm width. On one sensor side the strips are tilted by $+7.5°$ with respect to the vertical edge, creating a stereo angle between the front and back side strips. This allows reconstructing multiple hits from the same sensor at the expense of a poorer spatial resolution in the vertical direction. In all stations the sensitive areas to the left and to the right of the beam hole are covered by ladders of 10 sectors. The sensors are mounted on the ladder with an overlap of 5 mm. Simulation studies of the influence of gaps between ladders have shown that 4 % of the Monte-Carlo space points would be missed if the ladders did not slightly overlap within a station, resulting in a track reconstruction efficiency reduced by 0.4 %. An overlapping arrangement of ladders is therefore chosen, staggering the ladders at two $Z$ positions in a station. Around the beam hole, special ladders are employed. The full STS can be assembled from eight types of ladders. A summary of the ladder types is quoted in Table 5.5.

### 5.2.4.4 Station layout

The layout of each STS station is shown in Figure 5.19. On both sides of the beam pipe, the sensitive area is populated with ten-sector ladders, starting from the edges of the beam-pipe hole. Neighbouring ladders overlap by about 3 mm in order to avoid dead space caused by the guard ring structures of the sensors. The number of ladders was chosen such that the sensitive area defined in Table 5.5 is fully covered. The outer areas of stations 2—8 are equipped with ladders from previous stations to limit the number of read-out channels.
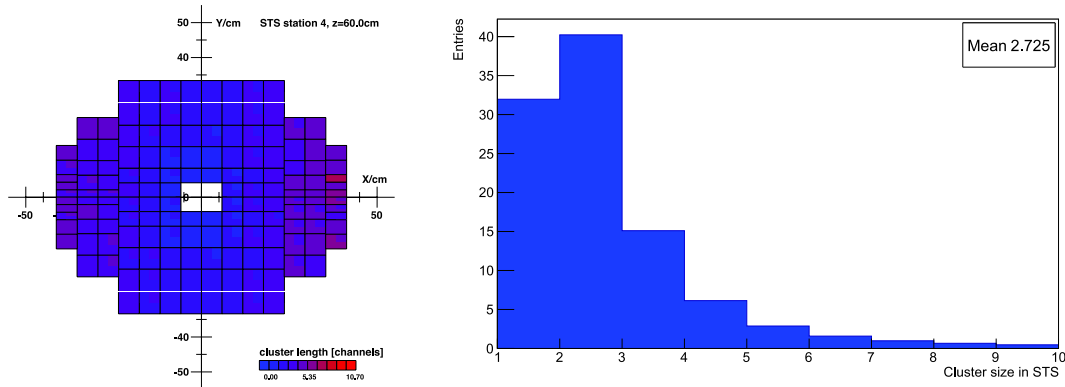
*Figure 5.23: Distribution of cluster sizes for the entire STS (right). Cluster size distribution in the microstrip sensors of STS station 4 for a threshold of 4000 e⁻ applied in the read-out electronics (left). The top right corner in every sector depicts the cluster size on the back side of the sensors; the colors differ due to the Lorentz shift of charges in the magnetic field.*

#### 5.2.4.5  Strip occupancies from multiple particle hits

The strip occupancies arising from multiple particle hits have been studied. They are shown in Fig. 5.20 for the sensors closest to the beam line in STS station 1, exposed to the most intensive flux of particles emitted from the target. The central Au+Au collisions at 10 and 25 A·GeV were considered. Only in a small region the occupancies reach up to 4 % and 15 %, respectively, and stay well below in the vast remaining area of the station. The hit multiplicities for the two sensors closest to the beamline are detailed in Fig. 5.21. For these strips in the hottest area, the maximal probability to have more than one particle hit is 3.6 % and 7 %, respectively.

#### 5.2.4.6  Breakdown of STS components

The presented layout allows constructing the full WA STS ($V1$ configuration) from three types of sensors and eight types of ladders. Table 5.6 summarizes the total number of sensors, ladders, and read-out channels.

The total number of channels in $V1$ configuration of the BM@N WA STS is 2053k, which is almost the same as for CBM STS (2133k). The reduced version of BM@N STS (four first stations) contains 937k channels.

### 5.2.5   Hit reconstruction

The microstrip sensors positioned in space according to the STS layout described above are then studied in terms of generating track hits, which are presented to the track reconstruction algorithms. Simulations have been performed that include the complete chain of physical processes caused by a charged particle traversing the detector: from charge separation in the silicon to the digitized output signals. The first step of STS hit reconstruction is performed by an algorithm called cluster finder. A cluster is a group of adjacent hit strips in a sensor with a common time stamp. A constant signal threshold of e.g. 4000 e⁻ is applied for every channel. The total charge of a cluster is defined as the sum of the single strip signals. The

cluster position is given by the center-of-gravity [160] equation:

$$X_{\text{COG}} = \frac{\sum\limits_{i \in \text{cluster}} S_i x_i}{\sum\limits_{i \in \text{cluster}} S_i} \ , \qquad (5.1)$$

where $x_i$ is the position of the $i$-th strip included in the cluster and $S_i$ — the signal amplitude on the strip; the sums are over all the strips included in the cluster. The accumulated charge per $n$-strip cluster is shown in Fig. 5.22. The colored histograms represent the energy (in ADC units) deposited in clusters of different sizes. In the left panel, the charge on the most significant strip of cluster sizes 1 (red) to 4 (blue) are shown, in the right panel the total charge on all strips in the clusters is shown. The cluster-size distribution itself is presented in Fig. 5.23 for a threshold of 4000 $e^-$ set in the read-out electronics. Due to the inclination angles of tracks caused by the outwards bending in the magnetic field the cluster sizes increase towards the sides of the stations.

In the next step, the association of two clusters lying on the opposite sides of the double-sided sensor is performed, yielding the hits. The realistic sensor response functions [161] include:

• signal sharing between strips,
• charge collection inefficiency,
• Lorentz shift due to presence of the magnetic field,
• channel dead time, and
• random noise added to the charge signal.

## 5.2.6 Track reconstruction
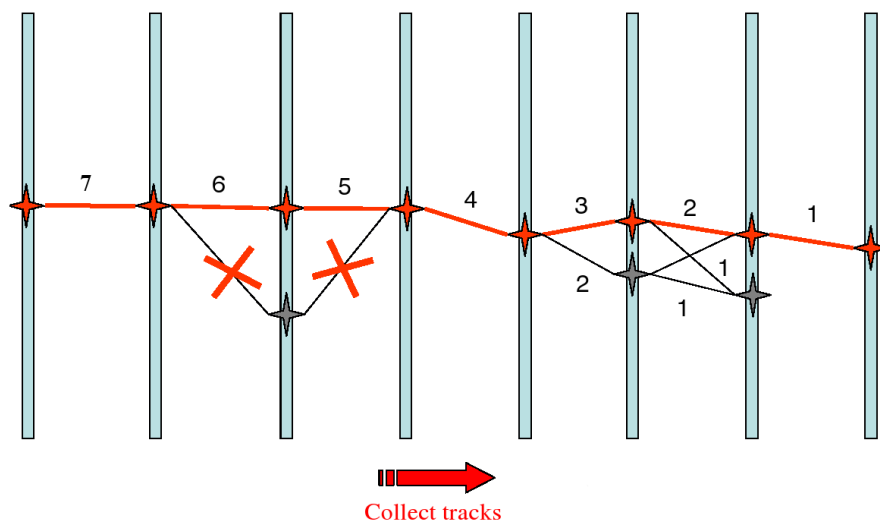


*Figure 5.24: Schematic illustration of the cellular automaton algorithm. It creates tracklets, links and numbers them as possibly situated on the same trajectory, and collects tracklets into track candidates.*

The track finding in the STS detector system, operated in an inhomogeneous magnetic field, is based on the cellular automaton method [162]. Subsequent track and vertex fitting makes use of a Kalman filter.
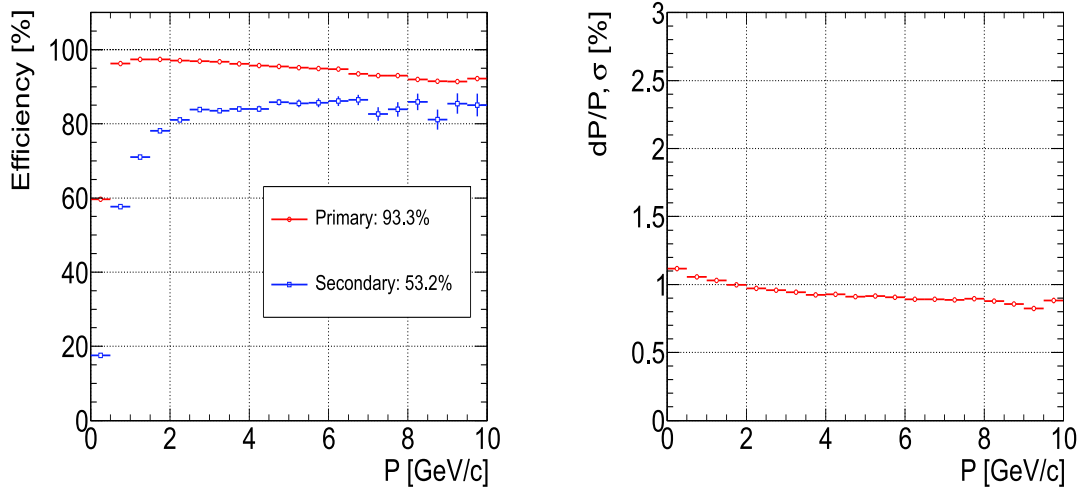
Figure 5.25: *Track reconstruction efficiency (left); momentum resolution in the STS as a function of the momentum for all tracks in the central Au+Au at 25 A·GeV projectile energy (right).*
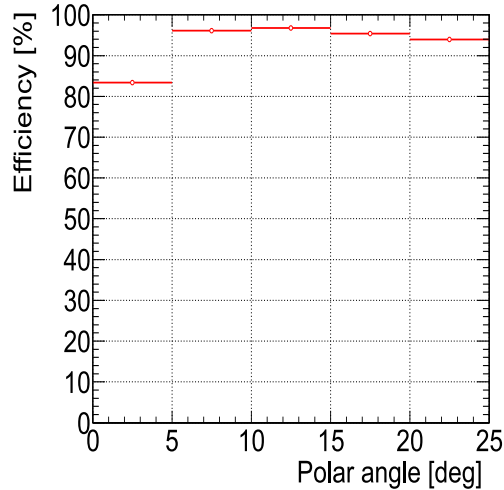


Figure 5.26: *Track reconstruction efficiency in the central Au+Au at 25 A·GeV projectile energy as a function of the polar angle of the track.*

### 5.2.6.1   Cellular automaton-based track finding

This method creates short track segments (tracklets) from hits in neighbouring detector stations and links them into tracks (see a simple illustration in Fig. 5.24). First, using all groups of neighbouring stations the algorithm generates a set of tracklets. A set of cuts, which reflect a geometrical acceptance of the detector system (e.g., forward tracks with minimum four hits and momentum larger than 100 MeV/c), is applied to possibly create only tracklets corresponding to tracks with enough hits to be reconstructed. Then the Kalman filter based track fitting procedure is used on the tracklet construction step and the $\chi^2$ of the fit is calculated. A cut on $\chi^2$ is applied in order to reject arbitrary combinations of hits and reduce the combinatorics. Since hits in the detector stations are sorted, tracklets are generated into groups with the same $Z$ position of its first hit. Therefore, every hit stores two pointers: to the first and the last tracklets of its group.

   Each tracklet has a counter meaning its possible position on a track (initially set to 1). For all tracklets the algorithm finds neighbours (possible track continuations according to the
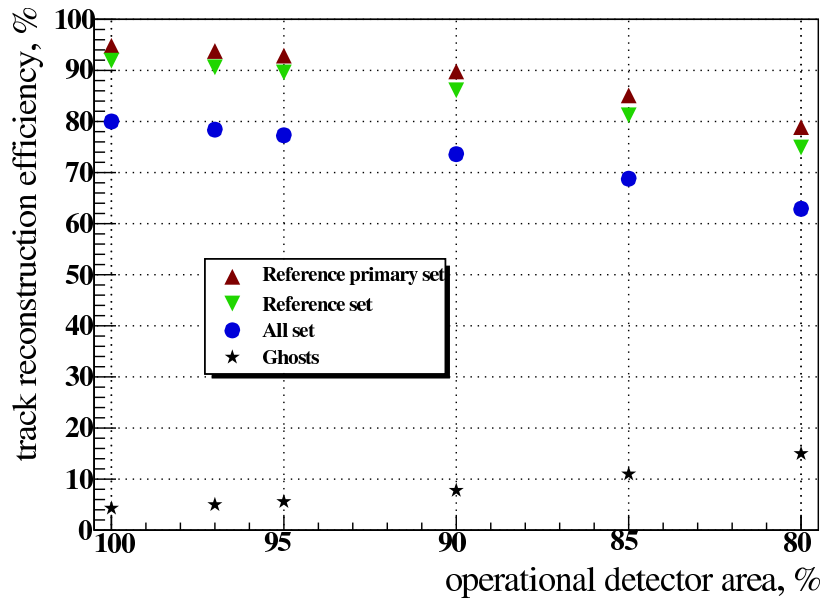
*Figure 5.27: Track reconstruction efficiency as a function of operational detector area.*

*Table 5.7: Residuals of track parameters as a function of a fully operational detector.*

| operational detector, % | 100 | 97 | 95 | 90 | 85 | 80 |
|---|---|---|---|---|---|---|
| residuals: | | | | | | |
| $X$, $\mu$m | 12 | 13 | 13 | 14 | 14 | 15 |
| $Y$, $\mu$m | 57 | 60 | 61 | 65 | 69 | 73 |
| $t_x$, mrad | 0.35 | 0.36 | 0.37 | 0.38 | 0.40 | 0.42 |
| $t_y$, mrad | 0.60 | 0.61 | 0.61 | 0.63 | 0.64 | 0.66 |

track model) and increases the counters of the tracklets. If neighbours are found, a counter of the current tracklet is incremented with respect to a neighbour with the largest counter:

$$\text{counter} = \text{counter}_{\text{neighb.}}^{\max} + 1 \ . \tag{5.2}$$

After tracklets are constructed, the algorithm builds track candidates out of the tracklets. It starts with the tracklets having the largest counter (counter$^{\max}$ = 6 in Fig. 5.24), for each of them takes a neighbour (at the right), which has a counter = counter$^{\max}$ − 1, continues further following the counters (e.g., goes from 4 to 3, but not 2), makes branches, but no empty layers, and finally keeps the best (with lowest $\chi^2$) track for each initial tracklet with the largest counter. Then, a competition between the track candidates is necessary to select only tracks satisfying some quality criteria. After the previous step a set of track candidates with the same number of hits has been created, therefore, $\chi^2$ is a well suitable criterion to sort them. After sorting the algorithm starts with the best (in terms of $\chi^2$) track and flags all hits of the track as used. It continues with the next track (with higher $\chi^2$), checks if the number of used hits is less than $N_{\max}$ (parameter, depends on track density) and flags its hits as used, or deletes the track. Then it proceeds with the next track candidate, etc. The algorithm repeats collecting tracks with decremented counter$^{\max}$ until the shortest tracks are collected.

In order to take into account detector inefficiencies after finding all tracks, the algorithm propagates short tracks through inefficient stations and gathers lost hits using the track model.

Also short track segments (clones) are merged into long tracks. Finally, the algorithm applies additional cuts to kill ghost tracks, which are mostly short tracks.

Being essentially local and parallel, the cellular automaton method avoids exhaustive combinatorial search, even when implemented on conventional computers. Since the cellular automaton algorithm operates with highly structured information, the amount of data to be processed in the course of the track search is significantly reduced. Employing possibly the simplest track model leads to utmost computational simplicity and a fast algorithm.

### 5.2.6.2   Track and vertex fitting

Track and vertex fitting is performed with a Kalman filter based procedure [162]. The propagation of tracks in an inhomogeneous magnetic field makes use of a specially developed analytic formula [163]. The formula has been derived under general assumptions on the magnetic field. Therefore, the precision of the extrapolation does not depend on the shape of the field. The extrapolated track parameters are expanded in a power series of the magnetic field components. Higher-order terms in the series can be cut off. The quality of the results obtained with the formula up to the third order is found to be equivalent to those achieved with a fourth order Runge-Kutta method. In the power series, terms of the same order are found to differ significantly from each other. This leads to an efficient realization of the analytic formula, where one keeps only a few major terms within the same order.

The performance of the track reconstruction is summarized in this section. The evaluation is done for UrQMD central Au+Au events at 25 A·GeV. For evaluation purposes all simulated and reconstructed tracks are subdivided into several categories: a reference set of tracks, a complete ("all") set, an extra set, and clone and ghost tracks [164]. By definition, a track from the "all" set should intersect the sensitive regions of at least four stations. In addition, a reference track has a momentum exceeding 1 GeV/c. The reference set of tracks can also include tracks of particular physics interest: secondary tracks from interesting decays and primary tracks coming from the target region.

For efficiency determination, a reconstructed track is assigned to a generated particle if at least 70 % of its hits have been caused by this particle. A generated particle is regarded as found, if it has been assigned to at least one reconstructed track. If the particle is found more than once, all additionally reconstructed tracks are regarded as clones. A reconstructed track is called a ghost, if it is not assigned to any generated particle (70 % criteria). Tracks of high-momentum particles are reconstructed with efficiencies of clearly exceeding 90 %, while multiple scattering in detector material leads to a significantly lower reconstruction efficiency for slow particles. The reconstruction performance is shown in the left panel of Fig. 5.25 for the minimum bias Au+Au collisions at 25 A·GeV. Reference primary tracks are reconstructed with up to 96 % efficiency, depending on the particle's momentum. Secondary tracks reach reconstruction efficiencies up to 85 %. At momenta larger than 6 GeV/c some hits are lost in the inner beam hole of some of the first tracking stations, resulting in a reduced reconstruction efficiency. The clone rate of the algorithm is 0.1 % and the ghost rate is 0.9 %. The momentum resolution obtained for primary tracks is shown the right panel of Fig. 5.25. The reconstruction efficiency of tracks originating at the target as a function of the polar angle, i.e. the emission angle of the particle w.r.t. the beam direction, is shown in Fig. 5.26. The drop in efficiency at small polar angles is attributed to both the dimensions of the beam hole and the higher hit densities towards the central areas of the tracking stations.

The stability of the track reconstruction algorithm with respect to inefficient detector area has been studied [165] also. A fraction of the strips has been randomly switched off event

by event to simulate the effect. The dependence of the track reconstruction efficiency on the operational fraction of the detector, still having finite charge collection and hit finding efficiencies, is shown in Fig. 5.27. The efficiencies for all reconstructible tracks, reference tracks, and primary reference tracks as well as ghost rate are presented. The algorithm is robust and shows slight degradation of the reconstruction efficiency with respect to the detector inefficiency. Decreasing the operational fraction of the detector from 100 % to 95 % leads to a reduction of the track reconstruction efficiency by only 3 %.

For the track fit quality evaluation residuals and pulls of the track parameters are calculated at the first Monte-Carlo point of the track. The parameters of the track are: track positions $X$ and $Y$, track slopes in the $XZ$ plane $t_x$ and in the $YZ$ plane $t_y$, and an inverse particle momentum, signed according to a charge, $q/p$. The track fit quality at the first track point has been investigated as well with respect to the detector inefficiency as defined above. Resolutions become slightly worse due to the smaller number of hits in a track (see Table 5.7). Both the resolutions and pulls of all track parameters are unbiased.

## 5.3 RPC Time-of-Flight detector

The particles identification (PID) by the time-of-flight (TOF) is a very distributed and known method. The trajectory by the outer tracking system (ST and DC, see sections 5.6 and 5.5) and the TOF information allows one to certainly know the particle type.

The simulation performed for the central Au+Au at 3.5 A·GeV and Cu+Cu at 5.0 A·GeV collisions shows good particle identification for the timing resolution of 80 ps and TOF base of 10 m. The separation of the secondary particles using $m^2$—$p$ plot is demonstrated in Fig. 5.4. The precision of the momentum reconstruction in the inner silicon tracker (see section 5.2) is $\Delta p/p = 2$ %. The reduction of the TOF base will lead to the PID quality degradation.

The fixed target experiments have the huge flows of the produced particles at the low angles (near the beam direction). Fig. 5.28 shows, that the occupancy on the central region of BM@N TOF wall for the peripheral collisions will be up to $1.5 \cdot 10^3$ Hz/cm$^2$.
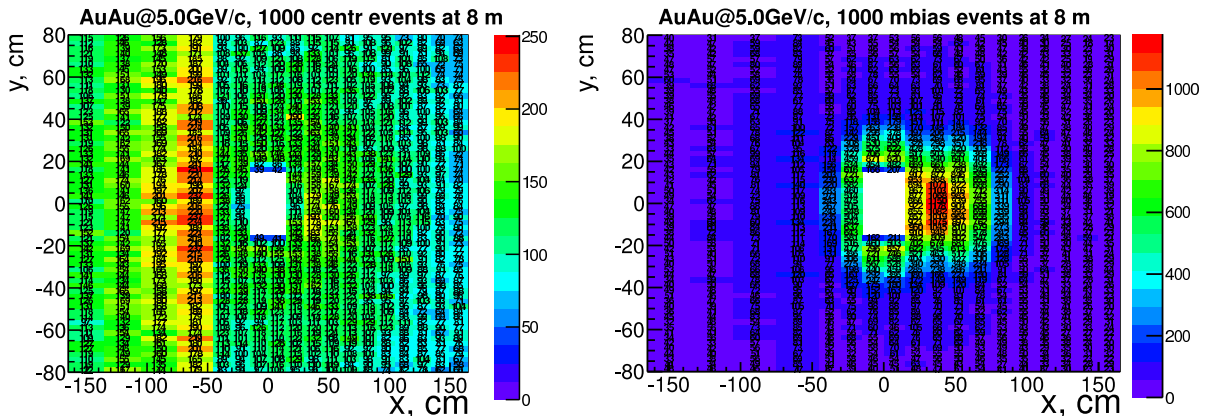


*Figure 5.28: BM@N TOF occupancies for the central (left) and minimal bias (right) collisions.*

The simulation results for one of the TOF wall configurations placed at the distance of 8 m are shown in the left and right panels in Fig. 5.29 for UrQMD Au+Au and Cu+Cu
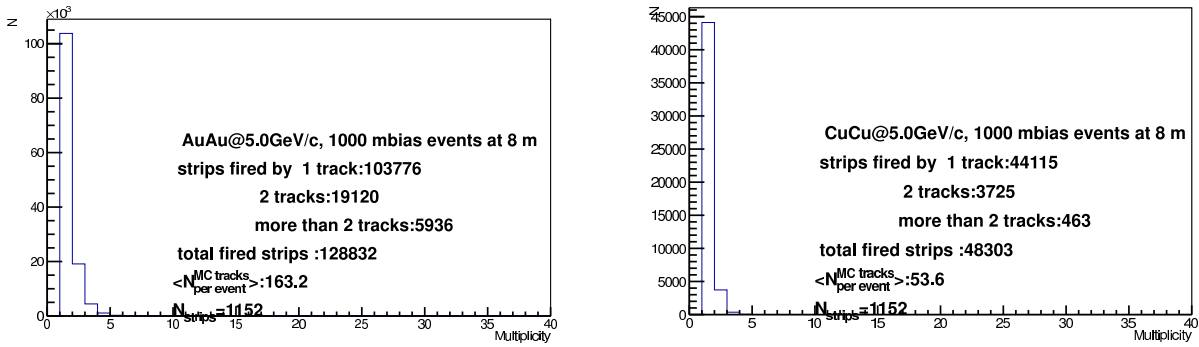
*Figure 5.29: The multiplicity for one of the configurations of the RPC wall placed at the distance of 8 m for the Au+Au (left) and Cu+Cu (right) minimal bias collisions.*

minimal bias collisions, respectively. One can see that the number of double hit events are $\sim 25$ % and $\sim 9$ % for Au+Au and Cu+Cu minimal bias collisions, respectively. The optimization of the cell sizes for BM@N TOF wall is in progress.

The TOF system of the BM@N experiment consists of two parts. First part — T0 detector (see section 5.4) located near target to provide a start signal, and second part — TOF wall situated about 8 m far from the start detector. In order to separate pions from kaons with momentum up to 3 GeV/c and protons from kaons up to 5 GeV/c the TOF system has to have time resolution better than 100 ps. In an assumption, that time resolution of start detector will be less than 50 ps, the time resolution of the TOF wall must be not worse than $\sim 90$ ps. Size of wall is 3.2×2.4 m$^2$, what means that a detector used to build TOF wall should be cheap enough. Monte-Carlo simulation shows that a flux rate of particles going through the wall can be up to 3.5 kHz/cm$^2$. The Multigap Resistive Plate Chamber (mRPC) as a candidate to the wall detector can meet all these requirements.
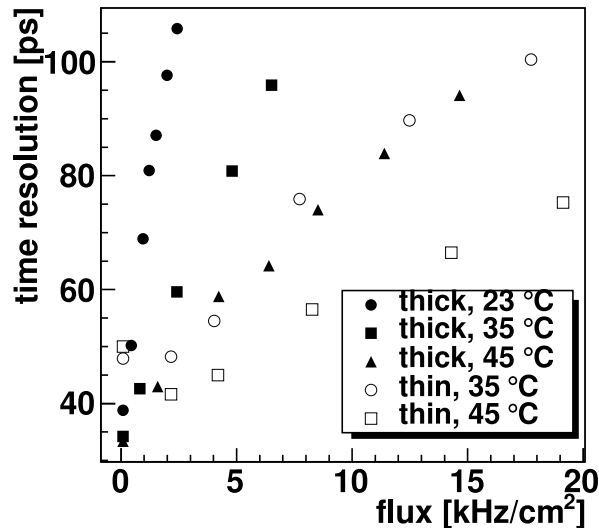


*Figure 5.30: Time resolution as a function of particle rate.*

In the most of contemporary TOF systems the main detectors are mRPCs of various designs [166–169]. A glass mRPC with pad readout was already chosen to construct the TOF system in such an experiment as ALICE [170], HARP [171], STAR [167], and PHENIX [168]. The mRPC time resolution now is comparable with one of the microchannel PMTs. The

existed technologies allows one to keep high efficiency up to occupancies of $10^5$ Hz/cm$^2$ [172, 173]. These mRPCs could be used in setups like CBM and BM@N. Glass mRPC suffers from grave shortcomings — low hit rate capability. Because of high bulk resistivity, $10^{12}$—$10^{13}$ $\Omega$·cm, a timing mRPC produced with ordinary glass works well up to several hundreds of Hz/cm$^2$ only. To increase the mRPC hit rate it is necessary to decrease a resistivity of glass plates. There are two ways to decrease a resistivity of "window" glass — to minimize its thickness and/or to heat a glass electrode. First our result obtained using both these methods was described in [174]. It was shown that "warm" mRPC can provide the high time resolution even at rate of $\sim 20$ kHz/cm$^2$ (see Fig. 5.30).

If the expected multiplicity of particles in the events is not very big, it should be more reasonable to use read-out with strips instead of pads to reduce the number of the FEE channels. This can be very useful in case of a large area of the TOF system. On the other hand, due to relatively small area ($\sim 8$ m$^2$) of the BM@N TOF wall the pad mRPC structure seems more adequate. Of course, the pads should have variable size, so regions with high occupancy should be equipped by the smaller pads.

In our tests [175, 176] with six- and ten-gap mRPCs equipped with the 25 mm wide strips the time resolution of $\sim 50$ ps was reached what is typical for mRPCs with the pad pick-up electrodes. High resolution was achieved at the efficiency above 98 % and at crosstalk signal in the adjacent strips less than 1 %. Neither the time resolution nor the efficiency dependence on the coordinate along the strip of 30 cm length has been observed. This results are in agreement with the data published in [177, 178] describing the performance of the mRPC equipped with wide strips. So, our suggestion to use "warm" mRPC with strip readout as timing detector for the TOF wall is based on our experience in operation with timing glass chambers.

There are two groups (from JINR [152] and IHEP (Protvino) [153]) demonstrated high performance of mRPC tested with the beams of relativistic particles and cosmic muons.

## 5.3.1 Warm float glass mRPC

### 5.3.1.1 Structure of the TOF wall
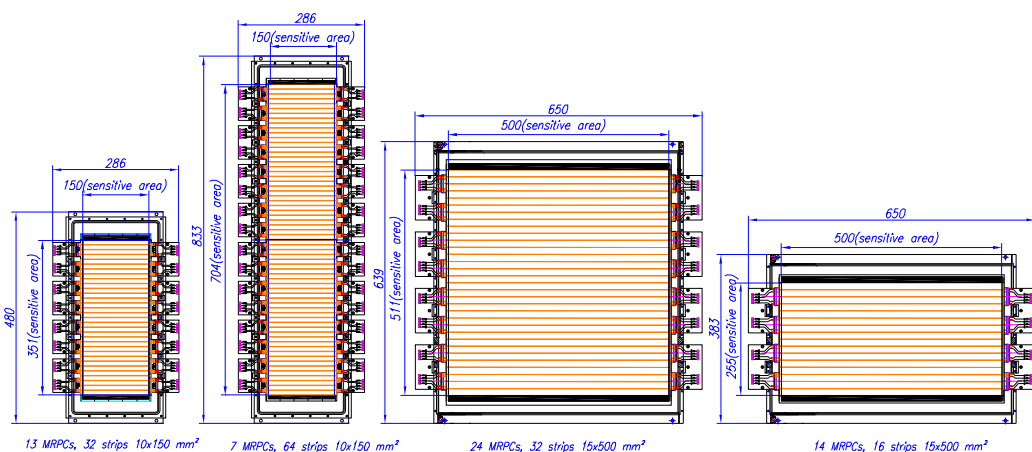


*Figure 5.31: Four types of mRPC proposed to cover the TOF wall.*

According to the Monte-Carlo simulation a rate of particles crossing the wall plane will be different in the different places of the TOF wall. This forces to cover the wall with modules having the different sizes of read-out electrodes. Four types of chambers are proposed. Size of those types is given in Fig. 5.31.
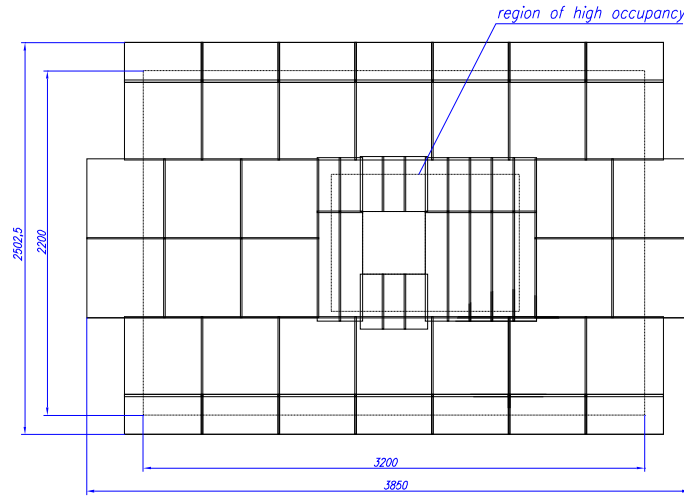
Figure 5.32: Arrangement of mRPCs on the wall plane.
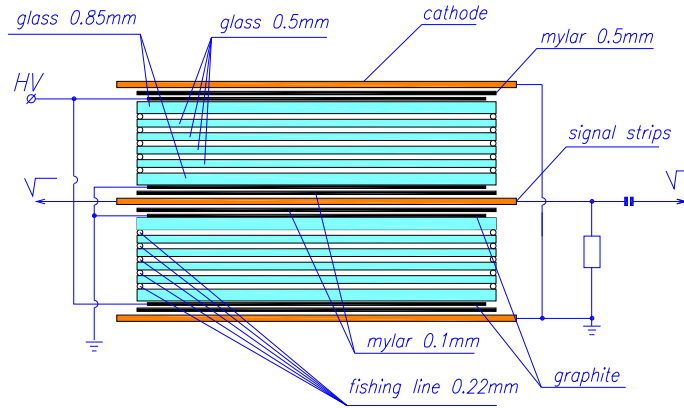


Figure 5.33: Schematic cross section of mRPC.

To reduce a fraction of the double-hit events in the same strip, the modules with lowest strip area will be mounted in the high occupancy region. Arrangement of 55 separated mRPCs of different size is shown in Fig. 5.32.

Active areas of adjacent mRPCs have overlap not less than 10 mm. The total number of strips is 1856, so the total number of the FEE channels is 3712.

### 5.3.1.2   Chamber design

All modules are ten-gap chambers. Schematic design of the chamber is given in Fig. 5.33. The chamber consists of two identical stacks with read-out strips between them. Each stack is formed by six glass plates with the $2 \times 10^{12}$ $\Omega$·cm bulk resistivity and thickness of 0.85 mm for outer plates and 0.5 mm for inner plates. The gap between the glasses of 0.22 mm is fixed by spacers — usually fishing-lines, which ran directly through the RPC working area.
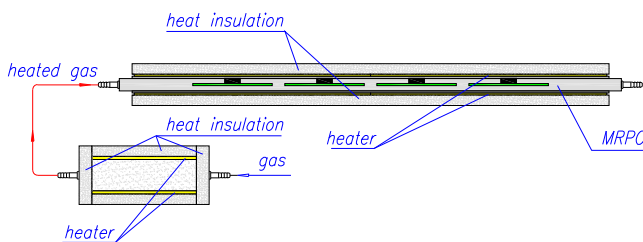


Figure 5.34: Scheme of mRPC heating.
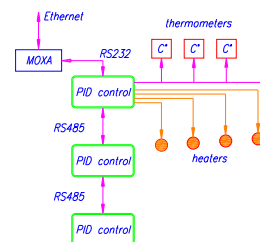


Figure 5.35: Thermal stabilization scheme of mRPCs.
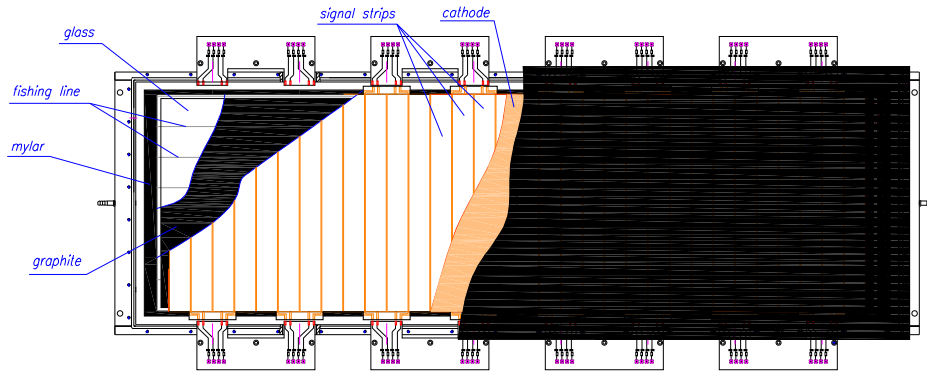
*Figure 5.36: The mRPC prototype drawing.*



*Figure 5.37: Photo of 128-channel TRB (with AddOn board) installed in beam test area to read-out signals from four mRPC prototypes.*

Graphite conductive coating with surface resistivity of $\sim 1 \ M\Omega/\square$ is painted to outer surfaces of external glass plates of each stack to distribute both the high voltage (HV) and its separate ground and thus to form the uniform electrical field in the stack sensitive area. Signal pulses are taken from the both ends of anode strips.

The entire mRPC assembly is put into a gas-tight aluminium box, which will be blown through by the gas mixture of 93% $C_2H_2F_4$ + 5% $C_4H_{10}$ + 2% $SF_6$.

### 5.3.1.3   FEE of mRPC and digitizing

FEE is based on NINO chip [179]. The output signal of NINO chip is the time-over-threshold (TOT) pulse, whose leading edge provides the time of the hit, while its pulse width is proportional to the input signal charge. The amplifier-discriminator design of the FEE channel is like the channel of the TOF AddOn board [180] of the HADES experiment. The signal from mRPC strip is linked to two inputs of NINO circuit. The final output signal of the amplifier is a superposition of signals from these two branches. The first circuit branch contains a fast amplifier and a shaper. It provides the final pulse with a leading edge. The second circuit branch amplifies, integrates and shapes a signal to provide the final output
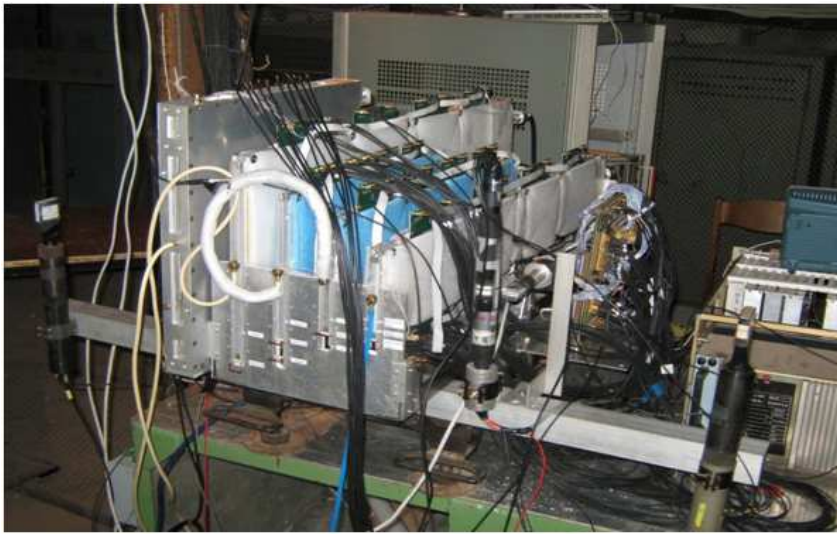
*Figure 5.38: Photo of prototypes mounted on moving table together with trigger and timing counters.*
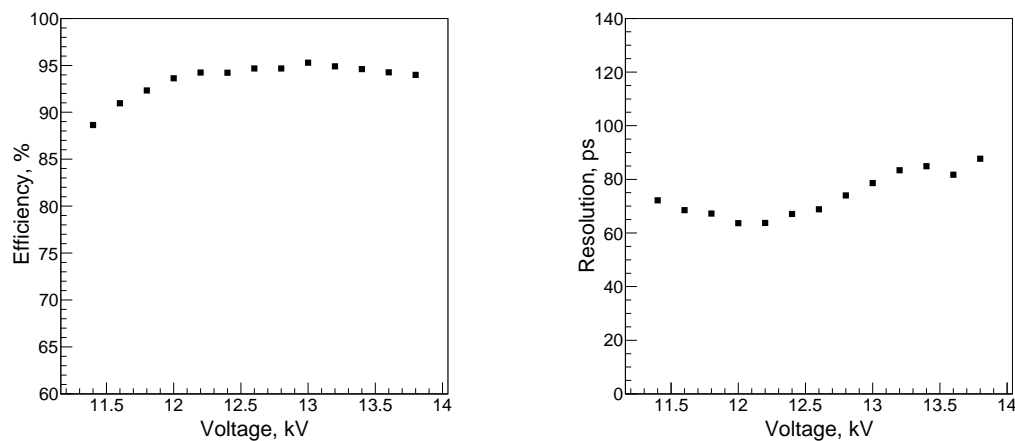


*Figure 5.39: Performance of warm mRPC (heated to $35°C$) at 4 kHz/cm$^2$ particle rate. Efficiency (left) and time resolution (right) both as a function of HV value.*

TOT pulse with a trailing edge. After integration of the primary pulse in the second circuit branch the width of the output TOT signal becomes insensitive to the structure of the input signal.

The time of leading and trailing edges of the TOT signals will be digitized by the high performance TDC chip HPTDC [183] in the 100 ps mode. A correction for the slewing effect can be done with the time-width correlation.

### 5.3.1.4   Heating and thermal stability of mRPC

An increase of the rate capability of modules made with usual "window" glass is possible by moderate heating. During the beam test of prototypes a system, which heated all the modules to needed temperature, was tested too.

The mRPCs are heated by EH chambers designed for this task. EH chamber has thickness of 1 mm and its size corresponds with size of mRPC's box. Heater fastens on both sides of
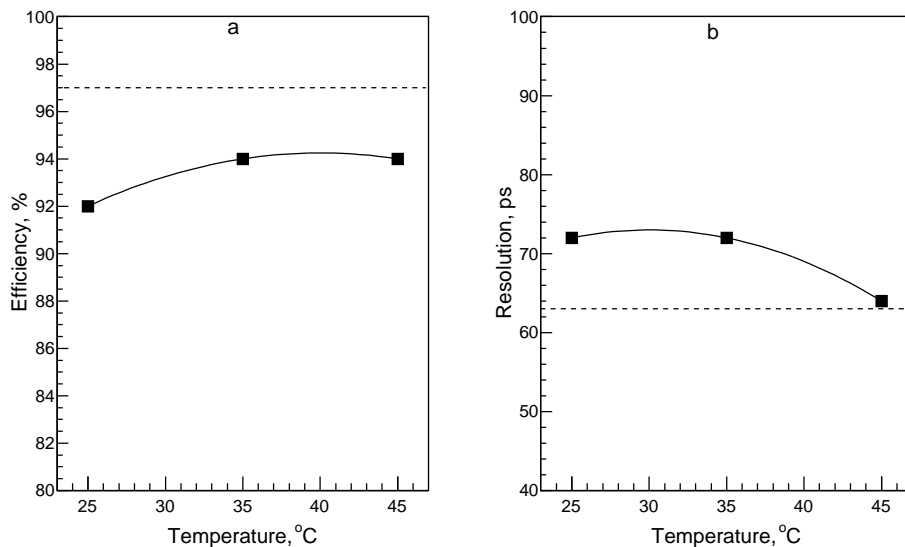
*Figure 5.40: The best efficiency (left) and time resolution (right) found for the module with $10 \times 150$ cm$^2$ strips at three values of temperature. Particle rate was 5 kHz/cm$^2$. Dotted lines — efficiency and time resolution of this mRPC at hit rate 400 Hz/cm$^2$.*

aluminium box (Fig. 5.34), the thermometers are placed inside the mRPC box.

System of thermal stability based on proportional-integral-differential regulation. The applied power of heater $U(t)$ is defined as follows:

$$U(t) = K_p e(t) + K_i \int_0^t e(\tau) \mathrm{d}\tau + K_d \frac{\mathrm{d}e}{\mathrm{d}t} \ , \tag{5.3}$$

where $e(t) = T_s - T$, $T_s$ — settled temperature, $T$ — measuring temperature in mRPC, $t$ — time, $K_p$, $K_i$, $K_d$ — proportional, integral and differential coefficients. Such system (Fig. 5.35) was tested, the settled temperature was sustained with accuracy of $\leq 1°$C. The number of channels of the temperature setting for the TOF wall is $\sim 350$.

### 5.3.1.5 Test of prototypes

To understand the performance of modules with proposed size of read-out electrodes the four mRPCs have been built and then tested with muon flux. Schematic design of the tested module is shown in Fig. 5.36.

For the beam tests the mRPC prototypes were equipped with FEE, which we consider as the prototype for further application in the BM@N TOF. We used 128-channels TOF AddOn board [180] coupled with HADES TRBv2 (Trigger and Readout Board) [181] (Fig. 5.37). TRB is a 128-channels multi-purpose electronic module playing the key role in the HADES Data Acquisition System [181]. TRB has four HPTDC chips operated in 100 ps mode.

### 5.3.1.6 Beam test setup and preliminary results

The test area "Muon" (U-70, IHEP, Protvino) provides a possibility to exposure the detectors in muon flux at the different particles rate. The muon flux inside the area variates from $\sim 20$ kHz/cm$^2$ at "north wall" of the area up to few hundreds of Hz/cm$^2$ at "south wall". All mRPC prototypes were mounted on the movable table. The chambers performance at

different particle rate was studied by moving the table into different places of test area. In Fig. 5.38 shown the photo of prototypes mounted one-by-one with timing scintillation counters and FEE board. Each mRPC has individual heater and temperature control sensors.

Efficiency and time resolution of the prototype with strip size of $10 \times 150$ mm$^2$ are presented in Fig. 5.39.

Fig. 5.40 confirms that a moderate warming of mRPC really helps to improve the characteristics of glass timing detector. The best efficiency and resolution of the same prototype, for which data in Fig. 5.39 were given, are presented in Fig. 5.40 for three different temperatures of operation. The module was tested at 5 kHz/cm$^2$ particle rate.

## 5.3.2   Float glass mRPC

### 5.3.2.1   mRPC prototypes construction
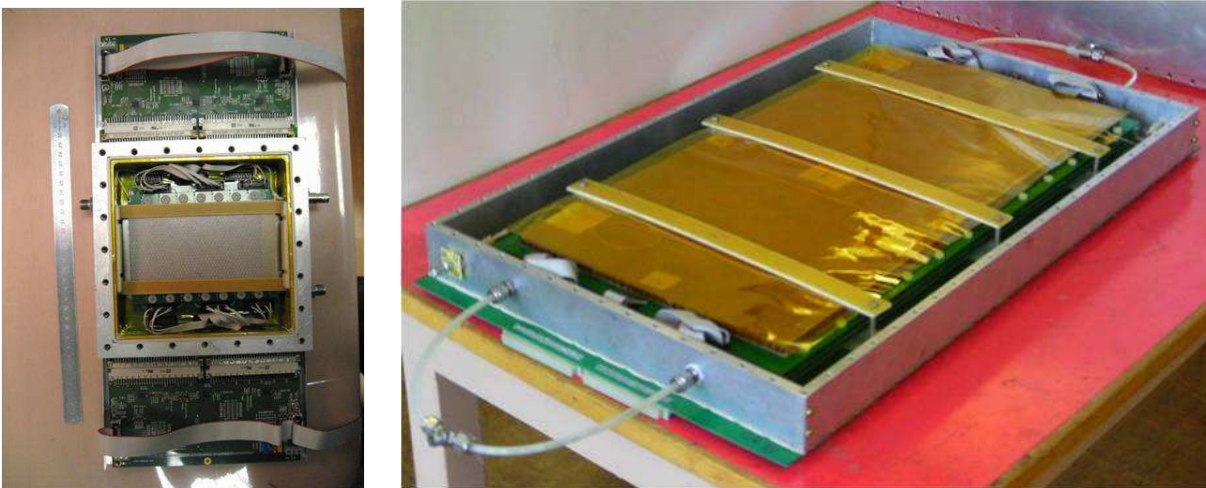


*Figure 5.41: First mRPC TOF prototypes manufactured in LHEP JINR, with the pad (left) and strip (right) structure.*
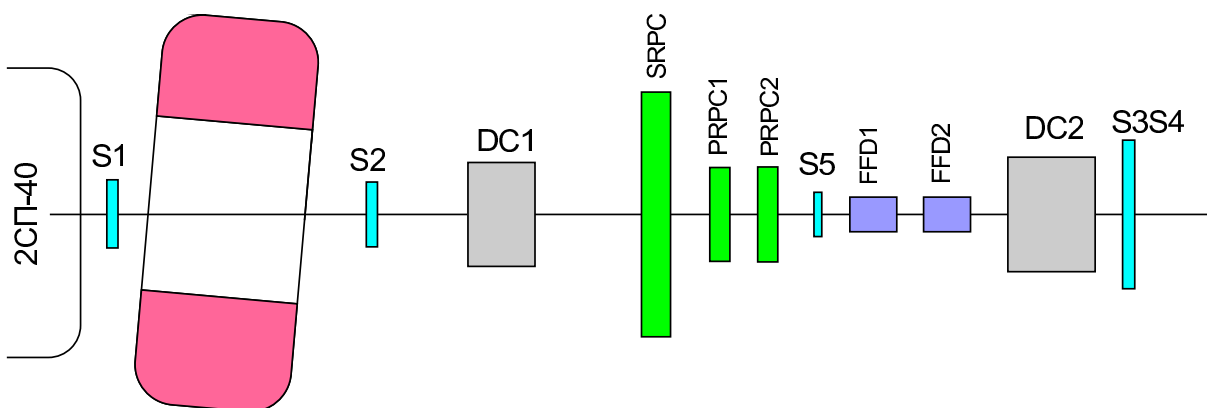


*Figure 5.42: Experimental setup scheme. See text for description.*

The design and study of the fast mRPC are performed at the LHEP JINR for the last time. In late 2012 the double-stack pad prototypes and big single-stack prototype with long
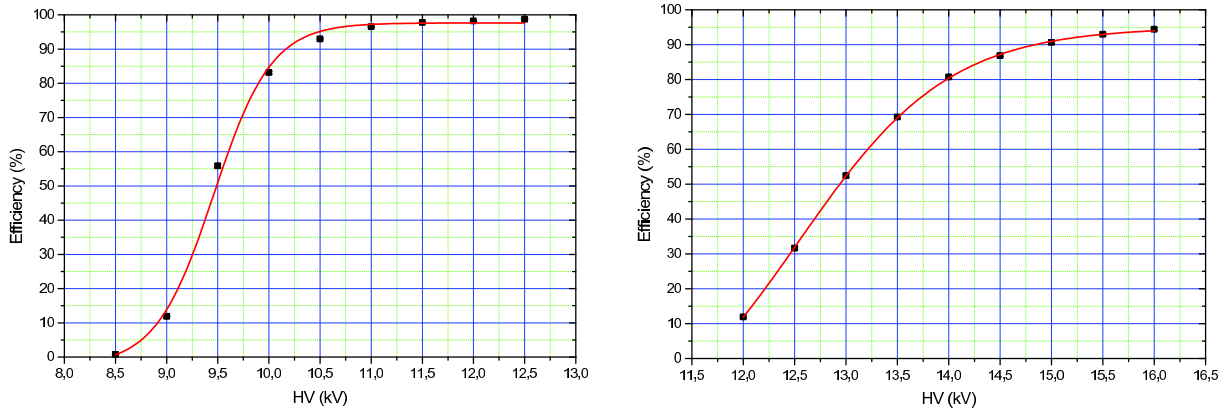
Figure 5.43: *The efficiency for the pad (left) and strip (right) prototype vs high voltage. The errors are lower than the symbols size.*
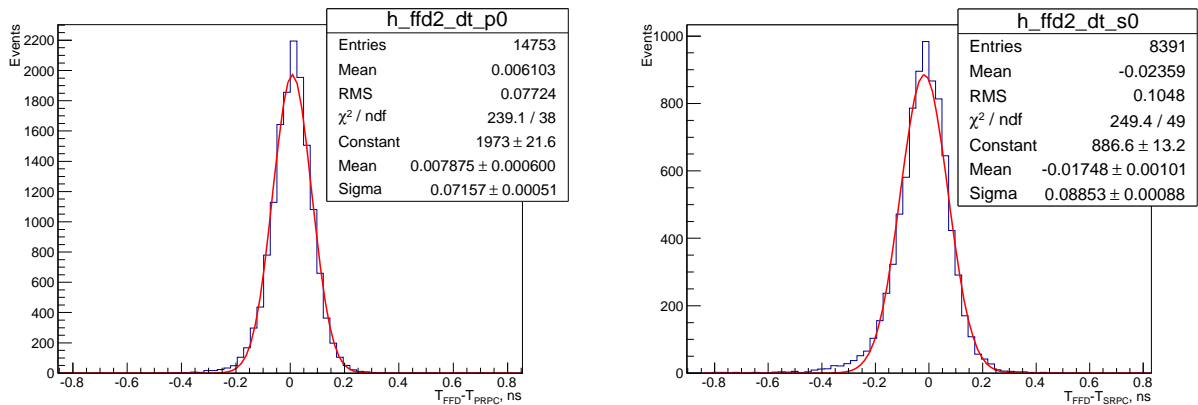


Figure 5.44: *The time distributions of the pad (left) and strip (right) prototype relative to FFD2. The prototype HVs are 11.5 kV and 14 kV, respectively.*

stripes (see Fig. 5.41) are manufactured. Both types have own advantages and limitations. The pad mRPCs are better studied and have more suitable signal read-out than the strip ones. The strip's read-out, however, allows one to reduce the number of FEE channels and obtain yet high resolution for both time and coordinate measurements.

The pad prototype contains two stacks, each of five gaps of 200 $\mu$m. The active detection area depends on the glass plate size, which is 150×75 mm$^2$ here. The HV is supplied to the outer glass plates with thickness of 0.7 mm. For the uniform voltage distribution these plates are painted by the graphite with the surface resistivity of 5—10 M$\Omega$/$\square$. The inner plates have thickness of 0.55 mm. The pads are formed on the printed circuit, the signal connectors from them are going to board sides, from where the twisted pairs are taken out through the gas box cover.

The strip prototype is single-stack with six gaps of 0.23 mm. The glass plates have the same thickness as in pad prototype, however with area of 600×300 mm$^2$. The strips of 600 mm length are formed on the printed circuit, too. The signal pulses are read-out from the both strip ends, so the obtained time is not dependent on the hit coordinate, while latter could be obtained also. The assembly process for such mRPCs is described in details in many sources, e.g. see [178].

The signal pulses were read-out by the 24-channel amplifiers using the NINO chips [179].
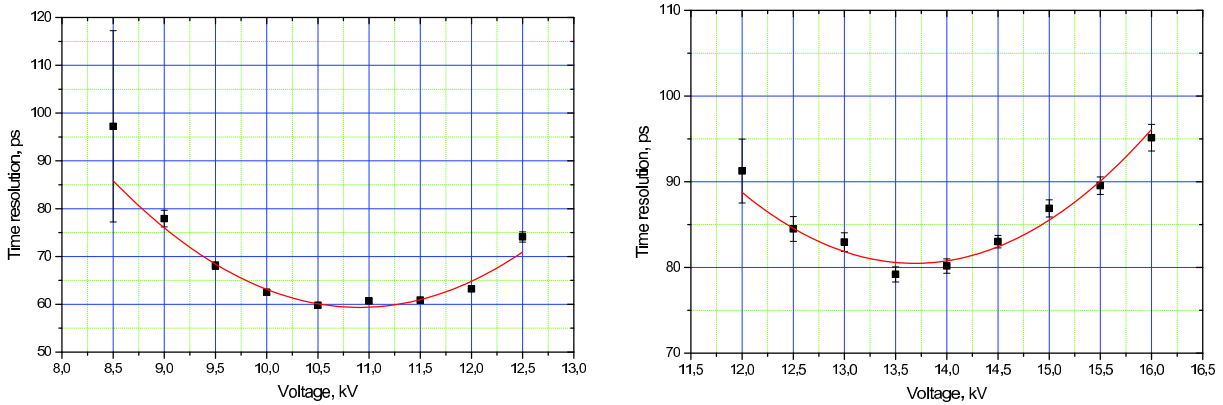
*Figure 5.45: Time resolution vs HV value for the pad (left) and strip (right) prototypes.*

In the near future we plan to use the NINO-based FEE designed in LHEP JINR. The LVDS outputs of NINO were supplied to 32-channel TDC module [182] in the VME standard. This TDC32VL designed in LHEP JINR using the HPTDC chips [183] has the time bin of 25 ps and provides the own time resolution of 20 ps, if the integral nonlinearity corrections are applied.

### 5.3.2.2 Prototypes beam tests

The last tests of the aforementioned prototypes were done in December 2012 on Nuclotron beams in LHEP JINR. The deuteron beam was slowly extracted and transferred into 205 building to expose the experimental setup shown in Fig. 5.42. The five scintillation counters S1—S5 produce the trigger. The DC1 and DC2 drift chambers were used for tracking. Two fast detectors (FFD1 and FFD2) provide the start signal for the prototypes tested: SRPC (strip) and PRPC1, PRPC2 (pad).

### 5.3.2.3 Test results

The efficiency (Fig. 5.43) and the time resolution of mRPC prototypes were measured during the test. The efficiency is relative to the FFD "tower" of $26.5 \times 26.5$ mm$^2$. The discrimination threshold of 250 mV for the mRPC signal is corresponded to charge of 75 pC. We can see that the strip prototype efficiency reaches a plateau at HV of $\sim 16$ kV.

The time resolution could be defined relative to three detectors: PRPC2, FFD1, and FFD2 (see Fig. 5.42). The FFD2 shows the best own time resolution of 38 ps during this test measurements including the FEE resolution, so prototypes time resolutions are relative to FFD2. The typical prototypes time distributions are shown in Fig. 5.44.

The time resolution for the pad prototype (including the own FFD2 one) is $\sim 61$ ps, while for the strip prototype — $\sim 80$ ps. We calculate the time resolution for each HV value and show their in Fig. 5.45. In the HV range of 10—12 kV the time resolution of the pad prototype is still $\leq 65$ ps. The prototype efficiency in this voltage range is best. At higher voltages the streamers are appear, which leads to doubling of output signals and efficiency decreasing. The strip prototype is under development now. Their best time resolution is shown in the HV range of 13—14.5 kV with the suboptimal efficiency of 50—80 %. First of all this is due to the increasing of the signals mirrored on the strip ends. This effect was described in [184] and could be eliminated by the prototype design refining and the proper matching of the signal line and amplifier.

## 5.4   T0 start detector
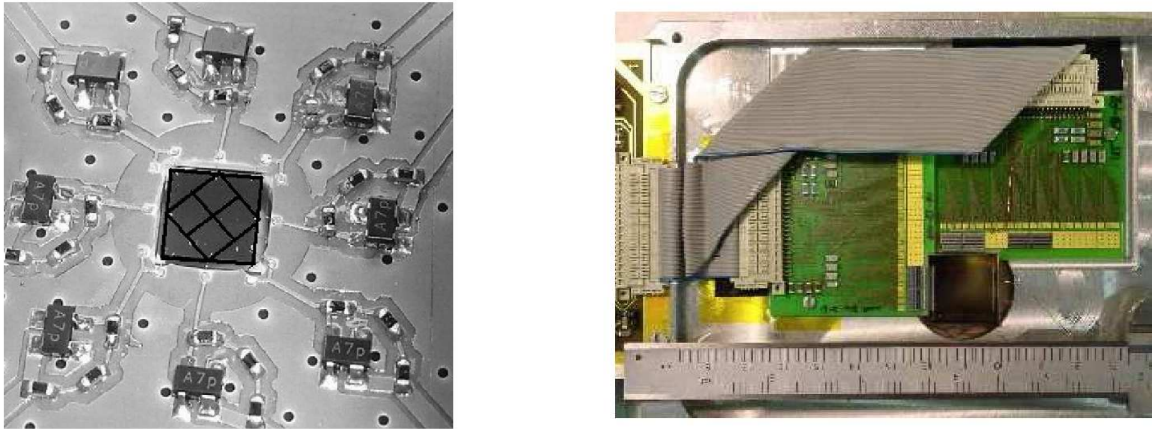


*Figure 5.46: The HADES monocrystalline diamond pad detector 4.7×4.7 mm² [154] (left) and the polycrystalline double-sided diamond strip module [155] (right).*
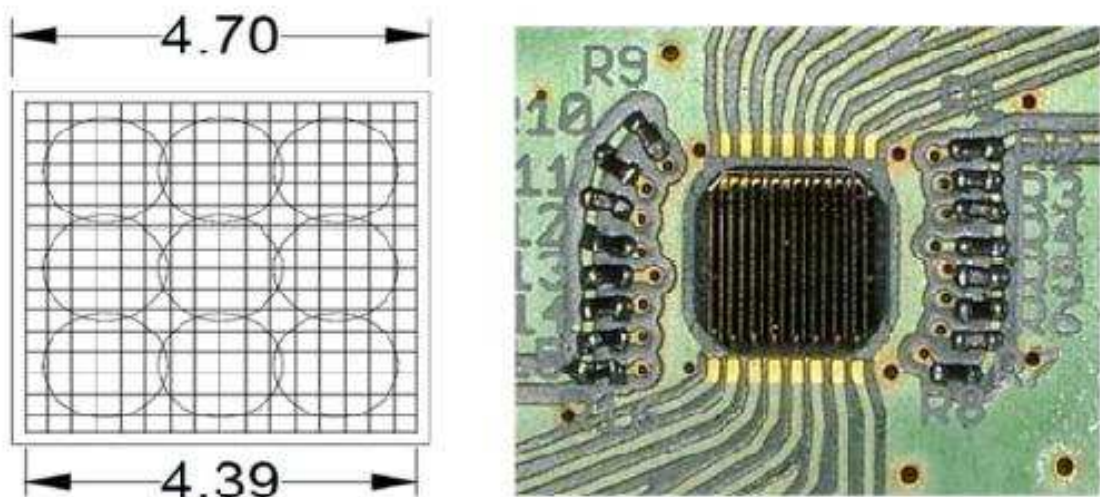


*Figure 5.47: The HADES diamond detector (right) with scheme of the beam spot positions on the detector (left).*

The working conditions of the BM@N experiment for the T0 detector require the use of diamond pixel or strip detector due to high radiation hardness. Two technologies, namely the monocrystalline pad diamond detector applied for HADES [154] and the polycrystalline double-sided strip module developed for ATLAS [155], are presented in Fig. 5.46.

Recently, HADES collaboration used double-sided multi-strip diamond based sensor. Detector has 16 strips with 200 $\mu$m width and 90 $\mu$m gap on each side. The detector thickness (along the beam) is about 60 $\mu$m. A holder allows one to move the detector across the beam spot. The picture of the diamond detector used by HADES and the scheme of the beam spot positions on the detector are shown in the right and left panels in Fig. 5.47, respectively.

The picture of the start diamond detector and the signal shape from one of the strips are presented in the left and right panels in Fig. 5.48, respectively. The time resolution
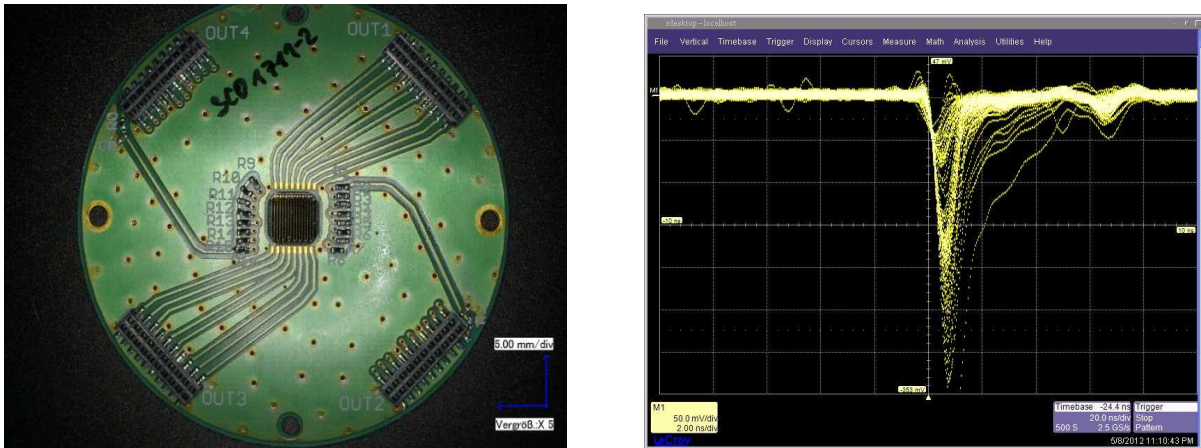
*Figure 5.48: The start diamond detector (left) and the signal shape from one of the strips (right).*

achieved was $\sim 60$ ps and $\sim 70$ ps for $X$ and $Y$ sides, respectively. It was also observed the decreasing of the signal amplitude by a factor of 2.7 after irradiation of $3.04 \cdot 10^{11}$ Au ions per $mm^2$.

## 5.5   DC tracking detector



*Figure 5.49: The view of NA48 drift chamber*

For intermediate tracking two drift chambers from NA48 (delivered from CERN to JINR) can be used [185]. The photo of NA48 drift chamber is shown in Fig. 5.49.

The simulation shows that the mostly hard situation in the sense of double hits appears for the minimal bias events. The simulation results for the DC placed at the distance of 5 m and 6 m are shown in Fig. 5.50. One can see that the occupancy value and the number of double hit events are acceptable for the case of Cu+Cu collisions. The DC will not be used for the tracking of the heavier systems.

These drift chambers [186] have an octagonal shape with a transverse width of 2.9 m. Their fiducial area is about 4.5 $m^2$. In order to achieve high detection redundancy, each
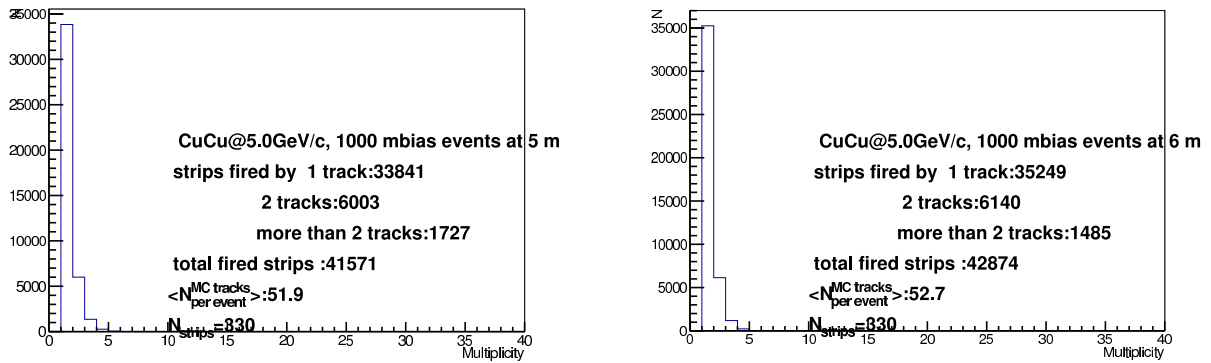
Figure 5.50: The multiplicity in the DC placed at the distance of 5 m (left) and 6 m (right) for the Cu+Cu minimal bias collisions.
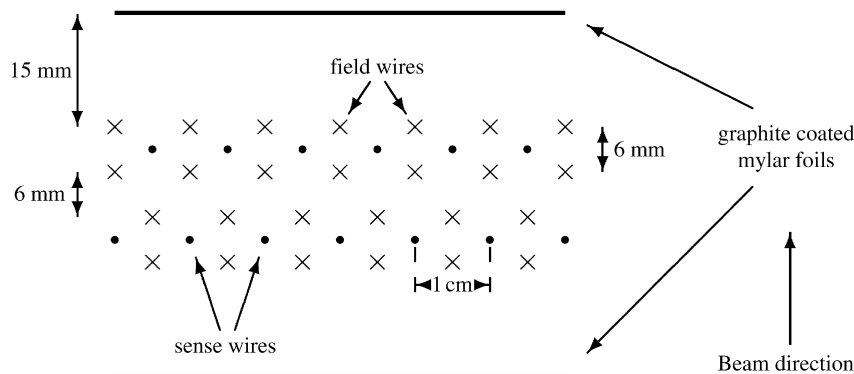


Figure 5.51: Drift cell geometry of the NA48 drift chamber (from [186]).

chamber contains eight planes of grounded sense wires orientated in four different directions, orthogonal to the beam axis: $0°$, $90°$, $-45°$ and $+45°$. Each so-defined view contains two staggered planes of wires to resolve left-right ambiguities. An additional feature of the chambers is a 160 mm diameter central hole for the beam pipe that required careful construction and positioning of an ensemble of rings on which the central wires of the different planes are soldered.

To minimize multiple scattering effects, the wire chambers are constructed with minimal amount of material along the beam direction. A schematic view of the geometry of one view is shown in Fig. 5.51. Sense wires have a diameter of 20 $\mu$m and made of gold-plated tungsten. The electric field is created by applying a negative voltage on two planes of gold-plated Ti-Cu wires located on each side of the sense wire planes, at a distance of 3 mm. The field wires have a diameter of 120 $\mu$m. The spacing between sense and field wires on a plane is 10 mm. Thin Mylar foils (22 $\mu$m) coated with graphite are used to shape the electric field in the drift cell and also to act as separating walls between two consecutive views.

All wires are stretched and soldered on thin (3.8—6.2 mm) G10 frames using printed circuits glued on the frames. Wires were pre-tensioned on stiff steel frames before they were transferred to the final G10 frames. The length of the wires is varied between 1.28 and 2.72 m. The nominal mechanical tension applied to the wires is 55 g for sense wires and 520 g for field wires. Such tensions ensured that field and sense wires hanging horizontally in the chamber have similar sagittas to within 30 $\mu$m. The precision obtained on the 1 cm gap between two wires is found to be better than 10 $\mu$m (RMS) and parallelism is achieved to better than 25 $\mu$m/m (RMS). The chamber frame support, on which the wire planes are mounted, consists of two 12 cm thick octagonal frames made of stainless steel. Between
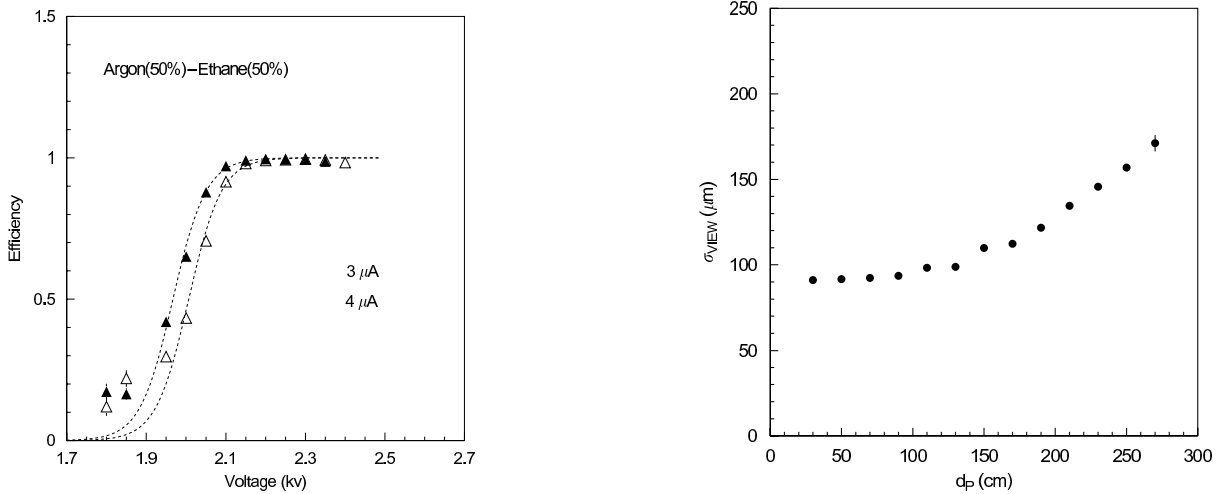
Figure 5.52: DC efficiency as a function of high voltage (left) and space resolution in a view as a function of the hit distance from the preamplifier (right) (both from [186]).
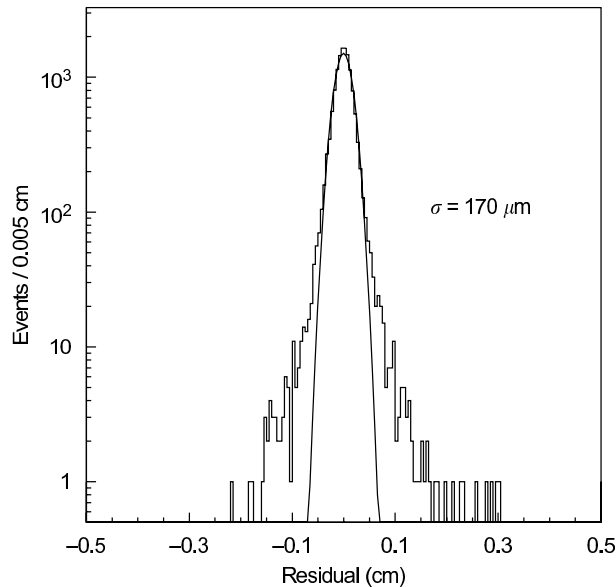


Figure 5.53: Distribution of coordinate residuals in one projection (from [186]).

these a total of 38 G10 frames are stacked in a chamber. These include field and wire planes, Mylar foils and spacers. Precise positioning of the G10 frames is ensured by 40 peripheral rods each of 32 mm diameter.

Inside the chamber, the G10 rings which held the central wires and the separating Mylar windows are tied together by four 5 mm diameter epoxy rods. The whole central structure is free to move inside the chamber. Given a total tension of about $3 \times 10^3$ N due to the central wires, the displacement of the internal structure was smaller than 100 $\mu$m. The total number of wires per chamber is 6160 and the amount of material in one chamber, including the gas mixture, corresponds to about $4 \times 10^{-3}$ of a radiation length.

A readout time measurement accuracy of about 1 ns with no deadtime is achievable with specially designed amplifiers and TDC circuits. The anode signals in the wire chambers are amplified, discriminated and transformed to logic pulses in electronic circuits located on the chambers. The output pulse is a logic 50 ns wide ECL pulse with 50 ns deadtime following the pulse, achieved by a delay element.

## 5.5.1 Wire chamber operation and performance at NA48

The NA48 drift chambers were operated with a 50% Ar + 50% $C_2H_6$ gas mixture flowing through a bubbler filled with demineralized water. The water was maintained at a constant temperature of about 4°C in order to keep the fraction of water vapour in the argon-ethane mixture at a level of a few per mille. The use of a small concentration of water vapour as an additive in drift chamber gas mixtures has proved to be very efficient in improving the operational stability of the chambers by limiting the occurrence of Malter effects on the field wires. The gas mixture was also filtered with a molecular sieve to prevent deposits from oil contaminants inside the drift chambers. The gas continu- ously flowed through each chamber at a rate of about 75 L/hour. The gas pressure inside the chamber was maintained at about 0.7 mbar above the surrounding pressure. Its value was continuously monitored during data taking. In addition, two oil bubblers located at the entrance and exit gas outlets of each chamber were used as safety devices to prevent gas pressure exceeding safety limits. The gas flows of argon and ethane were controlled to a precision of about 1 %, which guaranteed a stable and homogeneous gas mixture in the chambers.

The chambers were operated with a nominal high voltage value of $-2300$ V on the field wires and of $-1440$ V on the graphite planes. At the end of each SPS spill, the high voltage was ramped down by several hundred volts and then restored to its nominal value a few seconds before the beginning of the following spill. At the nominal beam intensity of $1.5 \times 10^{12}$ ppp on the target, the current drawn in the chambers varied between 20 and 40 $\mu$A per plane, depending on the location of the detector along the beam line. At the nominal high voltage values, the gas gain was measured to be about $8 \times 10^4$ and the average drift velocity of the electrons across the drift cell to be 45 $\mu$m/ns.

Signals at the output of the preamplifiers were discriminated with a typical threshold value of 30 mV corresponding to a peak current of about 3 $\mu$A detected on the sense wires. With nominal high voltage and discrimination threshold settings, the efficiency of the sense wire planes was measured to be about 99.5 % and found to be rather uniform all over the detection plane. The left panel in Fig. 5.52 shows the dependence of the average chamber efficiency as a function of high voltage for two threshold values.

Due to the use of long wires in the chambers, the hit-time resolution depends rather strongly on the hit location along the wire. The right panel in Fig. 5.52 shows a typical variation of the space resolution provided by one view of a chamber as a function of the distance of the hit from the preamplifier card. Using the information from track hits in all eight sense wire planes of a chamber and correcting for the incidence angle of the tracks, the average space resolution in each coordinate ($X$ or $Y$) was measured to be better than 100 $\mu$m. A typical distribution of coordinate residuals obtained by comparing the position measured in one projection with the one from two other views in the same chamber is shown in Fig. 5.53.

The decay vertex position for two-track charged events was measured using only the two chambers. The distribution of the closest distance of approach of the two tracks had an RMS spread of about 7 mm and the resolution on the vertex position along the beam line was about 0.5 m at the AKS position. The invariant $\pi^+\pi^-$ mass resolution for reconstructed $K^0$ decays was better than 2.5 MeV/c$^2$ and the resolution of the vertex decay time, using only drift chamber hits, was about 700 ps.

## 5.5.2   Front-end amplifiers

The chamber frames are enclosed in a Faraday cage of Cu plates adapted to the geometry, so only the amplifier card connectors are left unshielded. Single card contains the 16 channels of amplifier. A 64-pin ELCO-3182 connector is used for connection. It has two rows of 32 pins. One of them ends on the back-metallization of the chamber printed circuit boards and is connected to the ground. In the other row every second pin is connected to the ground. The amplifier consists of a grounded emitter input stage with feedback from a subsequent emitter follower. The amplifier transfer function is 30 mV/$\mu$A, the input impedance is 170 $\Omega$, the rise time is 8—10 ns. Cross-talk from neighboring channels is suppressed with $> 46$ dB. The output is AC-coupled to a discriminator chip (4-channel MVL407) on the board. The discriminator threshold of 30 mV is derived from an external differential DC-voltage. The discriminator output is shaped to a standard differential ECL pulse with 50 ns width followed by 50 ns of deadtime by means of a flip-flop, which resets itself with a delay line. A second hit arriving within 100 ns is therefore ignored. The output pulses are then transported via 10 m twisted pair cables to the TDC. The power consumption of the 16-channel amplifier card is 3.3 W. The inputs are protected against sparks by diodes. Test pulses can be given to the inputs of all even or all odd channels simultaneously. They are derived from standard ECL pulses with fixed (1:10) attenuation. The sensitivity of the amplifiers can be controlled by variation of the threshold voltage.

## 5.5.3   Power Supply

### 5.5.3.1   High Voltage Supplies

In order to avoid decoupling capacitors at the amplifier inputs, negative high voltage will be applied to the field wires and Mylar shaping wall. The chambers are normally operated with a gas amplification of 50000 at 2.6 kV between field and sense wires and at 1.5 kV on the shaping wall. The drift velocity in 92:8 mixture of carbon dioxide ($CO_2$) and isobutane ($C_4H_{10}$) is $\sim 15$ $\mu$m/ns. Each view of the drift chamber should have two separated high voltages: for field wires and shaping wall. Altogether we need 16 channels of high voltage for two drift chambers. MPOD mini-crate equipped with EHS F630x-305 module (16 channels of 3 kV and 3 mA) will be used to power drift chambers.

### 5.5.3.2   Low Voltage Supplies

Low voltage power supplies are needed for the front-end electronics (FEE). In order to keep line losses small, the power supplies will be located in the experimental area. MPOD mini-crate equipped with four MPV 8008D modules (8 channels of 8 V and 10 A) will be used to power FEE of the drift chambers. The FEE power consumption per channel is 207 mW, so the total consumption for two drift chambers will be less than 1 kW. In addition two power supplies are needed to power fans already installed along the perimeter of each chamber.

## 5.5.4   Gas system

In order to achieve good spatial resolution the counting gas for drift chambers will be a carbon-dioxide-based mixture. A mixture of carbon dioxide and isobutane in the ratio 92:8 is a good candidate because it is non-flammable. The gas mixture will be prepared

in the gas hut out of experimental area. From there the mixture is sent to a distribution system located close to the drift chambers. The primary counting gas components carbon-dioxide and isobutane are supplied in separate bottles, i.e. no pre-mixing gas will be used. The proportion should be 1 bottle of isobutane and 16 bottles of carbon-dioxide. The gas mixture continuously flows through each chamber at a rate of about 100 L/hour and released into the atmosphere outside the experimental hall. The gas flow of isobutane and carbon-dioxide should be controlled to a precision of about 1 %, in order to guarantee a stable and homogeneous gas mixture in the chambers. For one month of data taking we need more than 16 bottles of carbon-dioxide. It means that for each run of data taking two cassettes of 16 bottles of carbon-dioxide should be ordered and delivered to the gas hut.

### 5.5.5   DC Slow Control

The slow control for the BM@N drift chambers should monitor the following quantities:
• High Voltage:
† correct voltages for all views (critical);
† currents for all views (critical);
† failing views in case of over-current.
• Low Voltage:
† FEE supply voltages for all views (critical);
† FEE threshold voltages (critical);
† MPOD mini-crate supply voltages (critical).
• Gas system:
† input and output flow for each chamber;
† pressure in some parts of the gas system.
When quantities marked as critical became out of range the DC subdetector should be considered as out-of-duty for the data taking purposes. The slow control monitoring takes place in widely different locations and is also shared with other subdetectors, so the design of the DC slow control has not started yet.

## 5.6   Straw tracking detector
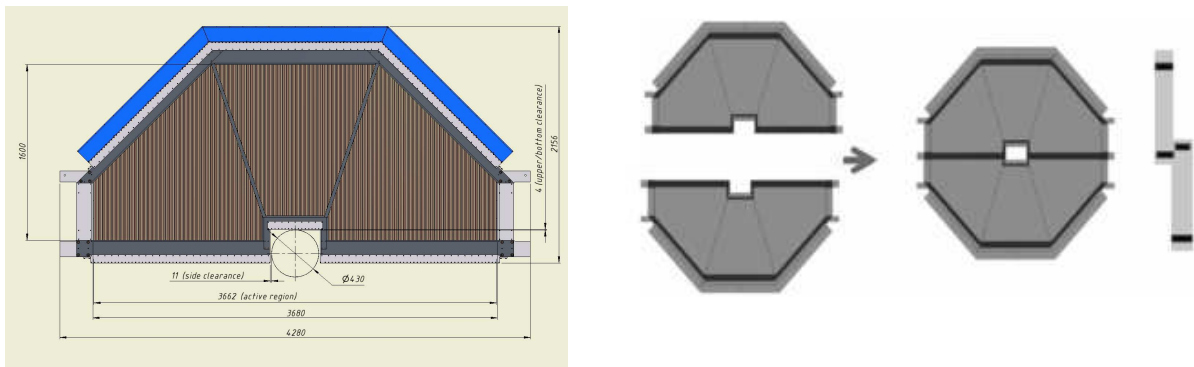


*Figure 5.54: Schematic view of the ST module (left) and the ST chamber (right).*

The intermediate tracking for the systems heavier than Cu+Cu requires an additional detector outside the magnet. For this purpose, the straw tracker (ST) will be placed at the
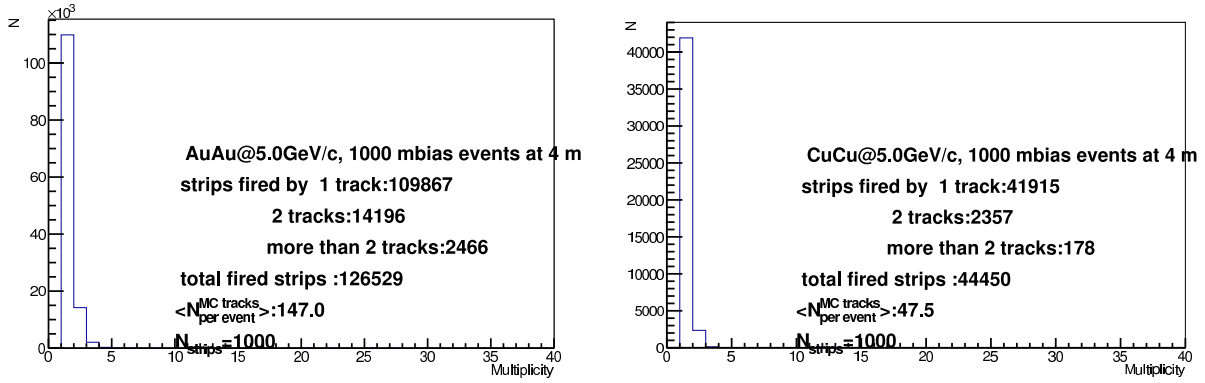
Figure 5.55: The multiplicity in the straw detector with 4 mm straw tubes placed at the distance of 4 m for the Au+Au (left) and Cu+Cu (right) minimal bias collisions.
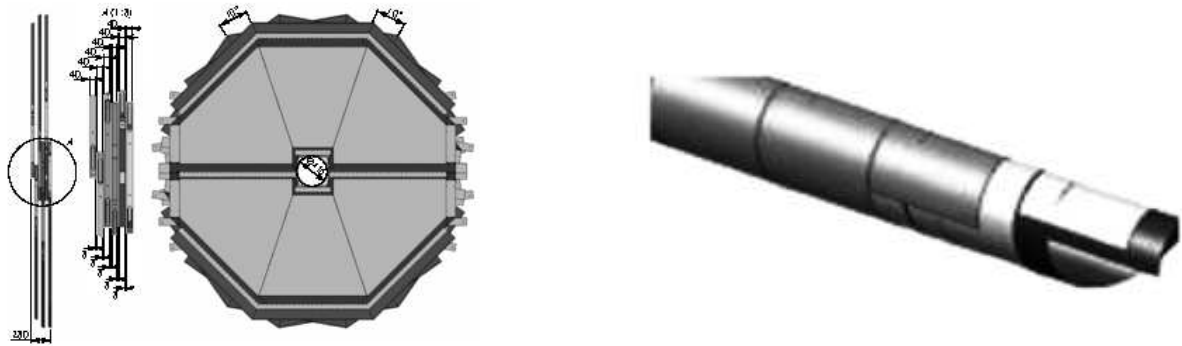


Figure 5.56: Schematic view of the ST with three chambers (left). The straw tube consisting of a carbon loaded inner layer 40 $\mu$m thick and an aluminized Kapton outer layer $\sim 25$ $\mu$m thick (right).

distance of 4 m from the target point. One of ST options can be detector similar to one developed for the CBM muon system [187].

Each straw station contains three identical octagonal chambers measuring $X$ and two rotated ($+10°$, $-10°$) coordinates of a passing charged particle. Each chamber consists of two identical modules with some overlap between them to avoid the dead regions. The chambers will have an inner hole for the beam pipe with a diameter of 20 cm. In Fig. 5.54 shown the schematic layout of the straw tracker module (left) and the straw chamber (right).

The simulation shows that the mostly hard situation in the sense of double hits appears for the minimal bias events. The simulation results for the ST design presented in Fig. 5.54 with the straw tubes diameter of 4 mm are shown in Fig. 5.55. The ST is placed at the
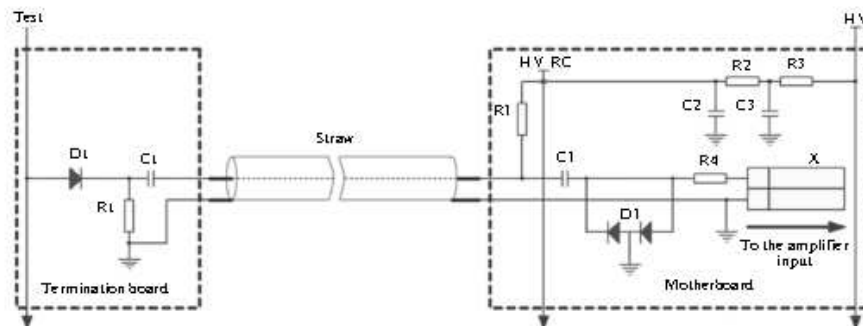


Figure 5.57: A simplified TB and MB circuit diagram for one channel.
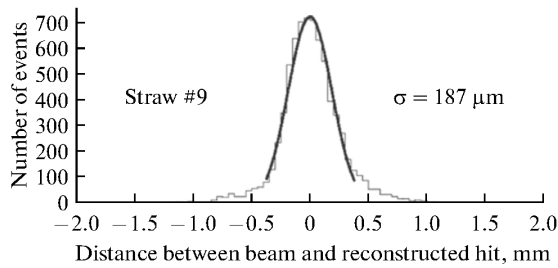
*Figure 5.58: Difference of coordinates measured in the 4 mm straw tube and predicted at the tube position using the track reconstructed by the silicon tracker.*
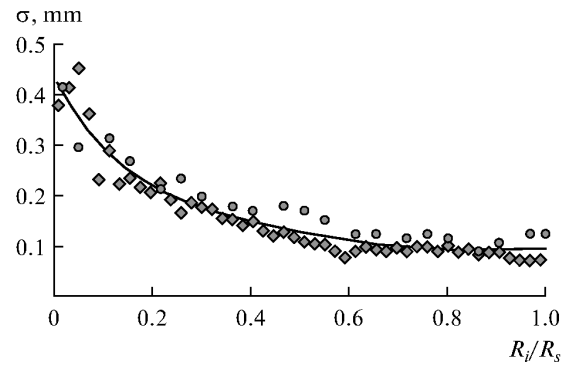
*Figure 5.59: Spatial resolution as a function of the scaled distance to the anode for the straws with 4 mm (circles) and 9.53 mm (diamonds) inner diameter. The straws were blown with the gas mixture 80 % Ar + 20 % $CO_2$, and the gas gain was about $7 \cdot 10^4$ for both tube variants.*

distance of 4 m from the target. One can see that the occupancy value and the number of double hit events are acceptable even for the case of Au+Au collisions.

Each module contains two layers of straw tubes, which are inserted into a carbon frame. The straws of one layer are glued together to form a plane. Every plane is divided into three sections. The central part, being closer to the beam axis, is exposed to higher rates. This part has a central half hole for the beam pipe. A plane of this kind has a much higher mechanical stability compared to individual straws. This improves the ruggedness and reduces the load onto the frame, which would be needed to keep individual straws straight enough by tension. The production technology was developed for the straw subsystem of the COMPASS spectrometer [188–190] and used for the different size chambers of the SVD-2 and OKA setups of U-70 accelerator at IHEP (Protvino).

Two straw planes are combined into one double layer and mounted on two carbon bars of the frame, which are transverse to the straws direction, as shown in the left panel in Fig. 5.54. Utilization of the carbon plastic for these bars is preferable over aluminium, because of relatively large temperature expansion coefficient of the latter. Aluminium bars were used for the other direction and as a support of the mother boards, etc. One layer of the straws is shifted by half a diameter with respect to the other in order to resolve the left-right ambiguities. The anode wires of the drift tubes are centered in the straws by two end plugs and one or two small plastic spacers. The diameter of these gold plated tungsten wires is 30 $\mu$m. The straw's ends of a double layer are gas-tight glued on each side of the frame, which serves at the same time as a part of the gas manifolds. The straws are supplied with the counting gas through the end plugs and the gas manifolds.

The length of the straw tubes is affected by humidity. In order to keep the straw tubes straight and exclude any possibility of the straw bending, they can be reinforced by carbon wires like it was done for the ATLAS TRT. But the long straws should be installed into the frame under a small pre tension and kept under low humidity. In order to minimize the effects of humidity, the straw planes will be closed by thin aluminium planes from both module sides to provide the possibility to surround the straws by a dry gas. The additional construction elements will include mother (MB) and termination (TB) boards, which will be located near outer and inner straw ends, respectively. The gas mixture will be 70 % Ar + 30 % $CO_2$, and the gas gain will be $\sim 5 \cdot 10^4$. The average intrinsic spatial resolution of the straw is about 170 $\mu$m.

The schematic view of the ST with three chambers and structure of a straw tube are shown in the left and right panels in Fig. 5.56, respectively. The straws for the prototype are wound from two Kapton film strips. Carbon loaded Kapton film of the 160 XC 370 type from DuPont and aluminized (500 Å) Kapton film of the NH-type will be used as inner and outer strips, respectively. Both films will be covered by a glue layer with thickness of 7 $\mu$m on one their side. The inner diameter of the straws will be 4 mm and the tolerance for diameter was specified to $0 + 30$ $\mu$m. Radiation hardness properties of the Kapton XC had been tested for the COMPASS straw tracker. The aging properties of straws were studied with 26 MeV proton beams from the Munich Tandem accelerator. In addition, the experience of the COMPASS experiment shows the good aging properties of similar straws [191]. During the module assembly some other internal straw components will be required. The gold plated tungsten-rhenium wire of 30 $\mu$m diameter (type 861, Luma) will be used as an anode. The wire under tension of 70 g is fixed by the crimp pins inserted in the polycarbonate end plugs. The diameter of the end plugs is $4.0 \pm 0.018$ mm. In order to decrease the wire displacement due to electrostatic and gravitational forces, spacers will be placed with the distance between them no more than 700 mm. The polycarbonate spacers are produced by the pressure molding. Their design is optimized in order to reduce the insensitive zone. The spacer diameter is $3.97 \pm 0.018$ mm, the length along the anode wire is $\sim 1$ mm, and the mass is 15 mg.

A simplified circuit scheme of one detector channel is shown in Fig. 5.57. The signal readout will be organized from one (outer) end of the tube. In order to avoid the pulse reflections, a proper termination on both ends of anode wire is foreseen. A serial resistor at the amplifier input together with the input resistance of the amplifier should provide the right impedance for the termination on the readout side of a straw. The inner ends will be connected to the TBs, where 100 pF capacitors will be used between anodes and termination resistors of 330 $\Omega$. The TB contains a special pulse line to test the full readout chain. The MBs will feed the anode voltage to and read the information from the straws on both module planes, and will be mounted on aluminium frame elements on the outer side of the chamber, while TBs for the straw anode termination will be mounted on the opposite side. The octagonal shape of the chamber requires several different types of MB. The MB contains also a coupling between straw tubes and amplifiers and HV protection diodes for the amplifier inputs. The MB buses also provide a conductive coupling of the straw cathodes to the appropriate ground buses of FEE. Both MB and TB printed circuits are produced in a multilayer technology.

To achieve the desired tracking performance the readout electronics has to amplify the incoming straw signals and perform the following functions:

- shaping of the amplified signal and removing of the ion tail;

- threshold application to detect MIP with proper spatial resolution and storing the timing information of the accepted signal into a pipeline;

- data gathering and compression from many channels, formation and sending it to the readout buffer.

Some ASIC should provide many channels of amplifier, shaper, discriminator and base line restorer, similar to the 8-channel analogue bipolar one used in ATLAS TRT [192]. The dynamic range for the threshold should be from 2 to 15 fC with a nominal threshold of $\sim 3$ fC (300 eV) and uniformity of $\pm 15$ %. The signal peaking time should be 5—8 ns,

and width at the base — about 35 ns. The input impedance of the amplifier should be about 300 $\Omega$, and cross-talk between neighboring channels — less than 0.5 %.

The straws with inner diameters of 4 and 9.53 mm have been tested in the SPS test beam at CERN, with the same gas mixture (80 % Ar + 20 % $CO_2$) and the gas gain $\sim 7 \cdot 10^4$ for both straw cases. The efficiency was about $\sim$ 98 and 99 % for the 4 and 9.53 mm straws, respectively. Fig. 5.58 shows the typical distribution of the deviations of the measured particle coordinates from those corresponding to the tracks reconstructed using the data from the pad silicon detectors. The spatial resolution for the 4 and 9.53 mm straws as a function of the scaled distance to the anode (normalized to the tube inner radius) is shown in Fig. 5.59. In both cases these dependences can be well described by a single curve ($\chi^2/$n.d.f. $= 0.94$). The observed universality of the dependence makes it possible to predict the coordinate resolution for the straws with different diameters given the operation parameters (gas composition and gas gain) to be similar. This fact also simplifies the track fitting task by providing the error parameterization curve. The spatial resolution varies from $\sim 450$ to $\sim 80 \ \mu$m near the anode and cathode, respectively.

Each ST chamber has two shifted by half diameter the straw layers, so allows one to obtain the single track efficiency for a double layer above 99 %. The double layer arrangement also helps to efficiently combine the radial resolution dependences of two layers. A simple estimate shows that the effective averaged spatial resolution of a two layer chamber will be from 90 to 120 $\mu$m in a wide range of the particle incident angles [187].

## 5.7   Scintillation Fiber Hodoscope detector
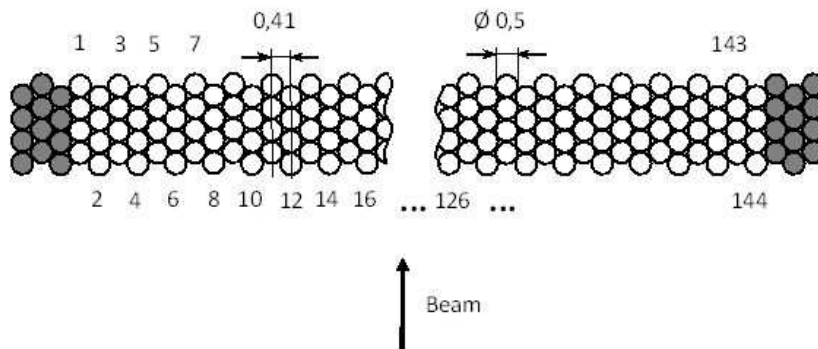


Figure 5.60: Cross section of $60\times60$ mm$^2$ SciFH detectors.
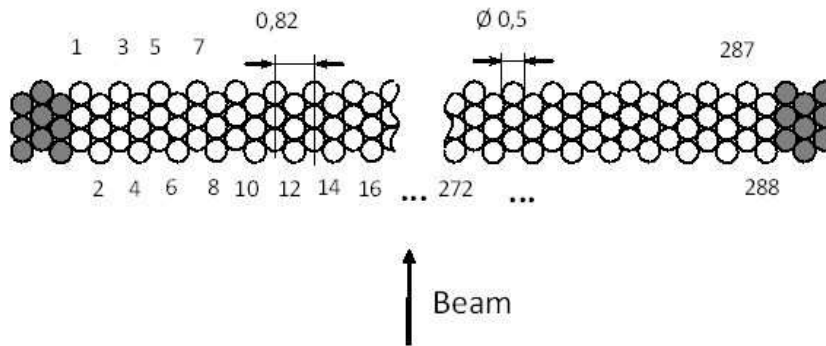


Figure 5.61: Cross section of $120\times120$ mm$^2$ SciFH detectors.

Table 5.8: Short specification of SciFH detectors for BM@N experiment.

| Sensitive area size | $60\times60$ mm$^2$ | $120\times120$ mm$^2$ |
|---|---|---|
| Sensitive part width | 59.1 mm | 118.2 mm |
| Total plane width | 61.6 mm | 120.6 mm |
| Scintillator | SCSF-78M, Kuraray | SCSF-78M, Kuraray |
| Diameter of fibers | 0.5 mm | 0.5 mm |
| Pitch of fiber columns | 0.41 mm | 0.82 mm ($2\times0.41$ mm) |
| Number of fiber columns | 144 | 288 |
| Number of layers | 4 | 3 |
| Thickness | 2.8 mm | 2.1 mm |
| Number of p.e. per MIP | $\sim 20$ | $\sim 15$ |
| Number of planes | 3 $(X, Y, U)$ | 3 $(X, Y, U)$ |

The test beams in 2013—2014 and the first stage of the experiment with low intensity require the use of the tracking detector before the analyzing magnet SP41. For this purpose the scintillation fiber hodoscopes (SciFH) will be used. This part of the tracking system will be based on detectors already used by DIRAC and COMPASS experiments at CERN [193].

Tracking system will contain two sets of SciFH detectors: 3 planes ($X$, $Y$, and $U$) with size of $60\times60$ mm$^2$ and resolution of 0.41 mm and 3 planes — with $120\times120$ mm$^2$ and 0.82 mm. The distance between target and hodoscopes as well as the rotation angle for $U$ plane will be optimized by the simulation.

Hodoscope planes consist of several layers of scintillating fibers with diameter of 0.5 mm, which are placed in parallel closely one to another. To avoid the dead areas between the
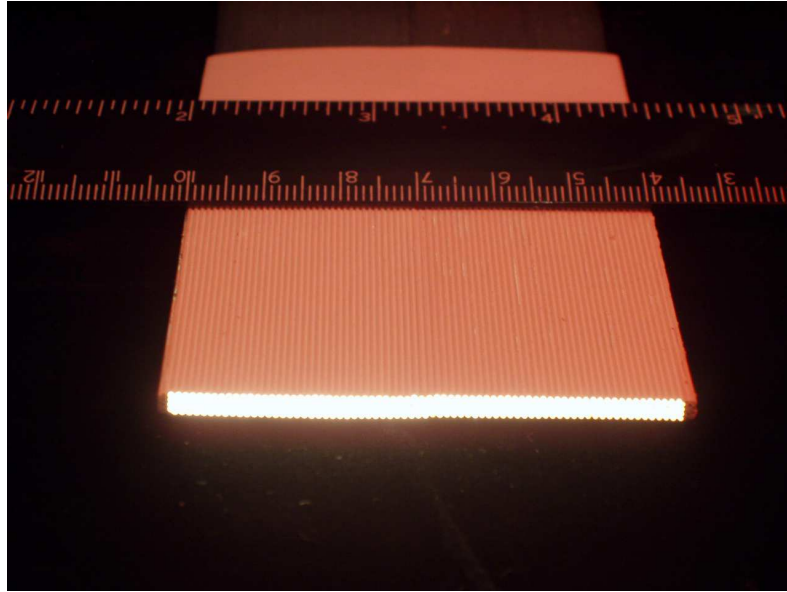
*Figure 5.62: The sensitive part of one SciFH plane.*



*Figure 5.63: Internal part of assembled SciFH detector.*

fibers in detector the pitch of fibers location is less than fiber diameter (detector cross sections are given in Figs. 5.60 and 5.61). The light from all scintillators is transferred via clear fibers with diameter of 0.5 mm to 16-channel multi-anode PMT Hamamatsu H6568 with $4\times4$ pixels of 1 mm$^2$ each. The clear fibers are fixed just opposite the PMT pixels by the special plastic spacers. The view of sensitive part of one SciFH plane is shown in Fig. 5.62. The partially assembled hodoscope is shown in Fig. 5.63. The parameters for SciFH tracker are given in Table 5.8. The total number of electronic channels is 864.

The performance of SciFH detector prototype has been investigated using the Nuclotron internal beam in December 2012. The scheme of this experiment is shown in Fig. 5.64, where $BL$ is the internal beam, $T$ is the multi-fiber carbon target, $S$ are four trigger counters, $H$ is SciFH plane. The fibers in SciFH were directed horizontally. The VME-based data acquisition system was used for the data taking from the scintillation detectors. TQDC-16 module [218] developed at LHEP JINR allows one to measure both amplitude and time appearance of each signal simultaneously. The timing and amplitude of the trigger counters
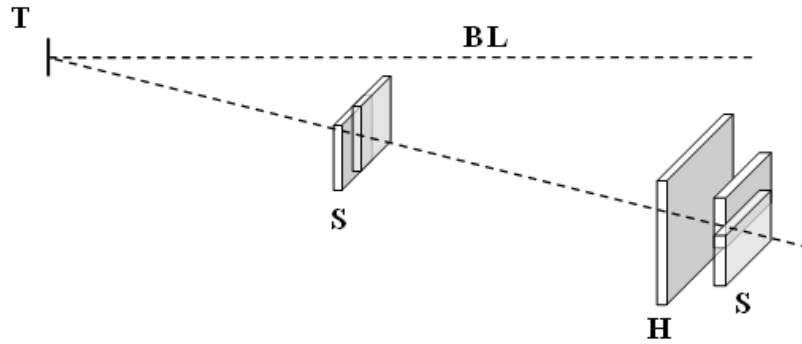
*Figure 5.64: The scheme of the test beam for SciFH prototype at internal target station of Nuclotron. $BL$ is the internal beam, $T$ is the carbon target, $S$ are four trigger counters, $H$ is SciFH.*
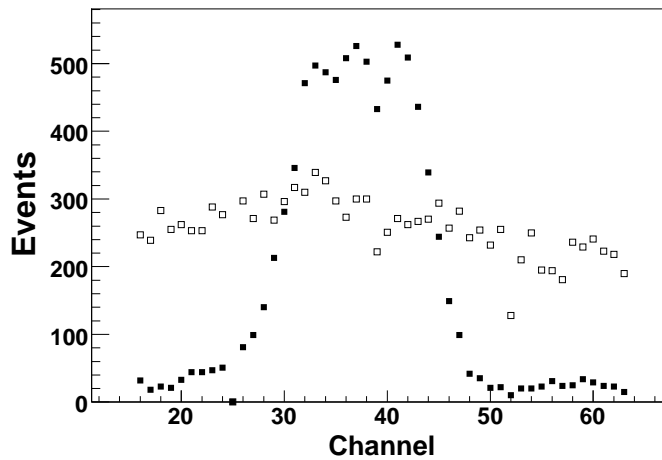


*Figure 5.65: The SciFH prototype efficiency: with (full symbols) and without (open ones) requirement of the trigger counters signals coincidence.*

signals were used to select MIPs and to estimate the timing resolution of the investigated SciFH prototype.

The results of the efficiency measurement of the SciFH prototype are presented in Fig. 5.65. The results with and without requirement of the trigger counters signals coincidence are represented by the full and open symbols, respectively. One can see rather good performance of the SciFH prototype as a tracking detector. The amplitude and timing data for one of the scintillation fibers are presented in the left and right panels in Fig. 5.66, respectively. The expected timing resolution for single scintillation fiber (without amplitude correction) is about 0.5 ns.
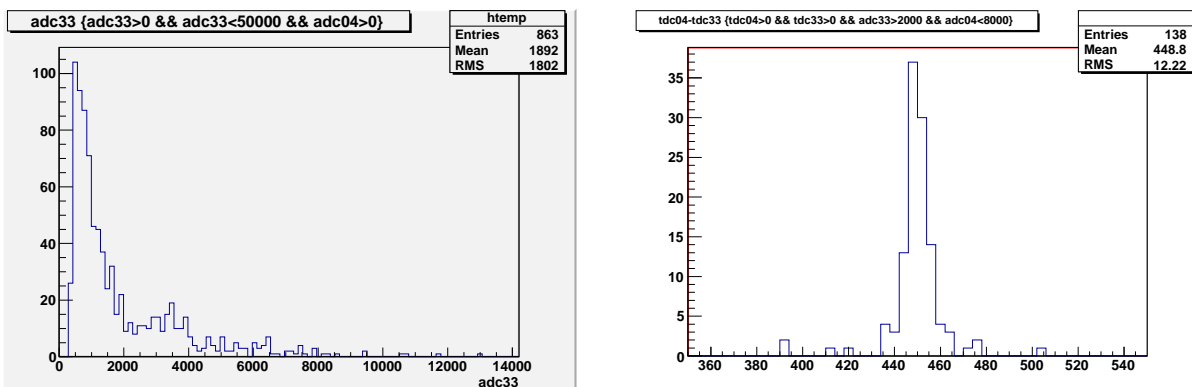


*Figure 5.66: The amplitude (left) and timing resolution (right) for one scintillation fiber.*

## 5.8 Zero Degree Calorimeter

### 5.8.1 Centrality determination using ZDC
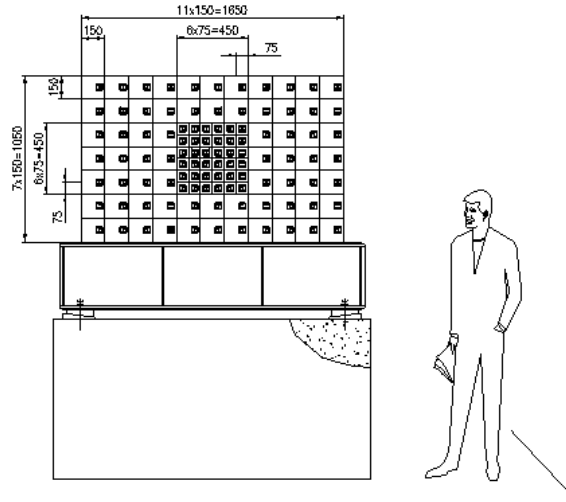


*Figure 5.67: Schematic view of ZDC consisting of 104 modules. Central part contains 6×6 modules of 7.5×7.5 cm² transversal size, peripheral part — 68 modules of 15×15 cm² transversal size.*
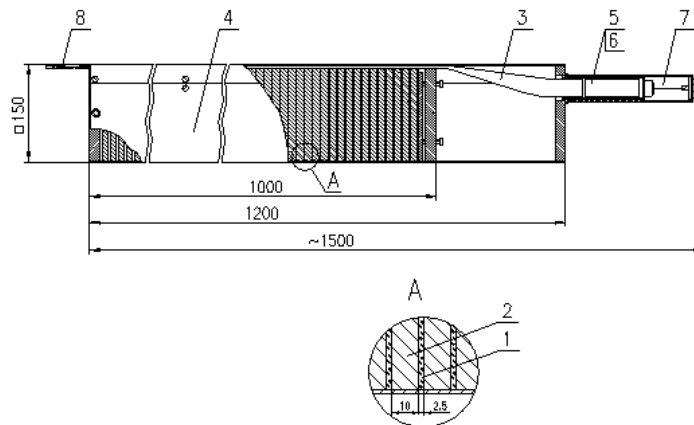


*Figure 5.68: Schematic structure of the 15×15 cm² ZDC module: 1/2 — 80 scintillator/lead sandwiches of 142×146 mm² with 2.5/10 mm thickness, 3 — wave-length-shifting (WLS) light guide (LG), 4 — metal (iron) rectangular container, 5 — FEU-84 PMT, 6 — μ-metal PMT shield against the magnetic field, 7 — PMT high voltage (HV) base and divider, 8 — optical connector and fiber bringing the LED signals to the PMT.*

In research of properties of a hadron matter in collisions of relativistic nucleus an important task is selection of events on basis of centrality parameter, as for the trigger organization on the central events, and also for studying the properties of a hadron matter depending on this parameter. The concept of centrality is based on use of the impact parameter value, which is possible to define as distance between centers of nucleus in the plane perpendicular to the direction of a beam. Because the impact parameter is not a measurable value, we need to use one of the related characteristics of collision, e.g. the part of a total energy, which is carried away by spectators — protons, neutrons and nuclear fragments. Most of spectators has a small transversal momentum and is emitted in a narrow

*Figure 5.69: The picture of the WA98 calorimeter transported from CERN.*

angle range near the beam direction. To measure the spectators energy the calorimeter at zero angle, so-called ZDC, is used.

One of the main characteristics of ZDC is the average part of the total spectators energy registered in the calorimeter related to the total spectators energy. With this part increasing the events classification by centrality appear more reliable. Other important ZDC characteristic is the energy resolution. The calorimeter provided error in measurement of the total spectators energy should be less, than average fluctuations of the spectators energy for the central collisions. Thus, angular acceptance (actually cross-section size) and energy resolution should provide high efficiency of events selection on basis of the centrality.
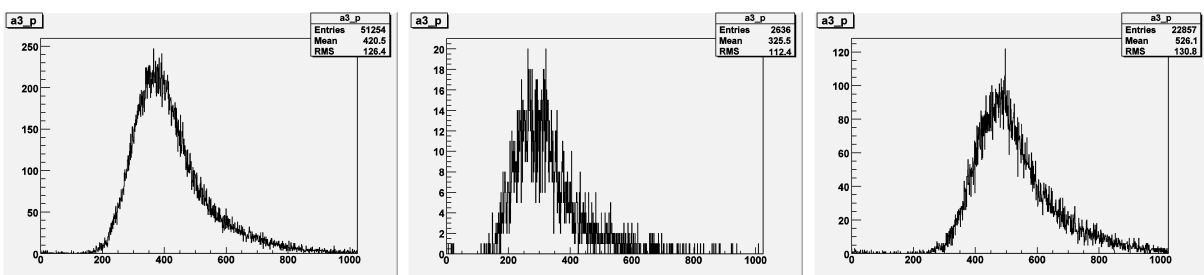


*Figure 5.70: The light output measurements for the scintillator plates: scintillator from ZDC periphery (left) and ZDC center (middle), new (reference) scintillator (right).*

*Table 5.9: Results of the light output measurements for 3 scintillators.*

| Scintillator | Scintillator from ZDC periphery | Scintillator from ZDC center | Reference scintillator |
|---|---|---|---|
| ADC channels | 420.5 | 325.5 | 526.1 |
| Coefficient | 0.8 | 0.62 | 1.0 |
| Number of p.e./mm | 10.6 | 8.2 | 13.2 |
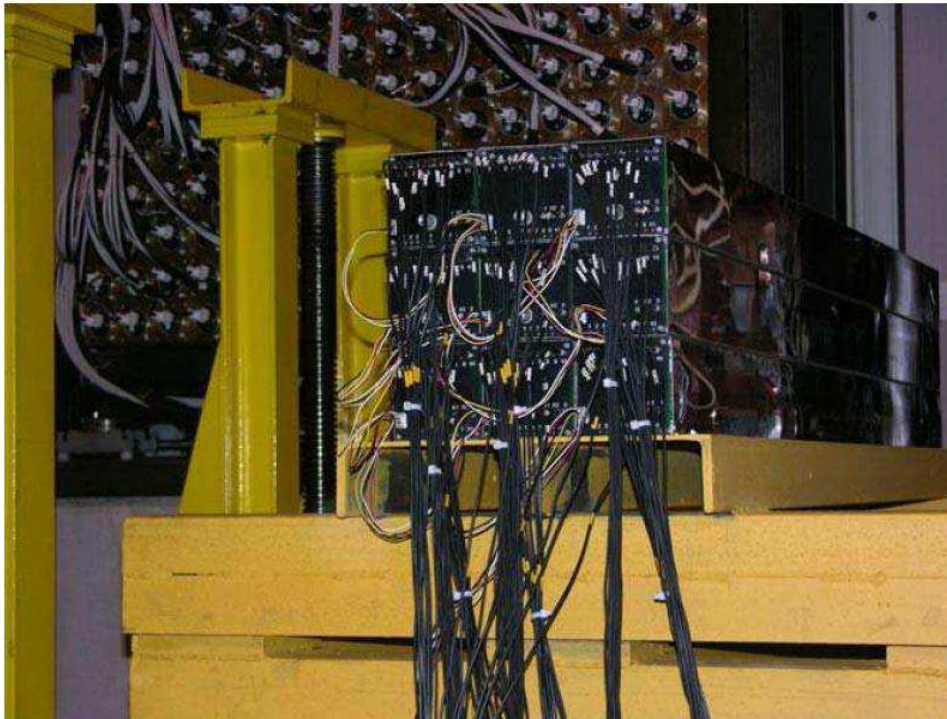


*Figure 5.71: The view of the nine modules of the PSD prototype [156].*

## 5.8.2 ZDC options

Main ZDC option for first stage of the experiment is shown in Fig. 5.67. It will be based on the COMPASS (WA98) $HCAL$ type hadron calorimeter [194]. The ZDC modules are stacked in an array of $11 \times 7$ modules of $15 \times 15$ cm$^2$ and with a central part consists of an array of $6 \times 6$ modules of $7.5 \times 7.5$ cm$^2$. This granularity allows one to operate with the nuclear beam intensities up to 1 MHz, which is sufficient for the first stage of the experiment. For the beam intensity of 10 MHz it will be necessary to remove several central blocks.

The ZDC module consists of 80 scintillator/lead layers with the sampling structure of 1/4. This sampling is optimal to obtain the $e/\pi$ and $e/$p ratios close to 1 and the good energy resolution for all particles in the energy range of 2—100 GeV with $\sigma_E/E \sim 50/\sqrt{E}$ % $\cdot$ GeV$^{-1/2}$. The results of the experiment at Nuclotron with the use of $^6$Li beam shown the same energy resolution for nucleons [195]. Schematic structure of the large ($15 \times 15$ cm$^2$) ZDC module is shown in Fig. 5.68.

The calorimeter time resolutions is close to 1 ns and allows one to use ZDC signal in the fast trigger logic. Calorimeter absorption length is equal about five nuclear interaction lengths. It consists of 80 cm of lead and 7 cm of iron corresponding to 4.6 and 0.4 nuclear interaction lengths, respectively. Scintillator plates are manufactured using the method of molding under pressure from the granulated polystyrene PSM-115. The additives composition is P-terphenyl of 1.5 % and POPOP of 0.05 %. For each module the light is collected
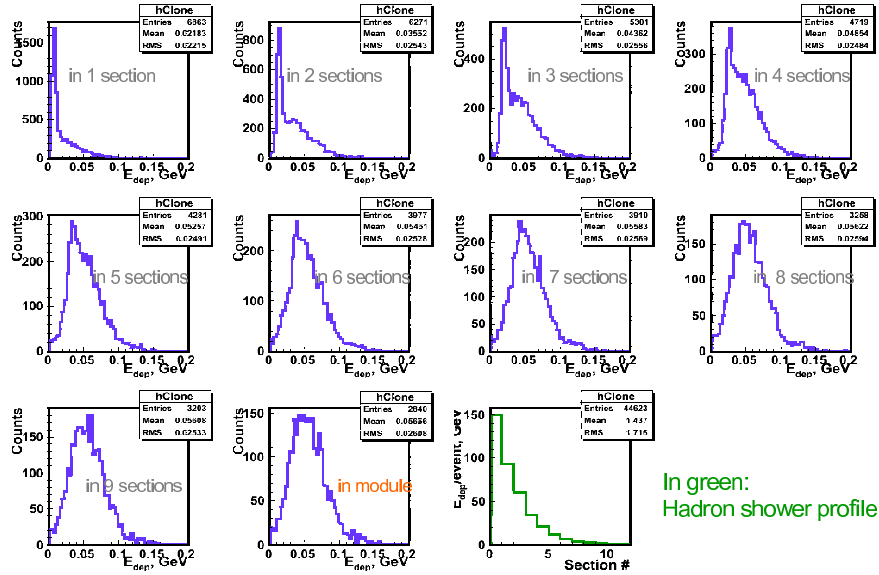
Figure 5.72: *The energy deposition in* 1, 1+2, ..., 1+2+...+10 *sections and the hadronic shower profile obtained for 3 GeV/c incident protons.*
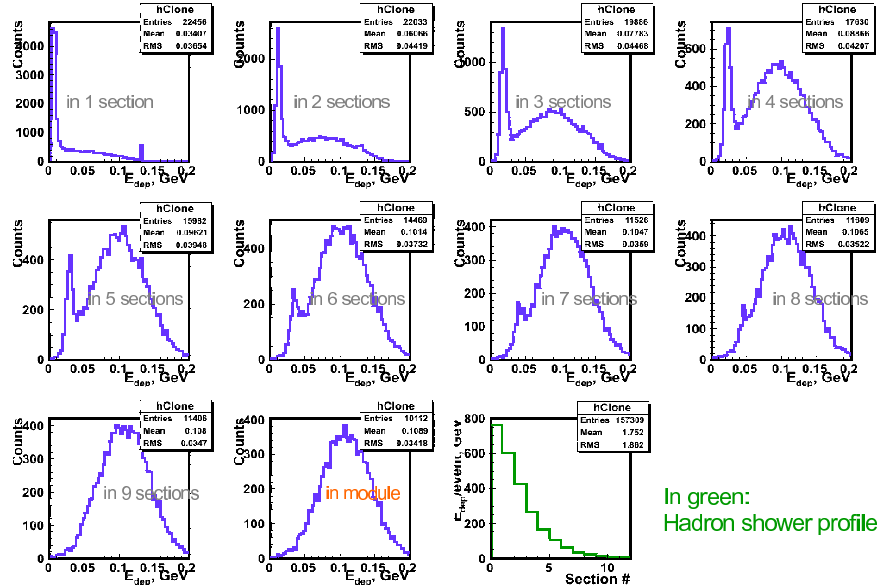


Figure 5.73: *The energy deposition in* 1, 1+2, ..., 1+2+...+10 *sections and the hadronic shower profile obtained for 6 GeV/c incident protons.*

from the side by the fast wavelength shifter (WLS) plate coupled to the PMT with an active base. The WLS is manufactured from the optical organic glass (PMMA — polymethylmethacrylate) with the surface painted by coumarin K-7 dissolved in the ethanol at 600°C. The deepness of K-7 diffusion has varied in range of 5—15 $\mu$m. It allows one to obtain the good light collection uniformity along the WLS length (1 m) with the attenuation length larger than 3 m. One optical cable is used to feed each PMT by the LED light. This light is emitted by one super-bright LED for all 104 cells to control the calorimeter stability during the long run time. The FEU-84A is used as the PMT for light detection in the wavelength range of 400—600 nm. It has bi-alkaline photocathode green extended to be close to WLS emitted light of 520 nm. High voltage (HV) base is the active Cockcroft-Walton voltage multiplier, which allows one to take PMT current with the high beam intensities up to 1 MHz. The HV is controlled by PC using single PCI card and a distributer unit placed near the calorimeter.

The parts of WA98 hadron calorimeter transported from CERN in October 2012 will be
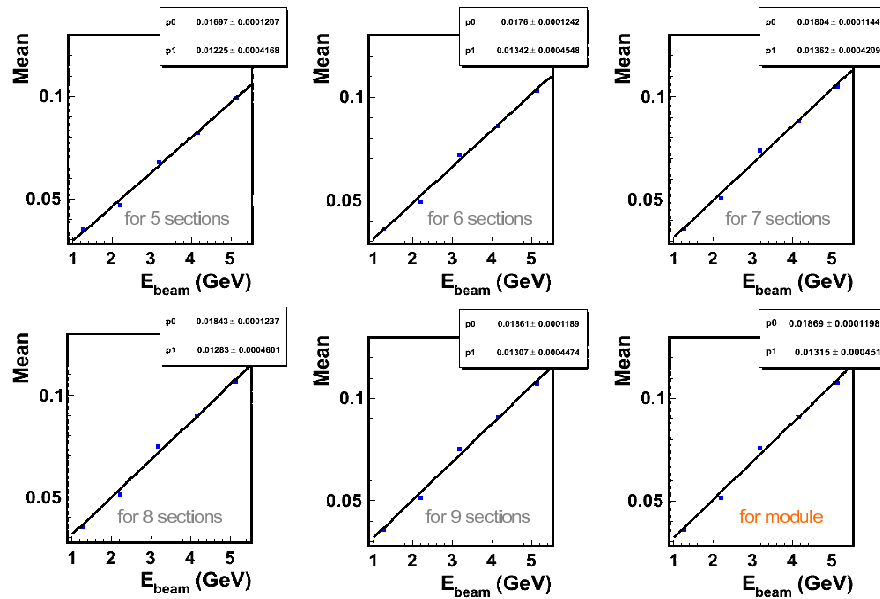
Figure 5.74: The energy response to incident protons for different number of sections.
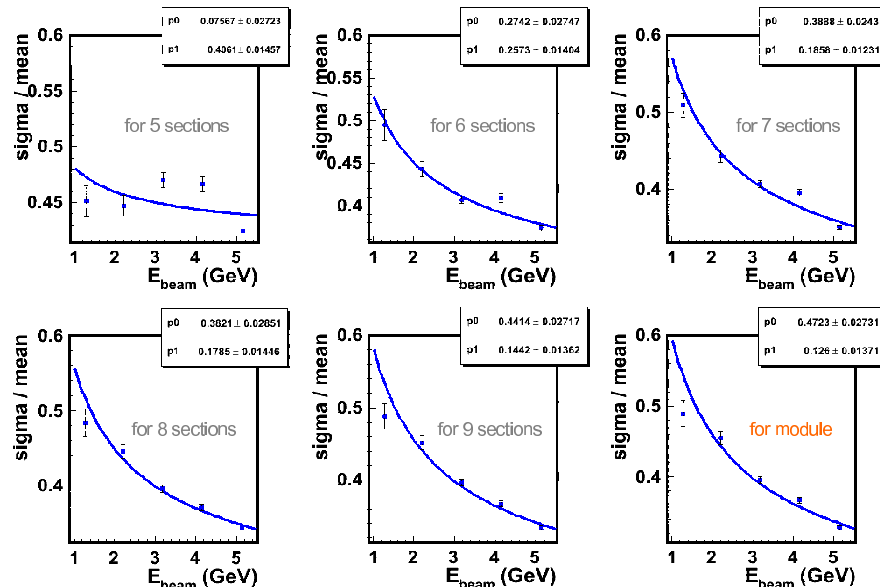


Figure 5.75: The energy resolution for different number of sections as function of the incident proton energy.

used for assembling of ZDC. The view of the WA98 calorimeter in 205 building is presented in Fig. 5.69.

Unfortunately, the light output from scintillators used in the WA98 calorimeter is decreased due to radiation damage. Also the light outputs for the scintillators taken from the center and periphery of the WA98 calorimeter are different. The measurements were performed using light guide $20\times150$ mm$^2$ and FEU-85 PMT. The LeCroy-2249A ADC has been previously calibrated using photo-diode, the bin width is equals to 0.46 p.e. The results of the measurements are presented in Fig. 5.70 and in Table 5.9. The light output is decreased for $\sim 20$ % and $\sim 40$ % for the periphery and center of the WA98 ZDC.

Another ZDC option is the use of Projectile Spectator Detector (PSD) [156] developed for NA61 experiment. This hadron calorimeter consists of lead/scintillator sandwich modules with the sampling satisfying the compensating condition. The light from the individual scintillator tiles is captured and transported with the WLS-fibers embedded in the scintillator

and extended along the lateral side to the rear end of the module. The WLS-fibers from the neighboring tiles is grouped in one bundle and viewed by a $3\times3$ mm$^2$ avalanche micro-pixel photo-diode. The construction ensures a longitudinal segmentation of the module in 10 independent sections. The results of beam tests of the calorimeter prototype are presented. The energy resolution about $50/\sqrt{E}$ % $\cdot$ GeV$^{-1/2}$ was obtained for the PSD prototype [156]. The nine modules of PSD prototype are shown in Fig. 5.71.

### 5.8.3   Response to protons at Nuclotron energies

The performance of PSD for protons at low energies has been studied at T10 PS beam line at CERN in 2012. The measurements with $20\times20$ cm$^2$ module segmented into 10 sections were performed for few proton momenta between 2 GeV/c and 6 GeV/c. The significant key of these measurements is the possibility to study the longitudinal development of hadronic shower at low projectile energies.

The results of the energy deposition in 1, 1+2, $1+2+\ldots+10$ sections and the hadron shower profile obtained for 3 GeV/c and 6 GeV/c incident protons are presented in Figs. 5.72 and 5.73, respectively. As one can see, the hadronic shower is more developed with the increasing of the proton energy. The longitudinal profiles for protons have the maximum energy depositions in the first section for proton momentum 3 GeV/c.

The energy response of PSD with different number of sections used for the energy calculation as a function of the incident proton energy is shown in Fig. 5.74. One can see a good linearity starting from the five sections of the energy summing.

The PSD energy resolution for different number of sections used for the energy calculation as a function of the incident proton energy is shown in Fig. 5.75. The energy resolution obtained for a whole module is in the good agreement with the previous measurements of PSD module at higher energies.

## 5.9   Forward Wall detector
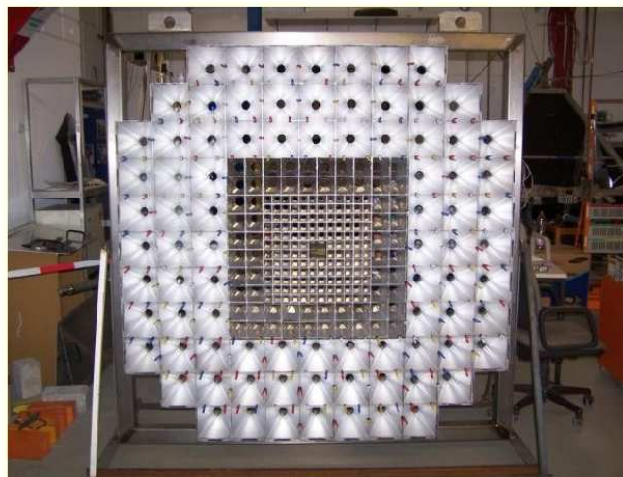


*Figure 5.76: The HADES Forward Wall (FW) consisting of the scintillation counters.*

The measurements of flows, global polarizations of the hyperons, etc. in the semi-central events require the precise reconstruction of the reaction plane. Apart from ZDC one of the devices, which is widely used for this purpose is so called Forward Wall detector. It allows
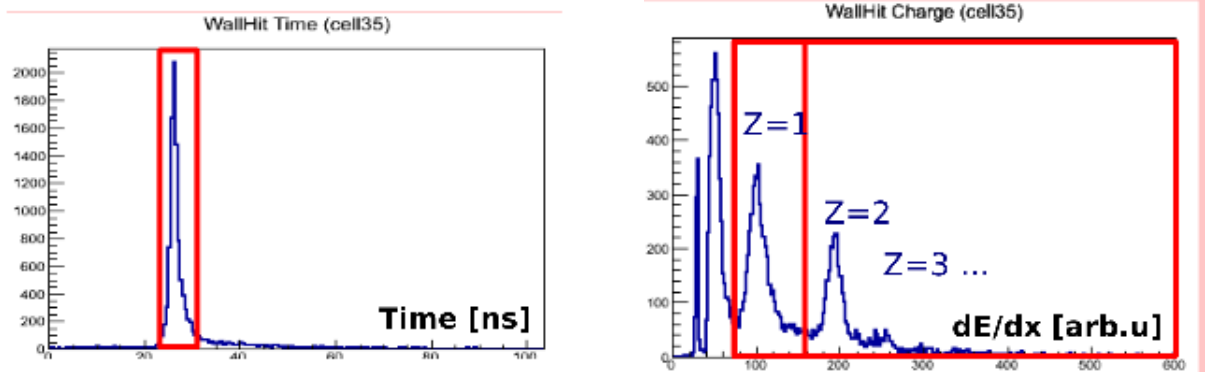
*Figure 5.77: Time-of-flight of the fragments detected in FW cell (left); the signal amplitude of the detected fragments (right). The prompt windows correspond to the spectator selection.*
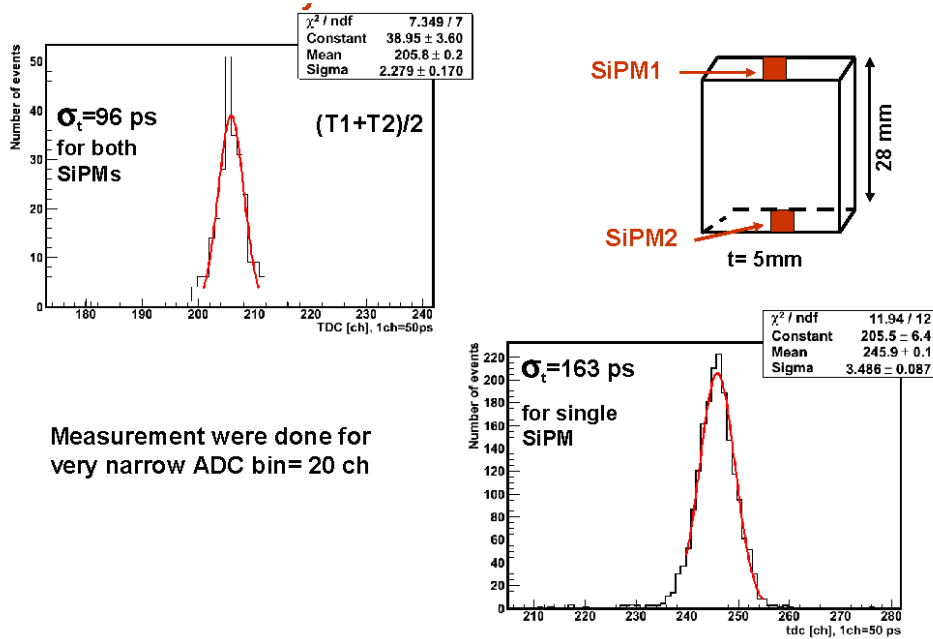


*Figure 5.78: The timing resolution obtained with SiPM KETEK PM3350 for $28 \times 28 \times 5$ mm$^3$ scintillator.*

one to detect the spectators and fragments. The picture of the HADES Forward Wall is presented in Fig. 5.76. It consists of 140 small $4 \times 4$ cm$^2$, 64 middle $8 \times 8$ cm$^2$, and 84 large $16 \times 16$ cm$^2$ scintillation plates coupled with PMTs covering the polar angle of $0° \leq \theta \leq 2°$, $2° \leq \theta \leq 3.3°$, and $3.3° \leq \theta \leq 7.2°$, respectively. Reaction plane vector $\vec{Q}$ is defined as

$$\vec{Q} = \sum_{i=1}^{N_{\text{sp}}} w_i \frac{\vec{r_i}}{|\vec{r_i}|} \ , \tag{5.4}$$

where $N_{\text{sp}}$ is the number of detected spectator fragments, $w_i$ is the weight number ($w_i \geq 0$ and $w_i \leq 0$ if flying forward and backward, respectively), and $\vec{r_i}$ is the position vector of the cell with $i$-th hit. The selection of the fragments requires to measure the time-of-flight and the signal amplitude from the scintillator. The time-of-flight and signal amplitude spectra for the detected fragments are shown in the left and right panels in Fig. 5.77, respectively. The prompt windows correspond to the spectator selection. The amplitude spectrum clearly demonstrates the presence of the fragments with $Z = 2$ and $Z = 3$. Finally, the resolution of the reaction plane reconstruction is about 40°—45° (RMS).

One of the option for the BM@N Forward Wall can be an array of scintillators placed in
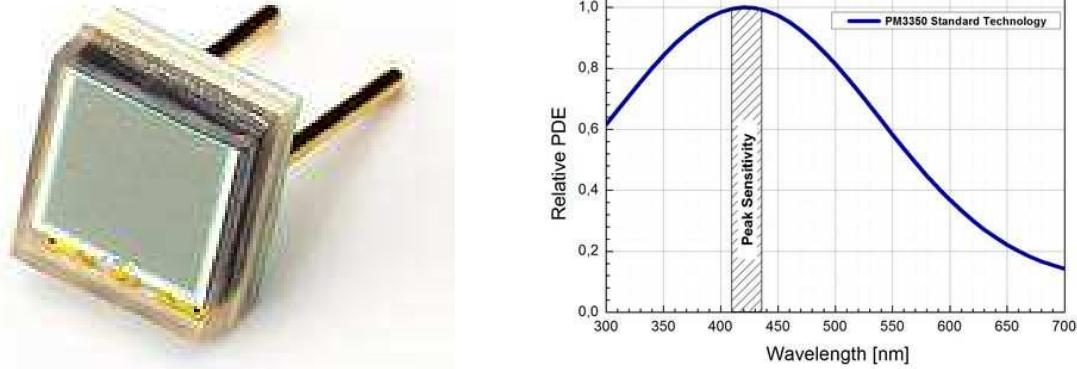
*Figure 5.79: The SiPM KETEK PM3350 (left); the quantum efficiency of PM3350 as a function of the light wavelength (right).*

front of ZDC and using the light collection by SiPM. The results of the test beam performed at CERN in 2012 for the scintillator with size of $28 \times 28 \times 5$ mm$^3$ read by two KETEK PM3350 ($3 \times 3$ mm$^2$) is shown in Fig. 5.78. The combining of the information from two SiPM allows one to reach the timing resolution of about 100 ps for narrow range of the signal amplitude. The modern version of the KETEK PM3350 has even larger quantum efficiency ($\geq$ 40—50 %) at 420 nm (see Fig. 5.79), therefore, one can expect even better timing resolution.

## 5.10   Electromagnetic calorimeters
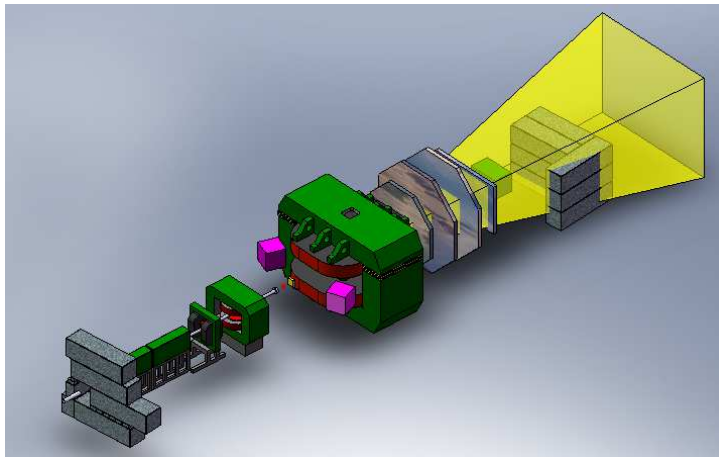


*Figure 5.80: The scheme of the experiments with ECAL for detection of hard photon, $\pi^0$ and $\eta$ mesons.*

Electromagnetic probes, such as real and virtual photons (i.e. di-leptons), provide key information on temperature and system size at the early stage of collision as well as on temperature evolution of the system from its formation to thermal freeze-out. Created over the course of the entire space-time evolution of the system, once emitted, they escape from the strongly interacting medium without any final-state interaction. Information on the direct thermal radiation (photons or di-leptons) can be used to derive a limit on the initial temperature of the quark-gluon plasma created in heavy-ion collisions.

The primary role of the electromagnetic calorimeter is to measure the spatial position and energy of electrons and photons produced in collisions. As one of the possible task is the measurements of $\pi^0$ and $\eta$ mesons, which have the branching ratio of the decay into $2\gamma$
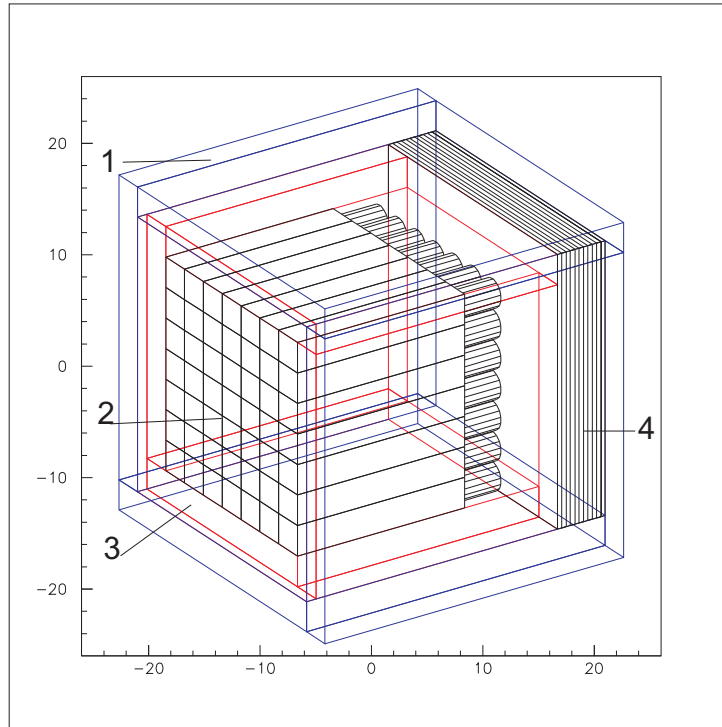
Figure 5.81: The scheme of ECAL for the soft photon registration: 1 — protection, 2 — BGO crystals, 3 — the lateral veto detector, 4 — the backward veto detector.
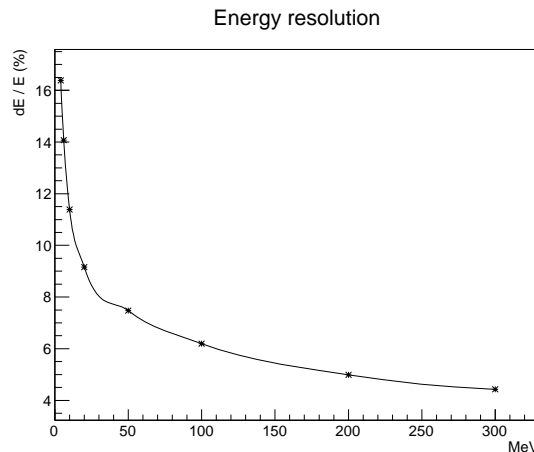


Figure 5.82: The energy resolution versus the hit photon energy.

of 100 % and 39 %, respectively. Also the hard photons can be detected and used as the trigger signal for the observables measured by the spectrometer. In this scheme the target is placed 3—4 m upstream the analyzing magnet SP41 and two arrays of the photon detectors are used to detect photons (see Fig. 5.80).

For BM@N we consider several options of the electromagnetic calorimeters.

## 5.10.1 BGO calorimeter

BGO calorimeter is prepared for the studies of the soft photon yield from hadron and nuclear interactions in SVD-2 experiment at U-70 and in BM@N experiment at Nuclotron.

A specific feature of the proposed photon detector is its capability to measure low energy deposition $E_{thresh.} \leq 5$ MeV. The good option for such ECAL is the BGO crystals using. The dimension of the one cell should be $\simeq 3 \times 3 \times 180$ cm$^3$. In this case the spatial localization of a photon equals to 5 cm. One should take into account the transverse dimension of
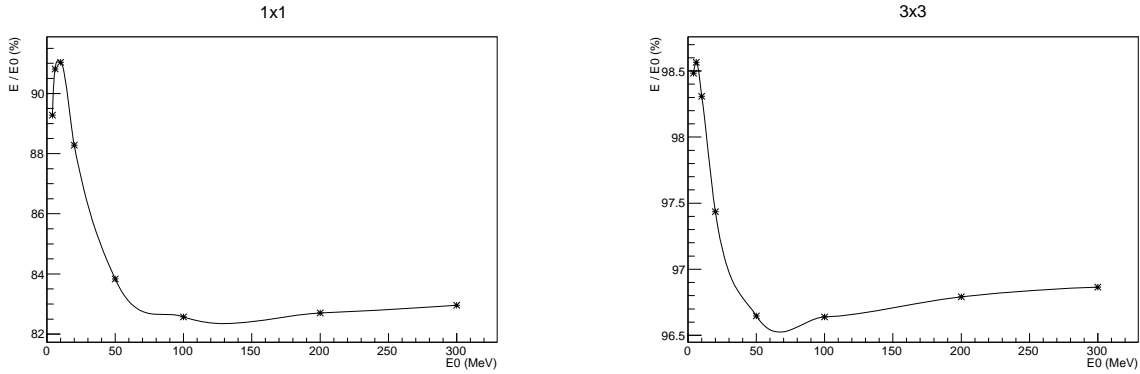
*Figure 5.83: The ratio of the collected energy to the hit photon energy (in percents): in the single crystal (left) and in the 3×3 crystals array (right).*
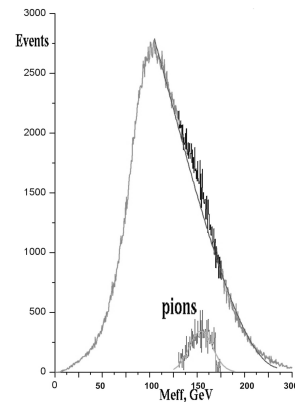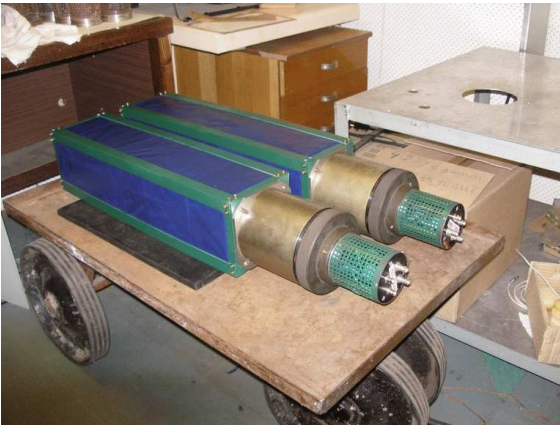


*Figure 5.84: Two SCG1 based photon detectors (left); the effective mass spectrum of two detected photons obtained in 2 GeV d+C collisions at the internal target of Nuclotron in 2010 (right).*

the photon shower $\sim$ 5 cm. From this very qualitative consideration one can conclude that transverse dimensions of a calorimeter should be $\sim 30 \times 30$ cm$^2$. Four central cells with a total area of 10 cm$^2$ will provide a high efficiency of the photon detection. The longitudinal dimension should be as usual $\sim$ 16 radiation lengths. For BGO crystals it equals to $\sim$ 18 cm. The important problem is to take into account the dissipated particles background in the experimental hall. Reduction of background may be provided by the calorimeter preshower.

The calorimeter is matrix consisting of $7 \times 7 = 49$ BGO scintillators each with cross section of $30 \times 30$ mm$^2$ and length of 180 mm (16 radiation lengths). The square aperture of central part is 441 cm$^2$. At the photon energy of $\sim$ 20 MeV the shower made by $\gamma$-quantum is spread on the 2—3 neighbour elements (Moliere radius is 2.3 cm). This gives additional information for its identification and the coordinate definition of hitting into ECAL. Veto-counters are manufactured from plastic scintillators. The scintillators surround the central area from one side and have the thickness of 1 cm. Signals of the veto-counters are included in the anti-coincidence with the central area (BGO) signals. The backplane of the calorimeter consisted of six plastic scintillators with the thickness of 4 mm and five layers of lead each of 5 mm. The aperture of ECAL is covered by the plastic scintillator with 1 cm thickness to exclude the loading by charged particles incoming from the target. ECAL on all sides except the front aperture is surrounded by the lead plates with 3 cm thickness (5.5 radiation lengths). This must reduce the background loading of device.

The Monte-Carlo simulation of ECAL performance was carried out using the GEANT4
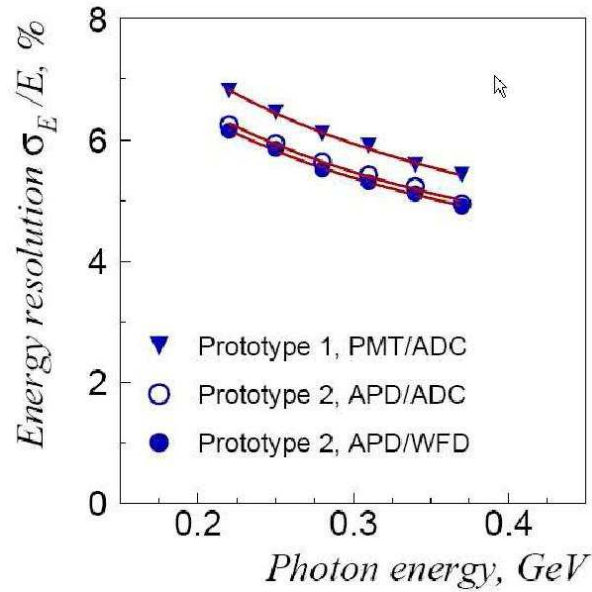
*Figure 5.85: Energy resolution of the "shashlyk" type electromagnetic calorimeter measured in the beam test.*
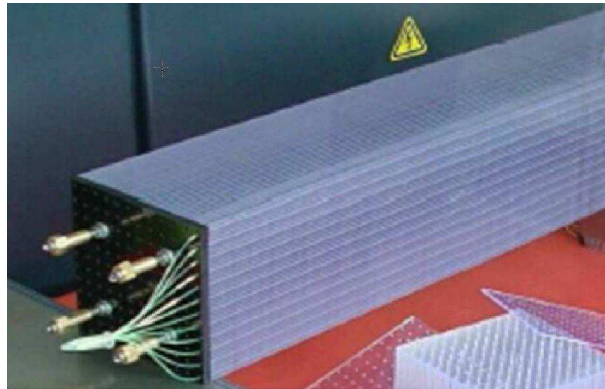


*Figure 5.86: The prototype of "shashlyk" type electromagnetic calorimeter for MPD [200].*

(version 4.9.5.1) package. The every ECAL crystal was hit by the $\gamma$ with the following energies: 4, 6, 10, 20, 50, 100, 200, 300 MeV. The detailed structure of the detector is shown in Fig. 5.81.

The energy resolution as a function of the hit photon energy is presented in Fig. 5.82. The ratios of the collected energy to the hit photon energy for single crystal and $3\times3$ crystals array are shown in the left and right panels of Fig. 5.83, respectively. One can see that more than 95 % of deposited energy is registered in the $3\times3$ crystals array for very wide energy range.

The measurements of soft photons with the BGO ECAL can be performed even at the stage 1 of the BM@N setup.

## 5.10.2 Lead Glass calorimeter

The simplest way to detect $\pi^0$ and $\eta$ mesons is the use of 2-arm photon detector with quite large acceptance. This can be usual lead glass based electromagnetic calorimeter. One of the option is to use SCG1 scintillation glass blocks from PINOT electromagnetic calorimeter [196]. The parameters of the SCG1 scintillation glass are the following: $X_0 = 4.25$ cm, $\tau = 80$ ns. The main difference of the SCG1 from the usual lead glass is that photons with the energy larger than 15 MeV can be detected. The energy resolution for the single photon
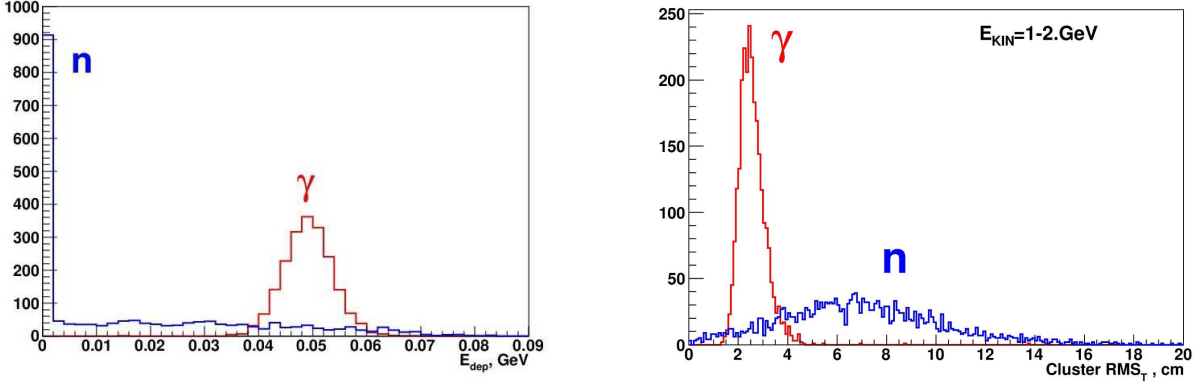
*Figure 5.87: The distribution of total energy deposition in scintillator for neutrons with $T_{\text{kin}} = 200$ MeV and photons with the same energy (left); RMS distribution for photon and neutron clusters, produced by particles with kinetic energy of $1 \leq T_{\text{kin}} \leq 2$ GeV (right).*

was $\sigma_\gamma = 0.8/\sqrt{E}$ MeV$^{-1/2}$.

The PINOT spectrometer consisted of 30 SCG1 modules of $15 \times 15$ cm$^2$ cross section and $14X_0$ thickness viewed by the R1512 PMT. Two of these modules presented in the left panel of Fig. 5.84 have been tested using the internal target of Nuclotron to detect $\pi^0$ from d+C collisions at 2 GeV. The effective mass spectrum of two detected photons is shown in the right panel of Fig. 5.84. One can see a good selection of $\pi^0$.

### 5.10.3   "Shashlyk" electromagnetic calorimeter

The Pb-scintillator electromagnetic calorimeter of the "shashlyk" type can be used in BM@N experiment being placed in front of ZDC. Such calorimeters were used previously by PHENIX [197], KOPIO [198], LHCb [199], etc. Such calorimeter is planned of MPD [200]. Calorimeters of this type are relatively not expensive, radiation hard, robust in design, and provide energy resolution $\sim 3\,\%/\sqrt{E}$. Spatial resolution of such calorimeters is determined by the optical segmentation and can be easily adjusted to requirements of the experiment. The prototypes of the "shashlyk" type calorimeters were extensively studied by several collaborations. As an example, the energy resolution measured in KOPIO experiment for various read-outs is shown in Fig. 5.85. A quadratic fit to these experimental data gives

$$\sigma_E/E = (1.91 \pm 0.1)\% \otimes (2.74 \pm 0.05)\%/\sqrt{E(\text{GeV})} \ , \tag{5.5}$$

where $\otimes$ means quadratic summation. The relatively large constant term of 2 % may be decreased by increasing the length of the module. However, this term is not essential for the photon energy range of 50—1000 MeV. The prototype of the "shashlyk" calorimeter module for MPD [200] is shown in Fig. 5.86. Such detectors can be used as a basic version for BM@N electromagnetic calorimeter with large aperture.

#### 5.10.3.1   Photo-detector

The micropixel avalanche photodiode (MAPD), which is a novel photo-detector with a multipixel intrinsic structure on a common silicon substrate is one of the best candidate to detect photons. An advanced version of MAPD with a deep micro-well for charge collection has density of pixels over $10^4$ mm$^{-2}$ [201]. Each independent avalanche region (vertical channels) with individual micro-wells for charge trapping/collection is created at a depth of about 3—5 $\mu$m using a special distribution of the inner electric field. Charge collection

in individual micro-wells provides the local self-quenching of avalanche processes in the MAPD.

Each pixel works as an independent photon micro-counter working in the Geiger mode on a common load. Actually, each pixel operates digitally (yes/no) in response to an incident photon, but the MAPD in whole is an analogue device, which can measure light intensity within the dynamic range corresponding to the total number of pixels.

The required design parameters of the calorimeter determine requirements also to the photo-detectors: they have to be compact, insensitive to magnetic field and have large dynamic range and linearity in measuring particles energy. Deep micro-well MAPD matches these requirements exactly. The present 3.3 mm$^2$ MAPDs can be easily used for the light detection from 9 fibers of a "shashlyk" calorimeter single tower.

### 5.10.3.2  Calibration and monitoring

In order to keep the energy and space resolution of the photo-detector at the required level, the detectors and read-out electronics have to be calibrated and monitored. Each detector will be calibrated before installation with a relatively low energy (of hundred MeV) electron test beam at several electron energies. Additional in situ calibration will be done during the data taking using the amplitude spectra from each detector. The truncated mean of the amplitude spectrum of each channel can be used for relative calibration, and the $\pi^0$ and $\eta$ peak positions — for absolute calibration. The same procedure will be applied to the SCG1 calorimeter.

Monitoring will be carried out permanently during the data taking. The following values will be monitored:

- The temperature of the MAPD photo-detectors with a 0.1°C accuracy. One measurement per module (about 20 detectors).

- The gain of the read-out electronics. For this purpose each preamplifier will have a calibration input. One measurement per channel.

- Transparency of the scintillator and their optical contacts with photo-detectors. This value will be monitored by calculating the truncated mean of the spectrum of each module for a certain time (typically 5—20 minutes) and compared with previous measurements. One value per detector.

- Light emitted by the LED or laser in each detector will be used for continuous calibration of the full chain.

### 5.10.3.3  Read-out electronics

The read-out electronics must be capable of measuring energies with a digitization uncertainty of 0.5 MeV in a dynamic range of 50—5000 MeV, and the time of arrival with respect to the common start with an uncertainty of the order of hundred picoseconds. Operation of this read-out electronics is required to be completely pipe-lined without dead time. To meet these performance requirements for energy and timing resolution, front-end electronics based on the sampling ADCs was built and tested (see section 5.10.3.4). All the above results were obtained with this electronics. This kind of read-out fully satisfies the needs of the device. Alternatives to the read-out electronics for the calorimeter are under study.

### 5.10.3.4   Neutrons identification

Possibility of neutrons registration by electromagnetic calorimeter was studied by MPD collaboration [200] using Monte-Carlo simulation based on GEANT4 package. Response of the calorimeter with sampling of 0.5 mm lead + 1.5 mm scintillator (170 layers) on neutrons with kinetic energy in the range of 50—1000 MeV has been simulated. Total thickness $H$ of the calorimeter is 34 cm ($16X_0$ or $0.8\lambda_I$). Cell size is $4\times4$ cm$^2$. Energy reconstruction has been simulated in assumption that energy deposition in the calorimeter is proportional to the energy deposition in the layers of scintillator. All the effects related with scintillation, light collection and transportation, efficiency of PMTs and performance of electronics have been neglected. To simulate realistic time shape of the signal (the physical part of it) one has supposed that the effective speed of light in optic fibers is 0.15 m/ns. Particle has been considered as detected if it produced cluster with energy of $\geq 30$ MeV (corresponding energy deposition in the scintillator is 7.5 MeV). The efficiency of neutron registration is practically independent on neutron energy and is about 50 % at $T_{kin} \geq 100$ MeV.

The distribution of total energy deposition in scintillator for neutrons with $T_{kin} = 200$ MeV and photons with the same energy is presented in the left panel in Fig. 5.87. As far as photon and neutron are neutral particles, they can be distinguished only on the base of calorimeter information. Usage of the calorimeter as time-of-flight detector provides possibility to separate neutrons and photons (measurement of $\beta$) and to measure the momentum of neutrons. In relativistic case separation of photons and neutrons can be performed using information about cluster shape. The RMS value, which characterizes spatial energy distribution in cluster, can be used to separate photons and neutrons with kinetic energy of $\geq 1$ GeV as shown in the right panel in Fig. 5.87.

The use of BGO, SCG1 and wide-aperture "shashlyk" type electromagnetic calorimeter can significantly enrich the physics program at BM@N setup.

## 5.11   Small Aperture Silicon Tracking System
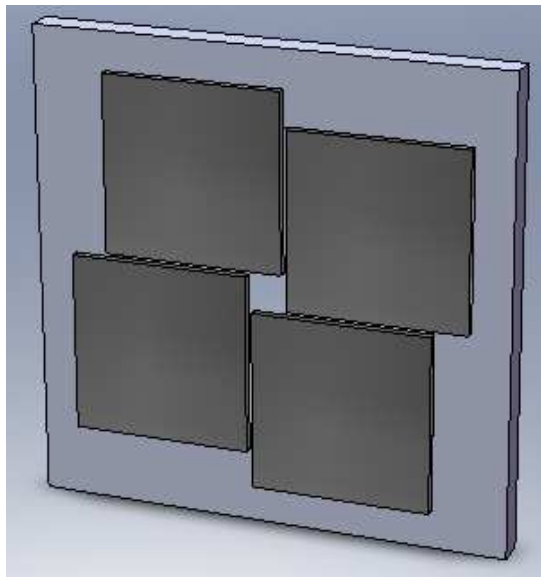


*Figure 5.88: The schematic view of the sensor positions in one station.*

At the stage 1 of the BM@N experiment we assume to use Small Aperture Silicon Tracking System (SA STS), which will consist of four stations equipped by the four $6.2\times6.2$ cm$^2$ sensors with the strip pitch of 58 $\mu$m.
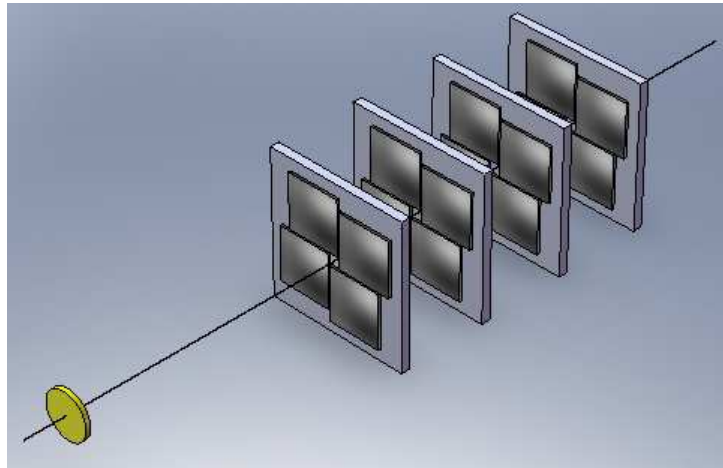
*Figure 5.89: Conceptional layout of the tracking stations and their building blocks.*

The schematic view of the sensor positions in one station is shown in Fig. 5.88.

The layout of the SA STS consisting of four stations is presented in Fig. 5.89.

This detector will provide the charged particle detection angle between $0.5°$ and $7.5°$. Since the number of channels is 16k, the commercially available triggered front-end electronics can be used.

# Chapter 6

# Data acquisition (DAQ) system

## 6.1  Introduction

The BM@N setup will contain more than 2000000 channels of the front–end electronics (see Table 6.1). The Au beam intensity of $10^7$ Hz and the Au target with 1% nuclear interaction length leads to the mean interactions rate $10^5$ Hz. The detectors occupancy from this Table assumes (as the most severe case) the average event multiplicity 164 from the minimal bias collision into the 82.5 msr around the forward direction, excluding 1.4 msr around the beam direction (see e.g. Figs. 5.28 (right) and 5.29); $10^7$ Hz Au for T0. This assumption allows us to estimate the average single event size as 150000 bytes and leads to the up to 120 Gbit/s data flow. The transportation of this data bandwidth through the 10 Gbit/s Ethernet requires 12 or more (for 1 Gbit/s Ethernet — more than 120) such Ethernet channels. On the other hand, the whole dataset belonging to some physical event should at some processing stage to appear on the single computer for the full event building. This requirement is true for the each event. So the system should contain more than one Event Builder (EvB) in principle. This fact requires to solve the nontrivial questions related with the data streams organization and management.

The proposed technical design has potential to be used by the larger experiments like MPD, SPD. It seems reasonable to implement and debug both hardware and software components of this design for the BM@N setup to obtain experience with the corresponding technologies. Anyway, the large scale DAQ system design is inevitable step for the upcoming NICA experiments.

Through the present chapter the term introductions are highlighted as **boldface text**, file and software package names — as *italic text*, C and other languages constructions and reproduced "as is" literals — as `typewriter text`. Reference to the manual page named "qwerty" in the 9th section is printed as *qwerty(9)*. Note also verbal construction like "*pipe(2)*d", which means "handled by *pipe(2)*". Subjects of substitution by actual values are enclosed in the angle brackets: `<num_of_packets>`, while some optional elements are given in the square brackets: [ `ng_filter` →] as well as the array members: Dig[n][m]. All the mentioned trademarks are properties of their respective owners.

### 6.1.1  LIT participation

The DAQ system should be able to store and analyze the data obtained from the different detectors both in free-streaming (STS) and triggered (for instance, RPC or ZDC) modes.

Table 6.1: Data flows estimations.

Digitization types legend: T — time, Q — charge, A — amplitude, c — coordinate (=channel number, embedded if we use hptdc).
Per each 1500 bytes Ethernet frame we have overhead: 40 bytes of *ngdp* packet header + 38 bytes Ethernet overhead = 78 bytes ($\sim$ 6 %).

| subdet | number of channels / number of stations / number of planes | digitization type | digitization time required, ns | required for precision / really acquired value, bit/channel (assuming hptdc) | dynamic range | detector occupancy (per event per plane) | synchronous trigger producer | synchronous trigger consumer | full data stream, bit per event / Mbit per second (w/o 6% overhead) | channels per board × boards per subdet |
|---|---|---|---|---|---|---|---|---|---|---|
| T0 | 64/1/2 | T+Q | ≤?30 | /64×?3 + 32, 16(?8) | | 100/32 | yes | yes | 15584+1024 (512) [a] / 1661 [b] | 32 × 2 |
| ZDC | ≤300/1/1 | A(?Q) | <120..150 | /64(32) | | 1.0 | ?yes | yes | 19200(9600) / 1920(960) | 128 × 3 |
| DTE | 64/1/1 | A(?Q) | <120..150 | /64(32) | | 1.0 | ?yes | yes | 4096(2048) / 410(205) | 64 × 1..2 |
| RPC | 1200/1/1 | T+Q(+c) | ≤100 | 12+?(+0) / ?64(32) | 0..64 ns | 0.16 | yes | yes | 12288(6144) / 1229(615) | 256 × 5..6 |
| DC | 4000/2/8 | (c+)T | ≤111 | (11+)?/?32 | 0..128 ns | 0.66 | no | yes | 84480 / 8448 | 256 × 16..20 |
| ST | 7000/1/3 | (c+)T | | (13+)?/?32 | | ≤0.16 | no | yes | 35904 / 3590 | 256 × 28..30 |
| Sum: | ∼ 16000 | | | | | | | | 172580/17258 | |
| STS | ∼ 2000000 /8/2 | c+A | | / 24+8 | | 0.016 | no | could | 1024000 / 102400 | 16384 × (8×16) |
| Sum: | ∼ 2016000 | | | | | | | | 1196580/119658 | |

[a] For T0 data flow calculations see section 6.3.4.2.

[b] 6% overhead included.

The software support of the current experiment from LIT JINR will be based on the experience obtained within CBM (FAIR) and CERN collaborations, including simulation of the detectors and magnetic fields of the analyzing magnet, development of algorithms, data processing and analysis. Mathematical methods with the use of the artificial neural networks, cellular automata and other modern approaches will be used for event selections in different detectors for the simulation and experimental data analysis. The high counting rate expected during the experiment requires the development of high-speed methods, algorithms and software tools of parallel processing for solving problems on multiprocessor and distributed computing complexes, including the use of Grid-technologies. The use of SIMD instructions, simultaneous multi-threading (SMT), algorithmic languages Ct, OpenCL and CUDA for solving problems on the multi-core, multiprocessor distributed computer complexes. These methods, algorithms and software will be used for the charged particles momenta reconstruction with the high accuracy and their identification, for the simulation of the physical processes in heavy ion collisions at Nuclotron energies, the calibration and alignment of the setup detectors. The data taking and analysis will be performed using distributed systems for the data processing. LIT will provide the mathematical support of the distributed systems for the data processing and development of methods and tools of data transfer and data storage.

## 6.2   Overview

Logically the whole proposed DAQ system for the BM@N setup could be subdivided by the three big subsystems:
• the Data AcQuisition subsystem itself (Fig. 6.1);
• the Fast Control and Trigger (**FC+T**) subsystem, which intended to produce and handle all the synchronous signals in the setup (Fig. 6.2);
• the Slow Control (**SC**) subsystem (Fig. 6.3).
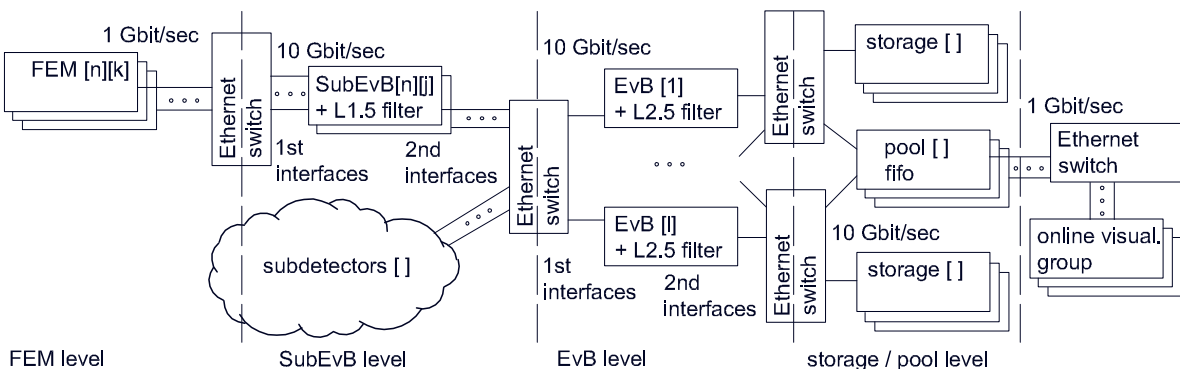


*Figure 6.1: The levels of the DAQ system.*
• *FEM*[n][k] — k-*th entity of the* n-*th subdetector;*
• *SubEvB*[n][j] — j-*th computer belonging to the* n-*th subdetector;*
• *EvB*[l] — l-*th computer of the Event Builders level;*
• L1.5 — *software filter on the SubEvB level;*
• L2.5 — *software filter on the EvB level;*
• *pool*[ ] — *computers of the pool level;*
• *storage*[ ] — *computers of the storage level.*
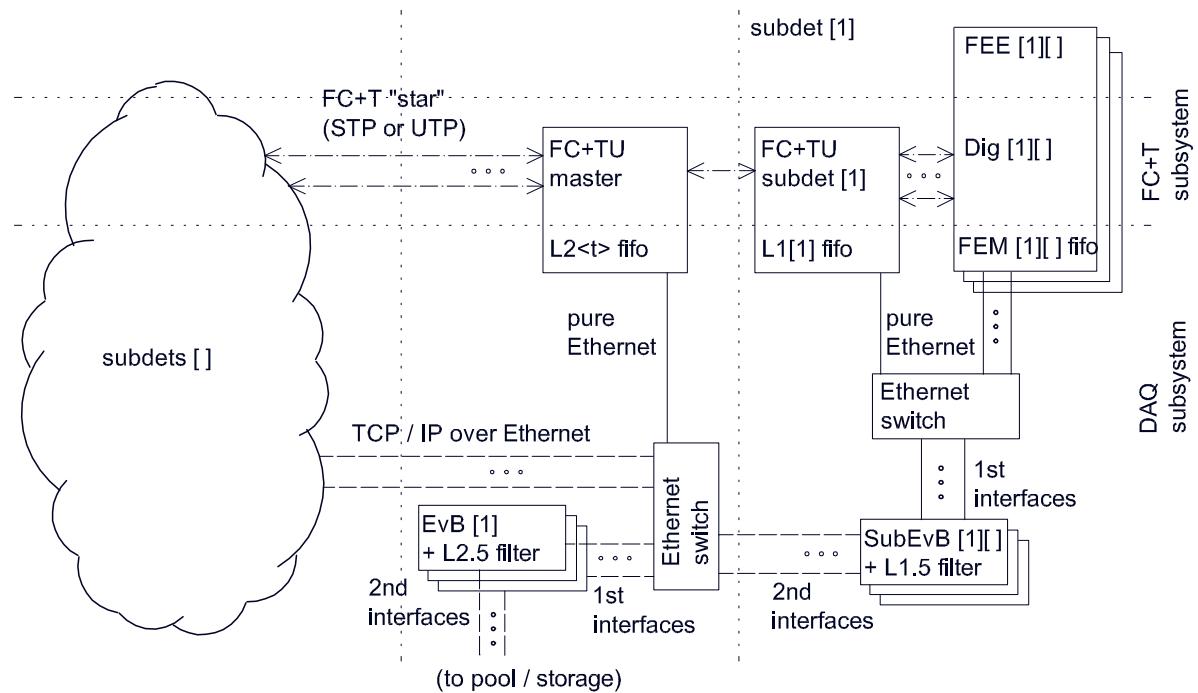
*Figure 6.2: The Fast Control and Trigger (FC+T) subsystem.*
- *FC+TU — Fast Control and Trigger Unit card, the basic hardware unit of the FC system, which are master (1 per setup) and subdet[n] (1 per n-th subdetector);*
  - *Dig[n][m] — m–th Digitizer card of the n–th subdetector;*
    - *For other elements see legend in Fig. 6.1.*
    *These elements are interconnected by the:*
  - *dedicated lines of the trigger production ("ascending") path;*
  - *dedicated lines of the trigger distribution ("descending") path;*
    - *"pure" Ethernet lines;*
  - *TCP/IP network over Ethernet lines.*

Of course, the same hardware card or board physically could contain parts of more than one subsystem due to the high electronics integration (see Table 6.2).

There are many reasons to functionally subdivide the hierarchy of the DAQ hardware units by the logical levels along the data stream, e.g.:

- to formalize and simplify the interactions between the DAQ elements,
- to provide for each subdetector the standalone working mode,
- to allow easy reconfiguration of the active subdetectors' set,
- to allow easy hardware replacement, etc.

We propose, that at least the four logical levels of the data processing (see Fig. 6.1) are needed:

- FEM level implements at least the queues of ready data fragments produced by the Dig[ ][ ] cards;
- SubEvB level — data preprocessing computers grouped by the subdetectors. SubEvB level requests the L1[ ] trigger packets and the corresponding ready data fragments from the FEM level, merges the sub–events, implements the queues of ready sub–events, and possibly the L1.5[ ] software filters for the sub–events rejection;
- EvB level – full events building computers. EvB level requests the L1<t> / L2<t> trigger packets and the corresponding ready sub–events from the SubEvB level, merges the full

*Table 6.2: Required cards description.*

| Card name | Intended to | Main contents | Upstream connections | Downstream connections | FC+TU part | DAQ part | SC part | Power source | Location on setup | Con-structive |
|---|---|---|---|---|---|---|---|---|---|---|
| FEE (TDC) | logic signals preparation for Dig cards | preamplifiers, shapers, discriminators (NINO), ?FPGA | specific subdetector outputs, SC master (serial bus or through Dig) | Dig cards (ribbons of twisted pairs or conductors on the same card) | no | no | slave (FPGA or common w/ Dig) | local converters or from Dig | on subdetector | some specific |
| FEE (QDC / ADC) | ?logic signals preparation for Dig cards | preamplifiers, shapers, discriminators, Q2T converters (?NINO), ?FPGA | specific subdetector outputs, SC master (serial bus or through Dig) | Dig cards (?ribbons of twisted pairs or conductors on the same card) | no | no | slave (FPGA or common w/ Dig) | local converters or from Dig | on subdetector | some specific |
| Dig | *ngdp*-packetized digital data preparation for FEM fifo | digitizer chips (hptdc [183], etc.), FPGA (FEM comm., SC slave, FC+T slave) | FEE outputs, FC+TU subdet (STP / UTP / optic), SC master (?serial bus or Ethernet through FEM) | FEM fifo (Ethernet) | slave, in: L0, Reset, maskable imitation, downscaling, L1 or L1[n]; out: [preL1[n][m]], ackL1 or ackL1[n] | no | slave (FPGA) | local converters | near subdetector (1..3 m) | suitable for Euromechanics crate |
| FC+TU master | synchronous signals production, TPMs exchange w/ FC+TU subdet[ ]s | FPGA (L1<t> / L2<t> fifo comm., SC slave), time-server GPS | SC master (Ethernet) | FC+TU subdet[ ]s (STP / UTP / optic), L1<t> / L2<t> fifo (Ethernet) | in: TPMs (L1[n], ackL1 / ackL2, out: L0, Reset, TPMs (L1 / L2, ackL1[n]) | L1<t> / L2<t> queue | slave (FPGA) | local converters | far subdetector (10.. 20 m) | ? suitable for Euromechanics crate |

Table 6.2 (continued).

| Card name | Intended to | Main contents | Upstream connections | Downstream connections | FC+TU part | DAQ part | SC part | Power source | Location on setup | Constructive |
|---|---|---|---|---|---|---|---|---|---|---|
| FC+TU subdet[n] | L1[n] synchronous trigger production, direct signals and TPMs retransmission | FPGA (L1[n] fifo comm., SC slave) | FC+TU master (STP / UTP / optic), SC master (Ethernet) | Dig[n][] (STP / UTP / optic), L1[n] fifo (Ethernet) | in: L0, Reset, TPMs (preL1[n][m], ackL1 (ackL2) / ackL1[n]); out: L0, Reset, TPMs (L1 (L2) / L1[n], ackL1[n][], imitation request, downscaling factor) | L1[n] queue | slave (FPGA) | local converters | far subdetector (10.. 20 m) | ? suitable for Euromechanics crate |
| SC | all firmware settings downloading | standalone comp. / SBC w/ Ethernet/serial bus | SC group GUIs (Ethernet) | SC slaves on FEE, Dig, HV/LV, SubEvB / EvB, FC+TU (Ethernet / serial bus) | no | no | master | local converters | far subdetector (10.. 20 m) | ATX / suitable for Euromechanics crate |
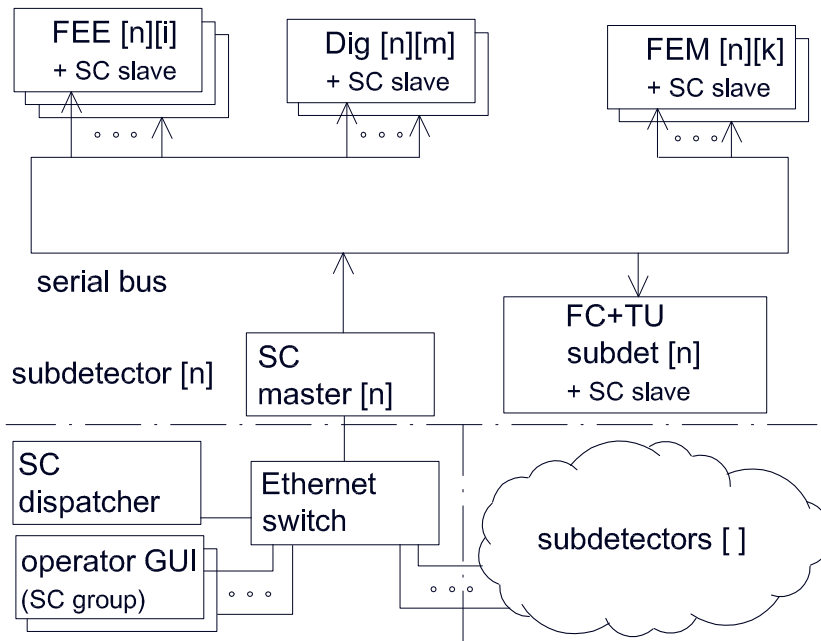
*Figure 6.3: The Slow Control subsystem.*

- *FEE[n][i] — i-th Front–End Electronic card of the n-th subdetector, which prepares signals for the Dig[n][m] card;*
- *SC master[n] — Slow Control master card (1 per n-th subdetector), the basic hardware unit of the SC system;*
- *SC slave — peer part for the SC master (integrated into FEE, Dig, HV/LV, FC+TU cards);*
- *SC dispatcher — the computer (1 per setup), which obtains the operator GUI requests and forwards ones to the specific SC master[] according to their destination.*

events, implements the queues of ready full events, and possibly the L2.5 software filters for the full events rejection;

• pool level — data postprocessing computers. Pool level requests the ready events subset from the EvB level, converts their from a native binary format to some ROOT [202] class representation, implements the queues of ROOT events, and provides their to clients for the online analysis and visualization. Also the ROOT events are histogrammed and these histograms are provided to clients for the online analysis and visualization;

• storage level (parallel to the pool level) — computers, which request the ready events from the EvB level and write their into the intermediate (HDD) storage. The storage level consists of some identical computer groups switchable while the data taking, so one group obtains the events from the EvB level while the other groups transfer the obtained data from the intermediate into the final storage, possibly slower than HDD.

Each intermediate level behaves as a server for the downstream level and as a client for the upstream level. This approach simplifies algorithms of inter–level interactions, which will be reduced to the ones only between neighbour levels.

In addition, some computer groups can be outside of the data stream:

• Fast Control and Trigger group — computers, which implement the FC+TU subsystem: trigger queues (see also sections 6.4.2.1 and 6.4.3.1) and the corresponding GUI;

• Slow Control group — computers, which implement the SC subsystem (see also section 6.3.6) and the corresponding GUI;

- DAQ Operator group — computers, which perform the control over the DAQ software components and provide the user interface for them;
- online visualization group — clients of the pool level.

The requirements to the proposed levels are described in section 6.4. Lets also introduce some terms absent in Figs. 6.1—6.3 legends:

**Packet** — the sequence of bytes, which contains the fixed length packet header (with at least the ID string, type, timestamp, number, length, flags, CRC32) followed by the packet body of known length (see [203] and *packet(3,5,9)*).

**Event merging** — simple kind of event building, which produces the new output packet to contain sequence of all the input packets (headers are preserved, the ID string reflects the encapsulation level). This operation performed on SubEvB and EvB levels leads to the full event's encapsulation level $\geq 2$.

**Trigger packet** — the packet is produced by the FC+TU master or FC+TU subdet[] card and contains the reliable (sub)event merging tag (number and/or timestamp) for the (Sub)EvB.

**Fragment**, **sub–event**, **full event** — the packets represent the data and are produced by the Dig[][], SubEvB[][], EvB[], correspondingly.

**Queue** — the software buffer of packets with the FIFO (First In — First Out) nature and some rule set (discipline) of the packets getting.

L1[n], L1<t> / L2<t> **fifo** — queues of the L1[n] or L1<t> / L2<t> trigger packets supplied by the FC+TU subdet[n] or master card, respectively.

# 6.3 Hardware requirements

Here we describe requirements to the hardware proposed for development (Table 6.2).

## 6.3.1 Trigger assumptions

Currently we assume for the whole BM@N setup the L1 central synchronous ("live") single-stage trigger to be the only trigger implemented by the hardware. This hardware belongs to the FC+T subsystem. This approach solves the deadtime account issues in the straightforward and clear manner (see also section 6.3.2), and allows us to establish the reliable triggers (and *ngdp* data packets) numbering. Such numbering will be simple and single tag (however see also section 6.4.1) for the (sub)events merging: the data fragments / sub-events will be selected to belong to the same N-th sub-event / full event, if and only if their reliable numbers are match with (i.e. corresponding integers are equal to) the N-th trigger number. The overall architecture of the FC+T subsystem we can see in Fig. 6.2. With the L1<t> hardware trigger (possibly of some type t) the higher level triggers are assumed to be the software filters on the SubEvB (L1.5[]) and EvB (L2.5) levels.

The whole setup's L1<t> will be assembled from the subdetector's L1[n], while L1[n] — from the Dig[n][] card's preL1[n][] by the hierarchy of analog and/or digital summators (n corresponds to the trigger-producer subdetectors). This hierarchy could be implemented as parts of the FEE[][]s, Dig[][]s and FC+TU subdet[]s (see sections 6.3.3, 6.3.4, 6.3.5), or as independent modules. Former option is preferable in respect of the power solution, cabling arrangement, SC implementation reasons (entia non sunt multiplicanda sine necessitate). The presence of the FC+TU subdet[] instances also allows to operate subdetectors easily in the standalone mode for test, calibration, etc. purposes (setup scalability

providing). Currently the trigger-producer subdetectors are T0 (existence of the beam particle), RPC (number of fired pads as the multiplicity characteristic), and ZDC (possibly with DTE) (total energy deposition as the centrality characteristic). The signals sum is discriminated according to the preset trigger conditions by some controlled discriminators, possibly on the FC+TU master card.

The nominal (mean over time) event rate on BM@N equals to the interactions rate $10^5$ Hz, i.e. 10 $\mu$s per event, during which we should provide the L1 trigger decision. Of course, the beam inhomogeneity in time tightens this requirement to $< 1..2$ $\mu$s. This requirement is reachable, if the FPGA processing (the main time consuming part of the trigger production) will be no longer than 0.5 $\mu$s (50 cycles at the 100 MHz). Note if we can use the trigger queues on the each involved digitizer chip type (hptdc has one of 16 triggers deep) and their possible trigger latency is $> 10$ $\mu$s (hptdc — up to 25..50 $\mu$s), this requirement could be softened.

The proposed FC+T hardware architecture is expected to support also the two-stage L2<t> triggers production. Possibly this will require the Trigger Protocol Messages (TPMs, see section 6.3.3.3) content expansions (e.g. to carry the reliable timestamps) and assortment additions, (sub)events merging tag change from the reliable numbers to timestamps, etc.

## 6.3.2   T0 subdetector, deadtime and data losses accounts

To be able to reconstruct the absolute values like cross-sections, etc. we should have the monitor data for the primary beam (i.e. primary particles counts per each L1<t> / L2<t> trigger). The primary beam quality characteristics like the time structure coefficient  (see Eq. 7.1) should be known also. This means the primary particles counts per each time slice of the constant duration should be acquired. The T0 subdetector should provide both mentioned data types as well as usual data about time and charge of beam particle hit in T0. Also the special data fragments should be produced for the BoB and EoB. Moreover, some inputs of the T0 Dig[][] cards (see section 6.3.4.2) should be reserved to handle some external signal sources (like scintillation counters) in the same manner as T0 channels. The T0 data in whole should be available for the online analysis in contrast with data from other subdetectors, which will be available only in subset due to data flow reasons.

The deadtime and data losses accounts for the whole setup are very important. For the complex setup with many data queues like BM@N the only deadtime source is the overflow of these queues. The proposed strategy of the overflows handling is follows. Each higher level client queue requests the lower level server queue for the data, so can not overflow itself. However, the Dig[][] card FPGAs send data fragments to FEM queues as soon as possible, because have not onboard buffers. The FEM queues will acknowledge the data obtaining for the Dig[][]s by the *ngdp* control packets. So, the "full" (or "near full") FEM queue state will be back propagated by the NAK[1] (or HIWAT[2]) response to the Dig[][] card FPGA, which suspends the read-out of the first instances of the data chain — buffers of the digitization chips (hptdc, etc.). These chips will produce error marks if their buffers are overflow. These errors should be packed by the Dig[][] card FPGAs into special error fragments, merged into error sub-events by each subdetector, and finally merged with T0 sub-events into T0 full events (see also section 6.5.8) to allow online calculations of the deadtime. Of course, the appearing of (some percentage of) free space in the FEM queues

---

[1]Negative acknowledge.

[2]High water mark.

should be immediately signaled by the ACK (LOWAT[3]) control packets to allow FPGAs to read-out chips again.

### 6.3.3 FC+TU cards

The FC+T subsystem is intended to produce and handle all the synchronous signals in the BM@N setup (`L0` clock, `L1<t>` / `L2<t>` and `L1[n]` triggers, etc.), while the FC+TU cards are basic hardware unit of it.

#### 6.3.3.1 Synchronization issues

BM@N timing system is a part of accelerator timing network. It is based on White Rabbit Network (WRN) [204]. The purpose of this system is to provide the control data and absolute time reference with sub-nanosecond accuracy and precision to accelerator and detector (sub)systems located in distinct experimental buildings. White Rabbit is a project, which aims the creation of an Ethernet-based network with low-latency, deterministic packet delivery and network-wide, transparent, high-accuracy timing distribution. The White Rabbit Network (WRN) is fully compatible with existing standards: Ethernet IEEE 802.3, Synchronous Ethernet and PTP. The WRN consists of White Rabbit Nodes and White Rabbit Switches interconnected by the fiber links. The information distributed over WRN includes frequency and International Atomic Time as well as the Ethernet traffic between nodes.

WRN has the following properties:

- Determinism, guaranteed by having worst-case upper bound of the frame delivery latency.

- Accuracy, a measure of the deviation between the clock of the WRN Grandmaster node and any other node. With single-mode fiber interconnection and bidirectional WDM transceivers the WRN achieves sub-nanosecond accuracy.

- Reliability, robust delivery of the data and timing to all nodes.

The WRN topology is a redundant tree with four levels. The root of the tree is a GPS receiver and Cesium backup clock that provide 10 MHz frequency reference, 1PPS signal and IRIG-B time data to two or more Layer 0 timing master WR switches. Layer 1 is the backbone with two WR switches. Layer 2 is distribution level and provides sufficient number of interconnections to end nodes. The WR switch has 18 ports, thus Layer 2 can accommodate up to 128 endpoints using redundant topology or up to 256 — without redundancy, while the Layer 3 — up to 2048 and 4096 endpoints respectively. It is important to keep minimum number of topology layers for timing accuracy. In heterogeneous system the subsystems demanding more time accuracy are connected directly at Layer 2, while others may use Layer 3.

Preliminary tests of WRN have shown the sufficient point-to-point timing accuracy of 160 ps (offset) and 6.5 ps precision (RMS jitter) over 5 km optical fiber under a harsh conditions: temperature variation and mechanical vibration [205].

While it is possible to include WR node in each `Dig[][]` module, the simpler solution is to group these modules into logical clusters (one per subdetector) with common network for both trigger and clock TPM distribution and single WR node in FC+TU `subdet[]` per cluster

---

[3]Low water mark.

(subdetector). This solution provides better local clock precision by using dedicated copper cables of minimum and equal length to each Dig[][] board. It is important to keep RMS phase noise of clock signal at order of picoseconds at least for ADC boards to maximize ADC resolution. On the other hand, the direct clock distribution on the cluster (subdetector) level is a traditional and simple way of synchronization, that requires minimum of hardware and logical components and is enough at the prototype stage.

### 6.3.3.2   FC+TU master

The **FC+TU master card** (1 per setup) should contain at least:
• 8..16 trigger (TPM) input/output downlink connectors (UTP/STP/optic);
• (at least for the FC+TU subdet[]s) one trigger (TPM) input/output uplink connector (UTP/STP/optic);
• Begin of Burst (BoB) input (and configurable burst length) to be able to produce BoB and End of Burst (EoB) triggers;
• 1 Gbit/s Ethernet port (RJ-45/optic);
• the FPGA, which:
† (re)distributes the direct signals — L0 clock (40 MHz), Reset, etc.;
† analyses the L1[n] trigger (TPM) inputs from FC+TU subdet[]s according to programmable (not wired) rules (trigger "ascending" path);
† produces the L1<t> / L2<t> trigger signals (of some type t) in form of the TPM (see section 6.3.3.3), delivers ones, and obtains the TPM responses (ackL1<t> / ackL2<t>) synchronously (trigger "descending" path);
† for each L1<t> / L2<t> trigger occurrence produces the trigger packet (of some type t, each packet is the Ethernet frame, which encapsulates the *ngdp* packet), supplies ones to the L1<t> / L2<t> fifo server, and obtains ACK / NAK  / HIWAT / LOWAT responses in the same form (through the Ethernet port);
† for each BoB / EoB trigger occurrence produces the trigger packet of the corresponding type;
† for each Begin of Run (BoR) command arrival resets the trigger numbers (for both TPMs and *ngdp* packets) to zero for all trigger types;
† implements the uniform SC slave (conversation with SC master through the Ethernet port);
• (at least for the FC+TU master) the hardware timeserver (GPS, etc.) with the ability to synchronize the L0 with the absolute time of the accelerator cycle begin and produce the absolute timestamp (`struct timespec {sec; nsec}`) for each trigger packet;
• the uniform power solution: single input (some of 12, 24, 48 V) and on–board converters;
• solution for the hardware reset (by power switching or FPGA reset).

The trigger *ngdp* packets produced by the FC+TU master should have both the reliable packet number and the absolute timestamp, as well as valid type, length, flags, CRC32 (i.e. the full packet header of 40 bytes), and possibly carry some information in the packet body (see also sections 6.4.1 and 6.5.8). The trigger *ngdp* packets are used by the EvB[]s. The number of triggers produced during the current burst for each event type is very useful (see section 6.5.8) to be present in EoB trigger packet body.

### 6.3.3.3   Trigger Protocol Messages

The **TPMs assortment** should be like the following:
• FC+TU subdet[n] ← Dig[n][]: preL1[n][] pre-triggers, ackL1 acknowledgments;

- FC+TU master ← FC+TU subdet[] : L1[] trigger, `ackL1` acknowledgments;
- FC+TU master → FC+TU subdet[] : L1<t> / L2<t> trigger (of some type: BoB, EoB, some kinds of event), ?`ackL1[]` acknowledgments;
- FC+TU subdet[n] → Dig[n][] : L1<t> / L2<t> triggers (with types mapped according to FC+TU subdet[n] configuration: localized kinds of event, possibly BoB, EoB, some out of burst tests), ?`ackpreL1[n][]` pre-trigger acknowledgments.

The ACK / NAK scheme (or more sophisticated HIWAT / LOWAT one to account the already used part of the trigger fifo and reduce the control TPMs / packets traffic) should be used for both the TPM and *ngdp* packet trigger exchange control. This means the future trigger production will be suspended until the proper acknowledgment (ACK / LOWAT) obtaining. The TPM could be implemented as the fixed length transfer, the front of start bit is the time moment of the trigger (for the trigger input of the hptdc, etc.), the 32-bit value is the reliable trigger number (used by the FPGA), and some (?16) bits for trigger type (BoB, EoB, some kinds of event). (For the timestamps tag scheme of the (sub)events merging the two 32-bit values for `sec` and `nsec` should be transmitted by each TPM, too.) All cable lengths should be aligned for the simultaneous TPMs arrival at each FC+TU subdet[] and Dig[][]. Of course, the TPM assortment could be expanded over these mentioned above if needed. It is very likely that the switch to/from the test/imitation/calibration mode, the downscaling factor, BoR and End of Run (EoR), etc. should be distributed as TPMs.

### 6.3.3.4 FC+TU subdet[n]

The **FC+TU subdet**[n] (1 per n-th subdetector) should be similar or identical to the FC+TU master one. It:
- redistributes the L0, Reset, etc.;
- redistributes the trigger TPMs (and possibly produces local trigger TPMs: e.g. test/calibration between EoB and BoB) to the Dig[n][] cards (trigger "descending" path);
- analyses the `preL1[n][]` TPM inputs from Dig[n][] according to programmable (not wired) rules and produces the L1[n] trigger signal in the TPM form, delivers it, and obtains the TPM responses (?`ackL1[]`) synchronously (trigger "ascending" path);
- (in the reliable numbers tag scheme) for each L1<t> trigger TPM obtained produces the *ngdp* trigger packet with: the same reliable packet number as present in trigger TPM, the mapped type, valid length, flags, CRC32, the same timestamp as present in trigger TPM, or otherwise produced locally by the TPM arrival time;
- (in the timestamps tag scheme) for each L1<t> trigger TPM obtained / L1[n] trigger TPM issued produces the *ngdp* trigger packet with: the same timestamp as present in L1<t> TPM, or otherwise produced locally by the L1[n] TPM issuing time, the mapped type, valid locally produced number, length, flags, CRC32;
- supplies these packets to the L1[n] fifo server (or trigger input channel buffer(s) of the SubEvB[n][](s), this means the multicast mode using or sending the same packet to more than one destination address) through the Ethernet port.

## 6.3.4 Digitizer cards

The **Dig cards** are intended to the digital data preparation for the lower entities (FEM queues) of the DAQ subsystem. Such data (and possibly error) fragments are produced in form of the Ethernet frame, which encapsulates the *ngdp* packet with the reliable packet number (the same as obtained by the trigger TPM, see section 6.3.3.3), type (corresponded to type

obtained by the trigger TPM by the configurable mapping in the Dig FPGA), timestamp the same as obtained by the trigger TPM (if present), valid length, flags, CRC32 (i.e. the full *ngdp* packet header of 40 bytes), and the body, which contains the data fragment itself. Types for both data and error fragments (packets) are online configurable 16-bit constant integer offsets relative to the trigger TPM type values.

The Dig[][] hardware is responsible to produce the binary data in the reasonably compact format. Probably for the calorimeters (ZDC, DTE) we need the charge value only, so in the Q2T scheme the common FPGA of Dig cards should calculate the difference between trailing and leading signal edges, i.e. produce 32 bits per hit instead of 64 ones preserving the same precision 100 ps/bin.

The Dig cards location on setup is probably near the corresponding subdetector (1..3 m), while its shape should be suitable for both the Euromechanics crate (6U/9U) and standalone positioning. The Dig card interconnections scheme we can see in Fig. 6.4.
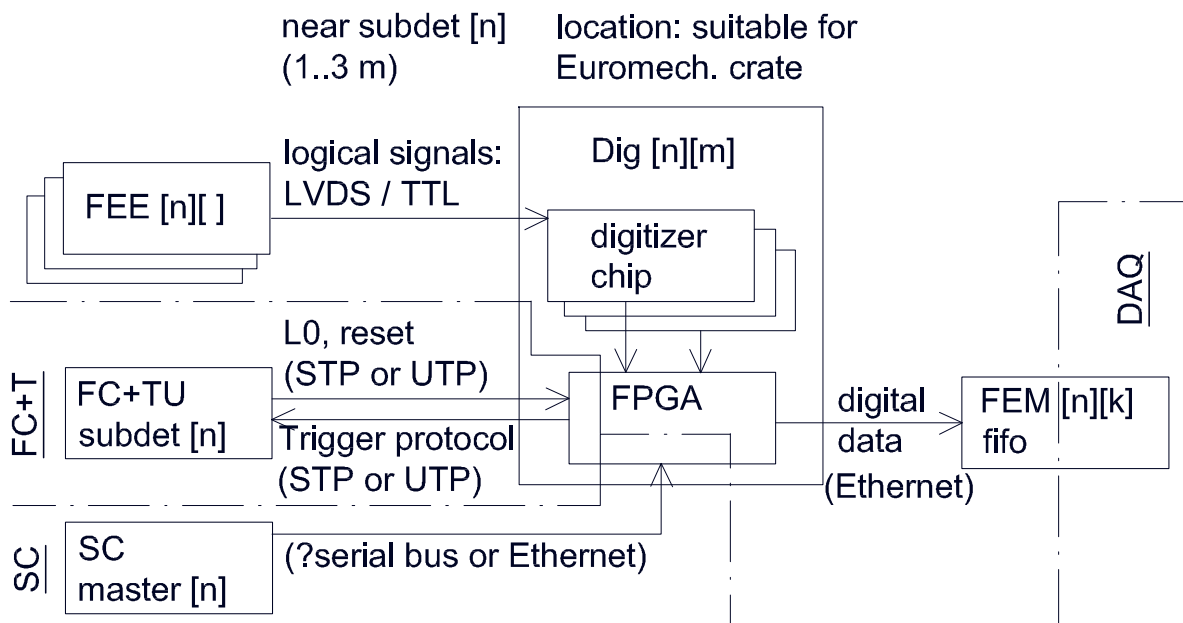


*Figure 6.4: The Dig card interconnections. See text for description.*

The Dig cards use some ready digitization chips: hptdc [183] (TDC, QDC through Q2T conversion), n–XYTER or something other (coordinate), etc. under the common FPGA control, so it is possible to have a very few (2..3) slightly different Dig card types (see, for example, Fig. 6.5) per BM@N setup. The common requirements for each of these types are to contain:

• connectors (with or without cables) or conductors (on the same printed circuit) to input data signals from the FEEs;

• the FC slave implementation in the common FPGA (see below for details);

• connector(s) (1 Gbit/s Ethernet) for the bidirectional conversations under the FPGA control:

† output — *ngdp*-packetized digital data fragments with the nanosecond precision timestamp (to FEM fifo), possibly SC responses (to SC master), etc.;

† input — backward ACK / NAK / HIWAT / LOWAT *ngdp* control packets to acknowledge the data fragments acception (from FEM fifo), possibly SC commands (from SC master),

etc.;
• the uniform SC slave implemented by the common FPGA;
• the means to support the test/imitation/calibration mode (not yet understood in details, however should not be forgotten);
• the uniform power input (some of 12, 24, 48 V) and on–board converters;
• solution for the hardware reset (by power switching or FPGA reset).
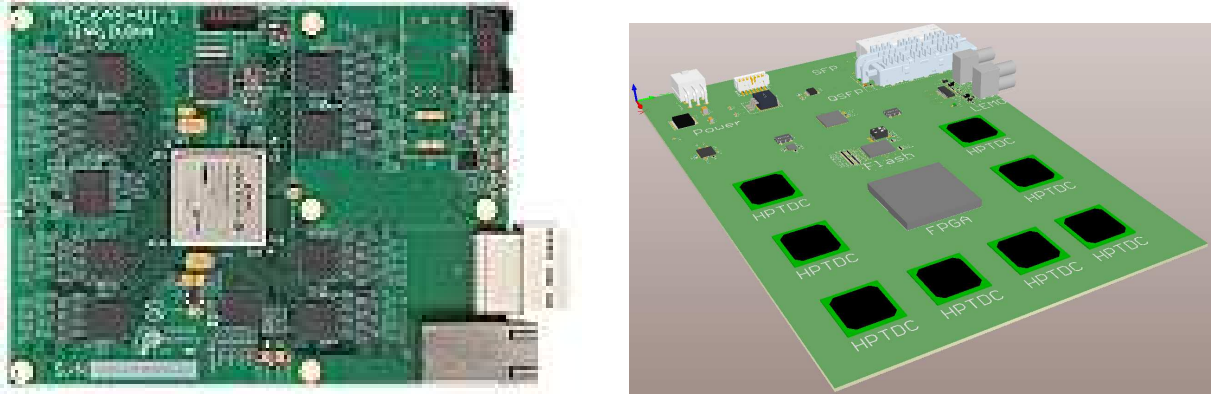


*Figure 6.5: Dig cards: ADC prototype (left) and TDC design (right).*

In respect of the FC+T subsystem the Dig cards should contain also:
• up to 8 signals sum inputs (UTP/STP/optic for digital) from the FEE[][]s;
• one trigger (TPM) input/output uplink connector (UTP/STP/optic);
• the common FPGA should in particular implement:
† the digital summator to produce the `preL1[n][]` TPMs (as part of the trigger production "ascending" path);
† the `L1[]` trigger TPM obtaining and the `ackL1` acknowledge TPM sending (trigger "descending" path);
† the different behaviour at arrival the different trigger TPM types (BoB/EoB, some kinds of event or test / calibration);
† the data fragments production (see above), where the *ngdp* packet has: the body, which contains the data fragment itself, and the full packet header of 40 bytes, namely:
∗ (in the reliable numbers tag scheme) the reliable packet number (from the `L1<t>` trigger TPM), timestamp (from the trigger TPM, if present, or otherwise produced locally by TPM arrival time), type mapped according to `Dig[n][]` configuration, valid length, flags, CRC32;
∗ (in the timestamps tag scheme) the timestamp (from trigger `L1<t>` TPM, if present, or otherwise produced locally by the`L1[n]` TPM arrival time), type mapped according to `Dig[n][]` configuration, valid length, number (locally produced), flags, CRC32.

### 6.3.4.1   Digitizer card with hptdc chips

The Dig card with hptdc chips for the TDC and QDC is probably suitable for work with all but the STS subdetector and could be considered now in details.

The maximal capacity of the hptdc read–out token ring is 16 chips, so we can have no more than 512 channels per Dig card. However the reasonable size of the Dig card (6U) as well as the data flow issues (see below) restricts us by 8 hptdc chips (256/64 channels in 100/25 ps/bin modes). To reduce the data flow we should not produce the local (slave) header and trailer hptdc words. Some subdetector variants of the hptdc handling should be used:

• RPC mode: leading and trailing edges (100 or ?25 ps/bin), 64 bit/hit;
• T0 mode: leading and trailing edges (25 ps/bin), 64 bit/hit, without hptdc trigger matching (see section 6.3.4.2);
• Q2T mode: leading and trailing edges (100 ps/bin), 64 bit/hit, or with subtraction by the common FPGA, 32 bit/hit;
• DC/ST mode: leading edge (100 ps/bin) + width (more rough like 1.6 ns/bin), 32 bit/hit.

The common FPGA of the Dig card should for each obtained trigger TPM:

† read–out and buffer the data fragment according to the trigger TPM type for further Ethernet transfer,

† account the data fragment length;

† save the data fragment nanosecond timestamp (number of L0 clock pulses from start multiplied by 25), it is assumed the times for the same trigger in different hptdc are differ no more than by single L0 clock;

† fill in the 40 bytes of the *ngdp* packet header and store it in the 0th..9th words of the buffer;

† produce the summary error word using all encountered hptdc error words (if any, or fill by zeros otherwise) and store it in the 10th word of the buffer;

† produce the data fragment packet mentioned above;

† (as the online configurable option) produce separate packet of all hptdc error words, if their are encountered for current trigger.

We assume the data fragment should always be carried by single Ethernet frame to avoid the nontrivial reassembling algorithms on the obtaining side (FEM fifo). So, the data buffer size should be $\leq$ MTU = 1500 bytes, i.e. $\leq$ 187.5 bytes per event per chip. Note the maximal hits number per event could be enforced by the hptdc as power of 2, so we can guarantee that for each event the data fragment will fit into the single Ethernet frame. With up to $2^5$($2^4$ for 64-bit hits) hits/event/chip the data of $(2^5 \times 8 + 2) \times 4 = 1032$ bytes $(2^4 \times 8 \times 8 + 2 \times 4 = 1032$ bytes) accompanied by the *ngdp* and Ethernet overheads of 40 and 38 bytes at the events rate of $10^5$ Hz leads to the data flow of up to yet acceptable 888 Mbit/s.

The alternative for the hptdc usage is the TDC implementation on base of the dedicated FPGAs.


### 6.3.4.2   T0 Digitizer cards

Probably the T0 Dig card should have the separate version of the FPGA firmware to produce also both  (a) hit counts per each trigger[4] and  (b) per each time slice (of the configurable duration, 5..10000 $\mu$s) for each T0 channel. This will require to perform the trigger matching (in the hptdc manner with configurable trigger latency  lt and time window twin) by the Dig FPGA itself, because each produced hit (i.e. detected beam particle) should be evaluated for these counts calculation. At least the following trigger TPMs should be recognized: BoB, EoB, some kinds of event.

Because the maximum read-out speed of the hptdc is 25 ns/word (or 50 ns/hit for 25 ps/bin mode), while the average hit production speed is 100 ns/hit (at beam of $10^7$ Hz), we should have $\geq$ 2 Dig cards (each of $\leq$ 32 channels) for T0 subdetector to have $\geq$ 4-fold

---

[4]Really between BoB and the first trigger, between two consequent ones, and between the last one and EoB.

performance reserve for intensity fluctuations.

For (b) we need not additional buffer in the FPGA other than for 2 Ethernet frames (currently produced and transferred) of 1500 bytes each. The FPGA increments the slice hit counter for each read-out hit, while hit timestamp fall into current slice, or otherwise stores counter value into Ethernet frame being produced and resets counter. The 16-bit counter will be optimal for both data fragment length and possible slice duration. At the arrival of the timeslice trigger TPM from the FC+TU subdet[T0] the FPGA switches Ethernet frames and starts the transfer.

For (a) we need the circle buffers for each input channel to keep hits during at least the trigger latency. For latency of 10 $\mu$s with hit rate of $10^7$ Hz we have 100 hits in all 32 channels, so buffer of 100 hits per each channel provides a big reserve. This leads to 800 bytes per channel and 25600 bytes per FPGA, which is not a problem now. The FPGA increments the trigger hit counter for each read-out hit and stores hit into aforementioned buffer according to hit input channel. At the L1<t> / L2<t> trigger TPM arrival the FPGA saves the value of trigger hit counter into temporary storage. After that FPGA reads each buffer backward to find hit(s) with timestamp(s) `ts` satisfying the $ts_{TPM}-$ `lt` $\leq$ `ts` $\leq ts_{TPM}-$ `lt` + `twin` condition[5] and counts number of encountered intermediate hits. After subtraction of this number from saved trigger hit counter we obtain the actual value of hits per trigger to be stored into data fragment together with found hit(s). The data fragment should be ordered by the channel number. Of course, other 2 buffers are needed to hold the currently produced and transferred Ethernet frames with (a) data fragment. The value of trigger hit counters between the L1<t> / L2<t> trigger last in burst and EoB trigger for each channel will be carried by the EoB data fragment.

Assuming all trigger counters are 32-bit and 3 hits of 64 bits per trigger, we have up to (if all 32 channels have hit(s)) $(3 \times 64 + 32) \times 32 + (40 + 38) \times 8 = 7792$ bit/hit (974 bytes/hit), including the 38 bytes Ethernet and 40 bytes *ngdp* overhead, because each such hit forms the own data fragment. This means we have the rest of 1 Gbit/s bandwidth equals to 27600000 byte/s (or 18400 frames/s) available to transfer the (b) data. This allows us to have up to 408825 and 817650 slice/channel for 16-bit and 8-bit slice hit counter, respectively, and to cover, e.g., more than 2 s of burst duration with slice of 5 $\mu$s. In Table 6.1 we account two 32-channel Dig cards, so have twice of the aforementioned value. With nominal $10^5$ Hz rate for both L1<t> / L2<t> and timeslice triggers we have $(15584 + 1024) \times 10^5 = 1660.8$ Mbit/s from these 2 cards.

## 6.3.5 FEE cards

The **FEE cards** are intended to the signals (possibly always logical: LVDS / LVTTL) preparation for the Dig card. The FEE cards are located on the corresponding subdetector and possibly do not require the crate-suitable shape. The FEE card interconnections scheme we can see in Fig. 6.6.

The FEE cards are specific for the serviced subdetector (here we can not essentially reduce entities to be designed), however in general each of them should contain and implement:
- the uniform SC slave (or be controlled through Dig);
- the means to support the test/imitation/calibration mode (not yet understood in details, however should not be forgotten);
- the means to feed output signals to the Dig card(s):

---

[5]To keep the `lt` and `twin` meanings the same as hptdc uses.
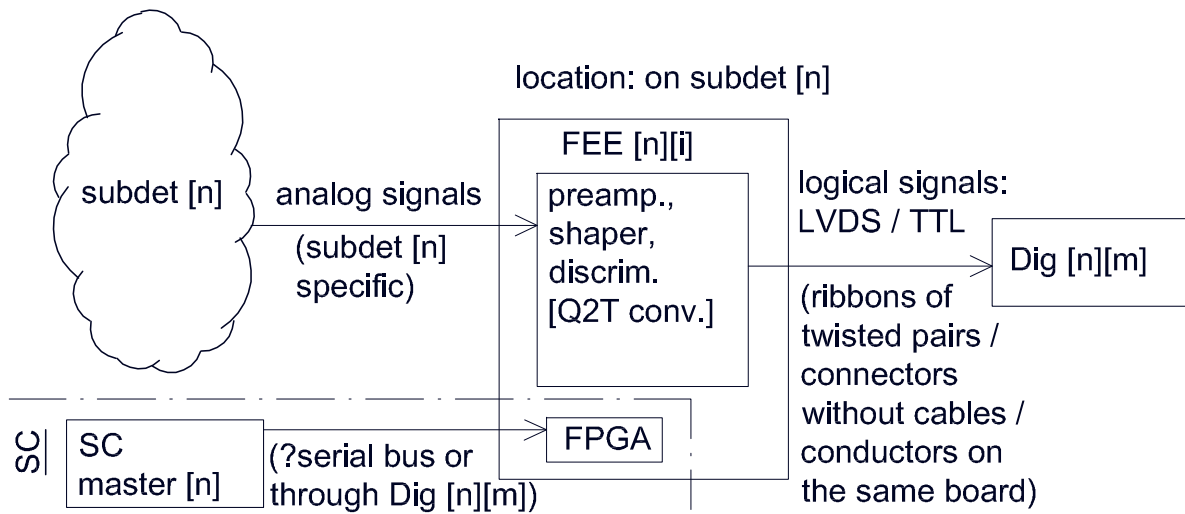
*Figure 6.6: The Front-End Electronic (FEE) card interconnections.*

† pin connectors for ribbons of twisted pairs, or

† wafer connectors without cables (mezzanine/AddOn), or

† conductors on the same printed circuit (at least for some detectors the FEE could be on the same card as Dig — IT(STS));

• power supply: the uniform power input (some of 12, 24, 48 V) and on–board converters (or obtains the ready voltages from the Dig card);

• solution for the hardware reset (by power switching or FPGA reset).

In respect of the FC+T subsystem the FEE cards should provide:

• the branching of the analog signals from the detector to feed both the main (digitization) dataway and the trigger production "ascending" path;

• the analog (?or digital) summator, ADC, and single digital output as part of the trigger production path.

The FEE cards in the TDC chains probably will use the NINO chips [206] to produce the logical output signals for the hptdc [183].

The FEE cards in the QDC chains probably will use the Q2T converters to produce the logical output signals for the hptdc, too.

## 6.3.6   Slow Control hardware

All the **SC master units** (typically 1 per n-th subdetector, see Fig. 6.3) should be similar or identical and contain at least:

• the standalone or Single Board computer (SBC, see also  section 6.3.7 ): 1 Gbit/s Ethernet, network bootable (PXE), optional local flash memory as the permanent storage, the proper heat sink by the low–profile passive cooler;

• the means to converse (connector of Ethernet and/or some standard serial bus (RS-485, etc.)) with SC slave parts;

• the uniform power input (some of 12, 24, 48 V) and on–board converters to ATX voltages.

All the hardware **SC slaves** embedded into the FEE, Dig, HV/LV, FC+TU cards should be uniform, i.e. contain the same connector(s) and intellect (FPGA, etc.), which implements

the same protocol. The only SC function should be hardware implemented for the SubEvB, EvB level computers is a remote reset solution (by power switching or motherboard reset).

### 6.3.7 Standalone computers architecture

Also we should choose a **hardware architecture of the standalone computers** to be used in all but FEM levels of the DAQ system and for the DAQ software design and implementation purposes. On the one hand, we have no special requirements to these computers hardware — other than performance and reliability. On the other hand, the big DAQ system can require from tens to some hundreds of units of such hardware with corresponding maintenance, etc. So, we should choose the most standard and generic hardware reasonably cheap due to a great volume of production. This architecture is called `AMD64/EM64T`, previously known also as `x86-64` and `IA-32e`, and should be used currently and in the near future. For the embedded SBCs involved in the BM@N DAQ they will be very desirable to have the same architecture (or the 32–bit `x86`). Note the SBC is preferable over the System–on–Chip (SoC) due to flexibility, replaceability, low integration efforts (printed circuit design is not required).

## 6.4   Software requirements

The operating system (OS) used on the online computers determines the DAQ system design and organization, consequently the inadequate OS selection is sure to strongly complicate implementation, maintenance, and using of the DAQ system. The OS itself should have adequate technical abilities for easy multiple installations, remote maintenance and backup, read–only boot filesystem and diskless network boot, boot without input and output devices, easy and centralized startup customization, etc.

UNIX–like OSs are optimal for the above requirements. UNIX is a multiprocess and multiuser OS with powerful mechanisms for interprocess and inter–computer communications, a very advanced virtual memory subsystem, support of sophisticated networking and graphics interfaces, extended tools for the software design. Costs for UNIX working itself are practically negligible on the modern hardware. Availability of the OS sources is a mandatory requirement for the present developments, while the freely distributable nature of some UNIX–like OSs is highly desirable. After all, high portability of UNIX programming and approximately unlimited quantity of the existing software are also very attractive.

To achieve the reasonable performance, we should choose C programming language (or C++ — only in such cases, where we can neither avoid an object–oriented design nor implement it using C) and ultimately avoid interpreted languages like Perl or CINT.

Because the FPGA firmware responsibilities are described  in section 6.3, here we formulate our requirements to the DAQ software modules only, which should be executed by CPUs of the standalone computers and/or SBCs.

### 6.4.1   (Sub)events merging tags

In the proposed design we could use two **(sub)events merging schemes** based on the reliable trigger numbers or the timestamps as the (sub)event merging tags. The former is suitable for the central `L1<t>` trigger only, while the latter — for any trigger architecture, however requires more expensive TPMs for timestamps propagation from the FC+TU master in the

central L1<t> case. In case of the two-stage L2<t> trigger the timestamp is the only possible merging tag, however should be produced locally by each Dig card instead of propagated from the FC+TU master. Anyway, the synchronization issues should be addressed by the FC+T subsystem. Note the packet queues implementation seems to be simpler for the timestamping scheme (see section 6.5.3 for details). Anyway we require the proper merging tag to be present on the each produced data fragment / sub-event and trigger packet. For the timestamps tag this means each data fragment packet should be timestamped by the Dig with the enough (practically nanosecond) precision: really ones could be the 64–bit numbers of the L0 clock pulses[6] from some start time moment (e.g. BoB), for which the absolute time ats with the nanosecond precision is saved (in the struct timespec form) by the FC+TU master.

The fragment searching in the queues by the corresponding merging tag will be the only method to obtain all the fragments belonging to each the full event. For the reliable numbers the correspondence means their equality. For the timestamping it is the falling of the data fragment timestamp tsd into the time window, defined by the reference times-tamp ts, parameter twin, and twin's usage policy. For example, for BOTH policy the ts−twin $\leq$ tsd $\leq$ ts+twin means tsd is corresponded to the reference ts. The time window possibly should be: twin $\leq 1/(2F_{L0})$ s, namely $\leq 12.5$ ns for the clock L0 with $F_{L0} = 40$ MHz frequency. After merging the sub-events are stamped by the reference timestamp ts of the L1[n] trigger packet, while the full events — by the absolute event time ets = ats+ts, where ts is the reference timestamp of the L1<t> / L2<t> trigger packet and the described above ats is carried in the L1<t> / L2<t> packet body. Anyway the strictly no more than one L1<t> / L2<t> trigger instance should be produced for each L0 clock pulse, because otherwise we will have uncertainty in the full event merging. The same sub–event could be collected into $\geq 1$ full event(s), if this required by the L1<t> / L2<t> triggers of the different types t. Alternatively (not so easy to implement) the trigger of type t, which represents the more complicated conditions (i.e., more sophisticated and rare physical event), should have precedence over the simpler ones in the L1<t> / L2<t> production to resolve EvB[]s competition for the same sub–events. On the other hand, the most simple L1<t> / L2<t> trigger type could appear as often as the L0 clock. This means, in principle (too huge data flow should be processed!) we can exploit the whole setup in the almost free–streaming mode to accept any hits in the inner tracker.

## 6.4.2  FEM, L1[n] — SubEvB levels software interactions

In Fig. 6.7 and Table 6.3 we can see scheme of the interactions between L1[], FEM queue servers and SubEvB sub-event merger client(s). This two-phase scheme is suitable for both sub-event merging tags and allows us to issue requirements for the L1[], FEM queues (as well as for the SubEvB merger, which we consider later together with SubEvB queue). For the reliable numbering scheme we have two options:
• to keep two phases and on the second (afterTrig) one (see also section 6.5.4) to replace the GETTSPACK request by the GETNTHPACK.
• to eliminate the first (Trig) phase and request the L1[] queue as well as the FEM queues by the GETPACK(type) during the single "afterTrig" phase.

---

[6]L0 pulse counts of 40 MHz possibly should be multiplied by 25 to express time in nanoseconds.

Figure 6.7: Two-phase FEM — SubEvB levels software interactions (in case of timestamps merging tag). See Table 6.3 for the description.

### 6.4.2.1 L1[n] queue

The software on the L1[n] **fifo server** will behave as follows:
- some driver in the OS kernel:
† for each Ethernet frame arrival from the FC+TU subdet[n] card on the dedicated interface decodes this frame and obtains the trigger packet, which carries the merging tag (i.e. it is reliably numbered and/or timestamped with the nanosecond precision);
† puts this packet into the tail of L1[n] queue in the OS kernel;
- this queue:
† answers the SubEvB[n][] client(s) requests by sending the next packet of the corresponding type from the queue (this packet is still available for other SubEvB[][]s), or by sending the answer packet in the absence case;

Table 6.3: Two-phase FEM — SubEvB levels software interactions.

| L1[n] fifo | SubEvB level |
|---|---|
| gives the packet of type type from the queue head (without removing), if any, or answers by the ANSW_COPYTRIG → | ← COPYTRIG(type) requests the trigger packet |
| FEM level | SubEvB level |
| gives the fragment(s) of type type: from the time window, defined by ts and twin / with the requested number num, if any, or answers by the ANSW_GETTSPACK / ANSW_GETNTHPACK → | ← GETTSPACK(ts,twin,type) / GETNTHPACK(num,type) requests the fragments corresponded to the trigger packet and puts the resulting sub–event into the queue tail |

† responds by ACK / NAK / HIWAT / LOWAT packets to the FC+TU subdet[n] card to propagate the "full" / "near full" state on the lower DAQ levels and prevent the queue overfull;

† supports the garbage collection to remove from the queue packets, which already obtained by all the connected clients;

† supports the queue cleaning — full or on the packet type basis.

### 6.4.2.2  FEM queue

The software of the **FEM fifo** will behave as follows:

• some driver in the OS kernel:

† for each Ethernet frame arrival from the Dig[][] card on the dedicated interface decodes this frame and obtains the data fragment packet, which is reliably numbered and/or timestamped with the nanosecond precision;

† puts this fragment into the tail of FEM queue in the OS kernel;

• this queue:

† answers the SubEvB[n][] client(s) requests by sending the data fragment(s) of the corresponding type and number (and/or timestamp) from the queue, or by sending the answer packet in the absence case;

† responds by ACK / NAK / HIWAT / LOWAT packets to the Dig[n][] card to propagate the "full" / "near full" state on the lower DAQ levels and prevent the queue overfull;

† supports the queue cleaning — full or on the packet type basis.

In case of the VME–based read–out electronics the software on each VME master (either the VME CPU board or the standalone computer linked with the VME controller board) should provide the FEM fifo functionality described above.

## 6.4.3  SubEvB, L1<t> / L2<t> — EvB levels software interactions

*Table 6.4: Two-phase SubEvB — EvB levels software interactions.*

| L1<t> / L2<t> fifo | EvB level |
|---|---|
| gives the trigger packet of type type from the queue head, if any, or answers by the ANSW_GETPACK → | ← GETPACK(type) requests the trigger packet |
| SubEvB level | EvB level |
| gives the sub–event(s) of type type: from the time window, defined by ts and twin / with the requested number num, if any, or answers by the ANSW_GETTSPACK / ANSW_GETNTHPACK → | ← GETTSPACK(ts,twin,type) / GETNTHPACK(num,type) requests the sub–events corresponded to the trigger packet and puts the resulting full event into the queue tail |

In Fig. 6.8 and Table 6.4 we can see scheme of the interactions between L1<t> / L2<t>, SubEvB queue servers and EvB event merger clients. This two-phase scheme is unavoidable for both full event merging tags and allows us to issue requirements for all the mentioned queues (as well as for the EvB merger, which we consider later together with EvB queue). For the reliable numbering scheme on the second (afterTrig) phase (see also section 6.5.4) we should use the GETNTHPACK requests instead of the GETTSPACK ones.
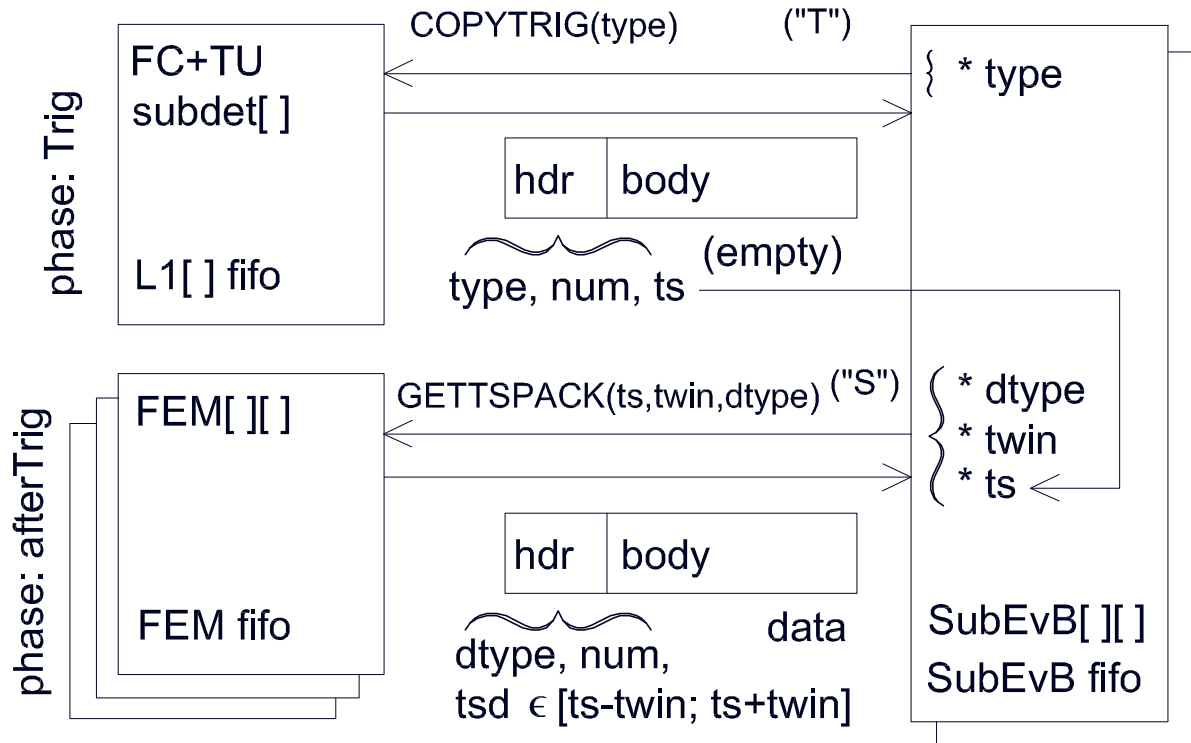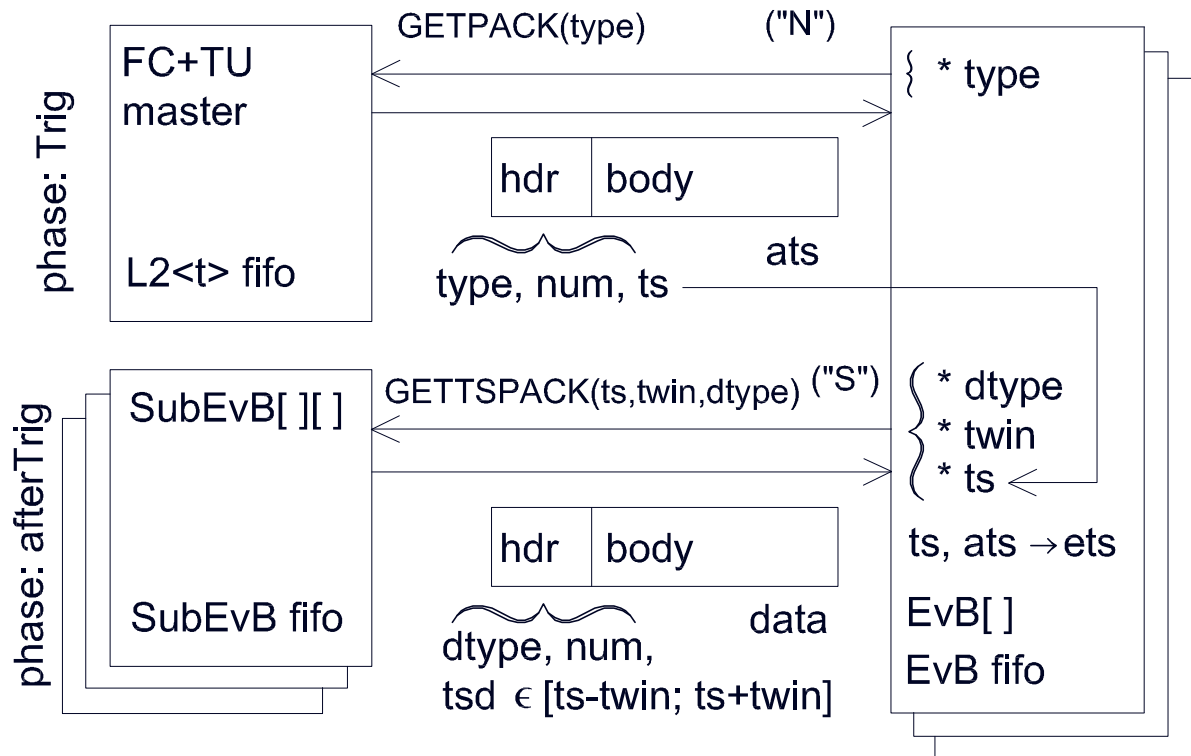
*Figure 6.8: Two-phase SubEvB — EvB levels software interactions (in case of timestamps merging tag). See Table 6.4 for the description.*

### 6.4.3.1 `L1<t>` / `L2<t>` queue

The software on the `L1<t>` / `L2<t>` **fifo server** will behave as follows:
- some driver in the OS kernel:
† for each Ethernet frame arrival from the FC+TU master card on the dedicated interface decodes this frame and obtains the trigger packet, which is reliably numbered and/or timestamped with the nanosecond precision;
† puts this packet into the tail of `L1<t>` / `L2<t>` queue in the OS kernel;
- this queue:
† answers the `EvB[]` clients requests by sending the next packet of the corresponding type from the queue, or by sending the answer packet in the absence case;
† responds by ACK / NAK / HIWAT / LOWAT packets to the FC+TU master card to propagate the "full" / "near full" state on the lower DAQ levels and prevent the queue overfull;
† supports the queue cleaning — full or on the packet type basis.

### 6.4.3.2 SubEvB level computers

The software on the **SubEvB[n][]** **computers** will behave as follows:
- sub-event merger entity in the OS kernel:
† requests the FEM queues for data fragments and `L1[n]` queue for trigger packets according to own configuration, obtains their, matches merging tags, and merges packets to produce the sub-event packet;
† puts this packet with number and timestamp given from the `L1[n]` trigger packet (for the "SubEvBT" / "SubEvBt" algorithms details see section 6.5.4) into the tail of SubEvB[n][]

queue in the OS kernel, possibly through some filter facility, which implements the `L1.5[n]` software trigger;

• this queue:

† answers the EvB[] clients requests by sending the sub–event of the corresponding type from the queue, or by sending the answer packet in the absence case;

† responds by ACK / NAK / HIWAT / LOWAT packets to the sub-event merger to propagate the "full" / "near full" state on the lower DAQ levels and prevent the queue overfull;

† supports the queue cleaning — full or on the packet type basis.

## 6.4.4   EvB — storage / pool levels software interactions
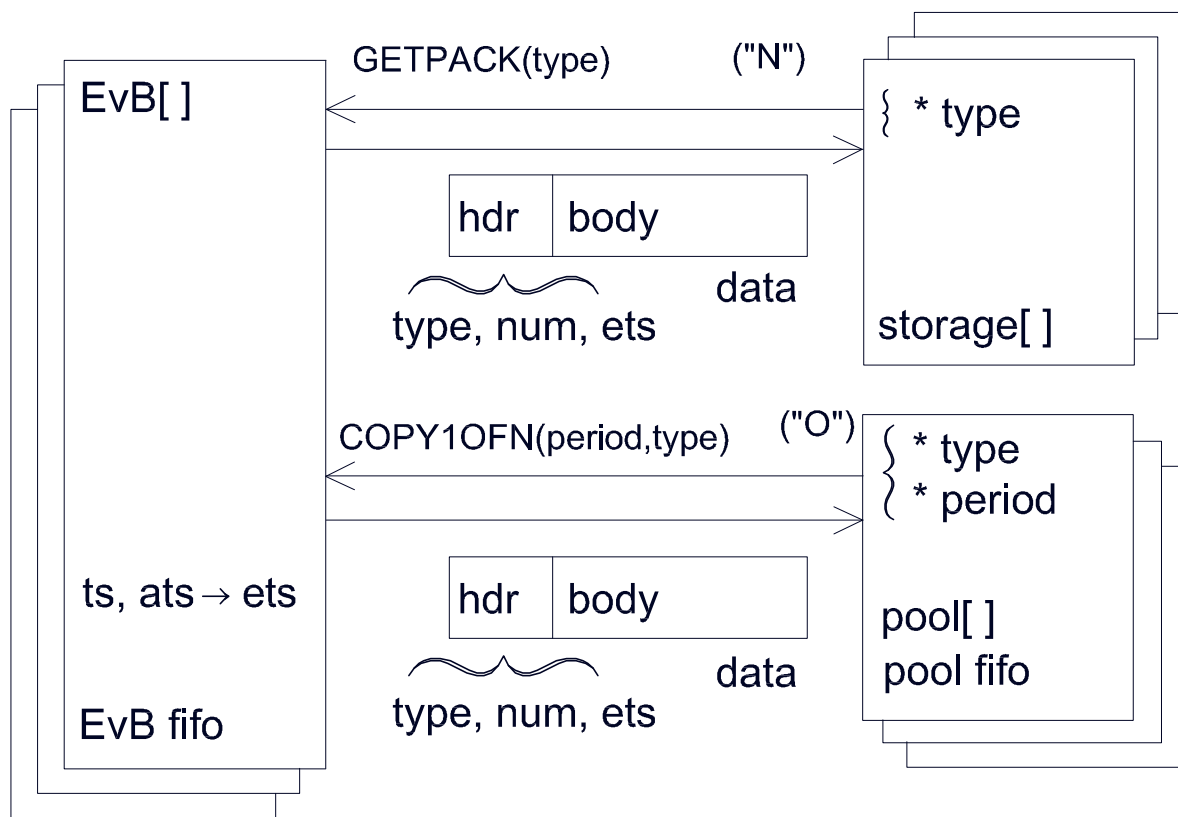


*Figure 6.9:  EvB — storage / pool levels software interactions.  See Table 6.4 for the description.*

In Fig. 6.9 and Table 6.5 we can see scheme of the interactions between EvB queue servers and storage, pool clients.  This scheme still the same for both merging tags and allows us to issue requirements for all the mentioned software entities.

### 6.4.4.1   EvB level computers

The software on the **EvB[] computers** will behave as follows:

• full event merger entity in the OS kernel:

† requests the L1<t> / L2<t> queue for trigger packets and SubEvB[][] queues for sub-events according to own configuration, obtains their, matches merging tags, and merges packets to produce the full event packet;

*Table 6.5: EvB — pool / storage levels software interactions.*

| EvB level | pool level | storage level |
|---|---|---|
| gives the full event (of type `type`) from the queue head, if any, or answers by the `ANSW_GETPACK` $\rightarrow$ | | $\leftarrow$ `GETPACK([type])` requests the full event and writes it to HDD |
| gives 1 of the N full events of type `type` from the queue head, if any, or answers by the `ANSW_COPY1OFN` $\rightarrow$ | $\leftarrow$ `COPY1OFN(N,type)` requests the full event and fills the pool of the ROOT events and histograms | |

† puts this packet with number and timestamp given from the `L1<t>` / `L2<t>` trigger packet (for the "EvBT" / "EvBt" algorithms details see section 6.5.4) into the tail of `EvB[]` queue in the OS kernel, possibly through some filter facility, which implements the `L2.5` software trigger;

• this queue:

† answers the `pool[]` client(s) requests by sending each N–th full event of the corresponding type from the queue (this packet is kept in the queue for the storage client), or by sending the answer packet in the absence case;

† answers the `storage[]` client requests by sending the next full event of the corresponding type from the queue (this packet is removed from the queue), or by sending the answer packet in the absence case;

† responds by ACK / NAK / HIWAT / LOWAT packets to the event merger to propagate the "full" / "near full" state on the lower DAQ levels and prevent the queue overfull;

† supports the queue cleaning — full or on the packet type basis.

### 6.4.4.2 Pool and storage level computers

*Table 6.6: Pool level — online visualization group software interactions.*

| ROOT events pool | online events processing (in particular, histogramming server) |
|---|---|
| gives the ROOT event of type `type` from the queue head, if any, or answers by the `ANSW_COPYTRIG` $\rightarrow$ | $\leftarrow$ `COPYTRIG(type)` requests the ROOT event and processes it |
| histogramming server | histograms visualization client |
| gives the current state of the ROOT histogram `histN` $\rightarrow$ | $\leftarrow$ requests the ROOT histogram `histN` and visualizes it |

The software on the **pool[] computers** will behave as follows:

• event pool entity in the OS kernel:

requests the `EvB[]` queues for the representative subset of full events according to own configuration (for the pool algorithm details see section 6.5.5), obtains these full events, and puts into the tail of `pool[]` queue in the OS kernel through the filter facility;

• this filter:

converts each of these full event packets into the representation by the corresponding ROOT

class, which is serialized and packetized again;
• this queue:
† answers the visualization group client(s) requests by sending the next ROOT packet of the corresponding type from the queue (this packet is kept in the queue for other clients), or by sending the answer packet in the absence case;
† supports the garbage collection to remove from the queue packets, which are already obtained by all the connected clients;
† supports the queue cleaning — full or on the packet type basis;
† provides two policies of the full queue handling: the cleaning of the oldest possibly not yet read packet (default) and the newcomer packet dropping.

For the proposed histogramming server and client see  section 6.5.6.

The **storage[] computers** possibly should be equipped by:
• the *writer(1)* utility [203];
• some network demultiplexer with the requests sending ability like the pool entity described above (possibly ported into the user context) to feed *writer(1)*.

Optionally EvB[] and storage[] entities could be situated on the same computers to feed *writer(1)* directly (without requesting) from the event merger.

### 6.4.5   SC software

In Fig. 6.3 we can see main elements of the SC subsystem.  The SC dispatcher and SC master[]s should contain CPUs and execute **SC software**.  The SC dispatcher obtains operator commands from the operator GUI and forwards their to the specific subdetector's SC master[], which interacts with SC slaves to perform the corresponding actions.  The correspondence between operator command and actions to be performed is established by the SC master[] local configuration. The remote network interactions between SC elements should be implemented by the standard client-server model (possibly using RPC) over TCP/IP or UDP/IP.

The SC slaves integrated into FEE, Dig, HV/LV, FC+TU cards are controlled by their firmware, while on SubEvB, EvB computers the SC slaves should be implemented by software (with exclusion of the remote reset solution, see  section 6.3.6).

## 6.5   Proposed software implementation

The key features of the proposed DAQ software, which are natural for the UNIX–like OS, are the following:
• splitting into the software modules interconnected by the experimental data streams;
• spreading of these modules over CPUs and networked computers easily;
• experimental data representation in the unified form of *ngdp* packets (see [203] and *packet(3,5,9)*);
• experimental data transportation by the streams of these packets, which (without using the media slower than memory) can:
† be buffered, copied, filtered, demultiplexed in a different manner;
† to cross the context boundaries from the kernel space to the user one and vice versa;
† be transferred between software modules locally and/or remotely, etc.
• software modules implementation in form of the user context processes or, in the kernel context, — the so called loadable kernel modules (KLD);

- implementation of the packet streams between the processes:
† locally — by the unnamed pipes and
† remotely — by the TCP/IP socket pairs;
- using the kernel threads to implement the process–like activity in the kernel context allows us:
† to avoid the preemptive scheduling;
† to reduce the unnecessary data copying in the memory at the context boundary crossing;
- using the **netgraph(4)** package [207] to implement the packet streams between the **netgraph(4)**–style kernel modules (nodes):
† locally — by the **netgraph(4)** data messages along the graph edges and
† remotely — by the TCP/IP **ng_ksocket(4)** pairs;
- high and easy scalability due to the object–oriented programming (OOP) style of the **netgraph(4)** package.

One of the freely distributable open source UNIX–like OSs with the **netgraph(4)** support, enough stable, reliable, modern, and dynamically developed simultaneously due to its very weighted up design policy, is FreeBSD.

## 6.5.1 *netgraph(4)* package: ready entities and possible improvements

The **netgraph(4) package** [207] provides the following entities of our interest:
- **ng_ksocket(4)** socket for the remote data exchange by IP protocol (TCP, UDP, etc.);
- **ng_ether(4)** interface for the remote data exchange by Ethernet protocol;
- **ng_socket(4)** socket for data and control messages interchange between the kernel context graph and the user context process;
- means for building the graph itself: **ngctl(8)**, **nghook(8)** utilities;
- service nodes for data flow managing: **ng_tee(4)**, **ng_one2many(4)**, **ng_split(4)**;
- nodes for debugging: **ng_source(4)**, **ng_hole(4)**, **ng_echo(4)**.

The **netgraph(4)** could be improved [208] in some aspects:
- the remote delivering of the **netgraph(4)** control messages is introduced;
- the function for the node insertion between the two already connected nodes is implemented (very useful for the software filters implementation);
- some additions for the **ngctl(8)**'s scripting language are implemented;
- the maximum data message size could be tuned by changing some OS kernel variables (without the kernel recompile).

## 6.5.2 *ngdp* framework

The **ngdp framework** [208] was implemented to be used for a big DAQ system software building and provides the following **netgraph(4)**–style node types:
- **ng_fifo(4)** supports the packets buffer with some queuing disciplines;
- **ng_em(4)** implements the SubEvB and EvB algorithms of the event merging;
- **ng_pool(4)** implements the pool level functionality according to the above requirements (see section 6.4.4.2);
- **ng_filter(4)** supports (chain of) KLD plug–in(s) with the filter procedure(s) and/or the external filter implemented by the (pipe of) user context process(es) or the (chain of) netgraph node(s);
- **ng_defrag(4)** reassembles the big *ngdp* packets obtained from the **ng_ksocket(4)** after

passing through network, which unavoidably fragments their to fit into the TCP/IP packets;
• ***ng_mm (4)*** (for Memory Mapping) provides the more efficient mechanism for the *ngdp* packets exchange between the kernel context graph and the user context process as the alternative to the standard ***ng_socket (4)***;
• ***ng_sv (4)*** (for SuperVisor) delivers the ***netgraph (4)*** control messages remotely, also could be used to automatize the remote ***netgraph (4)*** graph building;
• ***ng_mysource (4)*** and ***ng_kthsource (4)*** produce the packets stream for debugging.
The *ngdp* framework provides the following user context utilities:
• ***ngput (1)*** injects the ***pipe (2)***d packets into the graph;
• ***ngget (1)*** extracts the packets from the graph into the ***pipe (2)***;
• ***b2r (1)*** (for "binary–to–ROOT") converts the packetized binary data into the packetized ROOT class instances;
• ***r2h (1)*** (for "ROOT–to–histograms") is the runtime configurable histogramming server;
• ***histGUI (1)*** is the client for the ***r2h (1)***.

As we can see from the section 6.4 requirements, the SubEvB, EvB, and pool levels could be implemented by the very similar graphs like the following (shown in Fig. 6.10 with more details):

```
ng_ksocket ↘                                          ↗ ng_ksocket
···              ng_em(ng_pool) → [ ng_filter → [...]] ng_fifo         ···
ng_ksocket ↗                                          ↘ ng_ksocket
```
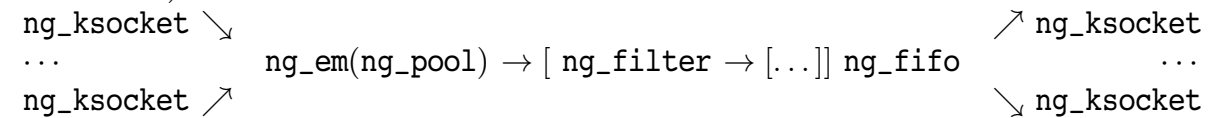
Of course, the queue and event merger nodes functionalities are slightly variated on the different levels. The FEM fifo as well as the L1[n] and L1<t> / L2<t> queues on the dedicated network nodes could be represented by the following scheme (see also Fig. 6.11):

```
                            ↗ ng_ksocket
ng_ether →   ng_fifo              ···
                            ↘ ng_ksocket
```
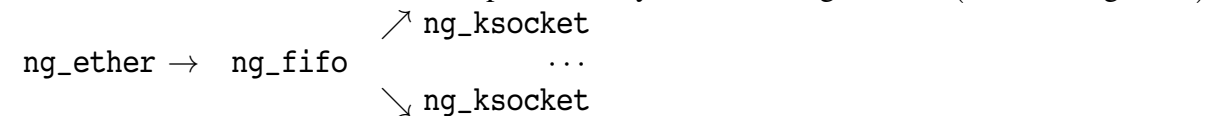
To work with the ***ng_ether (4)*** node the Ethernet headers should be stripped from the incoming packets and added to the outgoing ones. The `ng_fifo` node type should be able to do so, or the additional node type `ng_mux` with the single entry in the configuration map (see section 6.5.9) should be used.

For SubEvB level there is also option to implement FEM and L1[n] queues as the input channels of the event merger and, subsequently, use more fast medium (memory instead of network) to request and obtain the data packets, which should provide some performance benefit. This will lead to the following scheme, which requires to implement some configurable multiplexor `ng_mux` and essentially revise the event merger to be `ng_eml` (see also section 6.5.9):

```
                ↘                                          ↗ ng_ksocket
ng_ether → ng_mux →   ng_eml → [ ng_filter → [...]] ng_fifo         ···
                ↗                                          ↘ ng_ksocket
```
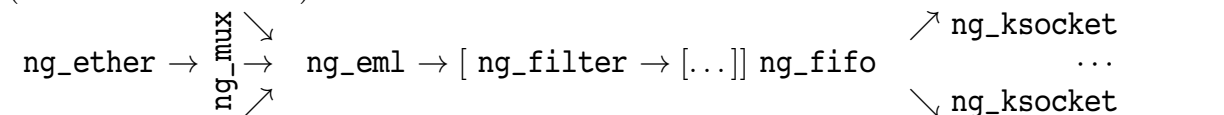
The further details about the *ngdp* provided entities can be found in [208, 209].

## 6.5.3   Queue node *ng_fifo (4)*

The **queue node type** (let it name as ***ng_fifo (4)***) according to the  section 6.4 requirements could be implemented with two mutually exclusive assumptions about the (sub)event merging tag will be used, namely:
• the reliable packet numbers. This requires the following modes (i.e. buffer disciplines) of the packet extraction from the queue (see also Table 6.7):
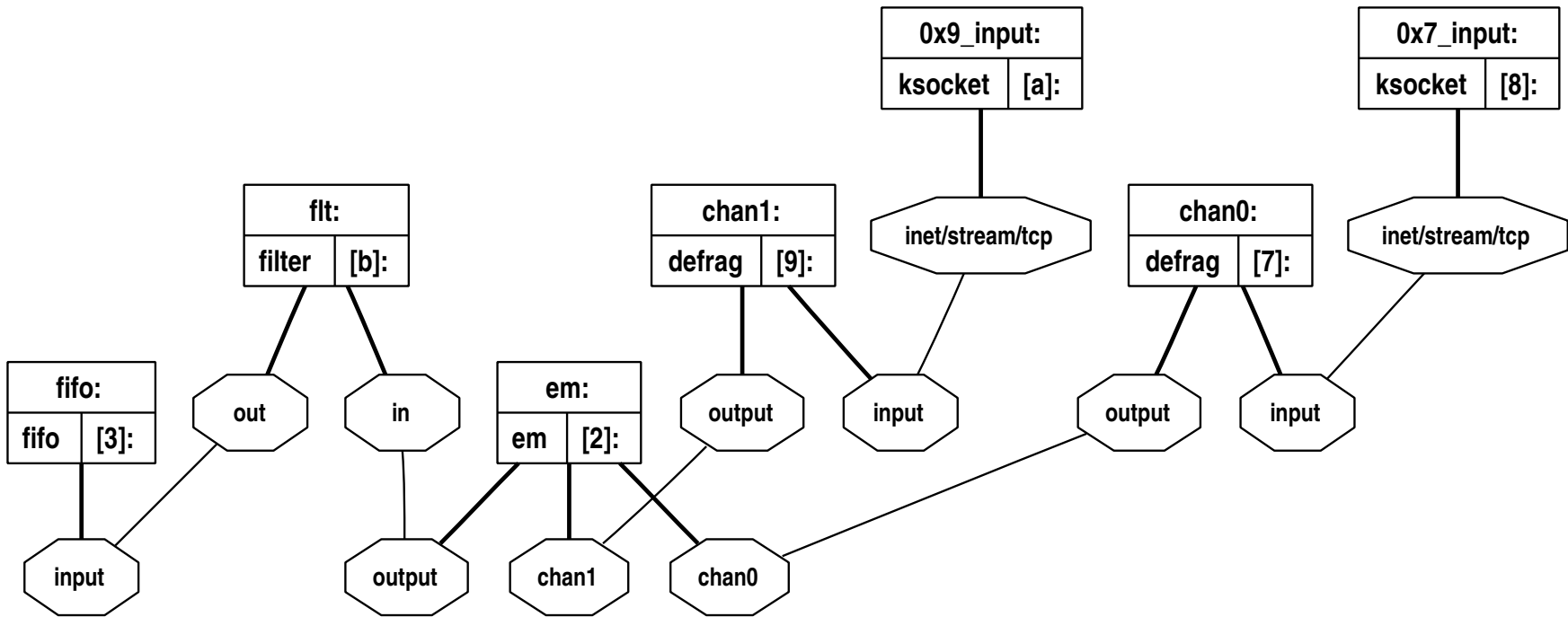
Figure 6.10: The SubEvB/EvB level implementation by the *ngdp* graph (automatically generated from the really built test graph).
Rectangles are nodes with: name (up), type (left), ID (right);
Octagons are hooks named within.
*ng_em* has two input channels (chan0 and chan1) from two data sources on FEM/SubEvB levels.
To simplify picture, the *ng_fifo* outputs are not shown (see Fig. 6.11 for the typical ones).
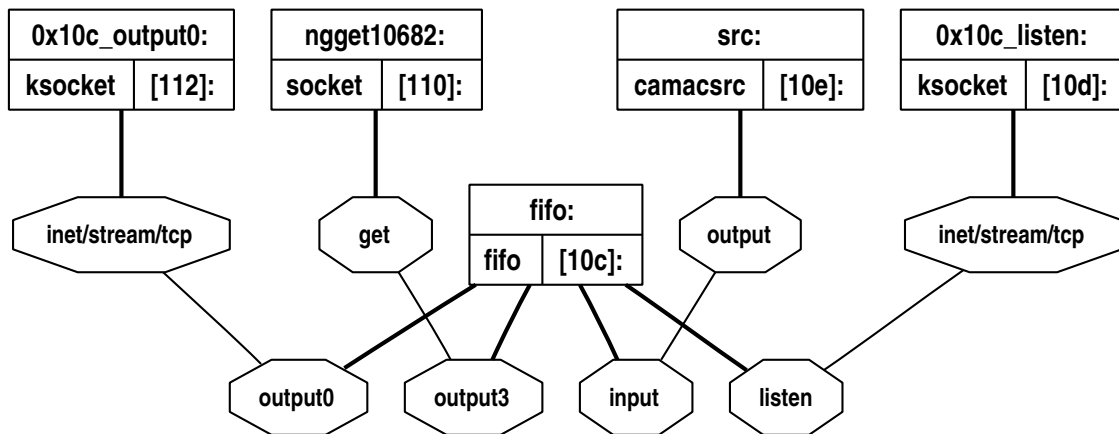
Figure 6.11: *The CAMAC FEM level implementation by the ngdp graph (automatically generated from the graph used by IntTarg CDAQ [210]).*
Legend the same as for Fig. 6.10.
*ng_fifo has two output streams – remote through accept()ing ng_ksocket and local through ng_socket, – as well as listen()ing ng_ksocket.*
*To implement the FEM queue the ng_camacsrc will be changed to the ng_ether.*

† "n": provides packet (of any type) from the queue head: GETPACK(). Possibly needed by EvB queue only.

† "N": provides packet of the defined type type: GETPACK(type). Needed by L1<t> / L2<t>, EvB, and pool queues.

† "T": provides packet of the defined type type without removing it from the queue: COPYTRIG(type). Needed by L1[n] queue, if it is not embedded into SubEvB, otherwise replaced by "N".

† "G": provides packet of the defined type type by its number num: GETNTHPACK(num,type). Needed by FEM and SubEvB queues.

† "O": provides one of each $N^{th}$ packets of the defined type type without removing it from the queue: COPY1OFN(N,type). Needed by EvB and pool queues.

• the timestamps. This requires the following buffer disciplines (see also Table 6.7):

† "N". Needed by L1<t> / L2<t>, EvB, and pool queues.

† "T": provides packet of the defined type type without removing it from the queue: COPYTRIG(type). Needed by L1[n] queue if it is not embedded into SubEvB, otherwise replaced by "N".

† "S": provides packet(s) of the defined type type from the time window [ts−twin, ts+twin]: GETTSPACK(ts,twin,type). Needed by FEM and SubEvB queues.

† "O". Needed by EvB and pool queues.

Both "nNTGO" [208] and "NTSO" set of the buffer disciplines are implemented now by two separate versions of ***ng_fifo (4)*** node type. It seems the latter one is more simple.

The FEM level could be partially based on the  VME and/or CAMAC hardware.   If the software to handle the VME master already exists under the OS without ***netgraph (4)*** support, then the most cheaper way is to implement the FEM queue in form of the process. This means:

• the ***ng_fifo (4)*** buffer implementation should be ported into the user context, the best way — to use the same C source for both the kernel node and the process.

• some converter should be inserted between the data reader from the VME and the FEM

Table 6.7: *Realistic queue disciplines for the different data processing levels.* "+" — *supported,* "+ (ts)" — *supported only for timestamp tag scheme,* "+ (n)" — *only for reliable number tag,* "−" — *need not.*

| Functionality, control and answer packet types and body contents, letter for legend | Supported on level: | | | | | |
|---|---|---|---|---|---|---|
| | FEM | L1[n] | SubEvB | L1<t>/ L2<t> | EvB | pool |
| Get the packet(s) of the defined type in the time window [ts−twin, ts+twin]: GETTSPACK with uint64_t timestamp, uint16_ts twin, and uint16_t packet type in the body ("S") | + (ts) | − | + (ts) | − | − | − |
| Answer: ANSW_GETTSPACK with uint16_t error code (EMPTY, NUMNOTFOUND, TYPENOTFOUND) in the body | + (ts) | − | + (ts) | − | − | − |
| Get an arbitrary packet of the defined type by its number: GETNTHPACK with uint32_t packet number and uint16_t packet type in the body ("G") | + (n) | − | + (n) | − | − | − |
| Answer: ANSW_GETNTHPACK with uint16_t error code (TYPENOTFOUND, NUMNOTFOUND, NUMNOTALREADY) in the body | + (n) | − | + (n) | − | − | − |
| Get the packet of the defined type without removing it from the queue: COPYTRIG with uint16_t packet type in the body ("T") | − | + | − | − | − | − |
| Answer: ANSW_COPYTRIG with uint16_t error code (EMPTY, NUMNOTFOUND, TYPENOTFOUND) in the body | − | + | − | − | − | − |
| Get the packet of the defined type: GETPACK with uint16_t packet type in the body ("N") | − | − | − | + | + | + |
| Answer: ANSW_GETPACK with uint16_t error code (EMPTY, NUMNOTFOUND, TYPENOTFOUND) in the body | − | − | − | + | + | + |
| Get one of each $N^{th}$ packets of the defined type without removing it from the queue: COPY1OFN with uint16_ts N (period) and uint16_t packet type in the body ("O") | − | − | − | − | + | + |
| Answer: ANSW_COPY1OFN with uint16_t error code (EMPTY, NUMNOTFOUND, TYPENOTFOUND) in the body | − | − | − | − | + | + |

queue to *ngdp*-packetize the data. Note this operation could be very CPU consuming dependent on the particular data format.

Other, the most right however expensive way is to reimplement the whole VME data read–out in the OS kernel as well as the data packetization and injection into the ***netgraph(4)*** graph. For the CAMAC hardware the number of DAQs are already built in this way using the *camac* package [211] and the ***ng_camacsrc(4)*** node [209] from the *ngdp* framework, e.g. SPILL DAQ, QUADRO DAQ [212], and IntTarg CDAQ [210], [213]. DAQ architectures like these are practically ready for the BM@N DAQ integration.

## 6.5.4   Event merger node *ng_em(4)*

The **event merger *ng_em(4)*** for both the SubEvB and EvB levels should work very similar for the timestamps merging tag scheme. The "SubEvBT" mode should (with some simplifications) behave as follows. The ***ng_em(4)*** node makes one loop over the configured merging rules (and corresponding requests) array and launches the kernel thread (see ***kthread(9)***) for each configured index, so each thread serves only its "own" request. The requests array example we can see in Table 6.8. Each request has the so called trigger input channel and is handled in two phases:

• In the first (Trig) phase each thread emits the COPYTRIG(type) ("T") control packet (see also Table 6.7) to the L1[n] trigger fifo through the hook of the trigger input channel and waits for a positive or negative response up to obtaining one or corresponding (trigger) timeout expiration. If the answer packet is obtained, the thread analyses the error code and repeats the request after either the same or increased trigger timeout. If the trigger input channel does not respond at all before the trigger timeout expiration, the thread repeats the request and waits during the increased trigger timeout. The trigger timeout can be increased up to the limit only. If the data packet from the L1[n] trigger fifo is successfully obtained, the ***ng_em(4)*** node extracts the ts timestamp[7] and goes to the second phase, which for each request index is handled by the same thread as the first phase. Note the FEM and L1[n] queues implementation as the SubEvB input channels will simplify this behaviour and replace the "T" request by the "N" one, however leads to essentially revised node type ng_eml (not implemented yet) and very high requirements to the memory size available for SubEvB.

• In the second (afterTrig) phase the thread emits the GETTSPACK(ts, twin, type) ("S") control packets (see also Table 6.7) to the FEM queues through all the hooks of the involved input channels (other than trigger one) using the ts trigger timestamp obtained in first phase. After that each thread waits for positive and/or negative responses up to obtaining all the required packets or regular timeout expiration. If the answer packet(s) is obtained, the thread analyses the error code(s) and either cleans the input channel storages and sends the full request again, or repeats request(s) in the failed input channel(s) (after either the same or increased regular timeout). If some input channel(s) does not respond at all before regular timeout expiration, the thread analyses the state of the responded channels and either repeats request(s) in the failed input channel(s), or cleans the input channel storages and sends the full request again. The regular timeout can be increased up to the limit only, too. If all the required data packets are obtained, the ***ng_em(4)*** node merges their (preserving the headers) into the sub-event packet of resulting type and with the number and timestamp of the trigger packet, and sends it to the output hook, if it exists, or drops packet otherwise.

---

[7]T type is also extracted and checked against the resulting type of the corresponding merging rule.

After that the thread sets a regular timeout to the nominal value, sends the full request again, and so on.

*Table 6.8: Merging rules configuration example of the non-T0 SubEvB[1][2]. The sub-event types are `ev` and `oev` with corresponding error types `err` and `oerr`. The same trigger types are used for both data-error pairs: `L1[1]ev` and `L1[1]oev`. The trigger packets are cloned remotely (on the `L1[1]` fifo server due to COPYTRIG requests using), or locally (on the SubEvB[1][] by the `ng_mux` node, when the `struct sockaddr` is obsolete).*

| input channel | out_type=ev (2000) | out_type=err (2100) | out_type=oev (2050) | out_type=oerr (2150) | struct sockaddr |
|---|---|---|---|---|---|
| `"chan0"` | in_type=20000 order=2 of number=3 | in_type=20100 order=3 of number=3 Optional | in_type=20010 order=2 of number=3 | in_type=20110 order=3 of number=3 Optional | 192.168.1.2 :54321 |
| `"chan1"` | in_type=20001 order=3 of number=3 | in_type=20101 order=2 of number=3 Optional | in_type=20011 order=3 of number=3 | in_type=20111 order=2 of number=3 Optional | 192.168.1.5 :54322 |
| `"chan2"` | in_type=510 order=1 of number=3 Trig L1[1]ev | — | in_type=511 order=1 of number=3 Trig L1[1]oev | — | 192.168.1.1 :12345 |
| `"chan3"` | — | in_type=510 order=1 of number=3 Trig L1[1]ev | — | in_type=511 order=1 of number=3 Trig L1[1]oev | 192.168.1.1 :12346 |

The "EvBT" mode for the timestamps merging tag uses the `L1<t>` / `L2<t>` fifo server in the trigger input channel and requests it by the `GETPACK(type)` ("N") control packets, while the regular inputs — by the `GETTSPACK(ts,twin,type)` ("S") ones like the "SubEvBT" mode. The requests array example we can see in Table 6.9.

For the reliable numbers tag merging we have two-phase "EvBt" algorithm (like described in [208]) with "N" trigger and "G" regular requests (see also Table 6.7). The SubEvB algorithm could be implemented as the single-phase "SubEvBt" one (see [208]), where `L1[n]` fifo has not dedicated meanings (it is simply one of the FEM queues, which requested by "N"), or like the two-phase "SubEvBT" algorithm described above, however uses the afterTrig phase "G" requests. The latter option seems preferable, because the two-phase algorithm should be more robust and less CPU-intensive. Anyway the existing ***ng_em(4)*** implementation [208] should be revised for BM@N purposes.

## 6.5.5  Pool node *ng_pool(4)*

The *ngdp* framework implements the **pool level functionality** by the ***ng_pool(4)*** node separately from the very similar ***ng_em(4)***. The existing ***ng_pool(4)*** algorithm [208] seems suitable for us. The requests array example we can see in Table 6.10. The production of the events in a ROOT class representation from the full events in a native binary format will be done by the ***ng_filter(4)*** node type using the ***b2r(1)*** utility [209].

Table 6.9: Merging rules configuration example of the non-T0 EvB[ ]. The full event types are ev, oev, BoB, and EoB.

| input channel | out_type=ev (10) | out_type=oev (11) | out_type=BoB (91) | out_type=EoB (81) | struct sockaddr |
|---|---|---|---|---|---|
| "chan0" | in_type=50 order=1 of number=... Trig L1ev | in_type=51 order=1 of number=... Trig L1oev | in_type=59 order=1 of number=... Trig L1BoB | in_type=58 order=1 of number=... Trig L1EoB | 192.168.0.10 :12345 |
| "chan1" | in_type=2000 order=2 of number=... | in_type=2050 order=2 of number=... | in_type=901 order=2 of number=... | in_type=801 order=2 of number=... | 192.168.1.52 :12345 |
| "chan2" | in_type=2001 order=3 of number=... | in_type=2051 order=3 of number=... | in_type=902 order=3 of number=... | in_type=802 order=3 of number=... | 192.168.1.51 :12346 |
| ... | ... | ... | ... | ... | ... |

Table 6.10: The pool[ ] requests array example.

| input channel | mask=0x7 period=20 | mask=0x3 period=10 | mask=0x1 period=1 | mask=0x1 period=1 | struct sockaddr |
|---|---|---|---|---|---|
| "chan0" | in_type=10 | in_type=11 | in_type=91 | in_type=81 | 192.168.10.1:54321 |
| "chan1" | in_type=10 | in_type=11 | — | — | 192.168.10.2:54321 |
| "chan2" | in_type=10 | — | — | — | 192.168.10.4:54321 |

## 6.5.6   *r2h(1)* histogramming server and *histGUI(1)* client

The *r2h(1)* **histogramming server** [209] could be executed to fill the ROOT histograms from the ROOT events. The *r2h(1)* could be fed by some network demultiplexer with the requests sending ability (e.g. the pool node *ng_pool(4)*), as it proposed above for the *writer(1)*. Optionally pool[ ] and histogramming server entities could be situated on the same computers to feed *r2h(1)* directly (without requesting) from the ROOT events pool.

The *r2h(1)* histograms assortment and parameters could be online configured using the *histGUI(1)* histogram visualization client [209] with the read–write access. This (single per server) client as well as many read–only *histGUI(1)* clients will be executed on the visualization group computers.

## 6.5.7   Inheritance from the *qdpb* framework

Note also some entities are inherited by the *ngdp* from the *qdpb* framework [203]:
• the application program interfaces (APIs):
† the *packet(3,9)* for the packet making, reading, writing, merging, etc.
† the *pack_types(3)* to deal with the packet types and corresponding attributes;
• the *writer(1)* utility to write the packet stream as the regular files on the HDD.
Some improvements for our needs are possible:
• the packet header could be improved by enlarging some existing fields and introducing the new ones (without keeping the backward compatibility);
• the packet body compression by the *zlib* [214] or XZ Embedded [215] package could be provided.

## 6.5.8 Reference and main data sequences: online and offline

More than one EvB[ ]s in the DAQ system will produce more than one event sequences (each with the whole set or at least subset of event types), which should be demultiplexed into the single chronologically ordered "main" sequence with BoB/EoB and BoR/EoR events in place for the offline analysis. The corresponding algorithm could not be implemented online for many reasons, in particular because it is problematic to clone BoB/EoB and BoR/EoR for each SubEvB[ ][ ], EvB[ ], writer[ ]. To simplify at least the offline chronologic ordering the "reference" event sequence should be produced. This sequence will contain other set of event types (at least uniquely mapped to the main set or possibly wider) and the same timestamps as in the main sequence. If the reference events will be merged by the single dedicated EvB, the reference sequence itself could be online chronologically ordered (e.g. by the special kind of EvB fifo, lets name it `ng_torder`, which implements the corresponding algorithm). The reference sequence should be stored on HDD by the single dedicated *writer(1)* to be available to assist the offline ordering of the main sequence. The reference sequence could be available for online analysis in whole (due to reasonable data flow) instead of "1 of N-th" online analysis of the main sequence. So, it is reasonable to feed the reference sequence by the T0 monitor data (possibly with some additions like BoB / EoB events, the error mark events from each subdetector) to be able to ensure online the acquired data quality (deadtime, data losses, number of triggers per type, etc.). The only reasonable discipline to be supported by the `ng_torder` queue is "n" (`GETPACK()` without type). Alternatively the As-Soon-As-Possible (ASAP) output policy (see also [209]) could be implemented, which means all the currently connected clients will obtain each output packet ASAP (without queueing and requesting).

The standard sorting algorithm implementations like *qsort(3)* or *mergesort(3)* are unsuitable for online chronologically ordering of the reference sequence due to very high memory requirements. Fortunately we could rely on essential property of full event stream produced by each EvB: packet numbers (and timestamps) for each type are increased monotonically. So, if we have "in hands" only one event of each type, we can say what of them have smallest timestamp (and should be output at first). Namely, the ordering algorithm should calculate timestamp differences between each produced event types, while the BoB and EoB types are treated specially, and the BoR is signaled by the packet numbers resetting to zero. Note the CPU-intensity of the algorithm will rapidly increase with the number of event types increasing (1 difference for 2 types, 3 — for 3, ..., $n_i = n_{i-1} + (i - 1)$ — for $i$). Of course, in case when some event type is more rare than others, the `ng_torder` again should have huge buffers capable to hold the whole burst for each frequent event type, or we should to do some special actions. For example, the EvB[T0] could provide the control packet at each negative request answer on the first (Trig) phase, so the `ng_torder` will know up to what time the corresponding rare event type will be absent. Also it will be very useful to have in the EoB trigger packet (available in EoB full event) the number of triggers produced during this burst for each event type. This allows us "to flush" at EoB arrival all the events belonging to current burst. The algorithm requires as the input parameters the number of produced event types and the minimum possible burst duration ($ts_{EoB}$ - $ts_{BoB}$). With this information the algorithm is able to discover packet losses analysing the sequences of packet numbers, however could not restore the proper chronological place for missed packets in the reference sequence in generic case.

In contrast, the *qsort(3)* or *mergesort(3)* could be used as the offline ordering algorithm for the main sequence, because the direct access data files will play the buffer role instead of

memory. Note the single sorting of any length data portion is not enough, so its trailer part should be sorted again with next portion and the ***mergesort(3)*** using is preferable. However, if the main sequence has not BoB / EoB events, we can not insert ones in such approach, because the reference sequence is unused. Also the data losses still unmarked.

Each stored data file as the main subsequence has not in generic case the property of monotonic increasing of packet numbers and/or timestamps even within each event type, due to additional reshuffling between EvB[]s and writer[]s. (This property survives only if each EvB[] has the only one associated writer[].) So, the ordering algorithm for the main sequence should operate with in-memory representation of the big data array like the whole burst. Using the direct access data files this representation for each event could be no more than 50..100 bytes. For some portions (like whole burst) of the reference sequence the singly-linked list of event representations will be built as well as the hash-table by timestamps. The list is used as template of the output (chronologically ordered) sequence. The hash-table elements will point to corresponding list elements and vice versa (for the garbage collection in hash-table). For each read-out event from the main subsequences the hash-function (and few comparison operations) finds the corresponding reference event and its place in the list. So, the special pointer in the found list element is assigned by address of the main event representation, which in particular contains the input file descriptor and offset of the main event. If the main event have not corresponded reference event but timestamp belongs to the current time range in the list (this means the reference event loss), the list is updated, and main event is collected as usual. If the main event belongs to the time range not yet in the list, its pointer will be stored in the separate "orphans" hash-table by timestamps. This allows us to traverse the data files only once (second reading is done at event output using already known packet offset and length) and sequentially, so each input event will appear in output. Periodically (after reading some input events portion) the output template part from head up to the first not yet encountered main event is written to output (the corresponding hash-table entries are removed) and its tail is prolonged by reading the reference sequence. The "orphans" hash-table is searched for main events after the list prolongation (from previous tail to current one) and the found events are collected into the list and removed from this hash-table. After that the regular reading of main subsequence files is continued. Of course, each main event not found during some predefined time period (like a few bursts) is assumed to be lost and the error mark packet with correct timestamp (from the reference counterpart) is outputted. The reference BoB and EoB are simply replicated into main sequence, if latter has not their. The BoB appearing with packet number of zero means the new run start, so the output file is switched.

## 6.5.9   Multiplexor node `ng_mux` (not implemented yet)

*Table 6.11: Configuration map example of the `ng_mux` node used together with configured by Table 6.8 the SubEvB[1][2] node.*

| remote address | output channel | remote address | output channel |
|---|---|---|---|
| 11:22:33:44:55:66 | "chan0" | 11:22:33:44:55:00 | "chan2" |
| 11:22:33:44:55:77 | "chan1" | 11:22:33:44:55:00 | "chan3" |

The multiplexor node type mentioned above in section 6.5.2 is intended to dispatch the input packets obtained from the Dig[][]s and FC+TU subdet[] through the Ethernet interface to the input channels of the `ng_eml` SubEvB[][]. These channels accumulate the packets locally instead of remote FEM and L1[] ***ng_fifo(4)*** queues on the dedicated

computers. The `ng_mux` should have single input hook connected to `lower` hook of the ***ng_ether(4)*** node and some output hooks according to the online configured map. Note the `ng_mux` should strip Ethernet header from the incoming packets and add it to the outgoing ones, while the correct source Ethernet address for the outgoing packets could be added by the ***ng_ether(4)*** node. The online configured map provides for each remote Ethernet address the corresponded local output hook name(s), and vice versa (see Table 6.11). The Ethernet address could be mapped to more than one hook, e.g. to handle FC+TU subdet[] trigger packets. This means each packet from such address will be copied to all these hooks.

# Chapter 7

# Beam requirements and tests

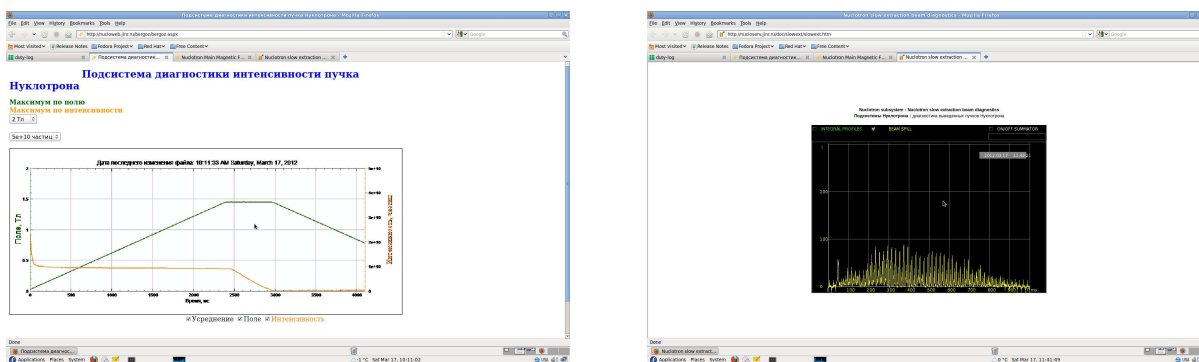## 7.1 Status of the beam (March 2012)



Figure 7.1: *The time dependence of the magnetic field and beam intensity in the accelerator ring (left) and time structure of the extracted beam measured at the focus F3 (right) for the 4.0 A·GeV deuteron beam.*
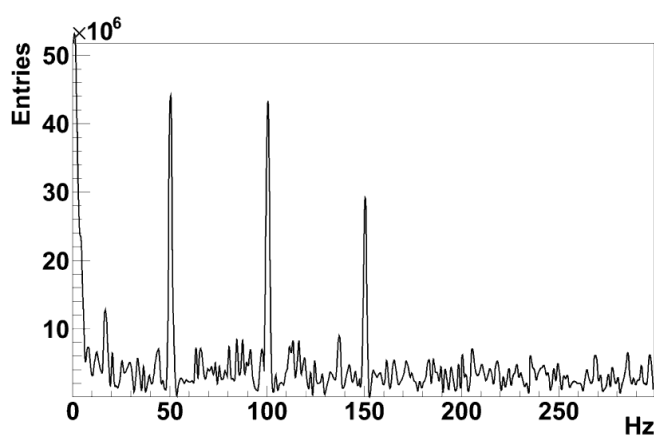


Figure 7.2: *The Fourier transform of the trigger rate timing dependence obtained from the signals coincidence of the scintillation detectors in the BM@N area for 4.0 A·GeV deuteron beam.*

Two beam tests were performed using reconstructed BM@N zone using 3.42 A·GeV carbon and 4.0 A·GeV deuteron beam. In both cases the beam was accelerated, slowly extracted and successfully transported to the BM@N zone. These energies corresponds to two lowest energy points of the project.

**Experimental hall 205**
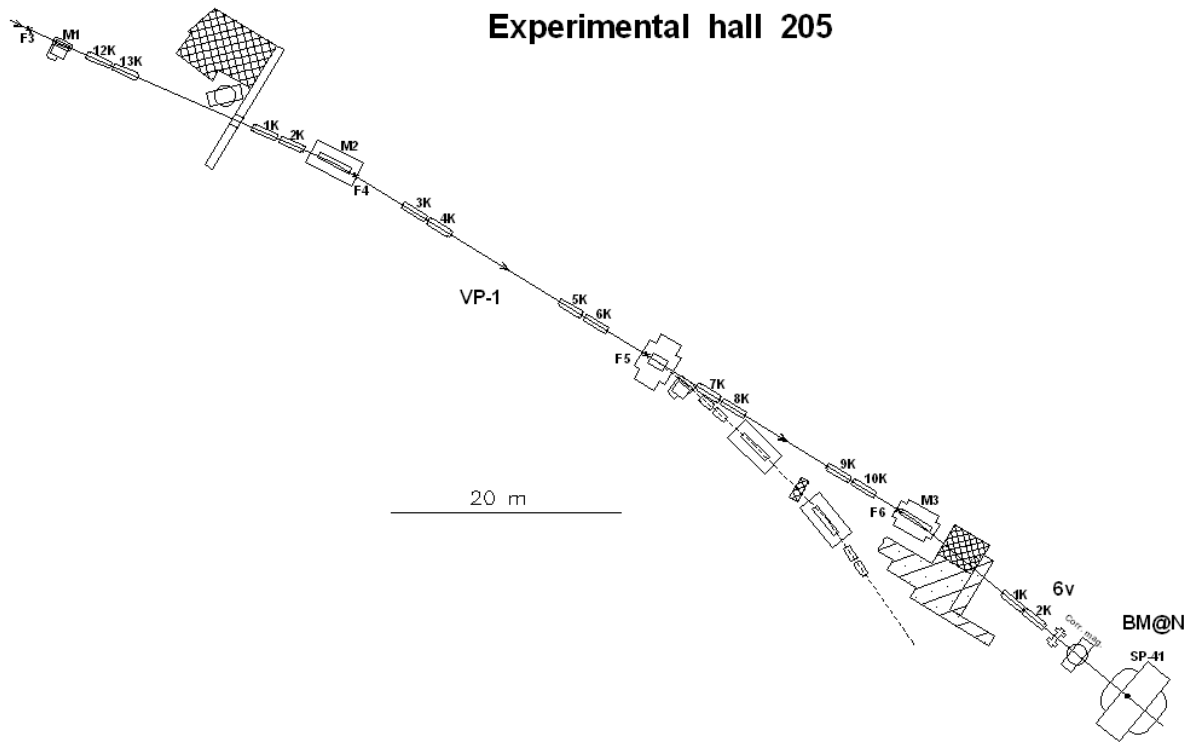
*Figure 7.3: Beam line scheme to the BM@N setup. $M_1$, $M_2$, $M_3$ are the bending dipole magnets, $nnK$ are the quadrupole lenses.*

*Table 7.1: Numerical values for the calculated regime of the $VP1$ beam line.*

|  | K12 | K13 | K1 | K2 | K3 | K4 | K5 | K6 | K7 | K8 | K9 | K10 |
|---|---|---|---|---|---|---|---|---|---|---|---|---|
| $k$, m$^{-2}$ | 0.171 | −0.109 | −0.138 | 0.208 | 0.174 | −0.115 | −0.136 | 0.196 | 0.182 | −0.122 | −0.120 | 0.154 |
| $I^*$, A | 1700 | 1080 | 1370 | 2060 | 1720 | 1140 | 1350 | 1940 | 1800 | 1210 | 1180 | 1520 |
| $I^{\mathrm{max}}$, A | 2030 | 1300 | 1640 | 2460 | 2060 | 1360 | 1610 | 2310 | 2150 | 1440 | 1420 | 1820 |

The left and right panels of Fig. 7.1 demonstrate the time dependence of the magnetic field and beam intensity in the accelerator ring and time structure of the extracted beam measured at the focus $F3$, respectively, for the 4.0 A·GeV deuteron beam. The ramping time of the field during this experiment was 3 kGs/s. The maximal value of the beam duty factor $(BDT)$, which can be reached in such conditions is about 10 %, while the requirement of the experiment is $BDT \geq 50$ %.

Next problem is the time structure of the extracted beam. Some periodical structures of the extracted beam can be observed in the right panel of Fig. 7.1. The Fourier transform of the trigger rate timing dependence obtained from the signals coincidence of the scintillation detectors in the BM@N area for 4.0 A·GeV deuteron beam is shown in Fig. 7.2. One can see

*Table 7.2: Numerical values for the calculated regime of the $6V$ beam line.*

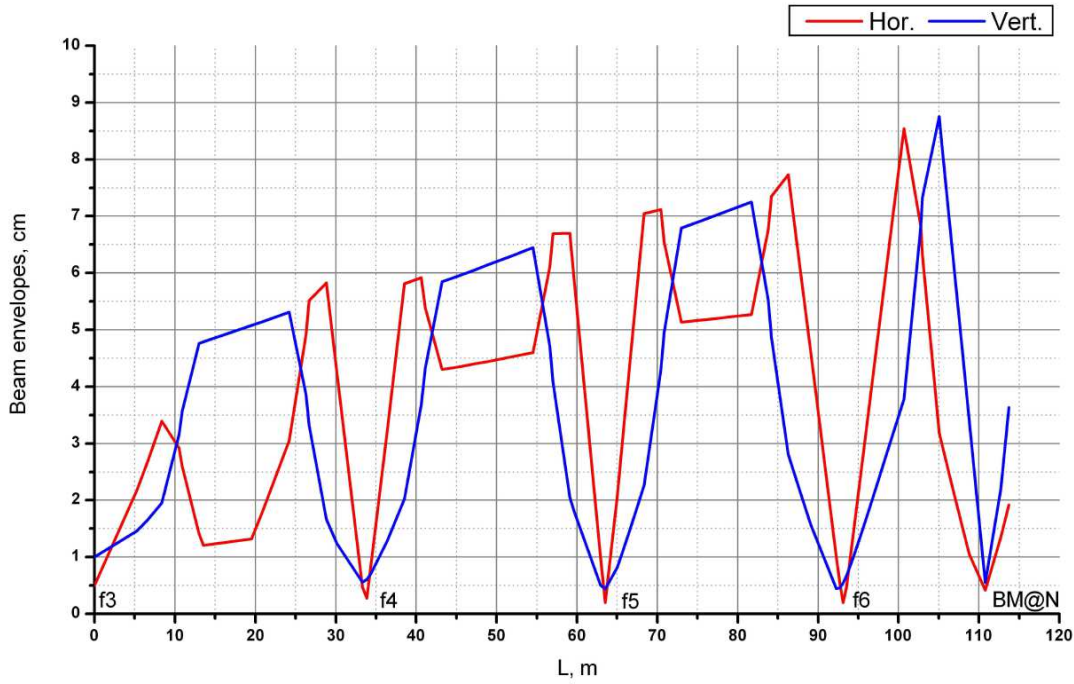|  | K1 | K2 |
|---|---|---|
| $k$, m$^{-2}$ | 0.215 | −0.223 |
| $I^*$, A | 2130 | 2210 |
| $I^{\mathrm{max}}$, A | 2550 | 2640 |
| $D^{\mathrm{max}}$ |  | $\sim 60$ % |

*Figure 7.4: A calculated option of the beam envelopes for beam emittances $\epsilon_{hor} = \epsilon_{vert} = 10\pi$ mm·mr.*

that $n \cdot 50$ Hz harmonics are very strong. Their are related with the pulsation in the current sources of the magnetic and resonance elements of the accelerator. The $Kdc$ coefficient reflecting the time structure of the beam is defined as

$$Kdc = \frac{1}{t_2 - t_1} \cdot \left[ \int_{t_1}^{t_2} (\mathrm{d}N/\mathrm{d}t)\mathrm{d}t \right]^2 / \left[ \int_{t_1}^{t_2} (\mathrm{d}N/\mathrm{d}t)^2 \, \mathrm{d}t \right] \, , \qquad (7.1)$$

where $\mathrm{d}N/\mathrm{d}t$ is the beam current, $(t_2 - t_1) = T_{\mathrm{ext}}$ is the time of the beam extraction. The conditions of the experiment require that the $Kdc$ coefficient should be about 0.85—0.95.

The successful running of the experiment requires the following parameters of the beam:

- Energy of the accelerated and extracted beam should be up to 4.65 A·GeV for $^{197}$Au and up to 6.0 A·GeV for symmetric nuclei like deuteron and carbon.

- The beam duty factor $BDT$ should be not less than 50 % in the energy domain of the experiment.

- The $Kdc$ coefficient reflecting the beam timing structure should be better than 85 %.

- The extracted beam emittance in the focal point $F3$ should be $\epsilon_{hor} = \epsilon_{vert} = 10\pi$ mm·mr in the energy domain of the experiment.

## 7.2   Beam transportation to the BM@N setup

The beam slowly extracted from the Nuclotron will be conducted through entire experimental hall to the BM@N working area. The total length of the beam path from the accelerator exit window to BM@N setup is about 150 m. The most part of the beam transportation is provided by the $VP1$ and $6V$ lines shown in Fig. 7.3. These lines include three bending
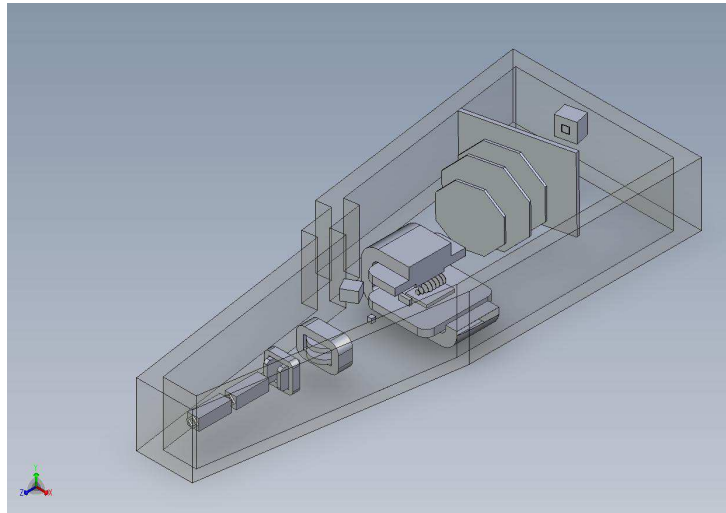
*Figure 7.5: The 6V beam line in 205 building consisting of the doublet of quadrupole magnets, two small dipole magnets and large aperture magnet SP41.*
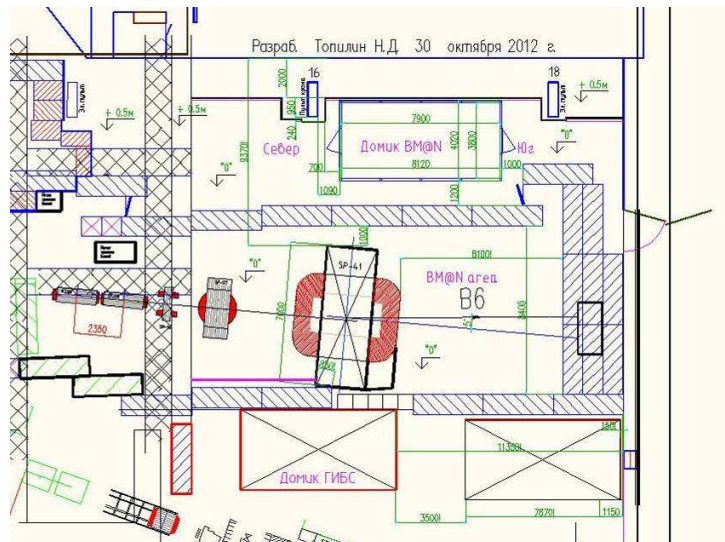


*Figure 7.6: The scheme of the BM@N experimental zone.*

dipole magnets $M_1$, $M_2$, $M_3$ and seven quadrupole lens doublets of the $K200$ type. The $6V$ beamline also includes two correcting magnets allowing to vary beam position at a target in the transverse plane. As a base it is suggested to use a typical optical scheme of the $VP1$ beam transportation line: three FDDF in the horizontal plane quartets form the beam crossovers at the $F4$, $F5$, and $F6$ points. The $1, 2K200$ of the $6V$ beam line forms the beam immediately at a BM@N target. Its polarity is chosen as $FD$.

A calculated option of the beam envelopes from the $F3$ focus point to the BM@N target position is given in Fig. 7.4. Requirements to the beam size at the target, $\approx 0.5$ cm $\times$ 0.5 cm, here have been satisfied. The calculation was done for extracted beam emittance values $\epsilon_{\text{hor}} = \epsilon_{\text{vert}} = 10\pi$ mm·mr. These are certainly higher then the expected ones for the claimed BM@N energy range $T_{\text{kin}} \geq 3.5$ A·GeV for $^{197}$Au. So, at this energy range the beam spatial parameters should be reached simpler. It is assumed that the existing power supply circuits of the beam lines will be used. Their realization allows one to supply the beam line lenses with DC currents up to 2200 A, or with higher currents in the pulse mode at a corresponding duty factor. Numerical values of this solution for $VP1$ and $6V$ are given in Tables 7.1

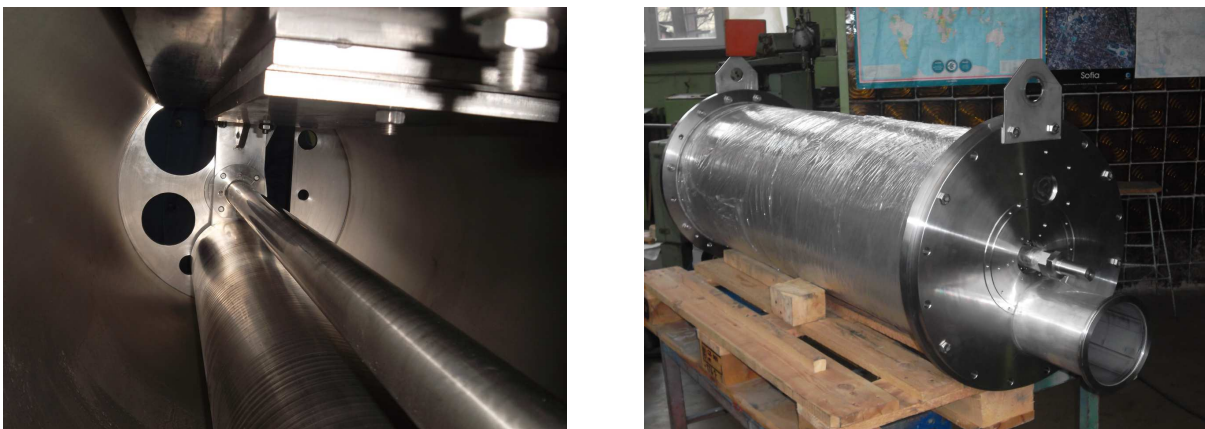Figure 7.7: Part of BM@N experimental zone before (left) and after (right) reconstruction.



Figure 7.8: New beam stopper inside (left) and outside (right) view.

and 7.2, respectively. The $k$ value equals $0.3 \cdot G/p$, where $G$ is the magnetic field gradient (T/m) and $p$ is the particle momentum (GeV/c). The minus sign of $k$ means defocusing in the horizontal plane. $I^*$ is lenses currents at the energy $T_{\mathrm{kin}} = 3.74$ A·GeV for the $^{197}$Au nuclei, the maximum energy for the beam lines to work in DC mode. $I^{\mathrm{max}}$ is the current, and $D^{\mathrm{max}}$ is the duty factor at the maximal energy. For the particular case $D^{\mathrm{max}}$ is defined by the $K2$ lenses of the $6V$ beamline.

The $M_1$ and $M_2$ bending dipole magnets provide beam transportation in the entire energy range. The $M_3$ have to be modernized or changed. Additional pole tips will be installed as an initial step.

The successful running of the experiment requires the serious investments to the beam lines, namely for:

- Test and recertification of the power supply circuits of the beam lines.
- Modernization of the water cooling of the lenses.
- Minimization of matter in the beam path (vacuum membranes, air gaps, diagnostic detectors). Currently, on an estimate, 6—8 g/cm$^2$ of the matter is present in the beam trace from the Nuclotron exit window to the BM@N setup.
- Improvement of the power sources stabilization of the beam line magnetic elements up to level of $\sim 0.5$ % for quadrupoles and 0.1 % for dipoles. Development and creation of the sources control system.
- Equipping of the beam lines with the additional profilemeters and other diagnostic apparatuses.
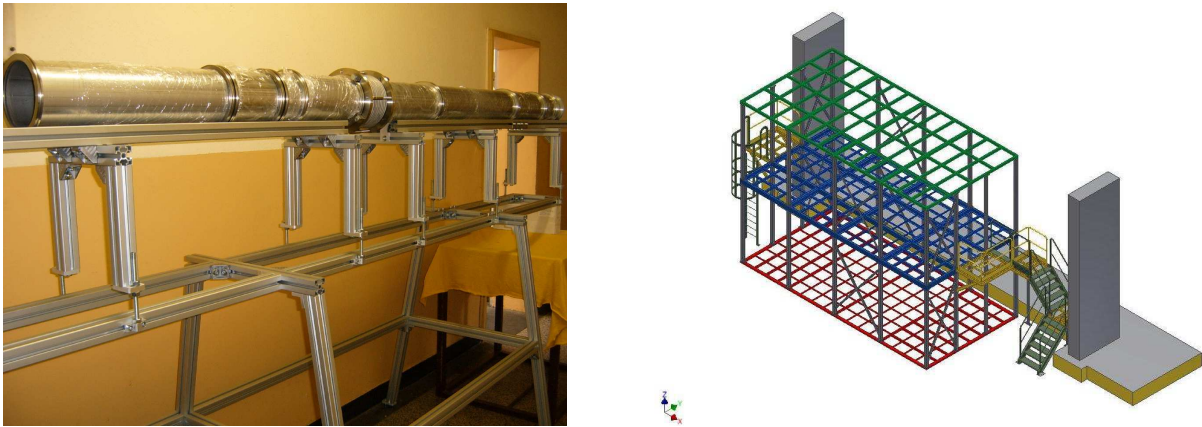
*Figure 7.9: Part of the beam pipe (left) and sketch of new experimental room (right).*
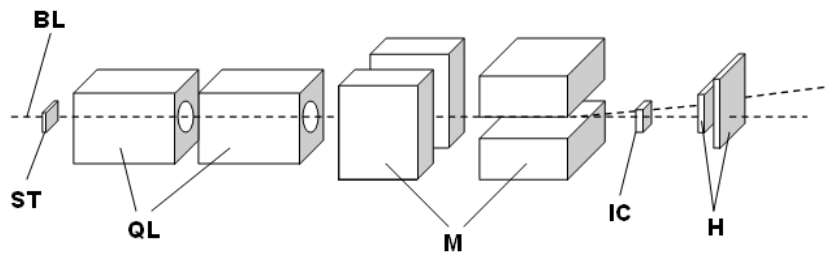


*Figure 7.10: The layout of the test beam in December 2011. BL is the optical axis of the 6V beam line, QL and M are the quadrupole and dipole magnets, respectively. IC is the coordinate ionization chamber, ST is the start scintillation counter, H are 2 planes of the scintillation hodoscopes.*

## 7.3 BM@N experimental zone

The setup will be placed in 205 building on the distance of about 110 m from the slow extraction line of Nuclotron. The magnetic scheme of the 6V line is shown in Fig. 7.5. The doublet of quadrupole lenses allows one to focus the beam on the target point, while two small dipole magnets can deflect the beam in the horizontal and vertical directions. The large aperture magnet SP41 will be used as an analyzing magnet at the first stage of the experiment. The field integral is approximately 2 T·m at the maximal current.

The positions of the cave and counting rooms of the BM@N experiment are shown in Fig. 7.6. The BM@N zone is under construction now. The part of the BM@N experimental
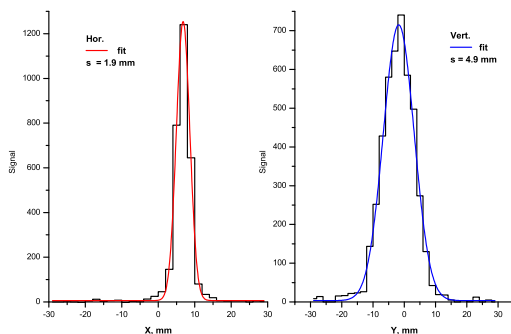


*Figure 7.11: The X- (left) and Y-coordinate (right) beam profile at the focus F4. The lines are the Gaussian fit results.*
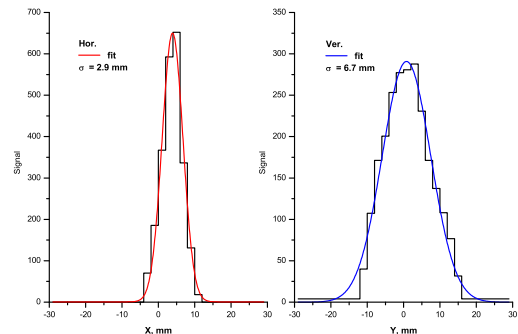


*Figure 7.12: The X- (left) and Y-coordinate (right) beam profile at the focus F5. The lines are the same as in Fig. 7.11.*
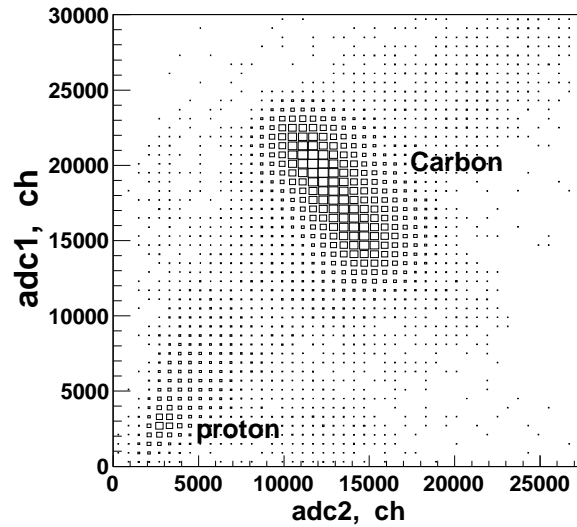
*Figure 7.13: The signal amplitudes correlation for one scintillation counter of the hodoscope.*
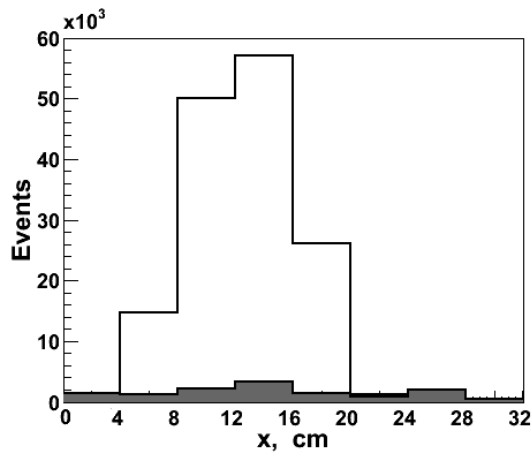


*Figure 7.14: The $X$-coordinate beam profile measured by scintillation hodoscope. The open and closed histograms are the carbon and singly charged particles, respectively.*
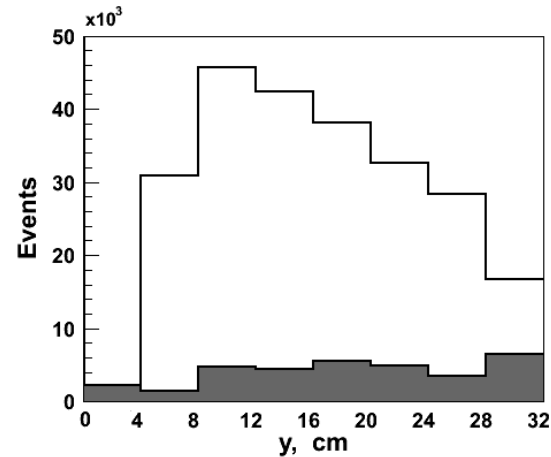


*Figure 7.15: The $Y$-coordinate beam profile measured by scintillation hodoscope. The histograms are the same as in Fig. 7.14.*

zone before and after reconstruction in October—November 2012 is shown in the left and right panel of Fig. 7.7, respectively.

New beam stopper presented in Fig. 7.8 will be installed 1.5 m upstream the lenses doublet in the first half of 2013. Part of the beam pipe and sketch of new experimental room are presented in the left and right panel in Fig. 7.9. The reconstruction of the experimental zone should be finished to the end of 2013.

## 7.4  Results of the test beams at Nuclotron

Two test beam experiments were performed with the 3.42 A·GeV carbon and 4.0 A·GeV deuteron beams in December 2011 [216] and March 2012 [217], respectively. The beam was accelerated, extracted, and transported using $VP1$ and $6V$ beamlines to the BM@N experimental area, where the hodoscopes and proportional chamber were installed. The beam diagnostic apparatus of the experiment were consisted of the proportional chambers placed at the focus points $F4$ and $F5$ of the $VP1$ beam transportation line for the estimation

*Figure 7.16: The layout of the test beam in March 2012. BL is the optical axis of the 6V beam line, QL and M1—M3 are the quadrupole and dipole magnets, respectively. IC is the coordinate ionization chamber, S1 and S2 are the start and stop scintillation counters, respectively. H are 2 planes of the scintillation hodoscopes.*



*Figure 7.17: The signal amplitudes correlation for one scintillation counter of the hodoscope.*

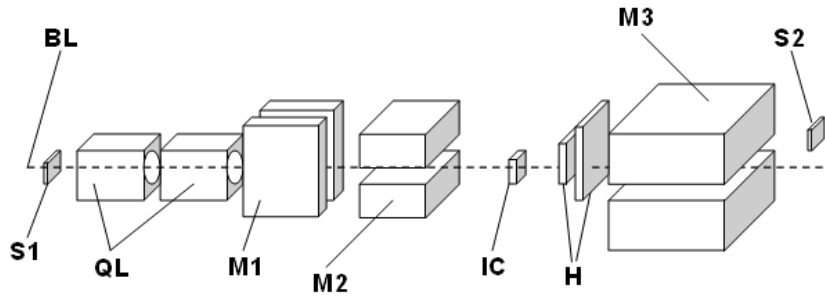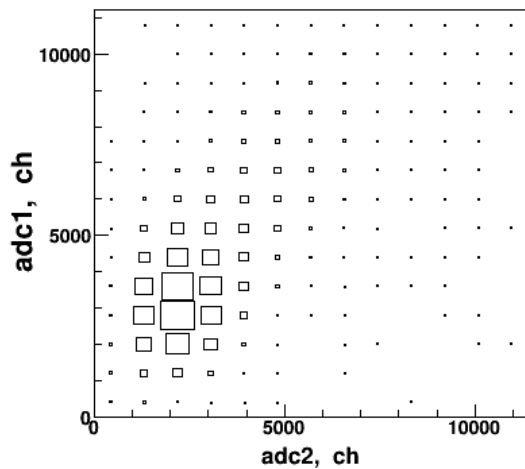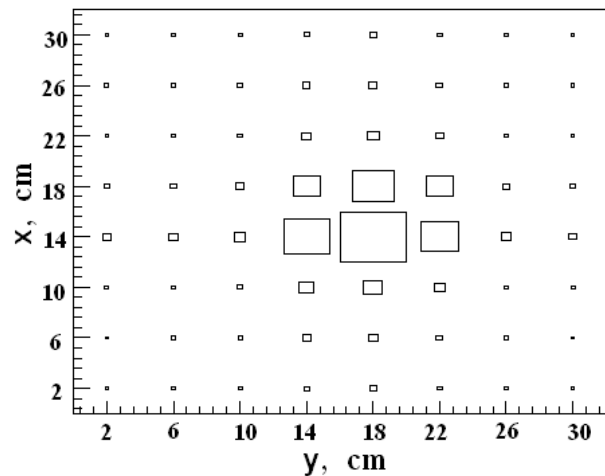*Figure 7.18: The $X$—$Y$ coordinate correlation for the deuteron beam profile measured by scintillation hodoscope.*

of the beam intensity and the beam size parameters.

The additional multiwire ionization chamber and two scintillation hodoscopes consisting of 8 scintillators with the size of $400{\times}40{\times}4$ mm$^3$ viewed by FEU-85 PMTs from both sides each were mounted at $\sim 2$ m and at $\sim 1.5$ m upstream the SP41 pole, respectively. The first and second hodoscopes provided the coordinate measurements in the horizontal and vertical planes, respectively. The start scintillation counter using the XP2020Q PMT was placed in front of the first quadrupole magnet. The scintillator size was $100{\times}40{\times}4$ mm$^3$. The scheme of the experiment is presented in Fig. 7.10. Here BL is the optical axis of the 6V beam line; QL and M are the quadrupole and dipole magnets, respectively; IC is the coordinate multi-wire ionization chamber; ST is the start scintillation counter, and H are 2 planes of the scintillation hodoscopes.

The beam was accelerated up to 3.42 A·GeV, extracted and transported using $VP1$ and $6V$ beamlines to the point, where the scintillation hodoscopes and ionization chamber were installed. During the experiment the lenses doublet of the $6V$ beam line was switched off, therefore, the beam was focused on the scintillation hodoscopes using last lenses doublet of the $VP1$ beam line.

The typical beam size distributions at the focuses $F4$ and $F5$ obtained with the multi-wire ionization chambers are demonstrated in Figs. 7.11 and 7.12, respectively. The beam
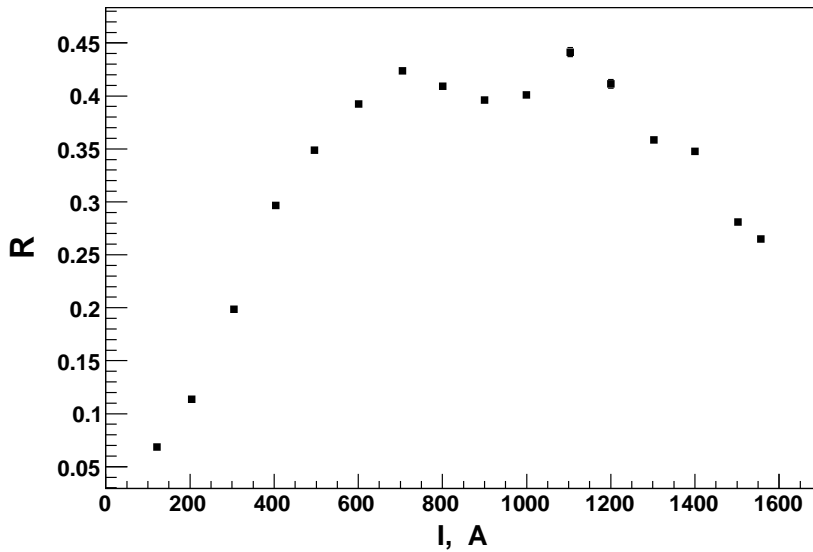
*Figure 7.19: The current curve of the analyzing magnet SP41.*

size $(1\sigma)$ in the horizontal direction is $\sim 2$ and $\sim 3$ mm at the $F4$ and $F5$ focus points, respectively. The beam size in the vertical direction is a bit larger, namely, it is $\sim 5$ and $\sim 6.7$ mm at the $F4$ and $F5$ focus points, respectively.

The VME-based data acquisition system was used for the data taking from the scintillation detectors. TQDC-16 module [218] developed at LHEP JINR allows one to measure the amplitude and time appearance of the signal. The correlation of the signal amplitudes taken from the both sides of one scintillation counter of the hodoscope is presented in Fig. 7.13. One can see the clean separation of the primary carbon nuclei and background single charged particles.

The beam profiles in the horizontal $(X)$ and vertical $(Y)$ planes are presented in Figs. 7.14 and 7.15, respectively. The open and closed histograms are the distributions for carbon and single charged particles, respectively. The particles were selected using the signal amplitudes correlation as shown in Fig. 7.13.

The methodical studies have been continued in March 2012 [217]. The layout of the experiment is presented in Fig. 7.16. Here BL is the optical axis of the $6V$ beam line; QL and M1—M3 are the quadrupole and dipole magnets, respectively; IC is the coordinate multi-wire ionization chamber; S1 and S2 are the start and stop scintillation counters, respectively, and H are 2 planes of the scintillation hodoscopes. The measurements were performed with 4 A·GeV deuteron beam transported to the $6V$ experimental zone.

The signal amplitudes correlation for one scintillation counter of the hodoscope obtained with 4 A·GeV deuteron beam is shown in Fig. 7.17. One can see that the peak position corresponds to one for single charged particles in Fig. 7.13. The $X$—$Y$ coordinate correlation for the beam profile is shown in Fig. 7.18. The size of the beam obtained with 4 A·GeV deuteron beam is less than in December 2012 due to inclusion of quadrupole magnetic lenses.

During March 2012 experiment the current curve of the analyzing magnet SP41 was obtained by means of the trigger counters S1 and S2. The ratio of the counts from these counters is presented in Fig. 7.19. The maximal value of current in the coils achieved with the existing source was 1560 A, what corresponds approximately 2/3 from the allowed current value for the coils. Also some correlation of the current value with the beam extraction was observed. These features were reflected in the technical requirements to the software for $3D$ Hall probes system.

# Chapter 8

# BM@N project cost and timelines

## 8.1   Time schedule

The time schedule of the BM@N experiment for 2013-2017 is presented in Fig. 8.1.
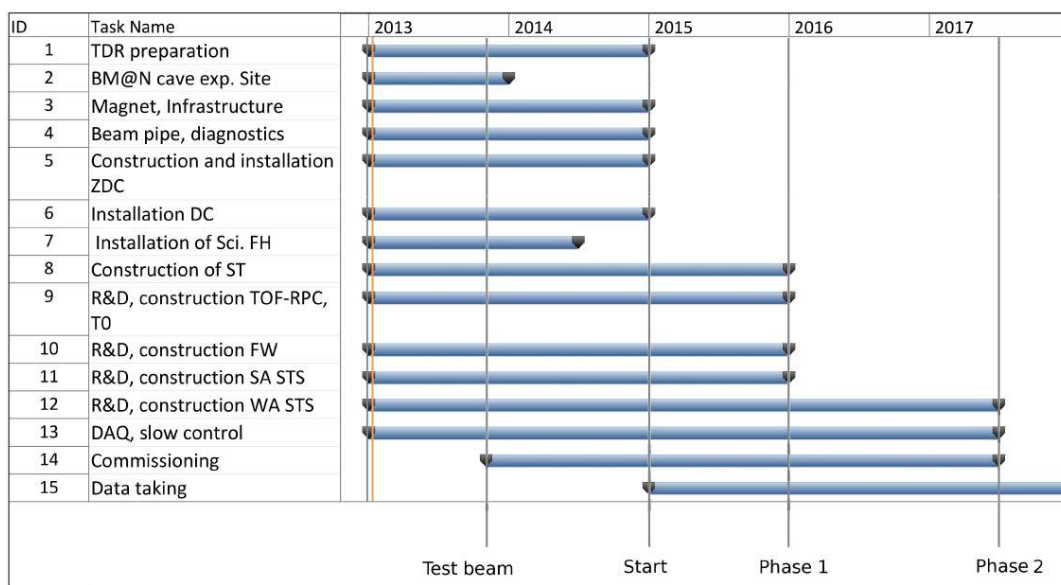


*Figure 8.1: The time schedule of the BM@N experiment.*

The duration of the experiment is 5 years in 2013—2017. The commissioning of the setup without and with inner tracker will started in 2015 and 2017, respectively. However, the BM@N experimental zone will be available for test beam measurements in 2013-2014. The main part of data taking with Au beam is planned in 2017.

The Technical Design preparation timetable is shown in Fig. 8.2. Four experimental parts: Magnet & Infrastructure, Outer tracker (DC, ST, and SciFH), TOF system, ZDC will be prepared in 2013. The Physics Book with the physical motivation and simulation of the main probes should be presented in January 2014. The other five TDRs: STS (small aperture and wide aperture), Forward Wall, Electromagnetic Calorimeters (BGO, Lead Glass, "shashlyk" type), FEE-DAQ, and Software will be presented in the second half of 2014.
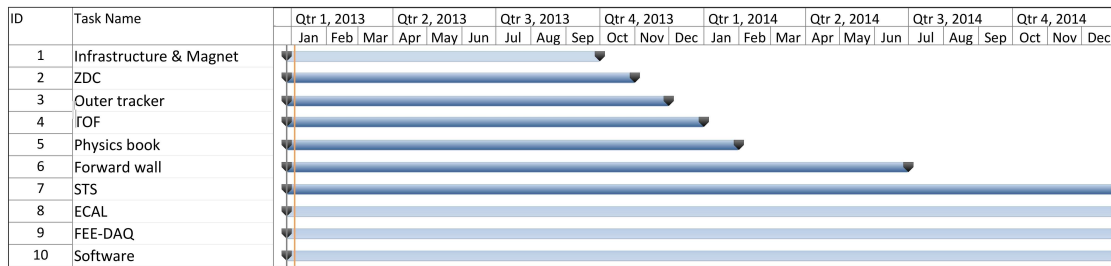
*Figure 8.2: TDRs preparation timetable.*

## 8.2 Request

The evaluated cost of the detectors construction and installation for the BM@N experiment is 22.15 M$. The cost of the subsystems is given in Table 8.1. This amount does not include the cost of the electromagnetic calorimeters except for the electronics and installation. The major cost of the project is the Wide Aperture STS, which estimated to 13 M$.

Our BM@N project cost estimation made in 2011 was 10.5 M$ with the request from JINR budget of 3.3 M$. The simulations performed in 2012 demonstrate the necessity to build the 8-station STS with the total channels number of $\sim 2000$k, that increases the cost of STS significantly.

The total beam-time request of Nuclotron beam including the tests and commissioning purposes is 2500 hours in 2013—2017. The main data taking will be performed with Au beam at 3.5, 4.0 and 4.65 A·GeV in 2017.

*Table 8.1: Preliminary BM@N subsystems cost estimation.*

| Subsystem | Cost (k$) |
|---|---|
| Magnet and Infrastructure | 1200 |
| Time-of-Flight detectors (RPC & T0) | 1100 |
| Drift Chambers (DC) installation | 650 |
| Straw tube Tracker (ST) | 700 |
| Scintillation Fiber Hodoscopes (SciFH) | 300 |
| Zero Degree Calorimeter (ZDC) | 400 |
| Forward Wall (FW) | 200 |
| Small Aperture Silicon Tracking System (SA STS) | 800 |
| Data Acquisition and Slow Control systems | 2000 |
| Computing system | 1000 |
| Electromagnetic Calorimetry | 800[1] |
| Wide Aperture Silicon Tracking System (WA STS) | 13000 |
| TOTAL: | 22150 |

---

[1]Only the cost of electronics and installation is included.

# References

[1] B. Friman, W. Nörenberg, and V.D. Toneev, Eur. Phys. J. A **3** (1998) 165.

[2] A. Andronic et al., Nucl.Phys. A **837** (2010) 65

[3] G.E. Brown, M. Rho, Phys. Rev. Lett. **66** (1991) 2720.

[4] T. Hatsuda, S. Lee, Phys. Rev. C **46** (1992) R34.

[5] M. Asakawa, C.M. Ko, P. Lévai, X.J. Qiu, Phys. Rev. C **46** (1992) R1159.

[6] G. Chanfray, P. Schuck, Nucl. Phys. A **545** (1992) 271c.

[7] M. Asakawa, C.M. Ko, Phys. Rev. C **48** (1993) R526.

[8] M. Herrmann, B. Friman, W. Nörenberg, Nucl. Phys. A **560** (1993) 411.

[9] C.M. Shakin, W.-D. Sun, Phys. Rev. C **49** (1994) 1185.

[10] R. Rapp, G. Chanfray, J. Wambach, Phys. Rev. Lett. **76** (1996) 368; Nucl. Phys. A **617** (1997) 472.

[11] F. Klingl, W. Weise, Nucl. Phys. A **606** (1996) 329; F. Klingl, N. Kaiser, W. Weise, Nucl. Phys. A **624** (1997) 527.

[12] B. Friman, H. J. Pirner, Nucl. Phys. A **617** (1997) 496.

[13] W. Peters, M. Post, H. Lenske, S. Leupold, U. Mosel, Nucl. Phys. A **632** (1998) 109; M. Post, S. Leupold, U. Mosel, Nucl. Phys. A **689** (2001) 753.

[14] D. Cabrera, E. Oset, and M.J. Vicente Vacas, Nucl. Phys. A **705** (2002) 90.

[15] S. Leupold, W. Peters, U. Mosel, Nucl. Phys. A **628** (1998) 311.

[16] D.B. Kaplan and A.E. Nelson, Phys. Lett. B **175** (1986) 57; A.E. Nelson and D.B. Kaplan, *ibid*, **192** (1987) 193.

[17] G.E. Brown and M. Rho, Phys. Rev. Lett. **66** (1991) 2720.

[18] E. Friedman, A. Gal, and C.J. Batty, Nucl. Phys. A **579** (1994) 518.

[19] A. Gal, Nucl. Phys. A **691** (2001) 268.

[20] M. Lutz, Phys. Lett. B **426** (1998) 12.

[21] A. Ramos and E. Oset, Nucl. Phys. A **671** (2000) 481.

[22] L. Tolós, A. Ramos, and A. Polls, Phys. Rev. C **65** (2002) 054907.

[23] X.S. Fang, C.M. Ko, G.Q. Li, and Y.M. Zheng, Phys. Rev. C **49** (1994) R608; G.Q. Li, C.M. Ko, and G.E. Brown, Phys. Lett. B **381** (1996) 17; C.M. Ko, J. Phys. G **27** (2001) 327.

[24] W. Cassing, E.L. Bratkovskaya, U. Mosel, S. Teis, and A. Sibirtsev, Nucl. Phys. A **614** (1997) 415.

[25] E.L. Bratkovskaya, W. Cassing, and U. Mosel, Nucl. Phys. A **622** (1997) 593.

[26] W. Cassing and E.L. Bratkovskaya, Phys. Reports **308** (1999) 65.

[27] W. Cassing, L. Tolós, E.L. Bratkovskaya, and A. Ramos, Nucl. Phys. A **727** (2003) 59.

[28] J. Schaffner-Bielich, V. Koch, and M. Effenberger, Nucl. Phys. A **669** (2000) 153.

[29] C. Hartnack, H. Oeschler, and J. Aichelin, Phys. Rev. Lett. **90** (2003) 102302.

[30] C. Fuchs, Amand Faessler, E. Zabrodin, and Yu-Ming Zheng, Phys. Rev. Lett. **86** (2001) 1974.

[31] D. Best et al., FOPI Collaboration, Nucl. Phys. A **625** (1997) 307.

[32] F. Laue et al., KaoS Collaboration, Phys. Rev. Lett. **82** (1999) 1640; A. Förster et al., J. Phys. G **28** (2002) 2011.

[33] V. Koch, Phys. Lett. B **337** (1994) 7.

[34] L. Tolós, A. Ramos, A. Polls, and T.T.S. Kuo, Nucl. Phys. A **690** (2001) 547.

[35] C. Hartnack, H. Oeschler, Y. Leifels, E.L. Bratkovskaya, and J. Aichelin, Phys. Rept. **510** (2012) 119.

[36] G. Agakichiev et al., Phys. Rev. Lett. **75** (1995) 1272; Th. Ullrich et al., Nucl. Phys. A **610** (1996) 317c; A. Drees, Nucl. Phys. A **610** (1996) 536c.

[37] M.A. Mazzoni, Nucl. Phys. A **566** (1994) 95c; M. Masera, Nucl. Phys. A **590** (1995) 93c; T. Åkesson et al., Z. Phys. C **68** (1995) 47.

[38] G.Q. Li, C.M. Ko, G.E. Brown, Phys. Rev. Lett. **75** (1995) 4007.

[39] W. Cassing, W. Ehehalt, C.M. Ko, Phys. Lett. B **363** (1995) 35; W. Cassing, W. Ehehalt, I. Kralik, Phys. Lett. B **377** (1996) 5.

[40] E.L. Bratkovskaya and W. Cassing, Nucl. Phys. A **619** (1997) 413.

[41] C. Ernst et al., Phys. Rev. C **58** (1998) 447.

[42] W. Cassing, E.L. Bratkovskaya, R. Rapp, and J. Wambach, Phys. Rev. C **57** (1998) 916.

[43] Y. Kim, R. Rapp, G.E. Brown, M. Rho, Phys. Rev. C **62** (2000) 015202.

[44] R. Rapp, J. Wambach, Adv. Nucl. Phys. **25** (2000) 1.

[45] R. Arnaldi et al., Phys. Rev. Lett. **96** (2006) 162302; J. Seixas et al., J. Phys. G **34** (2007) S1023.

[46] G. Agakichiev et al., Eur. Phys. J. C **41** (2005) 475.

[47] H. van Hees, R. Rapp, Phys. Rev. Lett. **97** (2006) 102301.

[48] C. Gale, S. Turbide, Nucl. Phys. A **783** (2007) 351.

[49] J. Ruppert, T. Renk, Phys. Rev. C **71** (2005) 064903; Erratum — *ibid.* **75** (2007) 059901.

[50] T. Renk, R.A. Schneider, W. Weise, Phys. Rev. C **66** (2002) 014902.

[51] K. Dusling, D. Teaney, I. Zahed, Phys. Rev. C **75** (2007) 024908.

[52] O. Linnyk, E.L. Bratkovskaya, V. Ozvenchuk, W. Cassing, and C.M. Ko, Phys. Rev. C **84** (2011) 054917.

[53] A. Toia et al., PHENIX Collaboration, Nucl. Phys. A **774** (2006) 743; Eur. Phys. J. **49** (2007) 243.

[54] Jie Thao for the STAR Collaboration, arXiv:1106.6146.

[55] O. Linnyk, W. Cassing, J. Mannien, E.L. Bratkovskaya, and C.M. Ko, Phys. Rev. C **85** (2012) 024910.

[56] G. Roche et al., DLS Collaboration, Phys. Rev. Lett. **61** (1988) 1069; R.J. Porter et al., DLS Collaboration, Phys. Rev. Lett. **79** (1997) 1229.

[57] E.L. Bratkovskaya, W. Cassing, R. Rapp, and J. Wambach, Nucl. Phys. A **634** (1998) 168.

[58] E.L. Bratkovskaya and C.M. Ko, Phys. Lett. A **445** (1999) 265.

[59] G. Agakichiev et al., HADES Collaboration, Phys. Rev. Lett. **98** (2007) 052302.

[60] E.L. Bratkovskaya and W. Cassing, Nucl. Phys. A **807** (2008) 214.

[61] L.P. Kaptari, B. Kämpfer, Nucl. Phys. A **764** (2006) 338.

[62] E.L. Bratkovskaya, W. Cassing, and U. Mosel, Phys. Lett. B **367** (1996) 12.

[63] E.L. Bratkovskaya, W. Cassing, U. Mosel, O.V. Teryaev, A.I. Titov, and V.D. Toneev, Phys. Lett. B **362** (1995) 17.

[64] E.L. Bratkovskaya, O.V. Teryaev, and V.D. Toneev, Phys. Lett. B **348** (1995) 283.

[65] A.R. Bodmer, Phys. Rev. D **4** (1971) 1601.

[66] R.L. Jaffe, Phys. Rev. Lett. B **38** (1977) 195; Erratum — *ibid.* 38 (1997) 617.

[67] J.T. Goldman, K. Maltman, G.J. Stephenson, K.E. Schmidt, F. Wang, Phys. Rev. Lett. **59** (1987) 627.

[68] J.T. Goldman, K. Maltman, G.J. Stephenson, J.L. Ping, F. Wang, Mod. Phys. Lett. A **13** (1998) 59.

[69] B. Schwesinger, F.G. Scholtz, H.B. Geyer, Phys. Rev. D **51** (1995) 1228.

[70] R.J. Oakes, Phys. Rev. **131** (1963) 2239.

[71] F.J. Dyson, N.H. Xuong, Phys. Rev. Lett. **13** (1964) 815.

[72] S. Graff, V. Grecchi, G. Turchetti, Lett. Nuovo Cim. **2** (1969) 311.

[73] A.T.M. Aerts, P.J.G. Mulders, J.J. de Swart, Phys. Rev. D **17** (1978) 260.

[74] J. Schaffner-Bielich, Nucl. Phys. A **691** (2001) 416.

[75] J.K. Ahn, et al., Phys. Rev. Lett. **87** (2001) 132504.

[76] H. Takahashi, et al., Phys. Rev. Lett. **87** (2001) 212502.

[77] R.H. Dalitz, D.H. Davis, P.H. Fowler, A. Montwill, J. Pniewski, J.A. Zakrzewski, Proc. Roy. Soc. Lond. A **426** (1989) 1.

[78] J. Schaffner, H. Stoecker, C. Greiner, Phys. Rev. C **46** (1992) 322.

[79] J. Schaffner, C.B. Dover, A. Gal, C. Greiner, H. Stoecker, Phys. Rev. Lett. **71** (1993) 1328.

[80] E.P. Gilson, R.L. Jaffe, Phys. Rev. Lett. **71** (1993) 332.

[81] J. Schaffner-Bielich, C. Greiner, A. Diener, H. Stoecker, Phys. Rev. C **55** (1997) 3038.

[82] J. Schaffner-Bielich, A. Gal, Phys. Rev. C **62** (2000) 034311.

[83] J. Belz et al. [E888 collaboration], Phys. Rev. Lett. **76** (1996) 3277; Phys. Rev. C **56** (1997) 1164.

[84] H.J. Crawford, Nucl. Phys. A **639** (1998) 417.

[85] G. Appelquist, et al. [NA52 (NEWMASS) collaboration], Phys. Rev. Lett. **76** (1996) 3907.

[86] T.A. Armstrong et al. [E864 collaboration], Phys. Rev. Lett. **79** (1997) 3612.

[87] L.E.Finch et al. [E864 collaboration], Nucl. Phys. A **661** (1999) 395.

[88] T.A. Armstrong et al. [E864 collaboration], Phys. Rev. C **70** (2004) 024902.

[89] J. Aichelin and J. Schaffner-Bielich, Relativistic Heavy Ion Physics (Landolt-Börnstein: Numerical Data and Functional Relationships in Science and Technology - New Series / Elementary Particles, Nuclei and Atoms), Springer, Heidelberg (2010); arXiv:0812.1341 [nucl-th].

[90] B.A. Li, L.W. Chen, and C.M. Ko, Phys. Rept. **464** (2008) 113.

[91] P. Ring and P. Schuck, 'The Nuclear Many Body Problem', 2005, Springer, Heidelberg.

[92] D.H. Youngblood, H.L. Clark, and Y.W. Lui, Phys. Rev. Lett. **82** (1999) 691.

[93] H. Stöcker and W. Greiner, Phys. Rept. **137** (1986) 277.

[94] J. Aichelin and C.M. Ko, Phys. Rev. Lett. **55** (1985) 2661.

[95] C. Sturm et al. [KaoS Collaboration], Phys. Rev. Lett. **86** (2001) 39.

[96] A. Förster et al., Phys. Rev. C **75** (2007) 024906.

[97] K. Tsushima, S.W. Huang, and A. Faessler, Phys. Lett. B **337** (1994) 245.

[98] K. Tsushima, A. Sibirtsev, and A.W. Thomas, Phys. Rev. C **59** (1999) 369; Erratum — *ibid.* **61** (2000) 029903.

[99] G. Agakishiev et al. [HADES Collaboration], Phys. Rev. C **82** (2010) 044907.

[100] G. Agakishiev et al. [HADES Collaboration], Eur. Phys. J. A **47** (2011) 21. arXiv:1010.1675 [nucl-ex].

[101] D. Brill et al. [KaoS Collaboration], Phys. Rev. Lett. **71** (1993) 336.

[102] L.B. Venema et al. [TAPS Collaboration], Phys. Rev. Lett. **71** (1993) 835.

[103] Y. Shin et al. [KaoS Collaboration], Phys. Rev. Lett. **81** (1998) 1576.

[104] Z.S. Wang, C. Fuchs, Amand Faessler, and T. Gross-Boelting, Eur. Phys. J. A **5** (1999) 275.

[105] F. Uhlig, A. Förster et al. [KaoS Collaboration], Phys. Rev. Lett. **95** (2005) 012301.

[106] C. Fuchs, Prog. Part. Nucl. Phys. **56** (2006) 1.

[107] A. Larionov and U. Mosel, Phys. Rev. C **72** (2005) 014901.

[108] H. Herrmann and the FOPI Collaboration, Prog. Part. Nucl. Phys. **42** (1999) 187.

[109] The CBM Physics Book 'Compressed Baryonic Matter in Laboratory Experiments', Eds: B.L. Friman, C. Höhne, J.E. Knoll, S.K.K. Leupold, J. Randrup, R. Rapp, and P. Senger; Springer, Series: 'Lecture Notes in Physics', Vol. **815** (2010), 960 p. ISBN: 978-3-642-13292-6.

[110] J. Ritman et al. [FOPI Collaboration], Z. Phys. A **352** (1995) 355.

[111] G. Agakishiev et al. [HADES Collaboration], Phys. Rev. Lett. **103** (2009) 132301.

[112] G. Agakishiev et al. [HADES Collaboration], Phys. Rev. C **80** (2009) 025209.

[113] A. Mangiarotti et al. [FOPI Collaboration], Nucl.Phys. A **714** (2003) 89.

[114] L. Ahle et al. [E866 collaboration], Phys. Lett. B **476** (2000) 1.

[115] M. Gazdzicki, M.I. Gorenstein, Acta Phys. Polon. B **30** (199) 2705.

[116] P. Chung et al. [E895 collaboration], Phys. Rev. Lett. **91** (2003) 202301.

[117] H. Sorge, Phys. Rev. C **52** (1995) 3291.

[118] J. Cleymans and K. Redlich, Phys. Rev. Lett. **81** (1998) 5284); Phys. Rev. C **60** (1999) 054908.

[119] P. Braun-Munzinger, J. Cleymans, H. Oeschler, K. Redlich, Nucl. Phys. A **697** (2002) 902.

[120] J. Cleymans, H. Oeschler, K. Redlich, S. Wheaton, Phys. Lett. B **615** (2005) 50.

[121] T.A. Armstrong et al. [E864 Collaboratio], Phys. Rev. C **59** (1999) 2699.

[122] C. Pinkenburg et al. [E895 collaboration], Phys. Rev. Lett. **83** (1999) 1295.

[123] P. Danielewicz et al., Phys. Rev. Lett. **81** (1998) 2438.

[124] P. Chung et al. [E895 collaboration], Phys. Rev. **66** (2002) 021901.

[125] C. Pinkenburg et al. [E895 collaboration], Nucl. Phys. A **698** (2002) 495c.

[126] S. Pal et al., Phys. Rev. C **62** (2000) 061903.

[127] W.J. Hogan, P.A. Piroue, and A.J.S. Smith, Phys. Rev. **166** (1968) 1472.

[128] Landolt-Börnstein, New Series, ed. H. Schopper, I/12 (1988).

[129] M. Antinucci et al., Lett. al Nuovo Cimento, **6** (1973) 121; M. Gaździcki and D. Röhrich, Z. Phys. C **71** (1996) 55; J. Bächler et al. [NA49 Collab.], Nucl. Phys. A **661** (1999) 45.

[130] G. Agakishiev et al., [HADES Collaboration], Phys. Rev. C **85** (2012) 054005.

[131] G. Agakishiev et al., [HADES Collaboration], Eur. Phys. J. A **48** (2012) 64.

[132] G. Agakishiev et al. [HADES Collaboration], Phys. Lett. B **690** (2010) 118.

[133] E.L. Bratkovskaya, J. Aichelin, M. Thomere, S. Vogel, and M. Bleicher, arXiv:1301.0786 [nucl-th].

[134] P.Senger and V.Friese, CBM Report 2011-1;
https://www.gsi.de/documents/DOC-2011-Aug-29-1.pdf .

[135] C. Blume, J. Phys. G **31** (2005) S57.

[136] A. Andronic, P. Braun-Münzinger, J. Stachel, and H. Stöcker, Phys. Lett. B **695** (2011) 203.

[137] V.D. Toneev and K.K. Gudima, Nucl. Phys. A **400** (1983) 173c.

[138] V.D. Toneev, N.S. Amelin, K.K. Gudima, and S.Yu. Sivoklokov, Nucl. Phys. A **519** (1990) 463c.

[139] N.S. Amelin, E.F. Staubo, L.S. Csernai et al., Phys. Rev. C **44** (1991) 1541.

[140] Yu.A. Batusov, J. Lukstins, L. Majling, and A.N. Parfenov, Phys. Elem. Part. Atom. Nucl. **36** (2005) 169.

[141] H. Stöcker et al., Nucl. Phys. A **827** (2009) 624c.

[142] E.L. Bratkovskaya, W. Cassing, and U. Mosel, Phys. Lett. B **424** (1998) 244.

[143] D. Kharzeev and A. Zhitnitsky, Nucl. Phys. A **797** (2007) 67.

[144] O. Rogachevsky, A. Sorin, and O. Teryaev, Phys. Rev. C **82** (2010) 054910.

[145] D.T. Son and P. Surowka, Phys. Rev. Lett. **103** (2009) 191601.

[146] X. Artru, M. Elchikh, J.-M. Richard, J. Soffer, and O.V. Teryaev, Phys. Rept. **470** (2009) 1.

[147] M. Jacob and J. Rafelski, Phys. Lett. B **190** (1987) 173.

[148] Z.-T. Liang and X.-N. Wang, Phys. Rev. Lett. **94** (2005) 102301; Erratum — *ibid.* **96** (2006) 039901.

[149] V.P. Ladygin, A.P. Jerusalimov, and N.B. Ladygina, Phys. Part. Nucl. Lett. **7** (2010) 349.

[150] A.V. Efremov, L. Mankiewicz, and N.A. Tornqvist, Phys. Lett. B **284** (1992) 394.

[151] Silicon Tracking System (STS), Technical Design Report, CBM Collaboration, December 2012, GSI, Germany.

[152] Kh.U. Abraamyan et al., Nucl. Instrum. Meth. A **628** (2011) 99.

[153] V.V. Ammosov et al., Instrum. Exp. Tech. **53** (2010) 175.

[154] J. Pietraszko et al., Nucl. Instrum. Meth. A **618** (2010) 121.

[155] M. Mikuz et al., Nucl. Instrum. Meth. A **579** (2007) 788; V. Adam et al., Eur. Phys. J. C **33** (2004) s1014.

[156] M. Golubeva et al., Nucl. Instrum. Meth. A **598** (2009) 268.

[157] J. Instr. V3 (2008) S08005 42.

[158] `http://fairroot.gsi.de`

[159] `http://wwwasd.web.cern.ch/wwwasd/geant`

[160] Nucl. Instr. Meth. Phys. Res. A **497** (2003) 389–396.

[161] A.Kotynia, Simulation of realistic detector response in the CBM Silicon Tracking System, CBM Progress Report (2009) 7.

[162] I. Kisel, Event reconstruction in the CBM experiment, Nucl. Instr. Meth. Phys. Res. A **566** (2006) 85.

[163] S. Gorbunov and I. Kisel, An analytic formula for track extrapolation in an inhomogeneous magnetic field, CBM-SOFT-note-2005-001 (2005) 18.

[164] I. Abt, D. Emeliyanov, I. Kisel, S. Masciocchi, Nucl. Instr. and Meth. A **489** (2002) 389.

[165] I. Kisel, I. Kulakov, I. Rostovtseva and M. Zyzak, CA Based Track Finder with STS Detector Inefficiency, GSI Scientific Report (2010) 51.

[166] ALICE Collaboration, Time of Flight System, Technical Design Report, CERN/LHCC 2000-12 ALICE TDR 8, 16 February 2000.

[167] The STAR TOF collaboration, Technical design update to proposal for a large area time of flight system for STAR, August 16, 2005.

[168] J. Velkovska et al. Time-of-Flight of the PHENIX high-Pt Detector. (2005) Conceptual Design Report.

[169] I. Deppner et al., Nucl. Instr. Meth. A **661** (2012) 121—124.

[170] A.V. Akindinov et al., Nucl. Insr. Meth. A **533** (2004) 74–78.

[171] V. Ammosov et al., Nucl. Insr. Meth. A **578** (2007) 119–138.

[172] Yi Wang et al., IEEE NSS-MIC, Dresden, Germany (2008) 19—25.

[173] L. Naumann, R. Kotte, D. Stach, J. Wustenfeld, Nucl. Instr. Meth. A **635** (2013) 113—116.

[174] V.A. Gapienko et al. Thin Glass MRPC Rate Capability at Moderate Warming. IHEP Preprint, **2012-7**, Protvino (2012) 1—11.

[175] V.V. Ammosov et al. Properties of a Six-Gap Timing Resistive Plate Chamber with Strip Readout. JINR Commun., **E13-2009-86**, Dubna (2009) 1–10.

[176] V.A. Gapienko et al. Test of Strip Readout MRPC with Amplifier Discriminator Based on the NINO Chip. JINR Preprint, **E13-2012-69**, Dubna (2012) 1–12.

[177] Y.J. Sun et al., Nucl. Instr. Meth. A **593** (2008) 307–313.

[178] M. Abbrescia et al., Nucl. Instr. Meth. A **593**, (2008) 263—268.

[179] F. Anghinolfi et al., IEEE Trans. Nucl. Sci. **51** 5, (2004) 1974—1978.

[180] M. Palka et al., IEEE Nucl. Sci. Symp. Conf., Rec.1 (2008) 1398–1404.

[181] I. Frohlich et al., IEEE Trans. Nucl. Sci. **55** (2008) 59–66.

[182] `http://afi.jinr.ru/TDC32VL`

[183] J.Christiansen. HPTDC. High Performance Time to Digital Converter. Ver.2.2 for HPTDC ver.1.3. CERN/EP-MIC, March (2004).

[184] K. Doroud, D. Hatzifotiadou, S. Lia, M.C.S. Williams, A. Zichichi, R. Zuyeuski, Nucl. Instr. Meth. A **660** (2011) 73–76.

[185] D. Bederede et al., Nucl. Instr. and Meth. A **367** (1995) 88; I. Augustin et al., Nucl. Instr. and Meth. A **403** (1998) 472.

[186] V. Fanti et al., Nucl. Instr. Meth. A **574** (2007) 433–471.

[187] V. Peshekhonov et al., Phys. Part. Nucl. Lett. **8** (2012) 172.

[188] V. Bychkov et al., JINR Commun., **R13-98-269**, Dubna (1998) (in Russian).

[189] V. Bychkov et al., Part. Nucl. Lett., **2** (2002) 64.

[190] V. Bychkov et al., Nucl. Instrum. Methods in Phys. Res. **556** (2006) 66.

[191] P. Abbon et al., Nucl. Instrum. Methods in Phys. Res. A **577** (2007) 455.

[192] B. Bevensee et al., IEEE Trans. Nucl. Sci. B **43** (1996) 1725.

[193] A. Gorin et al., Czech. J. Phys. Suppl. **49** (1999) 173.

[194] N.V. Vlasov et al., Instrum. Exp. Tech. **49** (2006) 41.

[195] V.P. Balandin et al., JINR Preprint, **R13-2008-196**, Dubna (2008) (in Russian).

[196] E. Chiavassa et al., IEEE Trans. Nucl. Sci. **33** (1986) 209.

[197] L. Aphecetche et al., Nucl. Instrum. Meth. in Phys. Res. A **499** (2003) 521.

[198] G. Atoian et al., Nucl. Instrum. Meth. in Phys. Res. A **531** (2004) 467.

[199] A. Augusto Alves Jr. et al., JINST **3** (2008) S08005.

[200] CDR of the MultiPurpose Detector, v.1.4, JINR, Dubna; `http://nica.jinr.ru`.

[201] Z. Sadygov, Nucl. Instr. Meth. in Phys. Res. A **567** (2005) 70.

[202] R. Brun and F. Rademakers. ROOT – An Object Oriented Data Analysis Framework. In *Proc. of the AIHENP'96 Workshop*, volume **A**(389) of Nucl.Instr.and Meth.in Phys.Res. (1997), pages 81–86, Lausanne, Switzerland, (1996). See also `http://root.cern.ch/`.

[203] K. I. Gritsaj and A. Yu. Isupov. A Trial of Distributed Portable Data Acquisition and Processing System Implementation: the *qdpb* – Data Processing with Branchpoints. JINR Communications, **E10–2001–116** (2001) 1–19.

[204] Maciej Lipinski et al., White Rabbit Specification: Draft for Comments, version 2.0 (06-07-2011).

[205] T.Włostowski. Precise time and frequency transfer in a White Rabbit network. Master's thesis, Warsaw University of Technology (2011).

[206] F.Anghinolfi et al. NINO, an ultra-fast, low-power, front-end amplifier discriminator for the Time-of-Flight detector in ALICE experiment. IEEE Trans. Nucl. Science, **51**(5) (2004) 1974–1978.

[207] `http://www.freebsd.org/cgi/man.cgi?query=netgraph&sektion=4` , (2008).

[208] A. Yu. Isupov. The *ngdp* framework for data acquisition systems. JINR Communications, **E10–2010–34** (2010) 1–20; arXiv:1004.4474 [physics.ins-det], (2010).

[209] A. Yu. Isupov. CAMAC subsystem and user context utilities in *ngdp* framework. JINR Communications, **E10–2010–35** (2010) 1–20; arXiv:1004.4482 [physics.ins-det], (2010).

[210] A. Yu. Isupov. New software of the control and data acquisition system for the Nuclotron internal target station. JINR Communications, **E10–2012–32** (2012) 1–20; arXiv:1203.5242 [physics.ins-det], (2012).

[211] K. I. Gritsaj and V. G. Olshevsky. Software package for work with CAMAC in Operating system FreeBSD (in Russian). JINR Communications, **P10–98–163** (1998) 1–16.

[212] A. Yu. Isupov, V. E. Kovtun, and A. G. Foshchan. Implementation trial of the DAQ system for the compact physics setup on base of the *ngdp* framework (in Russian). In A. K. Vlasnikov, editor, *Fundamental problems and applications of nuclear physics: from space to nanotechnologies. Book of Abstracts*, 59 International Meeting on Nuclear Spectroscopy and Nuclear Structure (NUCLEUS-2009), page 346, Cheboksary, Russia, (2009). Saint-Petersburg, 2009.

[213] A. Yu. Isupov, V. A. Krasnov, V. P. Ladygin, S. M. Piyadin, and S. G. Reznikov. The Nuclotron Internal Target Control and Data Acquisition System. Nucl. Instr. and Meth. A **698** (2013) 127–134.

[214] `http://zlib.net/` , (2012).

[215] `http://tukaani.org/` , (2012).

[216] S.M. Piyadin et al., Phys. Part. Nucl. Lett. **9** (2012) 589.

[217] A.A. Terekhin et al., In Proc. of the XXI-th International Baldin Seminar on High Energy Physics Problems, September 10-15, 2012, JINR, Dubna, Russia, to be published in Proceedings of Science.

[218] `http://afi.jinr.ru/TQDC-16`